

# 3D CFD modelling of overflow dredging plumes



# 3D CFD modelling of overflow dredging plumes

Proefschrift

ter verkrijging van de graad van doctor  
aan de Technische Universiteit Delft,  
op gezag van de Rector Magnificus prof. ir. K.C.A.M. Luyben,  
voorzitter van het College voor Promoties,  
in het openbaar te verdedigen

op woensdag 14 januari 2015 om 15.00 uur

door

Lynyrd DE WIT  
civiel ingenieur  
geboren te Gouda

Dit manuscript is goedgekeurd door de promotor:

Prof.dr.ir. C. van Rhee

Copromotor:

Dr. ir. A.M. Talmon

Samenstelling promotiecommissie:

Rector Magnificus	voorzitter
Prof.dr.ir. C. van Rhee	Technische Universiteit Delft, promotor
Dr.ir. A.M. Talmon	Technische Universiteit Delft, copromotor
Prof.dr.ir. J.C. Winterwerp	Technische Universiteit Delft
Prof.dr.ir. B.J. Boersma	Technische Universiteit Delft
Prof.dr.ir. W.S.J. Uijttewaal	Technische Universiteit Delft
Prof.dr.ir. H.J. de Vriend	Technische Universiteit Delft
Prof.dr.ir. T. De Mulder	Universiteit Gent

The work presented in this thesis is carried out as part of the Building with Nature innovation program. The Building with Nature program (2008-2012) is funded from several sources, including the Subsidieregeling Innovatieketen Water (SIW, Staatscourant nrs 953 and 17009) sponsored by the Dutch Ministry of Infrastructure and the Environment, and partner contributions of the participants to the Foundation EcoShape. The program receives co-funding from the European Fund for Regional Development EFRO and the Municipality of Dordrecht. This work was sponsored by NWO Exacte Wetenschappen (Physical Sciences) for the use of supercomputer facilities, with financial support from the Nederlandse Organisatie voor Wetenschappelijk Onderzoek (Netherlands Organization for Scientific Research, NWO).

Keywords: Mixing, sediment, sand-mud-water mixture, dredging, jets, plumes, buoyancy, turbidity, turbulent flow, large eddy simulation.

Copyright © 2015 by [L. de Wit](#)

ISBN 978-94-6186-408-6

Printed by PrintPartners Ipskamp B.V., the Netherlands on FSC-certified paper originating from well-managed and sustainable sources.

# Contents

<b>Summary</b>	<b>v</b>
<b>Samenvatting</b>	<b>vii</b>
<b>1 Introduction</b>	<b>1</b>
1.1 Background	1
1.2 Research aim	2
1.3 Research methodology	2
1.4 Outline	4
<b>2 Description processes dredging plume</b>	<b>7</b>
2.1 Near, mid and far field dredging plume	7
2.2 Turbulent buoyant jet in crossflow	8
2.3 Semi-empirical description buoyant JICF	9
2.4 Near field processes dredging plume	11
2.5 Historical research context	12
2.6 Modelling approach near field dredging plume mixing	14
2.7 Conclusion	14
<b>3 CFD model</b>	<b>15</b>
3.1 Navier Stokes	15
3.2 Modelling turbulence	16
3.3 Implementation sand-mud-air phases	17
3.3.1 Settling velocity sand-mud phases	17
3.3.2 Rise velocity air fraction	20
3.3.3 Transport of the sand-mud-air fractions	22
3.3.4 Sand-mud-air drift velocity	23
3.3.5 Interaction sand-mud phases with bed	24
3.4 Implementation TSHD	25
3.4.1 TSHD hull	25
3.4.2 TSHD propellers	26
3.5 Boundary conditions	27
3.5.1 The free surface	27
3.5.2 Solid walls	28
3.5.3 Inflow and outflow	28
3.5.4 Synthetic turbulence ambient inflow	28

3.5.5	Overflow inflow . . . . .	29
3.6	Flow solver numerical details . . . . .	30
<b>4</b>	<b>Validation artificial viscosity advection scheme</b>	<b>31</b>
4.1	Introduction . . . . .	31
4.2	Description different advection schemes . . . . .	33
4.2.1	Advection scheme CDS2 . . . . .	33
4.2.2	Advection scheme UPW5 . . . . .	33
4.2.3	Advection scheme AV4 . . . . .	33
4.2.4	Advection scheme AV6 . . . . .	34
4.3	Fourier analysis advection schemes . . . . .	35
4.3.1	Fourier analysis of spatial discretisation . . . . .	35
4.3.2	Results of Fourier analysis . . . . .	36
4.4	Test case JICF $Re = 82000, Ri = 0, \gamma = 2$ . . . . .	37
4.4.1	Model set up . . . . .	37
4.4.2	Boundary conditions . . . . .	38
4.4.3	Results different advection schemes . . . . .	38
4.4.4	Robustness LES results . . . . .	39
4.4.5	Conclusions for JICF $Re = 82000, Ri = 0, \gamma = 2$ . . . . .	42
4.5	Test case buoyant jet in weak coflow $Re = 32000$ density ratio 1.52 . . . . .	44
4.5.1	Model set up . . . . .	44
4.5.2	Boundary conditions . . . . .	45
4.5.3	Results different advection schemes . . . . .	45
4.5.4	Robustness LES results . . . . .	45
4.5.5	Conclusions for buoyant jet in weak coflow $Re = 32000$ density ratio 1.52 . . . . .	48
4.6	Test case buoyant JICF $Re = 4800, Ri = 1.08, \gamma = 2.1$ . . . . .	48
4.6.1	Model set up . . . . .	48
4.6.2	Boundary conditions . . . . .	49
4.6.3	Results different advection schemes . . . . .	50
4.6.4	Robustness LES results . . . . .	51
4.6.5	Conclusions for buoyant JICF $Re = 4800, Ri = 1.08, \gamma = 2.1$ . . . . .	52
4.7	Discussion and conclusions . . . . .	52
<b>5</b>	<b>General validation CFD model</b>	<b>55</b>
5.1	Turbulent channel flow . . . . .	55
5.1.1	Turbulent channel flow . . . . .	55
5.1.2	Synthetic turbulent inflow . . . . .	56
5.2	Suspended sediment transport . . . . .	57
5.2.1	Low sediment concentration channel flow . . . . .	57
5.2.2	High sediment concentration channel flow . . . . .	57
5.2.3	Sediment deposition at the bed . . . . .	59
5.3	Density currents . . . . .	60
5.3.1	Density current at sloping bed . . . . .	60
5.3.2	Radial spreading of density driven overflow plume at bed . . . . .	61
5.3.3	Density current at bed including deposition . . . . .	62

---

5.4	Flow near the TSHD	64
5.4.1	Flow past a cube	64
5.4.2	Backward facing step	65
5.4.3	Propeller flow	68
5.5	Air-water mixture	71
5.5.1	Air-water jet in crossflow	71
<b>6</b>	<b>Buoyant JICF - lab scale</b>	<b>73</b>
6.1	Introduction	73
6.2	Experimental set up	73
6.3	Simulation set up	75
6.4	Buoyant JICF results	77
6.4.1	Comparison with experimental results	77
6.4.2	Comparison with semi-empirical solutions	79
6.4.3	Concentration profiles of buoyant JICF	82
6.4.4	Stream wise horizontal velocity inside buoyant JICF	85
6.5	Accuracy of LES results	88
6.6	Conclusions	89
<b>7</b>	<b>Influence of near field processes on a dredging plume - lab scale</b>	<b>91</b>
7.1	Introduction	91
7.2	Experimental set up	92
7.3	Simulation set up	93
7.4	Results and discussions	94
7.4.1	Validation LES results	94
7.4.2	Instantaneous longitudinal sections	98
7.4.3	Dredging plume paths	99
7.4.4	Time averaged cross sections	100
7.4.5	Anisotropy of turbulence	103
7.4.6	Grid resolution check	105
7.5	Conclusions	106
<b>8</b>	<b>Validation of near field dredging plume - field scale</b>	<b>109</b>
8.1	Introduction	109
8.2	Field measurements	109
8.3	Simulations	111
8.3.1	Simulation set up	111
8.3.2	Boundary conditions	112
8.3.3	Simulated overflow mixture	112
8.4	Results	113
8.4.1	Introduction	113
8.4.2	Case 1 from 2002 campaign	114
8.4.3	Case 2 from 2002 campaign	114
8.4.4	Case 3 from 2007 campaign	115
8.4.5	Case 4 from 2007 campaign	116
8.4.6	Case 5 from 2007 campaign	118

8.4.7	Case 6 from 2011 campaign	119
8.4.8	Case 7 from 2011 campaign	120
8.4.9	Synthesis all 7 cases	121
8.5	Conclusions	123
<b>9</b>	<b>Influence of near field processes on a dredging plume - field scale</b>	<b>125</b>
9.1	Introduction	125
9.2	Simulations	126
9.2.1	Near field set up	126
9.2.2	Near field boundary conditions	126
9.2.3	Mid field set up	127
9.3	Conditions parameter study	128
9.3.1	Overflow density and particle sizes	128
9.3.2	Overflow pulsing and air entrainment	129
9.3.3	Ambient velocity and sailing speed	130
9.3.4	Dredging depth	130
9.3.5	Combinations of input	130
9.4	Results	131
9.4.1	Example individual results near field plume	131
9.4.2	Near field plume results for all conditions	133
9.4.3	Translation results beyond the near field	137
9.4.4	Practical guidelines to determine a far field source flux	142
9.5	Conclusions	146
<b>10</b>	<b>IMPROVE: IMPact Reducing Overflow Extension</b>	<b>147</b>
10.1	Introduction	147
10.2	Extended overflow test runs	148
10.3	Extended overflow results	149
10.4	Conclusions on overflow extension	151
<b>11</b>	<b>Conclusions and recommendations</b>	<b>153</b>
11.1	General	153
11.2	New developments	154
11.3	Overflow dredging plume mixing	154
11.4	Recommendations	156
	<b>References</b>	<b>158</b>
	<b>List of symbols</b>	<b>171</b>
	<b>List of publications</b>	<b>175</b>
	<b>Dankwoord</b>	<b>177</b>
	<b>Curriculum Vitae</b>	<b>179</b>



# Summary

## *3D CFD modelling of overflow dredging plumes*

Already since the start of civilisation dredging is carried out to create and maintain waterways and ports or to create new land. In recent times the scale of dredging and awareness of potential environmental impact of dredging have increased drastically. An often used dredging vessel is the trailing suction hopper dredger (TSHD). A TSHD pumps up a sediment-water mixture from the bed into a hopper. In this hopper the sediment is given time to settle and the process water is spilled overboard, often through a vertical shaft called the overflow. The spilled process water will contain some suspended sediment which has not deposited yet and this forms a turbid plume. Increased turbidity and deposition at the bed of the suspended sediment from the overflow dredging plume can have negative environmental impact and modelling these influences of dredging is often an essential part of the environmental impact assessment of dredging works.

Initial mixing of the overflow dredging plume under/near the TSHD is not well understood. Although the plume starts under the keel of a TSHD, it has initial downward velocity and it is denser than the ambient water, sometimes a part of the plume flows upward and reaches the free surface right behind the TSHD. This so called surface plume can stay suspended for long periods and is therefore important for the potential environmental impact. This thesis reports on detailed numerical simulations, laboratory scale experiments and field scale measurements of overflow dredging plume mixing in the near field within some hundred metres of the TSHD. Specific attention is paid to the generation of a surface plume.

The numerical simulations are carried out with a variable density 3D computational fluid dynamics (CFD) model. The intermittent turbulent plume behaviour is captured by large eddy simulation (LES). The model can cope with the sediment-water-air mixture which flows through the overflow, the TSHD hull is included by an immersed boundary technique and the TSHD propeller flow is imposed by a body force. A novel momentum advection scheme has been developed which combines negligible dissipation at physical relevant scales with sufficient dissipation at grid scale. First aspect is essential for LES, second aspect is needed to damp numerical wiggles which can arise in front of an obstacle like the dredging plume in a crossflow. The numerical model is validated for a wide range of benchmarks available from literature which each cover some aspects of dredging plume mixing.

The influence of several near field conditions on dredging plume mixing is first investigated on laboratory scale. Numerical results are validated with new laboratory measurements and the CFD model gives accurate results. Seven field measurement cases of overflow dredging plumes at actual dredging projects are used to validate the numerical model on full scale. Subject to inaccuracies inherent to field measurements, the simulated plume path, flux and concentration distribution are reproduced by the CFD model

in a satisfactory way. Finally a large set of 136 full scale CFD simulations is conducted to investigate the influence of several important near field processes in a systematic manner.

It turns out that the most important processes generating a surface plume are the expanding flow at the aft of the TSHD and the interaction between the plume and the TSHD propellers. Air in the overflow also enhances the generation of a surface plume. Propellers lift the dredging plume up by entrainment into the propeller jet. The crossflow velocity (combination of dredging speed and ambient velocity) and depth are dominant conditions for the generation of a surface plume and the ratio of fine sediments still in suspension (ratio with the fines flowing through the overflow) at a certain settling time behind the TSHD. A higher crossflow velocity or a smaller depth lead to more surface plume. A higher crossflow velocity leads to a larger ratio of fines still in suspension, but although a smaller depth leads to more surface plume, the ratio of fines still in suspension is lower due to the reduced vertical settling distance. Another important factor determining the ratio of fines still in suspension is obviously the sediment settling velocity, but this is not influenced much by near field processes and is mainly governed by the material being dredged. A lower overflow density, lower overflow velocity, more air entrainment or dredging under an angle with the ambient current all lead to more surface plume and a larger ratio of fines still in suspension. But the influence of these factors is conditional: only with a low crossflow velocity and a large depth they have significant influence. With a high crossflow velocity or a small depth, the plume is mixed over the water column independent of the other factors. A pulsing, discontinuous flow in the overflow has two effects on dredging plume mixing: it enhances vertical spreading of the plume and it gives a deeper plume path caused by the extra inflow momentum. For a low crossflow velocity first effect is dominant resulting in a larger surface plume, for a high crossflow velocity second effect dominates and a smaller surface plume is found with pulsing. When an overflow is near the aft of a TSHD, the influence of propellers is stronger compared to the situation with an overflow near the front of a TSHD.

Guidelines to determine a far field source flux of suspended sediments from a TSHD while dredging are given and the large set of dredging plume simulation results are translated into mathematical relations which predict without computational effort the vertical distribution and flux of an overflow plume downstream of a TSHD.

By the CFD simulations, laboratory scale and field scale measurements more insight has been obtained in near field dredging plume mixing. The processes governing the generation of a surface plume are understood in a better way. These insights are translated to be usable in every day dredging engineering practise and used in the IMPROVE (IMPact Reducing OVerflow Extension) concept to reduce the environmental impact.

# Samenvatting

## *3D CFD modelering van overvloei baggerpluimen*

Vanaf het begin van de beschaving wordt er gebaggerd voor aanleg of onderhoud van waterwegen en havens of om nieuw land te creëren. Recentelijk is de schaal van baggeren en het besef van potentiële milieu effecten enorm toegenomen. Een vaak gebruikt baggerwerktuig is de trailing suction hopper dredger (TSHD). Een TSHD zuigt een sediment-water mengsel vanaf de bodem in een beun. Hier krijgt het sediment de tijd om te bezinken en het proceswater wordt overboord gemorst, vaak via een verticale buis die een overvloei genoemd wordt. Dit proceswater bevat vaak gesuspendeerd sediment wat nog niet bezonken is in het beun en dit vormt een troebele pluim. Toename in troebelheid en bezinking van gesuspendeerd sediment op de bodem kan een negatieve milieu impact hebben. Daarom is het modelleren van deze invloeden van baggeren vaak een essentieel onderdeel van een milieu-effect-rapportage van baggerwerken.

Er is nog veel onduidelijk over de initiële menging van een overvloei baggerpluim onder/nabij het baggerschip. Hoewel de pluim onder de kiel van het baggerschip begint, de initiële snelheid neerwaarts gericht is en de pluim zwaarder is dan de omgeving, komt toch soms een deel van de pluim direct achter het baggerschip omhoog naar het wateroppervlak. Deze oppervlaktepluim kan zeer lang in suspensie blijven en is daarom belangrijk voor de potentiële milieu impact. Deze dissertatie behandelt gedetailleerde numerieke simulaties, laboratorium schaal experimenten en veldmetingen van overvloei baggerpluimen in het 'near field' binnen enkele honderden meters van het baggerschip. De ontwikkeling van een oppervlaktepluim krijgt specifiek aandacht.

De numerieke simulaties zijn uitgevoerd met een 3D CFD (computational fluid dynamics) model met variabele dichtheid. Om het intermitterende turbulente pluim gedrag te kunnen simuleren wordt gebruik gemaakt van LES (large eddy simulatie). Het model kan omgaan met het sediment-water-lucht mengsel wat door een overvloei stroomt, de TSHD boeg wordt met een immersed boundary method gesimuleerd en de schroeven van het baggerschip worden via een opgelegde kracht gesimuleerd. Een nieuw impuls advectieschema is ontwikkeld. Dit schema combineert verwaarloosbare dissipatie op fysisch relevante lengteschalen met voldoende dissipatie op grid schaal. Het eerste aspect is essentieel om LES te kunnen toepassen, het tweede aspect is nodig om numerieke instabiliteiten te dempen die ontstaan voor een obstakel in de stroming zoals een baggerpluim in dwarsstroming. Het numerieke model is gevalideerd voor een breed scala aan relevante testgevallen uit de literatuur.

De invloed van verschillende near field omstandigheden op de menging van een baggerpluim is eerst op lab schaal onderzocht. Het CFD model geeft nauwkeurige resultaten op lab schaal. Zeven veldmetingen van overvloei pluimen op baggerwerken zijn gebruikt om het numerieke model te valideren op prototype schaal. Binnen de marge van de meetonnauwkeurigheden die horen bij veldmetingen zijn de gesimuleerde pluim

paden, fluxen en concentratieverdelingen in voldoende nauwkeurige mate gereproduceerd door het CFD model. Tenslotte is een parameterstudie met 136 CFD simulaties uitgevoerd om de invloed van verschillende belangrijke near field processen systematisch te onderzoeken.

De belangrijkste processen die een oppervlaktepluim genereren zijn de divergerende stroming aan de achterzijde van het baggerschip en de interactie tussen de pluim en de schroeven van het schip. Lucht in de overvloed draagt bij aan extra oppervlaktepluimontwikkeling. Schroeven tillen de pluim op door aanzuiging in de schroefstraal. De dwarsstroming (combinatie van vaarsnelheid en stroomsnelheid) en de diepte zijn de dominante factoren voor het ontstaan van een oppervlaktepluim en de ratio van fijn sediment in suspensie (ratio tussen fijn sediment in suspensie t.o.v. fijn sediment door de overvloed) na een bepaalde bezinktijd. Een sterkere dwarsstroming of een kleinere diepte zorgen voor meer oppervlaktepluim. Een sterkere dwarsstroming zorgt voor een grotere ratio van fijn sediment in suspensie. Een kleinere diepte zorgt ook voor meer oppervlaktepluim, maar door de geringere bezinkafstand neemt de ratio van fijn sediment in suspensie af. Ook de valsnelheid van sediment is een belangrijke factor die de ratio van fijn sediment in suspensie bepaald, alleen hangt deze nauwelijks af van near field processen maar voornamelijk van het gebaggerde materiaal. Een lagere overvloed dichtheid, lagere overvloed stroomsnelheid, meer luchtinsluiting of baggeren onder een hoek met de stroming leiden allemaal tot een grotere oppervlaktepluim en een grotere ratio van fijn sediment in suspensie. Maar de invloed van deze factoren is voorwaardelijk: alleen met een zwakke dwarsstroming of een grote diepte hebben ze significante invloed. Met een sterke dwarsstroming of kleine diepte is de pluim gemixt over de water diepte, onafhankelijk van de overige factoren. Een pulserende, discontinue, stroming in de overvloed heeft twee effecten: het verhoogt verticaal mengen van de pluim en het geeft een dieper pluim pad door de extra instroom-impuls. Bij een zwakke dwarsstroming domineert het eerste effect en ontstaat een grotere oppervlaktepluim, bij een sterke dwarsstroming domineert het tweede effect en ontstaat een kleinere oppervlaktepluim. Met een overvloed aan de achterzijde van een TSHD hebben de schroeven meer invloed dan met een overvloed aan de voorzijde.

Richtlijnen zijn gegeven om een far field bronterm van gesuspendeerd sediment van een TSHD te bepalen. De resultaten van de parameterstudie zijn vertaald in relaties om zonder computerkracht de verticale verdeling en flux van de pluim te bepalen.

Met de CFD simulaties, lab schaal en prototype schaal metingen is meer inzicht verkregen in de near field menging van een baggerpluim. De processen die zorgen voor een oppervlaktepluim worden nu beter begrepen. Deze inzichten zijn vertaald om rechtstreeks bruikbaar te zijn in de ingenieurspraktijk en gebruikt in het IMPROVE (IMPact Reducerende Overvloed VERlenging) concept om de milieu impact te verkleinen.

# Chapter 1

## Introduction

*The subject of this dissertation is introduced and the research question and methodology are explained.*

### 1.1 Background

Dredging is carried out all around the world, for example to keep waterways and ports navigable or to create new land. An often used dredging vessel is the trailing suction hopper dredger (TSHD), see Figure 1.1 for a schematic picture of a TSHD. A TSHD pumps up a sediment-water mixture from the bed into a hopper. In this hopper the sediment gets time to settle and the process water is spilled back into the ambient water through a vertical shaft called the overflow. Some sediment, that has not deposited yet in the hopper, will flow through the overflow with the process water and form a turbidity plume under the keel of the TSHD, see Figure 1.1. Increased turbidity can have a negative environmental impact because it reduces light penetration, visibility and it can clog filter feeders. Attached to the sediment, contaminants can be dispersed by the TSHD plume. The suspended sediment from the turbidity plume will deposit on the bed sooner or later and when the sedimentation is too much it can smother benthos and vegetation. Therefore, many studies have been published on the environmental impact of dredging and most of them focus on increased turbidity levels and sedimentation, see for instance Pagliai et al. (1985), Nichols et al. (1990), Gilkinson et al. (2003), Erftemeijer and Lewis-III (2006), Kim and Lim (2009), Erftemeijer et al. (2012), Capello et al. (2013), Mestres et al. (2013). Whether there is negative environmental impact of a dredging project depends on the frequency, duration and intensity of stresses like turbidity and sedimentation caused by dredging and on the resilience of an ecosystem (Erftemeijer and Lewis-III 2006; Erftemeijer et al. 2012). Many ecosystems for example are resilient enough to cope with large natural variations in turbidity and sedimentation levels during natural events as storms.

The overflow plume is the main source of suspended sediments from a TSHD during dredging (Bray 2008). It is not well understood what happens with the overflow plume under the keel of the TSHD. Sometimes turbid water can be seen

at the free surface right behind a TSHD while dredging, but sometimes there is no visible turbid water at the free surface, see Figure 1.2 for some examples.

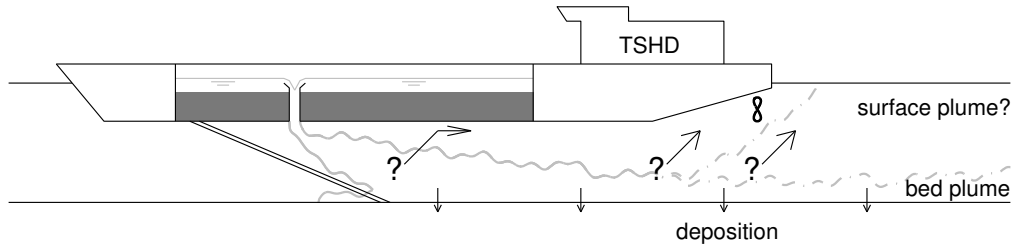


**Figure 1.1:** Schematic overflow dredging plume mixing which sometimes generates a surface plume with increased turbidity near the free surface and sometimes it generates only a bed plume with increased turbidity near the bed.

An overflow plume is denser than the ambient water, starts under the keel of the TSHD and has a downward initial velocity, therefore in principle one would expect the plume to flow downwards to the sea bed - not upwards to the free surface. Apparently there are extra processes which can cause a part of the plume to be transported upwards to the free surface. Some possible processes responsible for the generation of a surface plume are sketched in Figure 1.1 and they are: interaction between plume and TSHD hull; interaction between plume and TSHD aft and interaction between plume and TSHD propellers. Another possible cause of a surface plume is the entrainment of air with the plunging water into the overflow. As finer sediment settles slower in the hopper than coarser sediment, an overflow plume generally contains more fines than the dredged material (Rhee 2002). The fine sediment in the overflow plume can stay suspended for periods of hours to days, especially the fines in the surface plume. During this time the fines can be transported to environmental sensitive areas somewhere away from the dredging project, which makes the overflow dredging plume relevant for the environmental impact assessment of a dredging project.



**Figure 1.2:** Two examples with and one example without visible surface overflow dredging plume (right photograph from H. Elbers Royal Boskalis Westminster).

## 1.2 Research aim

The aim of this study is to provide insight in the overflow dredging plume mixing in the near vicinity of the TSHD and under its keel resulting in a practical translation to assess the plume deposition and flux without the necessity of long computer simulations. Specific attention is paid to processes which generate a surface plume and under which conditions this happens.

## 1.3 Research methodology

The research methodology is characterised by four steps:

- Process based CFD (computational fluid dynamics) simulations
- Experiments
- Field measurements
- Translation findings in practical guidelines and formula

The process based CFD simulations provide a 3D numerical test environment in which all conditions are known and governed perfectly. The influence of separate processes on overflow plume mixing and generation of a surface plume is investigated easily by changing just one condition and comparing the two model outcomes. In order for the CFD model to fulfil this aim as numerical test environment it must have incorporated all essential processes. As a basis, the rapid 3D non-hydrostatic Navier Stokes solver with variable density developed at the Laboratory for Aero and Hydrodynamics of the Delft University of Technology is used (Pourquié 1994). Adjustments to be able to deal with sediment, air, the TSHD and its propellers have been carried out within this study.

Before the CFD model results can be trusted, its results must be compared vigorously with scale experimental and field measurements. For this, existing experiments are used and new experiments are conducted. The new experiments include some specific processes responsible for the generation of a surface plume. In experiments the conditions can be governed much better than in a field measurement campaign, but not all processes can be incorporated in scale experiments.

Therefore also existing and new field measurements close to the TSHD are used to compare the simulated processes and outcomes with. The field measurements are carried out within the TASS (turbidity assessment software) framework<sup>1</sup>. The field measurements on themselves also provide knowledge on overflow dredging plume mixing nearby the TSHD and on the conditions when a surface plume is generated. In field measurements not all conditions are known or governed and it is very hard to obtain trustworthy plume data really close to

---

<sup>1</sup>TASS is initiated by SSB (Stichting Speurwerk Baggertechniek), which is a joint research framework of Royal Boskalis Westminster and Van Oord Dredging and Marine Contractors. The SSB is greatly acknowledged for making available the detailed and valuable data on field measurements of overflow plumes.

the overflow, like under the keel of the TSHD, but for this the experiments and CFD simulations are usable.

The combination of process based CFD simulations, experiments and field measurements can provide thorough and trustworthy insight in overflow plume mixing close to and under the keel of the TSHD. The main findings of this study will be translated into guidelines and formula usable in everyday dredging practice.

## 1.4 Outline

In Chapter 2 the different processes influencing the dredging plume are introduced and characteristic properties of the plume are given. Different zones of the plume with different dominant processes are identified. The rationale of present research approach is explained and linked to the existing research on dredging plume mixing. Then in Chapter 3 the CFD model is introduced with detailed information about the governing equations, boundary conditions, numerical solution methodology, and implementation of the sand-mud-air phases and the TSHD hull and propellers. Chapter 4 elaborates on a novel momentum advection scheme for the CFD model. The scheme is tested for three cases related to dredging plume mixing: non-buoyant jet in crossflow mixing, plume mixing and buoyant jet in crossflow mixing. Extra flow cases relevant for dredging plume mixing, like turbulent channel flow, suspended sediment transport, density current, flow past an obstacle, propeller flow and air-water flow are simulated in Chapter 5.

Next five chapters deal with actual dredging plume mixing. General buoyant jet in crossflow mixing without external influences is simulated on lab scale in Chapter 6 and compared with experiments. Chapter 7 continues with the influence of several processes on dredging plume mixing under the keel of a TSHD on lab scale. In Chapter 8 seven different measured cases from (full scale) dredging projects are used to validate the CFD model on field scale. In Chapter 9 136 full scale CFD simulations are presented for a systematic parameter study on the influence of variations in near field conditions. Chapter 10 investigates some alterations on the outflow location of the overflow flux from the TSHD to minimise the environmental impact of dredging plumes.

With Chapter 11 this dissertation ends with the conclusions and recommendations about dredging plume mixing.



## Chapter 2

# Description processes dredging plume

*The different processes influencing dredging plume mixing are introduced and some characteristic properties of plume mixing are discussed. A brief historical overview on previous research in this area is given and the rationale of the chosen modelling approach is explained.*

### 2.1 Near, mid and far field dredging plume

In this study near field is defined as the zone where plume mixing is dominated by density differences and interaction with the dredging vessel. Typically, the near field zone ends some hundred metres behind the TSHD, which corresponds to some minutes plume development. In the far field, plume mixing is mainly governed by sediment settling and ambient (tidal) currents. The far field typically covers the area of dozens of kilometres round a dredging project, for instance a complete estuary or sea, with a typical plume dispersion time scale of hours to days.

The focus of this study is plume mixing in the near field because near field mixing determines the amount and distribution of suspended sediment available in the far field. However, to be able to make the translation towards the far field, some mid field simulations are carried out as well. Mid field then covers a zone of some kilometres behind the TSHD, corresponding to 30 minutes plume development. In the mid field density differences (typically up to  $\Delta\rho = 3 \text{ kg/m}^3$ ) still have influence on plume mixing, but there is no interaction with the dredging vessel. Figure 2.1 gives a schematic overview of the near, mid and far field with the suspended sediment flux through the overflow  $S_{j0}$ ,  $S_{nf}$  from near to mid field and  $S_{mf}$  from mid field to far field. Due to deposition of sediment at the bed the suspended sediment is decreasing with increasing distance from the TSHD:  $S_{mf} < S_{nf} < S_{j0}$ .



**Figure 2.1:** Schematic overview of the near field, mid field and far field of a dredging plume with the suspended sediment fluxes  $S_{j0}$ ,  $S_{nf}$ ,  $S_{mf}$  indicated.

## 2.2 Turbulent buoyant jet in crossflow

The settling velocity of sediment in an overflow plume ranges from mm/s for (flocculated) mud (Smith and Friedrichs 2011) to cm/s for fine sand, which as long as the plume is not close to the sea bed, is one or two orders of magnitude lower than the dredging plume vertical velocity. Therefore, a dredging plume behaves like a turbulent (negatively) buoyant jet in crossflow (JICF) in the initial phase of the near field. Some other examples of buoyant JICF configurations are a chimney plume, fuel injection in an engine and an off-shore waste water outlet. As long as the jet starts fully turbulent, mixing of a buoyant JICF is not strongly dependent on the jet Reynolds number  $Re$  (Jirka 2004), but it is primarily governed by the Richardson number and velocity ratio (square root of the momentum ratio):

$$Ri = \frac{\rho_{j0} - \rho_{cf}}{\rho_{cf}} \frac{gD}{w_{j0}^2}, \quad (2.1)$$

$$\gamma = \sqrt{\frac{\rho_{j0} w_{j0}^2}{\rho_{cf} u_{cf}^2}}, \quad (2.2)$$

here  $\rho_{j0}$  and  $w_{j0}$  are the initial density and vertical velocity of the buoyant jet,  $\rho_{cf}$  and  $u_{cf}$  are the density and velocity of the crossflow,  $g$  is the gravity constant and  $D$  is the initial diameter of the jet (in this case equal to the diameter of the overflow). For overflow dredging plumes  $u_{cf}$  is determined by the vector sum of the TSHD sailing velocity and the ambient velocity:  $u_{cf} = \vec{u}_{TSHD} + \vec{u}_{ambient}$ . Dredging plumes created at a TSHD have typically  $\gamma = 0.3 - 4$  and  $Ri = 0.1 - 10$  and both initial momentum and buoyancy are important near the source (Fischer et al. 1979). There is an abundance of experimental studies concerning both buoyant and non buoyant JICF, see e.g. Fan (1967), Ayoub (1973), Chu and Goldberg (1974), Crabb et al. (1981), Andreopoulos and Rodi (1984), Margason (1993), but none of those studies has  $Ri$  and  $\gamma$  in the range of a dredging plume. An experimental study of the spreading character of dredging plumes on the seabed by Boot (2000), Winterwerp (2002) has the correct  $Ri$  and  $\gamma$  range. Also the MSC graduation study of Eekelen (2007) shows experimental results of buoyant JICF mixing in the  $Ri$  and  $\gamma$  range of interest.

Strictly speaking a dredging plume should be called an overflow dredging

buoyant jet, because it starts with both initial buoyancy and momentum and a plume starts with only buoyancy without initial momentum. But in this study we will use the term dredging plume because it fits better with standard nomenclature in dredging.

Buoyant and non buoyant JICF flow configurations have several characteristic large scale coherent structures like a counter rotating vortex pair, horseshoe vortices, wake vortices and shear layer vortices (Fric and Roshko 1994; Muldoon and Acharya 2010; Cavar and Meyer 2012). Due to all these flow structures the flow in a JICF is by definition highly turbulent and a buoyant JICF is very efficient at mixing. Figure 2.2 shows a sketch of buoyant JICF mixing. The cross section of a buoyant JICF is not a Gaussian profile with the maximum concentration in the centre, but the counter rotating vortex pair produces a kidney shaped profile with two concentration maxima outside the centre plane.

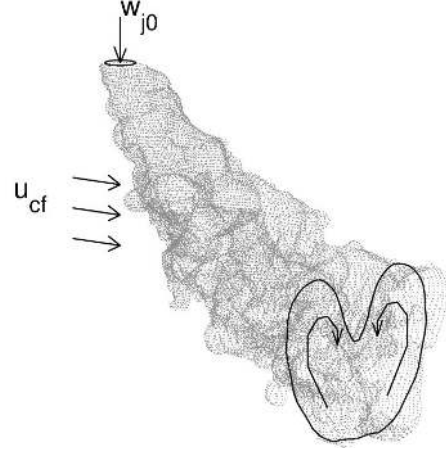


Figure 2.2: Schematic mixing of a (negatively) buoyant jet in crossflow.

## 2.3 Semi-empirical description buoyant JICF

The jet of a buoyant JICF injected perpendicularly to the flow starts with a vertical inlet velocity and a zero horizontal velocity. Moving downstream, the jet is accelerated in stream wise direction by the crossflow. The vertical momentum is important initially, but eventually buoyancy will take over. Fischer et al. (1979) has derived length scales to distinguish different flow regimes of a buoyant JICF. Within a distance of  $z < l_m$  from the source a buoyant jet acts as a jet and when  $z > l_m$  a buoyant jet acts as a plume. A length scale  $z_M$  is defined for the influence of initial momentum compared to the ambient current. As long as  $z < z_M$ , initial momentum is dominant over the ambient current. Another length scale is defined for the influence of initial buoyancy. As long as  $z < z_B$ , initial buoyancy is dominant over the ambient current. These length scales are given by:

$$l_m = \frac{(Q_{j0} w_{j0})^{3/4}}{B_{j0}^{1/2}}, \quad (2.3)$$

$$z_M = \frac{(Q_{j0} w_{j0})^{1/2}}{u_{cf}}, \quad (2.4)$$

$$z_B = \frac{B_{j0}}{u_{cf}^3}, \quad (2.5)$$

with the initial volume flux  $Q_{j0}$  and buoyancy flux  $B_{j0}$ :

$$Q_{j0} = \pi/4D^2w_{j0}, \quad (2.6)$$

$$B_{j0} = \frac{\rho_{j0} - \rho_{cf}}{\rho_{cf}}gQ_{j0}. \quad (2.7)$$

Independent of the ratio of initial momentum and buoyancy a buoyant JICF always ends as a bent over plume. As long as  $z_B > z_M$ , the transition to bent over plume happens after  $z > z_B$ . When  $z_M > z_B$ , this transition happens after  $z > z_C$ . Figure 2.3 summarises the length scales and associated flow regimes of a buoyant JICF derived by Fischer et al. (1979). The length scale  $z_C$  is given by:

$$z_C = z_M \left( \frac{z_M}{z_B} \right)^{1/3}. \quad (2.8)$$

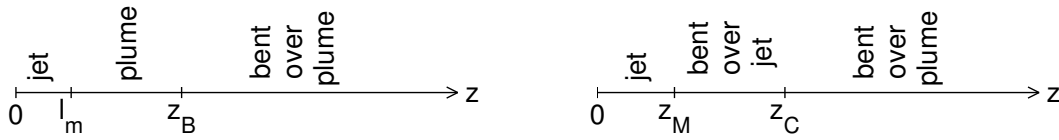


**Figure 2.3:** Length scales and flow regimes of a buoyant JICF in case  $Z_B > Z_M$  (left) and in case  $Z_M > Z_B$  (right).

For the end stage of a bent over plume, semi-empirical solutions of the buoyant JICF characteristics like path, vertical velocity and dilution can be derived from the balance of the mass and the momentum of the buoyant JICF. The most important assumptions for these semi-empirical solutions are that in the bent over phase the buoyant jet moves horizontally with the ambient velocity and that the spreading rate is constant. Following the analogy of an advected line thermal, the semi-empirical solutions of the buoyant JICF in the bent over plume phase are given by Lee and Chu (2003):

$$z_j = \left( \frac{3B_{j0}x_j^2}{2(1+k_n)\pi\beta^2u_{cf}^3} \right)^{1/3}, \quad (2.9)$$

$$w_j = \left( \frac{4B_{j0}}{9(1+k_n)\pi\beta^2x_j} \right)^{1/3}, \quad (2.10)$$

$$u_j = u_{cf}, \quad (2.11)$$

$$r_j = \beta z_j, \quad (2.12)$$

$$C_{j0}/C_j = \frac{\pi r_j^2 u_{cf}}{Q_{j0}}. \quad (2.13)$$

$z_j$  and  $x_j$  are the local buoyant JICF vertical and horizontal coordinate.  $w_j$  and  $u_j$  are the local buoyant JICF vertical and horizontal velocity.  $r_j$  is the local buoyant

JICF radius.  $C_{j0}$  is the initial jet concentration, and  $C_j$  is the local jet concentration. Hence,  $C_{j0}/C_j$  is the buoyant JICF dilution.  $k_n$  is the added mass coefficient and  $\beta$  is the spreading rate. Lee and Chu (2003) report spreading rates of  $0.34 < \beta < 0.62$  with  $k_n = 1$  from experiments. In Chapter 6 a different set of  $\beta, k_n$  is proposed which gives improved results. The buoyant JICF trajectory described by Equation 2.9 is comparable to the Briggs' classical plume trajectory (Contini and Robins 2001) in the bent over phase where the influence of the initial momentum is much smaller than the influence of the initial buoyancy. From Equations 2.9-2.13 the following asymptotic relations can be derived in the bent over phase:  $z_j \sim x_j^{2/3}$ ,  $w_j \sim x_j^{-1/3}$ ,  $r_j \sim z_j$ ,  $C_{j0}/C_j \sim x_j^{4/3}$ .

## 2.4 Near field processes dredging plume

A dredging plume can contain a wide variety in sediment particle diameter  $D_p$ , ranging from sand ( $D_p \geq 63\mu m$ ) to mud ( $D_p < 63\mu m$ ), but because finer sediment settles slower in the hopper than coarser sediment, an overflow plume generally contains more mud and fine sand than the dredged material (Rhee 2002). Under influence of turbulence, differences in settling velocity and Brownian motion, mud particles can cluster together to form flocs with typical sizes of 0.01-1 mm. The density of mud flocs is less than the density of individual mud particles, but the settling velocity is larger. Flocculation is especially important when the mud concentration is large, and therefore strong flocculation has been found for mud fractions inside an overflow plume with floc diameters of 40 – 800 $\mu m$  and floc settling velocities of 0.1 – 6mm/s (Smith and Friedrichs 2011). Even after flocculation the mud settling velocity is very small leading to large deposition periods, especially the mud in the surface plume can take hours to days before it has deposited at the seabed. Although the overflow plume leaves the vessel at the keel several meters below the water surface, the initial velocity is downward and it is denser than the ambient water (it is negatively buoyant), already close behind the dredger a part of the overflow plume can end up fully mixed near the water surface as a surface plume (Nichols et al. 1990; Whiteside et al. 1995). A surface plume can remain visible for considerable distances from a dredger (Newell et al. 1999).

General buoyant JICF mixing is not responsible for the generation of a surface plume, as it brings the plume further down - not up. Other dredging near field processes however, can generate a surface plume. When the dredging speed is high enough ( $\gamma$  small), or the overflow excess density is low ( $Ri$  small), or dredging is carried out in shallow water, the dredging plume can be influenced by the aft and propellers of the dredging vessel. When a TSHD is not sailing in line with the current but under an angle, the overflow plume will be pushed towards the side of the TSHD hull where it can be lifted upwards by the flow round the TSHD hull. Due to ship motions, waves can occur inside the hopper and the overflow discharge can be varying in time forming a pulsed plume under the keel. During measurements inside an overflow of a near empty TSHD a pulsing period of  $T_p = 1/f = 5.4s$  (Strouhal  $St = fD/w_{j0} = 0.18$ ) has been measured. The pulsing

disappeared when the load of the TSHD increased. In this case the pulsing period was equal to the ambient wave period, but in general the pulsing period will depend not only on the ambient wave period, but also on vessel/hopper characteristics. When the water level inside the vertical overflow shaft is much lower than the water level inside the hopper, the overflowing water forms a plunging jet in the shaft and significant amounts of air can be entrained into the overflow plume. There is experimental evidence that a main plume and the air content of this plume will separate into two separate plumes at a certain distance from the source (Socolofsky and Adams 2002; Zhang and Zhu 2013). The air reduces the excess density of the overflow plume and air bubbles rise towards the free surface; both mechanisms can lift sediment to the free surface. Therefore some TSHD's are equipped with a so called 'green valve' in the overflow to reduce the environmental impact of dredging plumes (Bray 2008); this valve causes an increased water level in the shaft by reducing the flow-through area of the shaft. In this way plunging is prevented and air entrainment is reduced. The amount of entrained air in an overflow without green valve can be estimated using the relation of Ervine (1998):

$$q_{air} = 0.00002(w_i - 1)^3 + 0.0003(w_i - 1)^2 + 0.0074(w_i - 1) - 0.0058, \quad (2.14)$$

with  $q_{air}$  as the volume flux of air per metre plunging width in [ $\text{m}^2/\text{s}$ ] and  $w_i$  as the vertical impact velocity in [ $\text{m}/\text{s}$ ] of a dropping water jet when it touches the water surface, 1 m/s is subtracted because minimal 1 m/s is needed for any form of aeration.  $w_i$  can be related to the drop height of a water jet by the assumption of initial zero vertical velocity and constant acceleration by gravity. In Figure 2.4 the air flux  $Q_{air} = q_{air}\pi D$  as a function of the drop height is compared to the water flux  $Q_{water} = \pi/4D^2w_{j0}$  in the overflow. Figure 2.4 shows that the percentage of entrained air depends strongly on drop height and  $w_{j0}$ : between 0 and 30% air entrainment can be expected for realistic overflow diameters in combination with realistic overflow velocities.

## 2.5 Historical research context

The settling behaviour of sediment in the hopper and the generation of the overflow spill flux is treated in Rhee (2002). A literature review by Dankers (2002) provides a good overview on the behaviour of fine sediment particles released through an overflow and the interaction of the sediment with the bed. Some field measurements of dredging plumes have been published (Wakeman et al. 1975; Hayes et al. 1984; Nakata et al. 1989; Nichols et al. 1990; Whiteside et al. 1995; RIZA 2005; Smith and Friedrichs 2011), but the plume results are site and project specific and do not give much information on how and why a surface plume is or is not generated.

Specific experimental dredging plume mixing studies have also been conducted. Boot (2000) carried out experiments of dredging overflow plumes for a MSc graduation and determined whether the plume radial spreading at the bed of the experimental flume was density driven or mixing dominated. These



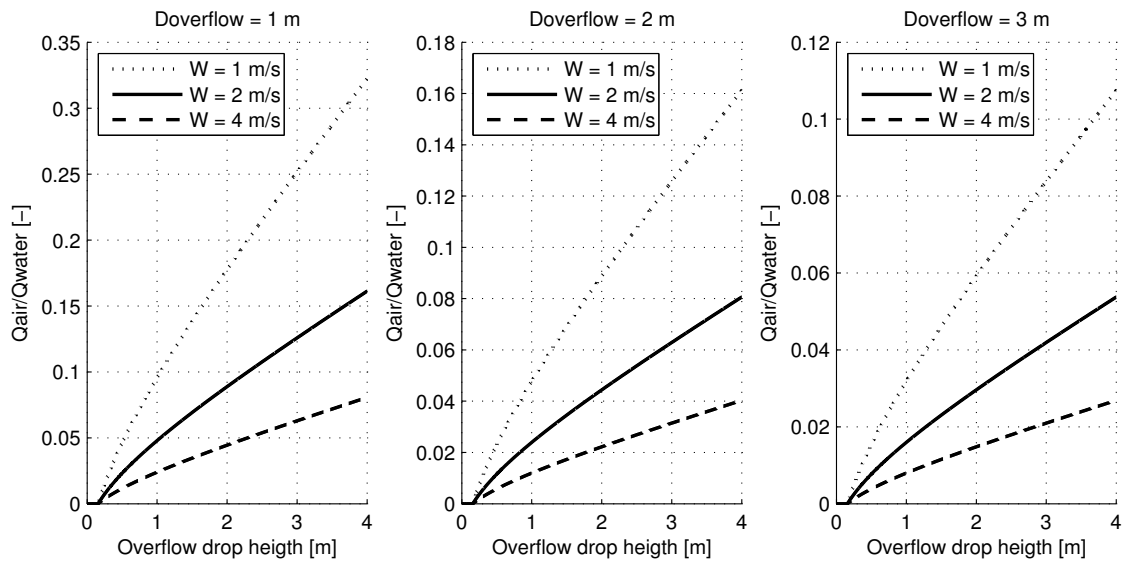


**Figure 2.4:** Estimate of the amount of entrained air in the overflow calculated with Equation 2.14 as a function of the overflow drop height.

results are used to classify dredging plumes in the paper of Winterwerp (2002). Another MSc graduation on dredging overflow plume mixing was carried out by Eekelen (2007). Experiments were conducted with as major aim to find mechanisms which generate a surface plume. In the experiments no surface plume was found as long as the plume and crossflow was continuous, but occasionally, for instance during start up or when the sediment mixer was clogged, the flow was disrupted (a pulsing flow) and separate sediment clouds formed a surface plume apart from the main plume. Air entrainment and interaction between the plume and the TSHD hull/aft/propellers were already defined as other possible processes causing a surface plume, but they were not incorporated in the experiments due to scaling issues and lack of resources.

The SSB has carried out dredging plume investigations in the TASS framework with field measurements (Aarninkhof et al. 2007; Aarninkhof et al. 2010), but not many results are published. Some of the TASS measurement results are used in the present study and are presented in a later chapter of this thesis. The TASS measurements are also used to develop the TASS model which, at the moment, consists of a hopper settling module and an overflow plume dispersion module (Spearman et al. 2011). The overflow plume dispersion module is able to simulate general density driven near field mixing of a dredging plume, but the specific processes responsible for the generation of a surface plume are not included and it needs a percentage for the surface plume as user input.

## 2.6 Modelling approach near field dredging plume mixing

Jet-integrated buoyant JICF models as [Jirka \(2004\)](#), [Jirka \(2007\)](#), and [Lee and Chu \(2003\)](#), [Lai and Lee \(2013\)](#) are suited for general buoyant JICF mixing behaviour, but they are not capable to represent the other relevant near field processes mentioned in Section 2.4. In this study, process based CFD (computational fluid dynamics) simulations are carried out to get insight in the 3D plume development near and under the keel of the TSHD. All relevant near field processes are included in the CFD model and results are compared with existing and new experiments and field measurements.

The flow of a buoyant JICF is highly turbulent and intermittent. In CFD simulations turbulence can be captured in several ways. Three often used approaches are DNS (Direct Numerical Simulation), LES (Large Eddy Simulation) and RANS (Reynolds Averaged Navier Stokes). In DNS all turbulent scales from the largest ones to the smallest Kolmogorov scales are solved on the grid and no separate turbulence model is used. In LES the larger turbulent scales which possess the majority of the turbulent energy are solved on the grid and the small turbulent scales (smaller than the grid size) are modelled by a turbulence model. In RANS all turbulent scales are modelled by a turbulence model. DNS requires such fine grids that it is not applicable for a practical problem as the mixing of a dredging plume with a high  $Re$  number and a large computational domain. In RANS the individual unsteady turbulent eddies in a dredging plume are filtered away by the turbulence model. Therefore, LES will be used to capture the individual unsteady turbulent eddies in a dredging plume which are important for the generation of a surface plume. Many LES simulations of non buoyant JICF have been published, see for example ([Schlüter and Schönfeld 2000](#); [Wegner et al. 2004](#); [Ziefle and Kleiser 2009](#); [Galeazzo et al. 2011](#)). Numerical LES simulations of buoyant JICF are more scarce however; we found one example with almost no initial buoyancy ( $Ri = 0.01$ ) ([Yuan and Street 1998](#)) and one example without initial momentum ( $Ri = \infty$ ) ([Devenish et al. 2010](#)).

## 2.7 Conclusion

General buoyant JICF behaviour, interaction with TSHD hull/aft/propellers, air entrainment and pulsing can influence the mixing behaviour of overflow dredging plumes in the near field in strong ways and can initiate the generation of a surface plume. The sediment settling velocity, including the influence of flocculation of mud, determines the rate of deposition of sediment from the dredging plume in the near field. Therefore all these processes are included in the present study. CFD simulations which employ the LES technique to capture the intermittent turbulent mixing behaviour, experiments and field measurements will be used to investigate the near field mixing behaviour of dredging plumes.



# Chapter 3

## CFD model

*In this chapter the CFD model used to simulate dredge plume mixing near a TSHD is introduced. The equations being solved are given together with the associated boundary conditions. Details are provided on the numerical discretisation, on the implementation of the sand-mud-air phases and on the implementation of the TSHD vessel.*

### 3.1 Navier Stokes

In the CFD model the Navier Stokes equations with variable density are solved:

$$\frac{\partial \rho}{\partial t} + \nabla \cdot (\rho \mathbf{u}) = 0, \quad (3.1)$$

$$\frac{\partial \rho \mathbf{u}}{\partial t} + \nabla \cdot (\rho \mathbf{u} \mathbf{u}) = -\nabla P + \nabla \cdot \boldsymbol{\tau} + \mathbf{F}, \quad (3.2)$$

where  $\rho$  is the density,  $\mathbf{u}$  is the velocity vector,  $t$  is time,  $P$  is the pressure,  $\boldsymbol{\tau}$  is a shear stress tensor and  $\mathbf{F} = [0, 0, (\rho - \rho_c)g_z]$  is the body force caused by gravitation. Pressure  $P$  is corrected for the hydrostatic pressure balance  $\frac{\partial P}{\partial z} = \rho_c g_z$  in vertical direction and thus  $P$  is the excess pressure over hydrostatic pressure. The density  $\rho$  is derived from the contribution of all volume fractions  $C_l$  in the mixture by:

$$\rho = \rho_c + \sum_{l=1}^{nfrac} C_l (\rho_l - \rho_c), \quad (3.3)$$

where  $\rho$  is the mixture density at each location in the grid,  $C_l$  and  $\rho_l$  are the volume concentration and density of each individual fraction and  $\rho_c$  is the density of the carrier fluid.

The CFD simulations are carried out on a cylindrical coordinate system  $r, \phi, z$  with pie-shaped grids, but results are presented in a Cartesian  $x, y, z$  coordinate system, see Figure 3.1. A staggered configuration of the variables, with pressure, density and volume concentration defined at the centre of a grid cell and each velocity component defined at an edge of the grid cell, is used for stability reasons. The grid is equidistant in  $\phi, z$  direction and variable in  $r$  direction. This choice allows for the use of structured solvers, that in general are faster than unstructured ones. The lateral expansion of the grid in downstream direction follows the

widening of the plume leading to an efficient distribution of the grid points. For some simulations a Cartesian grid is used, this is achieved by choosing  $r$  large and  $\Delta\phi$  small, leading to a constant  $\Delta y = r\Delta\phi$ .

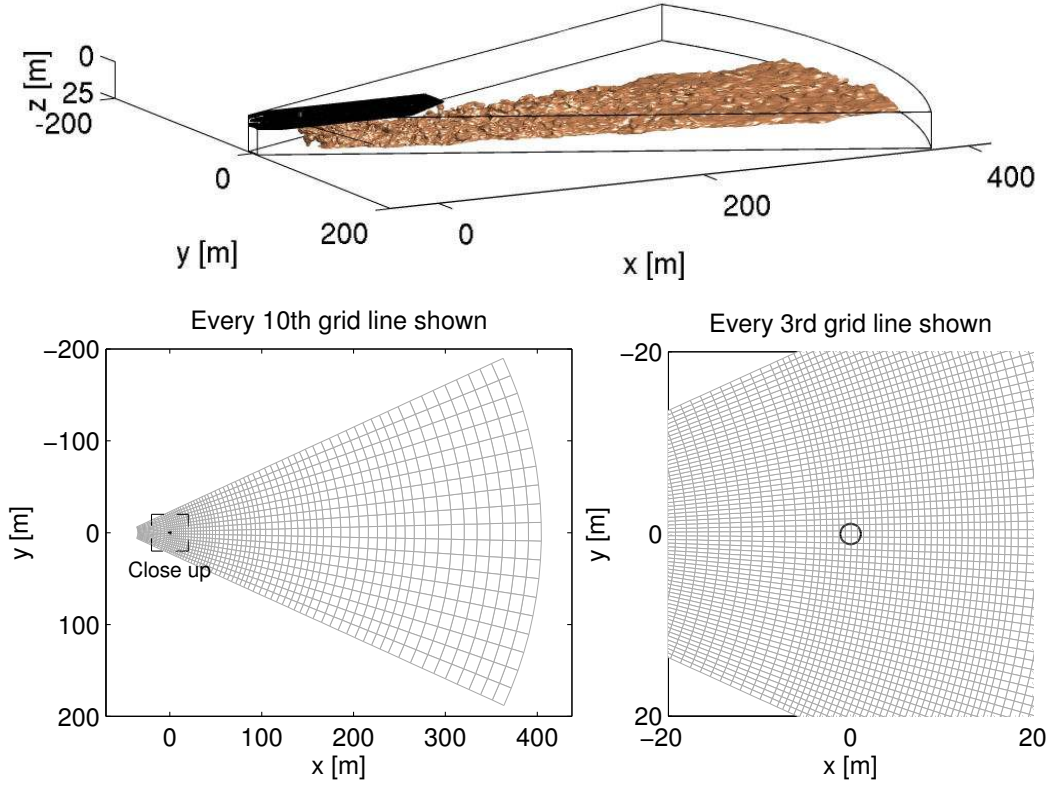


**Figure 3.1:** Example of the pie-shaped cylindrical grid used for simulating dredging plumes from a moving TSHD on full scale.

## 3.2 Modelling turbulence

In order to incorporate the influence of turbulence in the Navier Stokes equations the shear stress tensor is given by:

$$\boldsymbol{\tau} = \rho\nu_e(\nabla\mathbf{u} + \nabla(\mathbf{u})^T - 2/3\nabla\cdot\mathbf{u}), \quad (3.4)$$

and it contains a contribution from molecular and turbulent viscosity by the eddy viscosity concept:  $\nu_e = \nu_{mol} + \nu_t$ .

Three often used turbulent closures are DNS (Direct Numerical Simulation), LES (Large Eddy Simulation) and RANS (Reynolds Averaged Navier Stokes). In DNS all turbulent scales from the largest ones to the smallest Kolmogorov scales are solved on the grid and no separate turbulence model is used ( $\nu_t = 0$ ). In LES the larger turbulent scales which possess the major part of the turbulent energy are solved on the grid and the small turbulent scales (smaller than the grid size) are modelled by a turbulence model. In RANS all turbulent scales, large and

small, are modelled by a turbulence model. DNS requires such fine grids that it is not applicable for a practical problem as the mixing of a dredging plume with high  $Re$  number and large computational domain. In RANS the individual unsteady turbulent eddies in a dredging plume are filtered away by the turbulence model. Individual unsteady turbulent eddies in a dredging plume can influence the generation of a surface plume, thus therefore the LES approach is used in this study.

In the LES approach a spatial filter equal to the grid size is applied to the flow field and the contribution from smaller than grid scales is determined by a sub-grid-scale model:  $\nu_t = \nu_{sgs}$ . The WALE (wall adapting eddy viscosity) model (Nicoud and Ducros 1999) is used as sub-grid-scale model:

$$\nu_t = (C_s \Delta l)^2 \frac{(S_{ij}^d S_{ij}^d)^{3/2}}{(S_{ij} S_{ij})^{5/2} + (S_{ij}^d S_{ij}^d)^{5/4}} \quad (3.5)$$

with grid size  $\Delta l = (\Delta x \Delta y \Delta z)^{1/3}$ ,  $S_{ij}^d = \frac{1}{2}(g_{ij}^2 + g_{ji}^2) - \frac{1}{3}\delta_{ij}g_{kk}^2$  and  $S_{ij} = \frac{1}{2}(g_{ij} + g_{ji})$ .  $S_{ij}^d$  and  $S_{ij}$  are determined with the resolved velocities on the grid:  $g_{ij} = \frac{\partial u_i}{\partial x_j}$ ,  $g_{ij}^2 = g_{ik}g_{kj}$  and  $\delta_{ij}$  is the Kronecker delta ( $\delta_{ij} = 1$  for  $i = j$  and  $\delta_{ij} = 0$  for  $i \neq j$ ). In this study the value  $C_s = 0.325$  is adopted which corresponds to the often used value  $C_s = 0.1$  for the often used Smagorinsky sub-grid-scale model ( $\nu_t = (C_s \Delta l)^2 \sqrt{2S_{ij}S_{ij}}$ ). The advantage of the WALE model over for instance the Smagorinsky model is that it produces zero viscosity for pure shear flow and near a solid wall. Damping functions to force the turbulent viscosity to zero at walls are therefore not needed. This is especially advantageous because immersed boundaries with irregular shapes are used in this study. Applying a damping function at immersed irregular boundaries which are different in each simulation is a tedious job.

### 3.3 Implementation sand-mud-air phases

#### 3.3.1 Settling velocity sand-mud phases

Under the influence of gravity, sediment particles are settling. The terminal settling velocity is reached when buoyancy and drag reach equilibrium. For sand particles the terminal settling velocity is given by (Rijn 1993):

$$w_{0,p} = \frac{\Delta\rho/\rho_w g D_p^2}{18\nu} \quad \text{for } 1 < D_p \leq 100\mu\text{m}, \quad (3.6)$$

$$w_{0,p} = \frac{10\nu}{D_p} \left[ \sqrt{1 + \frac{\Delta\rho/\rho_w g D_p^3}{100\nu^2}} - 1 \right] \quad \text{for } 100 < D_p \leq 1000\mu\text{m}, \quad (3.7)$$

with  $w_{0,p}$  as the particle settling velocity,  $\Delta\rho = \rho_s - \rho_w$  as the density difference between sediment and water and  $D_p$  as the particle diameter. Equation 3.6 is the settling velocity in the Stokes (laminar) regime, Equation 3.7 is a formula by

Ruby and Zanke. Settling velocities of sand particles can be determined by the above mentioned formula. Mud particles (cohesive sediments) however, behave differently. Mud particles have characteristic sizes of  $D_p < 63\mu m$ , but under influence of turbulence, differences in settling velocities and Brownian motion they cluster together to form larger flocs. Flocs have typical sizes in the range 0.01 – 1 mm. The density of flocs is less than the density of the individual mud particles. The terminal settling velocity of mud flocs can be determined by an iterative formula of [Winterwerp \(1999\)](#):

$$w_{0,f} = \frac{\alpha \Delta\rho / \rho g D_p^{3-n_f}}{\beta} \frac{D_f^{n_f-1}}{1 + 0.15 Re_f^{0.687}}, \quad (3.8)$$

with coefficients  $\alpha, \beta = 1$ ,  $n_f = 2$ , particle diameter  $D_p$ , floc diameter  $D_f$  and  $Re_f = \frac{w_{0,f} D_f}{\nu}$ . The density difference  $\Delta\rho$  is defined by the difference in mud particle density and water density, not by floc density and water density. [Winterwerp \(1999\)](#) shows that  $n_f = 2$  is a proper value to calculate realistic mud floc settling velocities.

When the suspended sediment concentration is high, sediment particle-particle interactions are no longer negligible. In this regime the settling velocity is reduced by hindered settling. Hindered settling is caused by the return flow created by the settling particles, the increased mixture density which reduces the driving buoyancy force, the increased mixture viscosity and the particle-particle collisions. A well known empirical hindered settling formula is the one by [Richardson and Zaki \(1954\)](#):

$$w_s = w_0 (1 - C_t)^n, \quad (3.9)$$

with  $w_s$  as the settling velocity in a suspension with  $w_0$  as the settling velocity of an individual particle or floc as described by Equation 3.6, 3.7, or 3.8, and total volume concentration  $C_t$ :

$$C_t = \sum_{l=1}^{nfrac} C_l, \quad (3.10)$$

According to [Richardson and Zaki \(1954\)](#), coefficient  $n$  in Equation 3.9 varies between  $2.39 \leq n \leq 4.65$  depending on  $Re_p = \frac{w_{0,p} D_p}{\nu}$ . In this study the relation by [Rowe \(1987\)](#) is used:

$$n = \frac{4.7 + 0.41 Re_p^{0.75}}{1 + 0.175 Re_p^{0.75}} \quad (3.11)$$

As shown by [Rhee \(2002\)](#) the [Rowe \(1987\)](#) relation for  $n$  is a smoothed representation of the original coefficients found by [Richardson and Zaki \(1954\)](#). For hindered settling of flocs [Winterwerp \(1999\)](#) proposes the following relation:

$$w_{s,f} = w_{0,f} \frac{(1 - C_{floc})^M (1 - C_t)}{1 + 2.5 C_{floc}}, \quad (3.12)$$

with  $w_{s,f}$  as the settling velocity of flocs in a suspension with total volume concentration  $C_t$ ,  $w_{0,f}$  as the settling velocity of an individual floc described by Equation 3.8. The best value for coefficient  $M$  is shown to be  $M = 2$  in [Dankers and](#)

Winterwerp (2007). The volume floc concentration  $C_{floc}$  is defined by:

$$C_{floc} = \frac{SSC}{SSC_{gel}} = \frac{SSC}{\rho_s \left(\frac{D_p}{D_f}\right)^{3-n_f}} = C \left(\frac{D_p}{D_f}\right)^{n_f-3}, \quad (3.13)$$

where  $SSC$  is the suspended sediment concentration and  $SSC_{gel}$  is the gelling concentration of mud flocs. The gelling concentration is the concentration at which all flocs cluster together to form a gel and the settling velocity goes to zero. With this formulation  $C_{floc}$  can become larger than 1, hence to prevent incorrect settling velocities  $C_{floc}$  is limited at maximum 1.

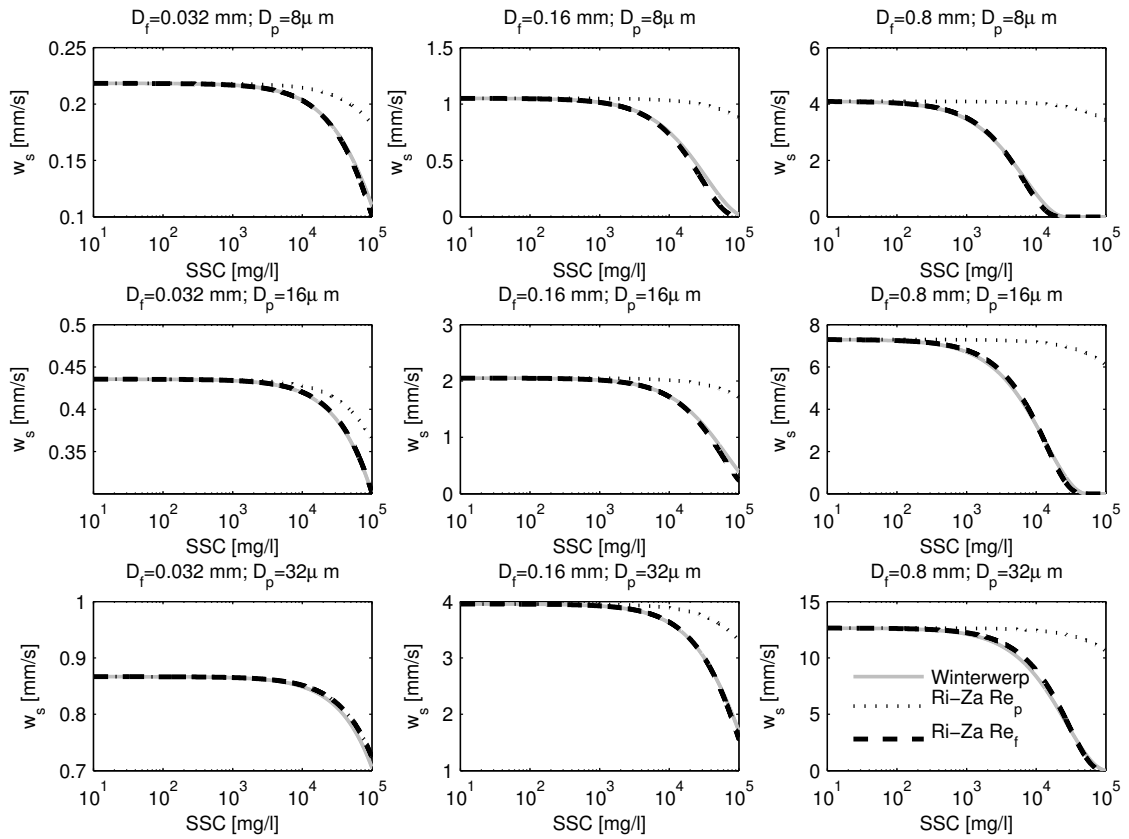


**Figure 3.2:** Comparison of different sediment hindered settling formulations from Winterwerp and Richardson-Zaki for flocs with different diameters.

For three different mud particle diameter  $D_p$  and three different floc diameters  $D_f$  the hindered settling velocity of the floc is calculated as function of the sediment concentration using the relation of Richardson-Zaki (Eq. 3.9) and the relation of Winterwerp (Eq. 3.12). For the Richardson-Zaki formula two calculations are performed: one in the ordinary way with the particle parameters  $D_p, C_t, Re_p$  and one with the floc parameters  $D_f, C_{floc}, Re_f$ . In the latter  $n$  is determined with  $Re_f$  instead of  $Re_p$  and  $C_{floc}$  is used:

$$w_s = w_0(1 - C_{floc})^n. \quad (3.14)$$

In all cases the settling velocity of an individual floc is described by Equation 3.8. The comparison between the two Richardson-Zaki and the Winterwerp hindered settling velocities is shown in Figure 3.2. It shows that the Richardson-Zaki hindered settling velocity using floc parameters instead of particle parameters is close to the Winterwerp hindered settling velocity. Therefore the Richardson-Zaki hindered settling velocity will be used in this study for both sand and mud fractions. For sand fractions the individual particle settling velocity is determined using Equation 3.6 or 3.7 and  $D_p, C_t, Re_p$  are used for the Richardson-Zaki hindered settling. For mud fractions Equation 3.8 is used together with  $D_f, C_{floc}, Re_f$  in Richardson-Zaki.

Figure 3.2 also shows that hindered settling does not play a role when  $SSC < 10^3$  mg/l. As Equation 3.8 is linear in the particle size  $D_p$  for  $n_f = 2$ , the settling velocity in Figure 3.2 simply increases linearly with  $D_p$  when the same floc is build up from larger individual particles. Only for large  $D_f$  the settling velocity stops to grow linearly with  $D_p$  because of the influence of  $Re_f$  in Equation 3.8. For the smaller flocs in Figure 3.2 the influence of  $Re_f$  is small and the hindered settling velocity is linear in  $D_f$ . But for the largest flocs  $Re_f$  becomes more important and the hindered settling velocity is not linear in  $D_f$  any more.

### 3.3.2 Rise velocity air fraction

Under the influence of gravity, air bubbles are rising, which can be seen as a negative (upward) settling velocity. The terminal rising velocity of air bubbles is reached when buoyancy and drag reach equilibrium. The relation between the terminal air bubble rise velocity and air bubble diameter for still water from Clift et al. (1978) for fresh water and from Chanson et al. (2002) for fresh water and sea water are presented in Figure 3.3. For fresh water Clift et al. (1978) and Chanson et al. (2002) agree for air bubbles larger than 1.5 mm. The difference between the air bubble rise velocity in fresh water and in sea water for similar bubble diameter is negligible. However, air bubbles created at a plunging jet in sea water are finer than in fresh water, air bubble coalescence is reduced and less air volume is entrained: in a scale experiment of a plunging jet with a nozzle diameter of 12.5 mm Chanson et al. (2006) found a wide variety in air bubbles chord lengths of  $< 0.5$  mm to  $> 10$  mm for fresh and sea water with a smaller mean air bubble chord length in sea water of 3 to 6 mm compared to the mean air bubble chord length of 4 to 7 mm in fresh water. The smaller air bubble size and lower air volume entrainment in sea water can partly be explained by physical properties as density, viscosity, salinity and surface tension, but these physical properties cannot explain all observed differences. Sea water also gives less air entrainment and smaller bubble sizes than saline water, therefore additional differences as organic matter and living organisms (e.g. plankton, algae) must play a role as well (Chanson et al. 2006). In a fresh water full scale experiment of a drop shaft with a drop height of 1.7 m, bubble chord sizes of  $< 0.5$  to  $> 25$  mm are measured with mean values of 8 to 10 mm in the drop shaft below the water line and mean values of 2 to 5 mm in the horizontal outflow channel (Chanson 2007).

The overflow of a TSHD is a sand-mud-water mixture drop shaft with drop



heights in the order of 0 to 3 m. Dredging often takes place at sea, therefore smaller air bubble sizes are expected than in the experiment of Chanson (2007) with fresh water. Based on the results of Chanson et al. (2006) and Chanson (2007) air bubbles in the overflow are expected to have diameters of  $<0.5$  to  $> 25$  mm with a mean diameter in the range of 1 to 9 mm. The sea water air bubble rise velocity for bubble sizes of 1 to 9 mm is 0.4 to 0.24 m/s. In the overflow dredging plume simulations of this study one air bubble fraction is used with a rise velocity of 0.25 m/s which is representative (less than 0.01 m/s difference) for a wide range of air bubble diameters from 3 to 10 mm, see Figure 3.3. At the free surface air can escape from the water. More air fractions can be used in the CFD model, but exact data on the air bubble size distribution in an overflow is lacking and an extra fraction causes an increase of about 15% in computational time. Air bubble coalescence and breakup are not taken into account. The compressibility of air is neglected. The increase in pressure between the free surface and the keel of the TSHD at about 10 m water depth halves the air volume and reduces the bubble diameter by approximately 26%. A reduction in bubble diameter of 26% has limited influence on the air bubble rise velocity. The estimate of the volume of air entrainment in the overflow in Figure 2.4 is defined at the plunge point, i.e. at atmospheric pressure. Hence, near the free surface the air volume and influence on mixture density and buoyancy in the model are as intended, but at a keel of 10 m deep they are overestimated by a factor two. Implementation of a compressible fraction in the applied incompressible CFD solver is not straightforward, and given the large uncertainty in the exact volume of air entrainment in the overflow, compressibility of air is ignored for now. The presented results on the influence of air on the overflow dredging plume provides valuable new insight, but improvement on the implementation of the air fraction is possible.

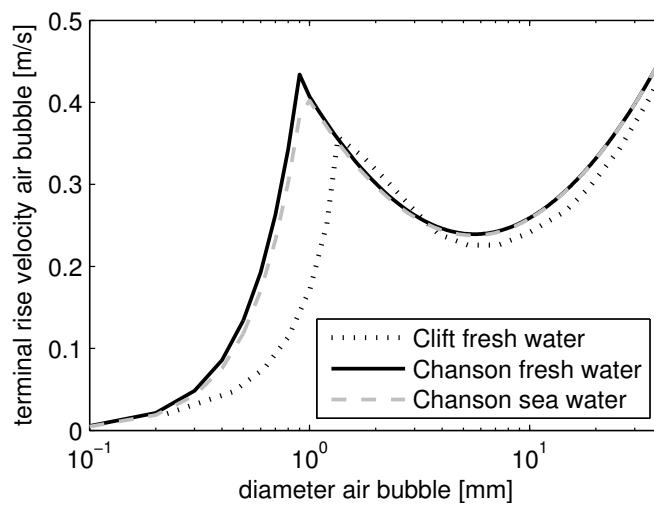


Figure 3.3: Terminal air bubble rise velocity in 20°C water.

### 3.3.3 Transport of the sand-mud-air fractions

The transport equation of the volume fraction  $C_l$  of each sand, mud or air fraction is given by:

$$\frac{\partial C_l}{\partial t} + \nabla \cdot (\mathbf{u}_l C_l) = \nabla \cdot (\Gamma \nabla C_l), \quad (3.15)$$

with the diffusion coefficient  $\Gamma = \frac{\nu_e}{Sc}$ , a Schmidt number  $Sc = 0.7$ , and the eddy viscosity  $\nu_e$ . In both horizontal directions the mixture velocity is used to transport fractions ( $u_l = u_{mix}$  and  $v_l = v_{mix}$ ) and in vertical direction the mixture velocity is corrected with a drift velocity to account for settling:

$$w_l = w_{mix} + w_{drift,l}, \quad (3.16)$$

in which  $w_l$  is the vertical transport velocity of an individual fraction,  $w_{mix}$  is the mixture velocity as calculated by the CFD model according to Equations 3.1-3.2 and  $w_{drift,l}$  is the drift velocity. The drift velocity will be explained in next section, but now the numerical discretisation of the transport equation is explained.

A volume fraction cannot become negative in real life and mixing can never increase a concentration. Numerically, this is only the case when special care is taken of the advection term in the transport equation of a volume fraction. In order to prevent non-physical under- or overshoot of a volume fraction a total variation diminishing (TVD) flux limiting scheme is used for the advection of volume fractions (Hirsch 1990). A TVD scheme is a blend between a high order scheme and a low order scheme. Away from gradients the method is more accurate by using the high order scheme. Near sharp gradients, accuracy is a term without meaning, and the scheme shifts towards the more stable low order scheme. The staggered flux limited scheme for  $C_{l,i+\frac{1}{2}}$  at a cell face in a one-dimensional case with  $C_{l,i}$  at the centre of a cell is given by:

$$\begin{aligned} C_{l,i+\frac{1}{2}} &= C_{l,i} + \frac{1}{2} \Psi(q_{i+\frac{1}{2}}^+) (C_{l,i+1} - C_{l,i}) (1 - CFL) \quad \text{if } u_{l,i+\frac{1}{2}} \geq 0 \\ C_{l,i+\frac{1}{2}} &= C_{l,i+1} + \frac{1}{2} \Psi(q_{i+\frac{1}{2}}^-) (C_{l,i+1} - C_{l,i}) (1 - CFL) \quad \text{if } u_{l,i+\frac{1}{2}} < 0 \end{aligned} \quad (3.17)$$

with  $CFL = \Delta t |u_{l,i+\frac{1}{2}}| / \Delta x$  and  $\Psi(q)$  as the flux limiter depending on the local change in gradient of the scalar  $C_l$ :

$$q_{i+\frac{1}{2}}^+ = \frac{C_{l,i} - C_{l,i-1}}{C_{l,i+1} - C_{l,i}} \frac{x_{i+1} - x_i}{x_i - x_{i-1}} \quad \text{and} \quad q_{i+\frac{1}{2}}^- = \frac{C_{l,i+2} - C_{l,i+1}}{C_{l,i+1} - C_{l,i}} \frac{x_{i+1} - x_i}{x_{i+2} - x_{i+1}} \quad (3.18)$$

The flux limited scheme in Equation 3.17 is a blend between the first order upwind scheme and the second order Lax-Wendroff scheme. An often applied blend between first order upwind and second order central (Equation 3.17 without the  $(1 - CFL)$  term) was found to be unstable for  $0.5 < CFL < 1$  with first order Euler time integration. Equation 3.17 is stable for  $0 < CFL < 1$  with first order Euler time integration. The limiter function  $\Psi(q)$  regulates the blend and with this blending the amount of artificial (numerical) diffusion is controlled. The limiter function can even generate anti-diffusion to make gradients sharper.



In this study the Van Leer limiter is used:  $\Psi(q) = \frac{q+|q|}{1+|q|}$ . More aggressive limiters, as for example the Superbee limiter, have less artificial diffusion, but can generate significant non-physical steepening of gradients; the Van Leer does not suffer from this drawback.

Diffusion in the volume fraction transport equation is discretised with the standard second order central scheme. Time integration is carried out with similar time integration scheme as used in the Navier Stokes flow equations, namely Wray's third order Runge Kutta (RK3) scheme (Wesseling 2000) with  $CFL < 1.6$ , but each RK3 sub-step is treated as a first order Euler explicit step. This choice leads to stable TVD results. Wray's RK3 time integration applied directly to the TVD scheme was found to be unstable for  $1 < CFL < 1.6$ . As initial condition  $C_l = 0$  is used and boundary conditions for  $C_l$  are described in Section 3.3.5 and 3.5.

### 3.3.4 Sand-mud-air drift velocity

The implementation of the drift velocity in the mixture model follows the approach of Manninen et al. (1996). Each fraction is transported in vertical direction by the sum of the mixture velocity and the drift velocity, see Equation 3.16. The drift velocity  $w_{drift,l}$  is the settling velocity corrected for the return-flow created by all settling fractions and it is given by:

$$w_{drift,l} = w_l - w_{mix} = w_{s,l} - \sum_{m=1}^{nfrac} C_m \frac{\rho_m}{\rho_{mix}} w_{s,m}, \quad (3.19)$$

where  $w_{s,l}$  and  $w_{s,m}$  are the settling velocity of fraction  $l$  respectively fraction  $m$ ,  $\rho_m$  is the density of fraction  $m$ ,  $\rho_{mix}$  is the mixture density and  $C_m$  is the volume concentration of fraction  $m$ .  $w_{s,l}$  is given by:

$$w_{s,l} = w_{0,l}(1 - C_t)^{n-1}. \quad (3.20)$$

$w_{s,l}$  is based on the Richardson-Zaki hindered settling velocity. The power  $n$ , given by Equation 3.11, is lowered to account for the return flow already incorporated in Equation 3.19.  $w_{0,l}$  is the settling velocity of an individual sand, mud or air particle without interaction with other phases.  $C_t$  is a summation of the volume concentrations of the sand and air fraction and the floc volume concentration for mud, see Equation 3.10. As  $C_t$  now consists of the sum of  $C$  for sand and air fractions and  $C_{floc}$  for mud fractions, it can be larger than 1. Therefore,  $C_t$  is limited at maximum 1.

The drift velocity of each fraction causes a force which is felt by the mixture flow. This force is incorporated to the LHS of Equation 3.2 by adding the advection of the drift velocity to the vertical momentum equation:

$$\frac{\partial}{\partial z} \cdot \left( \sum_{l=0}^{nfrac} C_l \rho_l w_{drift,l} w_{drift,l} \right), \quad (3.21)$$

with fraction  $l = 0$  defined as the carrier fluid phase.

### 3.3.5 Interaction sand-mud phases with bed

Sediment phases in the water column close to the bed can deposit. The deposition flux of sand and mud is given by:

$$Dep_l = C_l \rho_l w_l, \quad (3.22)$$

with  $Dep_l$  as the deposition flux of sand or mud fraction  $l$  in [kg/s per m<sup>2</sup>],  $C_l$  as the volume concentration of fraction  $l$  in the first computational cell above the bed and the drift velocity  $w_l$  determined by Equation 3.19 with  $w_{mix} = 0$  because it is the bed. Following Winterwerp and Kesteren (2004) and Winterwerp (2007), deposition of mud is simulated by Equation 3.22, and not by the classical Krone deposition function for mud in which there is no deposition above a critical bed shear stress. Winterwerp (2007) argues that this critical bed shear stress for deposition of mud does not exist. Erosion of mud phases from the bed is described with the classical Partheniades formulation for the erosion flux:

$$Ero_l = \begin{cases} M_l \left( \frac{\tau - \tau_e}{\tau_e} \right) & \text{for } \tau > \tau_e \\ 0 & \text{for } \tau < \tau_e \end{cases} \quad (3.23)$$

with  $Ero_l$  as the erosion flux of mud fraction  $l$  in [kg/s per m<sup>2</sup>]. For cohesive sediments  $M_l$  is an erosion rate in the range of  $1 \cdot 10^{-5} - 5 \cdot 10^{-4}$  kg/s per m<sup>2</sup>,  $\tau_e$  is the critical bed shear stress for erosion in the range of  $0.15 < \tau_e < 0.5$  N/m<sup>2</sup> (Rijn 1993). A more elaborate formulation for erosion of cohesive sediments is given by Prooijen and Winterwerp (2010), by writing an adapted version of the Partheniades erosion formulation, that is dependent on the time averaged bed shear stress, but with the influence of turbulent fluctuations on the bed shear stress incorporated. In this study turbulent fluctuations in the bed shear stress are already (partly) captured by the LES approach, therefore the classical Partheniades formulation is used to calculate erosion of mud fractions.

Erosion of sand is ignored in this study by choosing  $M_l = 0$  for sand phases. The small error made by neglecting erosion of sand phases has no big impact because sand will deposit on the bed quickly. For the source term of available sediments from a TSHD for far field mixing the mud phases are more important than sand phases. Interaction between sand and mud phases in the bed, like mud particles sheltering between and under sand particles or burial of one fraction under the other is ignored. Sheltering of mud particles between and under sand particles is not expected to be important in the few minutes that are simulated of the mixing process of a dredging plume. Burial of one fraction under the other is at least partly prevented by the different distance from the TSHD at which sand and mud phases deposit.

The erosion of mud depends on the shear stress acting on the mud. The instantaneous horizontal flow velocity in the first cell at  $\frac{1}{2}\Delta z$  above the bed is known from the LES model. By a law of the wall this flow velocity can be related to a shear stress, see Section 3.5.2. A law of the wall needs a roughness height  $k_s$  to determine the shear stress. It is not straightforward to determine the proper  $k_s$  for a correct bed shear stress acting on the mud in the bed. For the shear stress

acting on the flow  $k_s$  is chosen according to larger scale bed shapes, for LES simulations of a TSHD at open sea this  $k_s$  is often in the order of 0.01-0.2 m. This  $k_s$  is too large for the bed shear stress acting on mud particles in the bed. For the bed shear stress acting on sand in a bed rules of thumb like  $k_s \approx 3D_{90} \approx 6D_{50}$  are available (Rijn 1993). Jacobs (2011) uses  $k_s = 0$  (hydraulically smooth conditions) to translate LES velocities into a bed shear stress for simulations on laboratory scale with a sand-mud bed and for his case he concludes that it is recommended to recalibrate his LES simulations using hydraulically rough or transitional conditions. In this study  $k_s = D_{floc}$  is used for mud fractions as it agrees with the recommendation of Jacobs (2011) and is not far off from the rule of thumb often used for sand.

The deposition and erosion amounts  $Dep_l$  and  $Ero_l$  are subtracted and added each time step to  $C_l$  in the lowest grid cell. The total cumulative amount of deposition and erosion in the bed is also tracked to be able to show deposition amounts and locations. The computational grid is attached to the moving TSHD, this implies that the bed and the bed material in the model moves backwards with respect to the computational grid.

## 3.4 Implementation TSHD

### 3.4.1 TSHD hull

The shape of the TSHD hull is included in the computational domain by a direct forcing immersed boundary method (IBM) (Fadlun et al. 2000): a force is applied to make the velocity zero in all grid cells inside the hull. A schematised shape of a TSHD without front bulb and a straight sloping aft is used, see Figure 3.4. The drag heads and suction pipes are included as obstacles because they can cause extra mixing of the overflow dredging plume.

The flow velocity near the TSHD hull is slightly different from the vector sum of the trailing speed and ambient velocity because the hull is an obstacle which influences the flow. There are lateral and vertical variations in the flow velocity past the hull. The simulation grid of a plume simulation starts approximately 15 overflow diameters in front of the overflow and the front end of the bow of the TSHD is missing to save valuable computational time. In order to generate the correct inflow velocity profiles (including the blocking effect) for

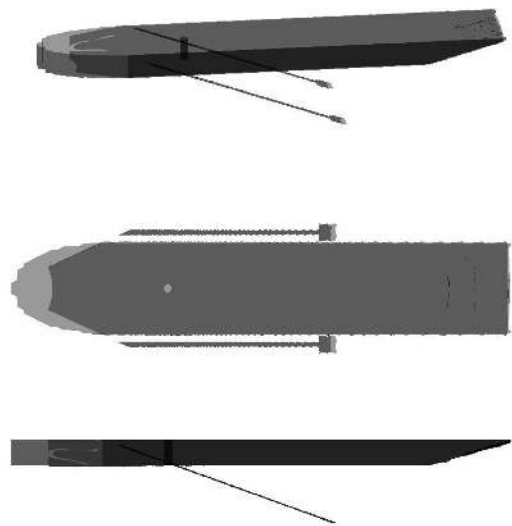
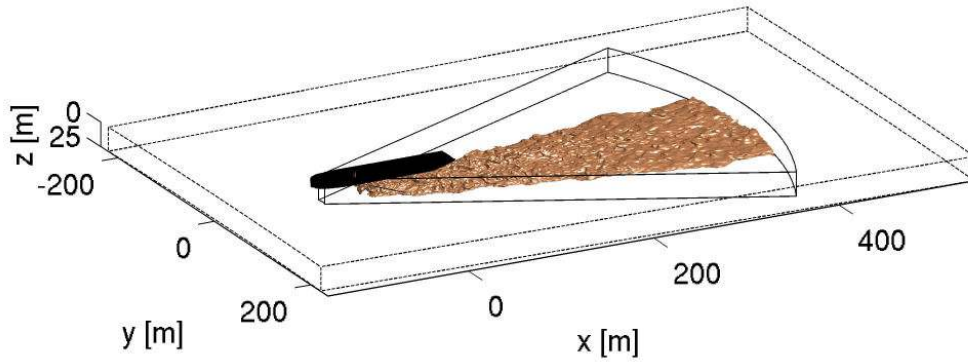


Figure 3.4: Schematised shape of TSHD hull with drag heads and suction pipes.

the dredging plume simulations, an extra simulation with much larger domain is conducted, see Figure 3.5. In this larger domain the full TSHD hull is captured and the time averaged flow profiles of this extra simulation are used as inflow boundary conditions for the dredging plume simulations.



*Figure 3.5: The inflow conditions around the TSHD hull at the pie-shaped plume grid come from a second simulation on a larger grid indicated with black dashed lines.*

### 3.4.2 TSHD propellers

When a TSHD is dredging, the propellers at the back of the TSHD generate a strong backward jet flow to keep the TSHD with drag heads moving. The flow velocity generated by propellers is in the order of 5-10 m/s. The overflow plume generated by a TSHD might be impacted by the propeller flow. Therefore the propellers of a TSHD are included in the CFD model. The propellers are included using a body force source term in the momentum equations.

In the CFD model propellers are defined by input on the total propeller power (Watt), the number of propellers (1 or 2), the location and diameter of each propeller and the rotation direction of the propeller(s). The propeller power is divided by the number of propellers and converted into a constant thrust by dividing it by the theoretical propeller outflow velocity  $u_{pr0}$ :

$$T_{pr} = \frac{P_{pr}/n_{pr}}{u_{pr0}}, \quad (3.24)$$

with  $T_{pr}$  as the constant thrust for a propeller,  $P_{pr}$  as the total power,  $n_{pr}$  is the number of propellers. In this way, the propellers are modelled using a constant thrust, but as input propeller power is used because data on propulsion power of a TSHD is easier to obtain than data on propulsion thrust.  $u_{pr0}$  is given by [Blaauw and Kaa \(1978\)](#):

$$u_{pr0} = 1.15 \left( \frac{P_{pr}/n_{prop}}{\rho D_{pr}^2} \right)^{1/3}, \quad (3.25)$$

with propeller diameter  $D_{pr}$ .  $D_{pr}$  is equal to the propeller diameter for a propeller in a duct and is equal to 70% of the propeller diameter without duct. In the CFD model the propellers have no duct. In case a propeller with duct is simulated then the corresponding diameter in the CFD model should be increased to  $1/70\% = 143\%$ .

By its propeller blades a propeller generates jet flow with a strong rotation. Therefore, following [Stern et al. \(1988\)](#), the propeller thrust  $T_{prop}$  in the CFD model is divided in a body force directed in flow direction  $f_{pr,x}$  and a rotational body force  $f_{pr,\psi}$ . In this study simpler formulations of  $f_{pr,x}$  and  $f_{pr,\psi}$  are used than in [Stern et al. \(1988\)](#), but they suffice.  $f_{pr,x}$  and  $f_{pr,\psi}$  are given for a grid cell  $(j,k)$  inside the propeller outflow plane by:

$$f_{pr,x}(j,k) = \frac{0.75T_{pr}}{\pi/4D_{pr}^2\Delta x(j,k)}, \quad (3.26)$$

$$f_{pr,\psi}(j,k) = \frac{0.25T_{pr}1.5r_{pr}(j,k)/(0.5D_{pr})}{\pi/4D_{pr}^2\Delta x(j,k)}, \quad (3.27)$$

with  $\Delta x(j,k)$  as the grid size in line with the TSHD and  $r_{pr}(j,k)$  as the radial distance from the centre of the propeller.  $f_{pr,x}$  is directed in line with the TSHD, perpendicular to the propeller plane.  $f_{pr,\psi}$  is the rotational component in the propeller plane, which is zero at the propeller centre and maximum at the outer part. The factor 1.5 originates from the integral of  $f_{pr,\psi}$  over the total propeller disc.  $f_{pr,\psi}$  leads to axial velocities in the propeller disc in the order of 58% of the outflow velocity. These axial velocities are larger than the axial velocities found in propeller experiments ([Prosser 1986](#); [Nienhuis 1992](#); [Lam et al. 2011](#)), which are in the order of 20-40% of the outflow velocity. However, in this way satisfactory results are obtained for the downstream propeller velocity decay, see Section 5.4.3.

Behind each propeller a TSHD possesses a rudder. A rudder acts as splitter plate for the rotating flow generated by the propeller. At the rudder the flow splits in upward and downward direction, this leads to increased mixing in vertical direction ([Rhee and Kim 2008](#)) and can even lead to vertical splitting into two propeller jets ([Prosser 1986](#)). In the CFD model a rudder is not taken into account.

## 3.5 Boundary conditions

### 3.5.1 The free surface

At the free surface a rigid lid approach is used with free-slip conditions and  $\frac{\partial C_l}{\partial n} = 0$ . A rigid lid can be applied when water surface gradients remain small, which is the case for dredge plume simulations.

### 3.5.2 Solid walls

At solid walls a wall function is used to apply the shear stress  $\tau_w = \rho u_* u_*$ , with friction velocity  $u_*$  belonging to the wall parallel velocity  $U_w = \sqrt{u^2 + v^2}$  in the first grid cell at  $z_n = \Delta z/2$  from the wall. For hydraulic smooth walls the following standard law of the wall with logarithmic layer, buffer layer and viscous sub-layer is used:

$$\begin{aligned} U_n^+ &= z_n^+ & \text{for } z_n^+ \leq 5 \\ U_n^+ &= 5.0 \ln z_n^+ - 3.05 & \text{for } 5 < z_n^+ < 30 \\ U_n^+ &= 2.5 \ln z_n^+ + 5.5 & \text{for } z_n^+ \geq 30 \end{aligned} \quad (3.28)$$

with  $U_n^+ = U_n/u_*$  and  $z_n^+ = \frac{u_* z_n}{\nu}$ . For hydraulic rough walls the following standard law of the wall is used:

$$U_n^+ = \frac{1}{\kappa} \ln \frac{z_n}{z_0}, \quad (3.29)$$

with  $z_0 = 0.11\nu/u_* + k_s/30$  and Nikuradse roughness height  $k_s$ .

### 3.5.3 Inflow and outflow

In the simulation domain of Figure 3.1 the inflow boundary comprises both lateral boundaries and the boundary at low  $x$  coordinate (low  $r$  coordinate). At the inflow boundary velocity and volume fraction  $C_l$  profiles are prescribed. For a Cartesian box simulation both lateral boundaries are no inflow boundaries, but a free slip zero gradient boundary condition is applied in that case. At the outflow boundary at high  $x$  coordinate (high  $r$  coordinate) a zero gradient condition for all variables is applied. At the outflow boundary the pressure is made zero at one point and all other other pressure boundaries have a zero gradient. For Cartesian box simulations also periodic boundaries are applicable in stream wise and lateral direction.

### 3.5.4 Synthetic turbulence ambient inflow

The influence of ambient turbulence on the inflow conditions can be captured by prescribing turbulent fluctuations on top of the stationary inflow velocity profile. Adding random noise leads to long adaptation lengths for accurate turbulent flow as random noise does not have the correct correlations in place and time and the turbulent energy is uniformly spread over all wave lengths. In this study the synthetic eddy method (SEM) of Jarrin et al. (2006) is used to create turbulent inflow conditions of the ambient flow. Realistic coherent structures are generated by SEM and the corresponding velocity fluctuations are added to the stationary inflow log-profile. SEM needs profiles of the desired Reynolds stress tensor and the expected length scales of the turbulent eddies. The length scales can vary in space and can be different in all three directions. For turbulent channel flow SEM needs a short adaptation length as it gives correct turbulent velocity profiles within 5-10 flow depths from the inflow boundary (Jarrin 2008).



The desired Reynolds stress tensor in this study is taken from DNS of turbulent channel flow data with  $Re_\tau = 590$  (Moser et al. 1999). The stream wise and lateral length scale for SEM are chosen close to the length scales given in Xie and Castro (2008) for turbulent channel flow:

$$L_x = \frac{1}{2} \frac{H}{U_n} \frac{u_*}{\kappa} \log \frac{H-z}{z_0}, \quad (3.30)$$

$$L_y = 0.22H, \quad (3.31)$$

with flow depth  $H$  and  $z$  defined positive downward and zero at the free surface. The vertical length scale for SEM is given by the Bakhmetev profile:

$$L_z = \frac{H-z}{H} \sqrt{z/H}. \quad (3.32)$$

### 3.5.5 Overflow inflow

The flow from the overflow is prescribed by a idealised fully developed 1/7th power law velocity profile at the top of the domain with a block shaped profile of the inflow volume fraction  $C_l$ . Turbulent fluctuations can be added to the jet inflow velocity based on jet azimuthal modes. They generate an in-stable initial flow which quickly transits to turbulent flow. Adding turbulent fluctuations to the jet inflow is necessary for accurate non-buoyant JICF, or non-buoyant and buoyant jet without crossflow results, but for buoyant JICF and dredging plumes it is not necessary, see the tests in Chapter 4. Azimuthal forcing has been used several times for buoyant and non-buoyant jet simulations (Menon and Rizk 1996; Chen et al. 2008; Worthy 2003). The fluctuating component of the velocity at every grid point  $(i, j)$  of the jet inflow can be written as:

$$w'(m, n) = Aw_{j0} \sum_{m=1}^M \sin \left( \frac{2\pi ft}{m} + \theta(i, j) \right), \quad (3.33)$$

with  $A$  as the amplitude of the fluctuations,  $w_{j0}$  is the mean jet inflow velocity, the number of modes  $M = 6$ , the frequency  $f$  in the range of Strouhal =  $\frac{fD}{w_{j0}}$  in between 0.2-1, and  $\theta(i, j)$  as the azimuthal angle defined from the centre of the plume outflow.

The overflow discharge can be constant in time with a constant  $w_{j0}$ , but it can also fluctuate in time:

$$w_{j0}(t) = w_{j0} + w_{j0} \sin(2\pi t/T_p) \quad (3.34)$$

with pulsing period  $T_p$ . Hence, pulsing is applied with an amplitude of 100% and a duty cycle of 50%. For pulsed runs the average inflow discharge is similar to non-pulsed runs but the average inflow momentum is larger.

### 3.6 Flow solver numerical details

The flow equations are solved on a staggered mesh with a parallel (domain decomposition) finite volume method using a pressure-correction algorithm. The basis of this CFD code is explained in [Pourquié \(1994\)](#). In the pressure-correction algorithm the time increment of the Navier Stokes equations (Equations 3.1-3.2) is split in two sub-steps. First comes the predictor step, which at time step  $n_t$  reads:

$$\frac{(\rho \mathbf{u})^* - (\rho \mathbf{u})^{n_t}}{t^{n_t+1} - t^{n_t}} = RHS^{n_t} - \nabla P^{n_t} + \mathbf{f}_{IBM}^{n_t}, \quad (3.35)$$

where  $RHS^{n_t}$  contains the advective, viscous and (non-IBM) body force terms.  $\mathbf{f}_{IBM}^{n_t}$  is the IBM body force. The predictor step is followed by the correction step:

$$\frac{(\rho \mathbf{u})^{n_t+1} - (\rho \mathbf{u})^*}{t^{n_t+1} - t^{n_t}} = -\nabla \delta p, \quad (3.36)$$

Finally the pressure can be updated with:

$$P^{n_t+1} = P^{n_t} + \delta p. \quad (3.37)$$

$\delta p$  is obtained by solving the Poisson equation:

$$\frac{\nabla \cdot (\rho \mathbf{u})^{n_t+1} - \nabla \cdot (\rho \mathbf{u})^*}{t^{n_t+1} - t^{n_t}} = -\nabla^2 \delta p, \quad (3.38)$$

with the divergence of the predictor velocity  $\nabla \cdot (\rho \mathbf{u})^*$  as input and the divergence of the new velocity  $\nabla \cdot (\rho \mathbf{u})^{n_t+1}$  following from conservation of mass ([Najm et al. 1998](#)):

$$\nabla \cdot (\rho \mathbf{u})^{n_t+1} = - \left( \frac{\partial \rho}{\partial t} \right)^{n_t+1} = - \left( \frac{3\rho^{n_t+1} - 4\rho^{n_t} + \rho^{n_t-1}}{3t^{n_t+1} - 4t^{n_t} + t^{n_t-1}} \right). \quad (3.39)$$

Equation 3.15 is fully explicit, therefore  $\rho^{n_t+1}$  can be obtained from Equations 3.15 and 3.3 without iteration. The IBM body force to get the desired velocity  $\mathbf{V}^{n_t+1}$  is given by:

$$\mathbf{f}_{IBM}^{n_t} = \begin{cases} \frac{(\rho \mathbf{V})^{n_t+1} - (\rho \mathbf{u})^{n_t}}{t^{n_t+1} - t^{n_t}} - RHS^{n_t} + \nabla P^{n_t} & \text{if inside immersed boundary} \\ 0 & \text{if outside immersed boundary} \end{cases}$$

The pressure-Poisson equation is solved with a fast cosine transform solver in  $\phi, z$  direction and a tri-diagonal matrix algorithm (TDMA) in  $x$  direction. Time integration of the advective, viscous and (non-IBM) body force terms in the predictor step of Navier Stokes is performed by Wray's RK3 scheme ([Wesseling 2000](#)) with  $CFL < 1.6$ . In each sub-step of the RK3 method, first the old pressure gradient is used to get a prediction, then a full pressure correction is carried out within the sub-step for stability reasons. Spatial integration of Navier Stokes is carried out using the second order central scheme for all terms except advection of momentum. In LES the discretisation of momentum advection is a critical issue; in this study a novel artificial viscosity advection scheme is presented and tested in Chapter 4.



# Chapter 4

## Validation artificial viscosity advection scheme

*In previous chapter the CFD model is introduced. This chapter deals with one of the most important choices in LES: the momentum advection scheme. A novel scheme is introduced and compared with three other relevant advection schemes for three test cases: non-buoyant JICF, buoyant jet in weak coflow and buoyant JICF. All simulations are conducted with a rather coarse grid resolution of 10 cells of the initial jet diameter. For full scale dredging plume simulations a much finer resolution at the overflow is not achievable, therefore this resolution is also used in these laboratory scale tests to find out how accurate (or inaccurate) LES results of jet simulations are with this resolution.*<sup>1</sup>

### 4.1 Introduction

Choosing the discretisation of advection of momentum in LES is a delicate task. In LES simulations one needs an advection discretisation which is stable and has little numerical dissipation at the same time. Having an energy consistent advection scheme is crucial for stable turbulent results (Ducros et al. 2000; Kravchenko and Moin 1997; Morinishi et al. 1998; Morinishi 2010; Verstappen and Veldman 2003). For the novel artificial viscosity advection scheme introduced and tested in this chapter, the second order central advection scheme (CDS2) in divergence form on a staggered mesh is taken as a basis. This scheme is energy consistent (Kravchenko and Moin 1997; Morinishi et al. 1998; Morinishi 2010). Velocity components at index  $m+1/2$  are staggered half a grid cell from all scalar variables at index  $m$  (jet concentration, density, pressure). Written out for  $x$  direction the advection of momentum from Equation 3.2 is discretised on a staggered mesh by:

$$\nabla \cdot (\rho \hat{u} \check{u})|_{m+1/2} = \frac{\rho \hat{u} \check{u}|_{m+1} - \rho \hat{u} \check{u}|_m}{\Delta x}, \quad (4.1)$$

---

<sup>1</sup>A modified version of this chapter has been published as: Wit, L. de, van Rhee, C. (2014), Testing an improved artificial viscosity advection scheme to minimise wiggles in large eddy simulation of buoyant jet in crossflow, *Flow, Turbulence and Combustion*. DOI:10.1007/s10494-013-9517-1

where  $\hat{\mathbf{u}}$  is the *advective* velocity,  $\check{\mathbf{u}}$  is the *advected* velocity and  $m$  is the grid index. In all different momentum advection schemes introduced in this chapter the *advective* velocity is interpolated by the second order accurate midpoint rule:

$$\hat{\mathbf{u}}_m = \frac{\mathbf{u}_{m+\frac{1}{2}} + \mathbf{u}_{m-\frac{1}{2}}}{2}, \quad (4.2)$$

Due to the staggered arrangement  $\rho_m$  does not need interpolation. The key difference between the different advection schemes tested in this chapter lies in the determination of the *advected* velocity.

A fully central discretisation scheme for advection has no numerical dissipation. This is positive from physical LES point of view: all dissipation is coming from the sub-grid scale model. A drawback of central schemes is their notorious sensitivity to give wiggles. Wiggles are non physical high frequency oscillations on grid scale which make a simulation unstable. An important condition for the development of wiggles is a high Peclet cell number ( $Pe = \frac{u\Delta x}{\nu}$ ) in combination with large stream wise gradients in the advected variable (Kaltenbach and Choi 1995). The flow in front of an obstacle like the jet of a JICF is such area. Especially in LES, with a low turbulent viscosity, generation of wiggles in front of obstacles is an issue. A fix to prevent wiggles is to decrease  $Pe$  by either increasing dissipation (higher viscosity  $\nu$ ), or by decreasing the grid size  $\Delta x$ . CDS2 is bounded and will not have wiggles for  $Pe < 2$ , but grid refinement up to the situation where wiggles are gone is not achievable in practice for engineering high  $Re$  flow situations. Leaving wiggles is no option as they can cause a simulation to crash or they can interact with coherent flow structures. Increasing dissipation therefore is a remedy often used for high  $Re$  engineering flow simulations, but this needs to be done with care in LES.

In MILES/ILES (Monotone Integrated LES/Implicit LES) a wiggle-free, dissipative numerical scheme, like high order upwind or ENO/WENO (Weighted Essentially Non-Oscillatory), is used for dissipation on grid scale as a replacement of the sub-grid scale model (Pirozzoli 2011; Karaca et al. 2012). Although accurate results have been obtained by MILES/ILES, this approach is controversial because it depends so heavily on numerical dissipation, not on modelled physical dissipation. The numerical dissipation from high order upwind schemes is often more than the desired dissipation in LES from a sub-grid scale model (Park et al. 2004; Sagaut 1999; Kogaki et al. 1997), in this chapter this is demonstrated for a 5th order upwind scheme UPW5. WENO schemes don't do a better job than high order upwind schemes in this respect, as high order upwind schemes have less dissipation than WENO schemes of the same order (Pirozzoli 2011). In this work the MILES/ILES approach is not followed, but physical LES is applied with a sub-grid scale model responsible for dissipation of turbulent kinetic energy at sub-grid scale. A novel artificial viscosity scheme, called AV6, is presented which increases the dissipation on grid scale but has negligible impact on longer physical relevant scales. This combination of characteristics makes this scheme suitable for LES of high  $Re$  flow situation on engineering scale. AV6 combines UPW5 (Wicker and Skamarock 2002) and the ideas of artificial viscosity of Jameson et al. (1981). It has an adjustable amount of dissipation to damp

wiggles sufficiently with negligible impact on larger scales. CDS2 forms the basis of AV6. More accurate central schemes than CDS2 have been used in LES, like spectral methods (Moser et al. 1999) or compact schemes (Lele 1992; Boersma 2011). However, spectral schemes are hard to apply for complex geometries and compact schemes are computationally expensive. Because the rest of the CFD code is second order accurate in space, CDS2 is used as basis of AV6 in this work, but the artificial viscosity approach of AV6 is easily applicable to higher order central schemes as well. Results of AV6 are compared with CDS2, the original Jameson scheme AV4 and a fifth order upwind scheme UPW5. All advection schemes are explained in the following section.

## 4.2 Description different advection schemes

### 4.2.1 Advection scheme CDS2

With the second order central scheme CDS2 the advection flux is given by:

$$\rho \hat{\mathbf{u}} \ddot{\mathbf{u}}|_m = Flux^{2nd} = \rho_m \frac{\hat{\mathbf{u}}_m}{2} \left[ \mathbf{u}_{m+\frac{1}{2}} + \mathbf{u}_{m-\frac{1}{2}} \right]. \quad (4.3)$$

CDS2 is second order accurate, energy consistent and by its symmetry it has no dissipation. The advective velocity  $\hat{\mathbf{u}}$  is calculated using the midpoint rule in equation 4.2.

### 4.2.2 Advection scheme UPW5

Following Wicker and Skamarock (2002) the fifth order upwind biased advection scheme UPW5 can be written as:

$$\rho \hat{\mathbf{u}} \ddot{\mathbf{u}}|_m = Flux^{6th} - \epsilon \cdot Diss^{6th}. \quad (4.4)$$

In UPW5  $\epsilon = 1/60$ . The sixth order central flux is given by:

$$Flux^{6th} = \rho_m \frac{\hat{\mathbf{u}}_m}{60} \left[ 37(\mathbf{u}_{m+\frac{1}{2}} + \mathbf{u}_{m-\frac{1}{2}}) - 8(\mathbf{u}_{m+\frac{3}{2}} + \mathbf{u}_{m-\frac{3}{2}}) + (\mathbf{u}_{m+\frac{5}{2}} + \mathbf{u}_{m-\frac{5}{2}}) \right], \quad (4.5)$$

and the sixth derivative dissipation term given by:

$$Diss^{6th} = \rho_m |\hat{\mathbf{u}}_m| \left[ 10(\mathbf{u}_{m+\frac{1}{2}} - \mathbf{u}_{m-\frac{1}{2}}) - 5(\mathbf{u}_{m+\frac{3}{2}} - \mathbf{u}_{m-\frac{3}{2}}) + (\mathbf{u}_{m+\frac{5}{2}} - \mathbf{u}_{m-\frac{5}{2}}) \right]. \quad (4.6)$$

Because the advective velocity  $\hat{\mathbf{u}}$  is calculated using the midpoint rule in equation 4.2, the formal accuracy of UPW5 is second order.

### 4.2.3 Advection scheme AV4

An artificial viscosity method for advection has been developed by Jameson et al. (1981) for modelling compressible turbulent flows with shock waves. High order

dissipation with 4th or higher derivatives are used to suppress high frequency oscillations, see for example (Jameson et al. 1981; Pirozzoli 2011; Kawai et al. 2010). This concept of using high order dissipation bears similarities with other concepts in turbulence modelling as hyperviscosity (Dantinne et al. 1997) or variational multi scale (Hughes et al. 2001; Bricteux et al. 2009). On those two approaches sub-grid scale dissipation in LES is applied only to the high frequency part of the energy spectrum by either applying high order dissipation in hyperviscosity, or by filtering the velocity field by an high pass filter and then applying a sub-grid scale model in variational multi scale. The Jameson artificial viscosity scheme, and the one proposed in this chapter, differ from those two concepts as it applies the high order dissipation as a numerical measure to suppress the numerical problem of wiggles, and it applies a standard sub-grid scale model with second order dissipation for the modelled physical dissipation on sub-grid scale. In the Jameson artificial viscosity scheme dissipation terms with 2nd and 4th derivatives are added to the CDS2 advection flux. The 2nd derivative dissipation is only active in zones where there are shocks, fourth derivative dissipation is only active in smooth zones to suppress high frequency oscillations. In simulations without shocks, like dredging plume simulations, only 4th derivative dissipation is needed (Franke and Frank 2002). Here, this scheme is called AV4:

$$\rho \hat{u} \ddot{u}|_m = Flux^{2nd} - \epsilon \cdot Diss^{4th}. \quad (4.7)$$

In AV4  $\epsilon$  is a small constant (order 1/256) governing the amount of artificial dissipation.  $Flux^{2nd}$  is explained in Equation 4.3 and the fourth derivative dissipation term  $Diss^{4th}$  is given by:

$$Diss^{4th} = \rho_m |\hat{u}_m| \left[ 3(u_{m+\frac{1}{2}} - u_{m-\frac{1}{2}}) - (u_{m+\frac{3}{2}} - u_{m-\frac{3}{2}}) \right]. \quad (4.8)$$

The advective velocity  $\hat{u}$  is calculated using the midpoint rule in equation 4.2 and AV4 is second order accurate. The original Jameson scheme was defined on a collocated mesh, here AV4 is defined on a staggered mesh. The basis of AV4, the  $Flux^{2nd}$  part, is energy consistent.

#### 4.2.4 Advection scheme AV6

Dissipation with a 6th derivative is more effective to remove wiggles than a 4th derivative. Therefore the idea of Jameson et al. (1981) is used to add a little dissipation to a central discretisation of advection, but it is done with 6th derivative dissipation instead of 4th derivative. This advection scheme is called AV6:

$$\rho \hat{u} \ddot{u}|_m = Flux^{2nd} - \epsilon \cdot Diss^{6th}, \quad (4.9)$$

with  $\epsilon = 1/512$ . AV6 uses 6th derivative dissipation to suppress high frequency oscillations because higher order derivative dissipation is more effective in dissipation on grid scale. This line of reasoning with higher order derivatives could be extended to 8th, 10th or even higher derivative schemes, but then the numerical

stencil becomes wider and wider. Wide stencils are a disadvantage near boundaries and for domain decomposition. For AV6 a stencil as wide as the UPW5 scheme is used with 6th derivative dissipation. Near boundaries the grid points outside the boundary needed for  $Diss^{6th}$  are extrapolated from the last boundary value by:  $\mathbf{u}_{m+\frac{5}{2}} = \mathbf{u}_{m+\frac{3}{2}} = \mathbf{u}_{m+\frac{1}{2}}$ . This simple treatment was found to be stable enough for wiggle free results near boundaries. Because the advective velocity  $\hat{\mathbf{u}}$  is calculated using the midpoint rule in equation 4.2, the formal accuracy of AV6 is second order. The basis of AV6, the  $Flux^{2nd}$  part, is energy consistent. AV6 is different from the artificial viscosity scheme in Kawai and Lele (2010), Kawai et al. (2010) as artificial viscosity in AV6 is absorbed in the advective flux and in Kawai and Lele (2010), Kawai et al. (2010) it is absorbed in diffusion and they apply a 4th derivative to the rate of strain and AV6 applies a 6th derivative to the velocity.

## 4.3 Fourier analysis advection schemes

### 4.3.1 Fourier analysis of spatial discretisation

In order to examine the dissipation and dispersion behaviour of the advection schemes of Section 4.2 a Fourier analysis of the discretised Advection-Diffusion equation has been performed. The Advection-Diffusion equation is given by:

$$\frac{\partial \phi}{\partial t} = -U \cdot \nabla \phi + \nabla \cdot \nu_e \nabla \phi, \quad (4.10)$$

where  $U$  is the advection velocity and  $\phi$  is the transported quantity. In this Fourier analysis only space is discretised, time is kept continuous. Advection is discretised by a specific advection scheme of Section 4.2, diffusion is discretised by the second order central scheme.  $\phi$  can be described by the periodic function:

$$\phi_m(t) = \phi_\omega(t) e^{i\omega x_m}, \quad (4.11)$$

with  $i^2 = -1$ , wave number  $\omega = 2\pi/L$ , wave length  $L$ , spatial coordinate  $x_m = m\Delta x$ . When this function is put into Equation 4.10  $\phi_\omega(t)$  is obtained, which leads to the following solution:

$$\phi_m(t) = \phi_\omega(0) e^{i\omega(x_m - \tilde{U}t)} e^{-(\Psi_{av} + \Psi_{sgs})t}, \quad (4.12)$$

with starting condition  $\phi_\omega(0)$ , modified phase speed  $\tilde{U}$  and a damping term consisting of a contribution from the artificial viscosity in the advection scheme  $\Psi_{av}$  and a contribution from the sub-grid scale viscosity  $\Psi_{sgs}$ . The values for  $\tilde{U}$  and  $\Psi_{av}$  of each advection scheme are given in Table 4.1.  $\Psi_{sgs} = 2 \frac{\nu_e}{\Delta x^2} (1 - \cos(\omega \Delta x))$ . As can be seen the phase speed and damping of each advection scheme is depending on  $\omega \Delta x$ , which is equal to  $2\pi \Delta x / L = 2\pi / ppw$ .  $ppw = L / \Delta x$  is the number of grid points per wave length.

*Table 4.1: Modified phase speed and damping of different advection scheme.*

Advection	$\tilde{U}$	$\Psi_{av}$
CDS2	$\frac{\sin(\omega\Delta x)}{\omega\Delta x} U$	0
UPW5	$\frac{\sin(3\omega\Delta x) - 9\sin(2\omega\Delta x) + 45\sin(\omega\Delta x)}{30\omega\Delta x} U$	$-\frac{1}{60} \frac{2\cos(3\omega\Delta x) - 12\cos(2\omega\Delta x) + 30\cos(\omega\Delta x) - 20}{\Delta x}  U $
AV4	$\frac{\sin(\omega\Delta x)}{\omega\Delta x} U$	$\frac{1}{256} \frac{4(\cos(\omega\Delta x) - 1)^2}{\Delta x}  U $
AV6	$\frac{\sin(\omega\Delta x)}{\omega\Delta x} U$	$-\frac{1}{512} \frac{2\cos(3\omega\Delta x) - 12\cos(2\omega\Delta x) + 30\cos(\omega\Delta x) - 20}{\Delta x}  U $

### 4.3.2 Results of Fourier analysis

The relative phase speed of all advection schemes is shown in Figure 4.1a. The modified phase speed of UPW5 is more accurate than CDS2, AV4 and AV6. The difference is caused by the  $Flux^{2nd}$  term in CDS2, AV4, AV6 and the  $Flux^{6th}$  term in UPW5.

For all advection schemes and each  $ppw$  the amount of sgs viscosity  $\nu_e$  is determined which results in  $\Psi_{av} = \Psi_{sgs}$ . In this way the numerical dissipation of a scheme can be expressed in terms of a viscosity. This allows for a direct comparison of the numerical dissipation and the viscosity that results from the sub-grid model. A characteristic  $U$  and  $\Delta x$  belonging to the non-buoyant JICF test case of Section 4.4 are used to get numerical values for the damping in Figure 4.1b. For this test case  $\nu_{mol} = 1.7 \cdot 10^{-5} \text{ m}^2/\text{s}$  and the typical time-averaged sgs viscosity inside the jet  $\nu_e$  is in the order  $10^{-3} \text{ m}^2/\text{s}$ . CDS2 does not possess dissipation and is therefore not shown.

All three schemes in Figure 4.1b share the desired property that small wave lengths with small  $ppw$  are damped more than wave lengths with larger  $ppw$ . This means all schemes damp wiggles ( $ppw = 2$ ) to some extent by the artificial viscosity and that wave lengths with  $ppw > 50$  encounter negligible artificial viscosity. There are differences in how the three schemes behave at  $ppw = 10$ , the minimum resolution of interest in this chapter. At  $ppw = 10$  the artificial viscosity imposed by AV6 is comparable to the molecular viscosity in this example and approximately 2% of the typical sgs viscosity. For UPW5 the artificial viscosity is more than 8 times more than molecular viscosity and 17% of the typical sgs viscosity. For  $ppw < 6$  the damping of UPW5 exceeds the influence of typical sgs viscosity, for AV6 this limit is at  $ppw < 3$ . This analysis illustrates the often stated issue of upwind schemes, even a high order upwind scheme like UPW5, of having too much damping to carry out LES (Park et al. 2004; Sagaut 1999). AV4 shows inferior performance compared with AV6 for all wave lengths. It has less wanted damping of short scale oscillations, and more unwanted damping of wave lengths with large  $ppw$ . The choice of  $\epsilon = 1/256$  for AV4 in this chapter was a trade-off.

The damping is characterised independent of  $U$  and  $\Delta x$  by showing  $Pe$  in Figure 4.1c. It shows that the artificial viscosity terms in the advection schemes decrease  $Pe$ . Lower  $Pe$  indicates more damping. For wiggles with  $ppw = 2$  UPW5 has  $Pe = 4$ , AV4 has  $Pe = 60$  and AV6 has  $Pe = 30$ . At the minimum resolution of interest in this chapter of  $ppw = 10$  AV6 results in  $Pe = 3500$ , AV4



results in  $Pe = 600$ , UPW5 results in  $Pe = 400$ . As a comparison: a first order upwind (UPW1) scheme has  $Pe = 2$  for all wave lengths. And a blend of 5% UPW1 and 95% CDS2, as for example used in a challenging LES of high  $Re$  flow past an obstacle (Krajnovic et al. 2011), has  $Pe = 40$  for all  $ppw$ . AV6 is a better option than this blend of 5% UPW1 and 95% CDS2 as AV6 has more damping of wiggles with  $Pe = 30$  and two orders of magnitude less unwanted damping at  $ppw=10$  with  $Pe = 3500$ .

In this analytical Fourier analysis the theoretical improved behaviour of AV6 over both UPW5 and AV4 is demonstrated. Now flow simulations are used to find the behaviour of AV6 in the full Navier Stokes equations.

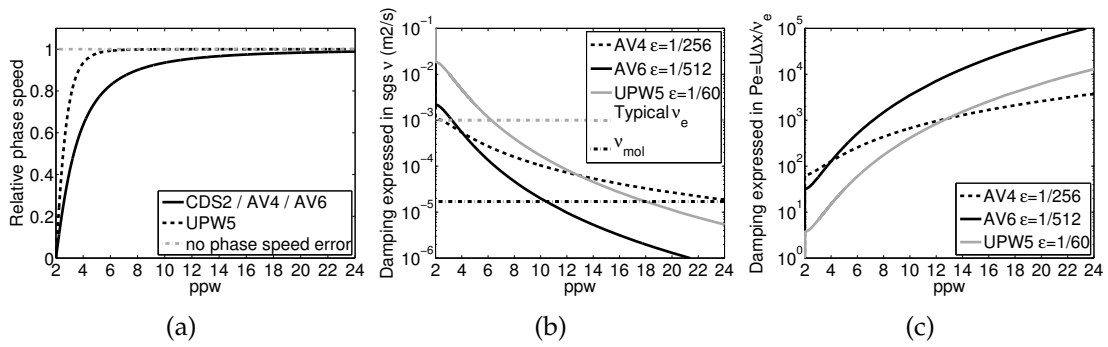


**Figure 4.1:** Relative phase speed  $\tilde{U}/U$  of the different advection schemes (a). Influence of artificial viscosity expressed in terms of a sgs viscosity based on Fourier analysis. Damping influence using  $\Delta x$  and  $U$  from first test case JICF (b). Damping influence showed independent of  $\Delta x$  and  $U$  by showing  $Pe$  (c).

## 4.4 Test case JICF $Re = 82000, Ri = 0, \gamma = 2$

### 4.4.1 Model set up

For the non-buoyant JICF simulation a set up corresponding to the case with  $\gamma = 2, Re = 82000$  from Andreopoulos and Rodi (1984), Andreopoulos (1983) is chosen. The simulation set up parameters are  $D = 50$  mm,  $u_{cf} = 13.9$  m/s,  $w_{j0} = 27.8$  m/s,  $\rho_{cf} = \rho_{j0} = 1.225$  kg/m<sup>3</sup>,  $\nu_{mol} = 1.7 \cdot 10^{-5}$  m<sup>2</sup>/s. This experimental data has a high  $Re$  which makes it interesting to see whether a LES with moderate resolution can deliver acceptable results. The simulation grid is shown in Figure 6.3. The grid size in  $r$  direction is growing from  $\Delta r = 0.1D$  at the jet origin in two steps to  $\Delta r = 0.12D$  halfway and  $\Delta r = 0.15D$  at the outflow boundary. The lateral grid size in  $\phi$  direction is growing linear from  $r\Delta\phi = 0.1D$  at the jet origin to about  $r\Delta\phi = 0.22D$  at the outflow boundary. The grid size in  $z$  direction is constant  $\Delta z = 0.1D$ . The grid resolution in this simulation is 10 cells for the jet diameter at outflow and typically  $>25$  cells for the jet diameter in the bend over phase. The grid dimension in  $r$  is  $r = -4D..14D$  in stream wise direction,  $r\Delta\phi = -4.5D..4.5D$  at the jet outflow location,  $z = -2..8D$ . The total number of

grid cells is 1.3 million. All simulations are started up for 4 times the model area flow through periods ( $70 \text{ times } D/u_{cf}$ ), then all turbulent and average quantities are stored 17 flow through periods ( $278 \text{ times } D/u_{cf}$ ).

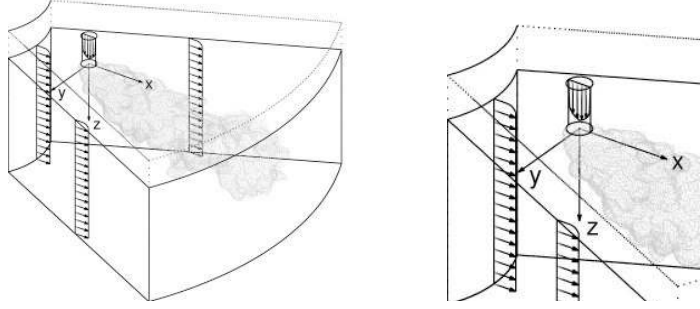


**Figure 4.2:** Pie shaped cylindrical grid used for JICF. Full grid (left), zoom near injection zone (right).

#### 4.4.2 Boundary conditions

A constant crossflow velocity profile with  $u_{cf}$  above  $z = 0.278D$  and a  $1/7$ th power law profile under  $z = 0.278D$  is prescribed.  $0.278D$  was the boundary layer thickness in the experiments. The jet inflow is perturbed by azimuthal forcing, see Equation 3.33. After testing for this JICF, it was found that an amplitude of  $A = 0.5$  for  $w'$  and zero for  $u', v'$  in combination with Strouhal=0.4 gave the best results. The value of  $A = 0.5$  is higher than values in literature (Menon and Rizk 1996; Chen et al. 2008; Worthy 2003) which apply  $A = 0.2$  for buoyant and non-buoyant jets with  $Re = 1000 - 6360$ . But for the non-buoyant JICF with  $Re = 82000$  a simulation with  $A = 0.2$  resulted in a less accurate JICF path which was  $0.5D$  further away from the wall. Including a part of the jet inflow pipe in the computational domain is essential in order to get the correct deflected jet outflow velocity profile (Yuan et al. 1999; Schlüter and Schönfeld 2000). In this study a  $2D$  pipe is simulated by IBM.  $2D$  was found to be long enough; tests with a  $4D$  pipe (not shown) resulted in comparable results and tests with no pipe gave less accurate results. At the IBM wall a hydraulic smooth wall function according to Equation 3.28 is applied.

#### 4.4.3 Results different advection schemes

The effect of different advection schemes is clearly visible in the instantaneous velocity field  $v/u_{cf}$  in Figure 4.3. The jet acts as an obstacle and the zone in front shows strong wiggles with CDS2. UPW5 has eliminated all wiggles, but effects of numerical damping on the length scale of the jet diameter are visible. AV4 and AV6 both have damped wiggles and smaller eddies remain in existence than with UPW5. AV6 has slightly more damping of wiggles than AV4.



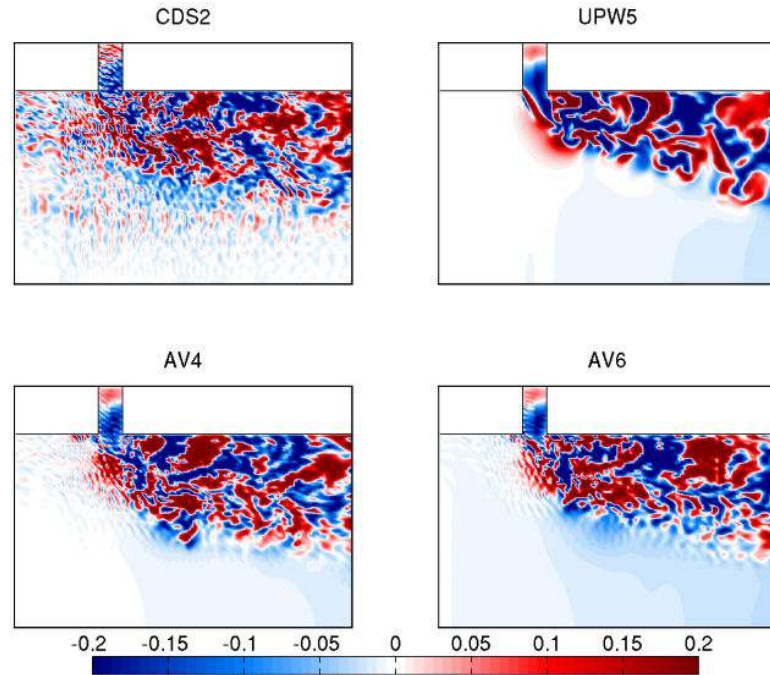


**Figure 4.3:** Instantaneous non-buoyant JICF ( $Re = 82000, Ri = 0, \gamma = 2$ ) lateral velocity field  $v/u_{cf}$  in symmetry plane of different advection schemes.

Time averaged results are shown in Figures 4.4-4.8. The results of CDS2, AV4 and AV6 are very close to each other. This is remarkable, apparently the wiggles in instantaneous CDS2 results do not have a large negative impact on the time averaged results. The shape and magnitude of stream wise velocity and jet concentration in CDS2, AV4 and AV6 is correct, however the wall normal velocity is too large and the bend in the stream wise velocity profile is about  $0.5D$  too far from the wall. UPW5 results in the best jet path which deviates  $< 0.1D$  from the measured one. However, with UPW5, the jet peak concentration at  $x/D = 6$  and  $x/D = 8$  is under-predicted by roughly 20%, AV4 and AV6 show less under-prediction than UPW5 and CDS2 shows correct peak values. All advection schemes result in turbulent kinetic energy profiles in Figure 4.6 which over-predict the turbulent kinetic energy at  $x/D = 4$  by more than 100%, at  $x/D = 6$  it is over-predicted by roughly 50%, only at  $x/D = 10$  it is simulated at the correct level. In the simulations the peak of turbulent kinetic energy near the wall is higher than the second peak inside the jet. In the measurements however, the second peak in the jet is larger than the peak near the wall. The jet outflow velocity profiles in Figure 4.8 are close to the measured one for all advection schemes. Although differences with the measurements exist, overall the results are similar in quality with another LES of this case (Schlüter and Schönfeld 2000).

#### 4.4.4 Robustness LES results

AV6 is used to show the dependency on sub-grid scale model and grid resolution. Results obtained with the  $\sigma$ -sub-grid scale model, no sub-grid scale model and

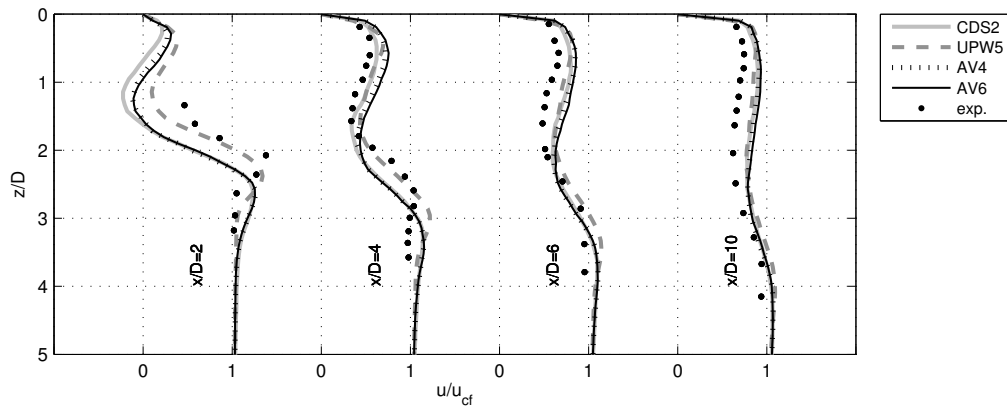


**Figure 4.4:** Comparison non-buoyant JICF ( $Re = 82000, Ri = 0, \gamma = 2$ ) mean stream wise velocity in symmetry plane of different advection schemes.

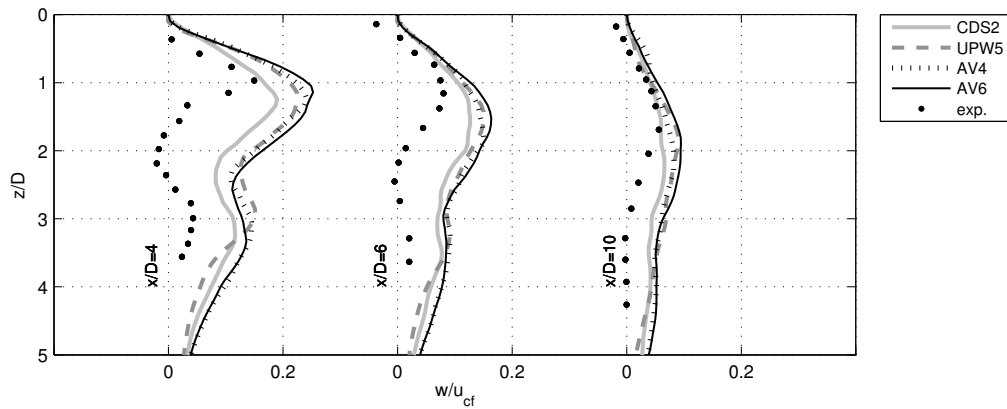


**Figure 4.5:** Comparison non-buoyant JICF ( $Re = 82000, Ri = 0, \gamma = 2$ ) mean wall normal velocity in symmetry plane of different advection schemes.

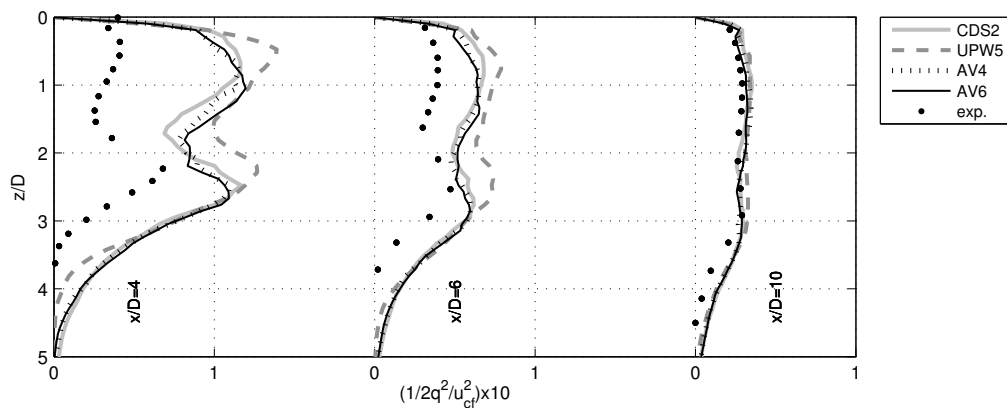


**Figure 4.6:** Comparison non-buoyant JICF ( $Re = 82000, Ri = 0, \gamma = 2$ ) turbulent kinetic energy in symmetry plane of different advection schemes.

a fine simulation on a 1.5 times finer grid size in all three dimensions (0.067D at outflow, 4.2 million cells) are shown in Figures 4.9-4.11. The fine velocity and turbulent kinetic energy profiles are better than the results with normal grid size,

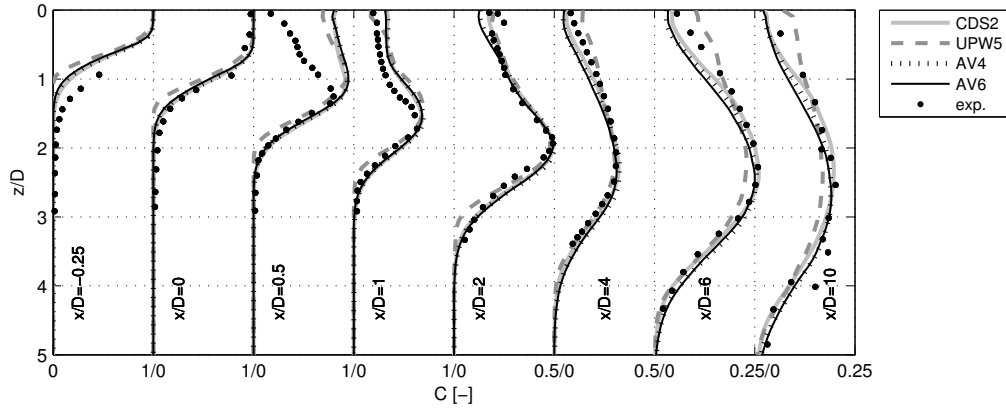


**Figure 4.7:** Comparison non-buoyant JICF ( $Re = 82000, Ri = 0, \gamma = 2$ ) mean jet concentration in symmetry plane of different advection schemes.

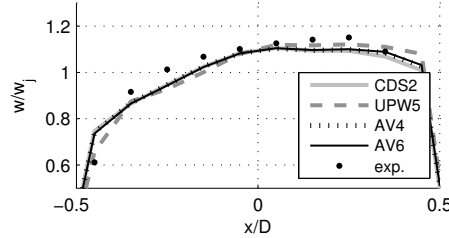


**Figure 4.8:** Comparison non-buoyant JICF ( $Re = 82000, Ri = 0, \gamma = 2$ ) mean jet outflow velocity in symmetry plane of different advection schemes.

but they still differ from measured profiles. The fine jet concentration profile is comparable with the jet concentration profile obtained with normal grid size. When only a moderate grid resolution is manageable because of a very large simulation domain and limited CPU power, then the base resolution of 10 cells over the jet diameter at outflow and  $>25$  in the bend over phase is the minimum to get reasonably accurate LES predictions of jet concentration profiles of a non-buoyant JICF with  $\gamma = 2$ , but more than 1.5 times finer is necessary for accurate velocity and turbulent kinetic energy profiles. The results of the  $\sigma$ -sgs model are similar to the base case results obtained with WALE, therefore the results are independent of which sub-grid scale model is used. Time averaged results without sub-grid scale model are similar to results with the WALE or  $\sigma$ -sgs model in this test, this could lead to the idea that the artificial viscosity is overtaking the dissipative role of the sub-grid scale model. In order to compare the dissipative role of the sub-grid scale model with the dissipation from artificial viscosity at different frequencies the spectral distribution of the kinetic energy of the velocity inside the non-buoyant JICF has been plotted in Figure 4.12. The spectra in Figure 4.12 obtained for different advection and sub-grid scale models show that the artificial viscosity of the advection scheme is working differently from the sub-grid scale viscosity. CDS2 with WALE, AV4 with WALE, AV6 with WALE and AV6 with  $\sigma$ -sgs all show comparable spectra close to the expected  $-5/3$  slope; this gives an indication that the effect of the artificial viscosity of AV4 or AV6 on

resolved scales is less than the effect of viscosity from the sub-grid scale model on these scales. Another indication is obtained from the spectrum of AV6 without sub-grid scale model: it does not show a  $-5/3$  slope, but it has too much energy in the smallest resolved scales near the cut-off edge. The spectrum of UPW5 has a clear  $-5/3$  slope, but deviates considerably from the CDS2 spectrum and damping of the artificial viscosity in UPW5 has significant influence on resolved scales.

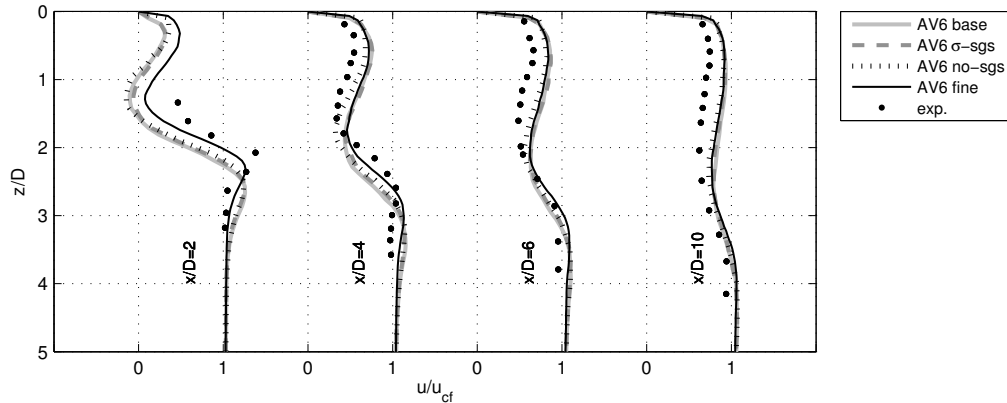


**Figure 4.9:** Comparison non-buoyant JICF ( $Re = 82000, Ri = 0, \gamma = 2$ ) mean stream wise velocity in symmetry plane for different grid resolutions and sub-grid scale models: WALE (base),  $\sigma$ -sgs and no sgs model. Base grid size is  $0.1D$  and fine grid size is  $0.067D$  at outflow.

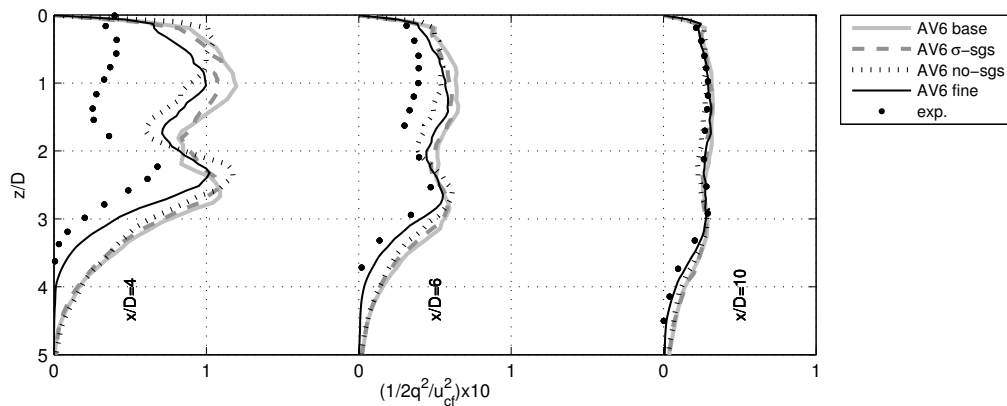


**Figure 4.10:** Comparison non-buoyant JICF ( $Re = 82000, Ri = 0, \gamma = 2$ ) turbulent kinetic energy in symmetry plane for different grid resolutions and sub-grid scale models: WALE (base),  $\sigma$ -sgs and no sgs model. Base grid size is  $0.1D$  and fine grid size is  $0.067D$  at outflow.

#### 4.4.5 Conclusions for JICF $Re = 82000, Ri = 0, \gamma = 2$

In this test CDS2 suffers from strong wiggles in the instantaneous flow fields, AV4 and AV6 damp those wiggles adequately. But the time averaged results of AV4 and AV6 are very close to CDS2, apparently the wiggles in CDS2 have no negative impact on the time averaged results in this case. UPW5 damps the

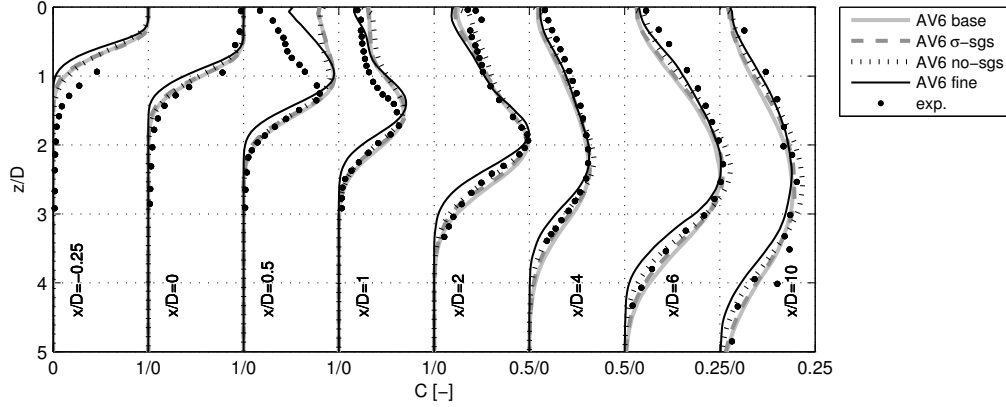


**Figure 4.11:** Comparison non-buoyant JICF ( $Re = 82000, Ri = 0, \gamma = 2$ ) mean jet concentration in symmetry plane for different grid resolutions and sub-grid scale models: WALE (base),  $\sigma$ -sgs and no sgs model. Base grid size is  $0.1D$  and fine grid size is  $0.067D$  at outflow.

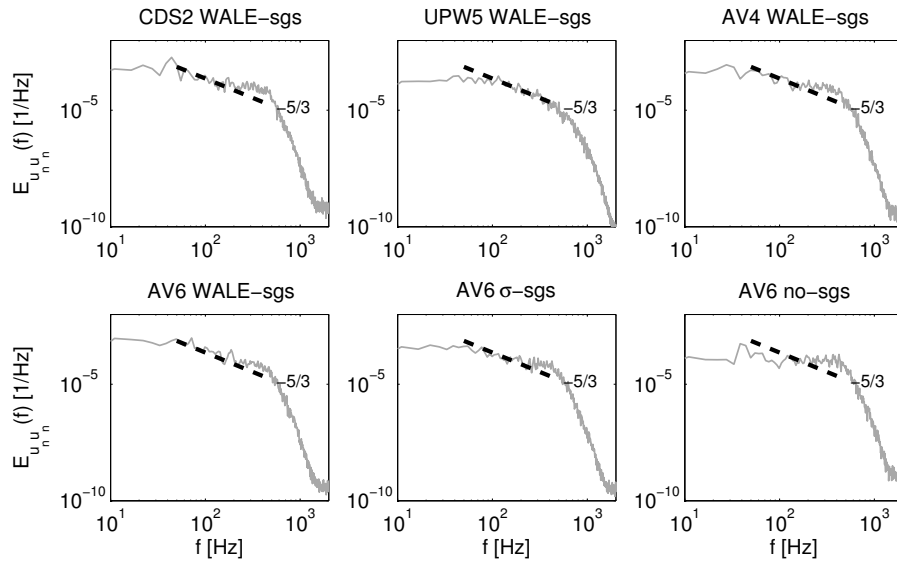


**Figure 4.12:** Spectra of normalised horizontal stream wise velocity ( $u_n = u/\bar{u}$ ) inside non-buoyant JICF ( $Re = 82000, Ri = 0, \gamma = 2$ ) at  $x/D = 4, y/D = 0, z/D = 2.9$  to compare damping of artificial viscosity from the advection scheme with damping of the sub-grid scale model. The black dashed  $-5/3$  line is only given as indication of the slope, not as a correct level of turbulent kinetic energy or length of the inertial sub range.

wiggles adequately, but also shows effects of numerical damping on length scales of the jet, which are absent for AV4 and AV6. Although the velocity profiles of AV4 and AV6 are less accurate than UPW5, the jet concentration profiles are more accurate than UPW5.

## 4.5 Test case buoyant jet in weak coflow $Re = 32000$ density ratio 1.52

### 4.5.1 Model set up

For the buoyant jet in weak coflow simulation a set up corresponding to [Amielh et al. \(1996\)](#), [Djeridane et al. \(1996\)](#) with  $Re = 32000$ , density ratio  $\rho_{j0}/\rho_{co} = 1.52$  is chosen. The simulation parameters are  $D = 26$  mm, coflow velocity  $u_{co} = 0.9$  m/s, jet velocity  $u_{j0} = 10$  m/s,  $\rho_{co} = 1.8316$  kg/m<sup>3</sup>,  $\rho_{j0} = 1.205$  kg/m<sup>3</sup>. Because the experiment is about a CO<sub>2</sub> jet in air coflow two molecular viscosities are involved. In the model however, only one molecular viscosity can be prescribed. In the simulations the dynamic molecular viscosity of the coflow (air) is used  $\mu_{mol} = 1.82 \cdot 10^{-5}$  kg/ms, this leads to a  $\nu_{mol} = \mu_{mol}/\rho = 1 \cdot 10^{-5}$  m<sup>2</sup>/s at the CO<sub>2</sub> jet outflow. Therefore in the simulations  $Re$  is slightly too low at  $Re = 26000$ . However, a test with  $\nu_{mol}$  lowered to achieve  $Re = 32000$  resulted in similar outcomings (not shown). The simulation grid is a Cartesian box, see [Figure 4.13](#). The grid is made orthogonal by choosing  $r$  large and  $\Delta\phi$  small, leading to an almost constant  $\Delta y = r\Delta\phi$  over the domain. The inflow of the jet is not in  $z$  direction, but in  $r$  direction. The grid size in  $r$  direction is growing from  $\Delta r = 0.12D$  at the jet origin in two steps to  $\Delta r = 0.15D$  halfway and  $\Delta r = 0.2D$  at the outflow boundary. The grid size in  $\phi$  and  $z$  direction is constant  $0.1D$ . The grid resolution in this simulation is 10 cells for the jet diameter at outflow, approximately 20 cells for the jet diameter at  $x/D = 5$ , 30 cells at  $x/D = 10$ , and 45 cells at  $x/D = 20$ . The grid dimension is  $r = -2D..29D$  in stream wise direction, and  $r\Delta\phi = z = -5.5D..5.5D$  in both lateral directions. In the experiment the confinement was round with a radius of  $5.5D$ , but because the confinement had little effect on the experimental results this difference between simulation and experiment is not important. The total number of grid cells is 2.9 million. All simulations are started up for 125 times  $D/u_{j0}$ , then all turbulent and average quantities are stored 384 times  $D/u_{j0}$ .

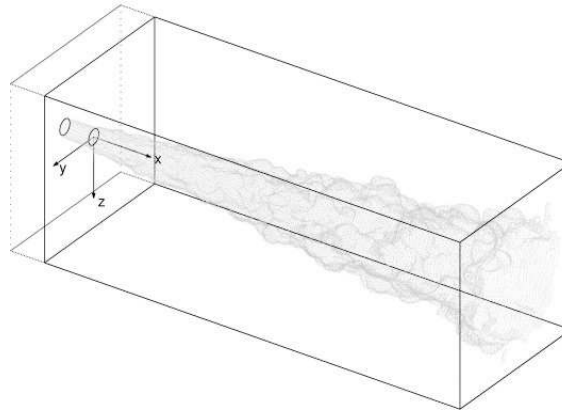


**Figure 4.13:** CFD grid outline of buoyant jet ( $Re = 32000, \rho_{j0}/\rho_{co} = 1.52$ )

## 4.5.2 Boundary conditions

The coflow is prescribed in the model area at  $r = -2D$  outside the jet inflow pipe. The jet inflow pipe is  $2D$  long and simulated by IBM. As jet inflow conditions a  $1/7$ th power law profile is used with maximum velocity equal to  $u_j$ . Lateral sides consist of symmetry boundaries. The jet inflow is perturbed by Azimuthal forcing with  $A = 0.1$  for  $w'$  and zero for  $u', v'$  in combination with Strouhal=0.4, see Equation 3.33. This value of  $A = 0.1$  is less than  $A = 0.5$  used for the non-buoyant JICF in previous test and also less than the literature value of  $A = 0.2$  (Menon and Rizk 1996; Chen et al. 2008; Worthy 2003).

## 4.5.3 Results different advection schemes

This test case of a buoyant jet in weak coflow is interesting for testing the different advection schemes because this case is not very sensitive for wiggles. Therefore the extra dissipation in AV4, AV6 and UPW5 to remove wiggles is not needed and possible negative effects of this extra dissipation on the LES results can be found. Time averaged centreline results are shown in Figure 4.14. Radial profiles are shown in Figures 4.15-4.16. The radial profiles are averaged in radial direction, but because an orthogonal grid is used in both lateral directions this averaging is not as smooth as in a cylindrical grid aligned with the jet direction. The radial velocity profiles in Figure 4.15 are shown relative to  $D$ , the radial stream wise rms fluctuations are shown relative to the local velocity half width  $Lu$  which is the radial distance where the velocity is 50% of the centreline value.

Just like in previous test the CDS2, AV4 and AV6 time averaged results are similar and they are reasonably accurate. UPW5 is radically different. UPW5 over-predicts the turbulent fluctuations by almost 100%, subsequently the jet spreads too fast and both velocity and jet concentration decay too soon. The velocity and jet concentration profiles of CDS2 and AV6 are within 10% from the measured values. Absolute values of turbulent fluctuations differ approximately 20%. The results presented here are less accurate as the LES results of Wang et al. (2008). But in Wang et al. (2008)  $> 50$  cells are used over the initial diameter of the jet, in our simulation only 10 cells are used and 45 cells over the jet diameter is only reached at  $x/D = 20$ .

## 4.5.4 Robustness LES results

AV6 is used to show the dependency on sub-grid scale model and grid resolution. Results obtained with the  $\sigma$ -sub-grid scale model, no sub-grid scale model and a fine simulation on a 1.5 times finer simulation in lateral  $y, z$  directions ( $0.067D$  at outflow, 6.4 million cells) are shown in Figure 4.17. The fine results are slightly better than the results with normal grid size, but the difference is limited. When only a moderate grid resolution is manageable, then the base resolution of 10 grid cells over the jet diameter at outflow is considered to be the under-limit for reasonably accurate LES of a buoyant jet. The results of the  $\sigma$ -sgs model are similar to the base case results obtained with WALE, therefore the results are



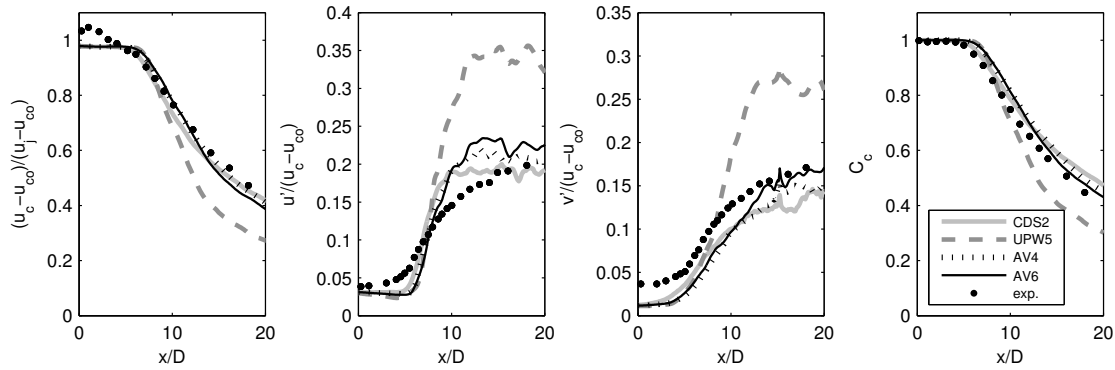


**Figure 4.14:** Comparison buoyant jet ( $Re = 32000, \rho_{j0}/\rho_{co} = 1.52$ ) centre line results of different advection schemes.  $u_c$  and  $C_c$  are the velocity and jet concentration on the centreline.

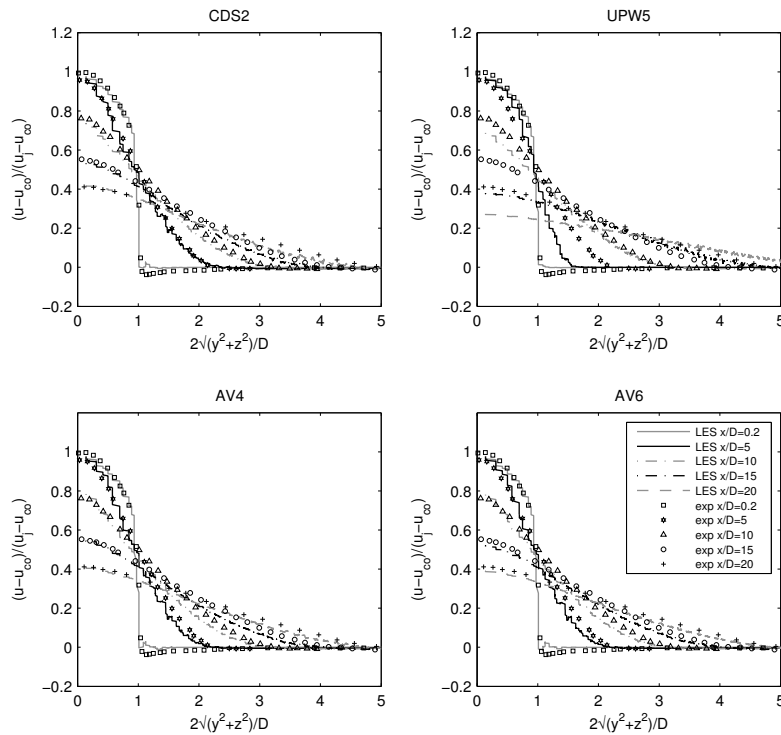


**Figure 4.15:** Comparison buoyant jet ( $Re = 32000, \rho_{j0}/\rho_{co} = 1.52$ ) radial profiles stream wise velocity of different advection schemes.

independent of which sub-grid scale model is used. Results without sub-grid scale model are inaccurate for this test as the jet starts spreading too close to the jet origin with velocity and concentration centreline profiles decreasing too close to the jet origin due to overestimated  $u'$  and  $v'$  fluctuations at small  $x/D$ . Without sub-grid scale model the  $u'$  and  $v'$  fluctuations decrease to unrealistic low values at larger  $x/D$ . The spectra of the velocity inside the buoyant jet in Figure 4.18 obtained for different advection and sub-grid scale models confirm this incorrect behaviour without sub-grid scale model. The spectrum of AV6 without sub-grid scale model is too flat being far from the expected  $-5/3$  slope with too much



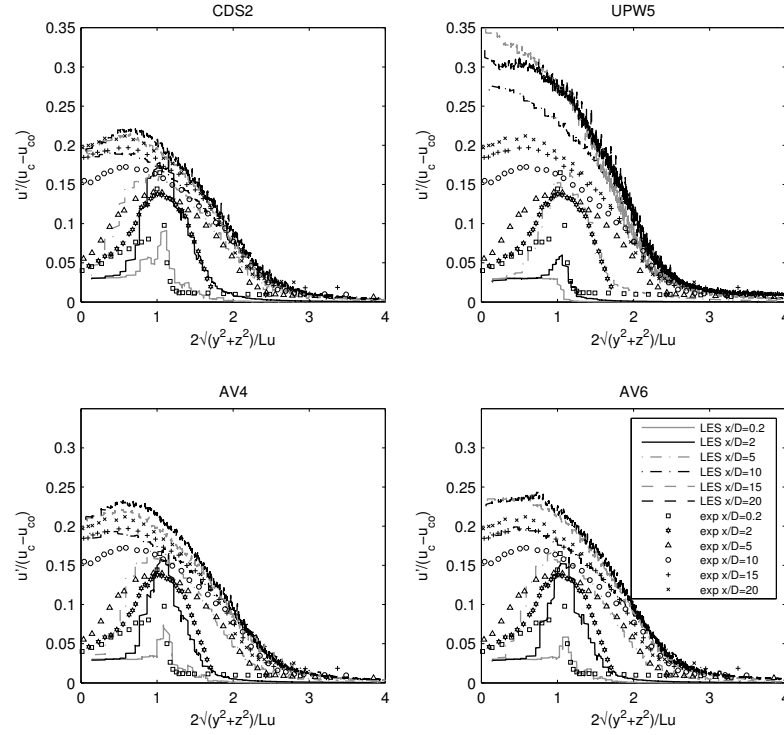


**Figure 4.16:** Comparison buoyant jet ( $Re = 32000$ ,  $\rho_{j0}/\rho_{co} = 1.52$ ) radial profiles stream wise rms fluctuations of different advection schemes.

turbulent kinetic energy in the smallest resolved scales near the cut-off edge. The spectra of CDS2, AV4 and AV6 with WALE or  $\sigma$ -sgs model are all comparable with each other close to the expected  $-5/3$  slope. This confirms that the effect of artificial viscosity of AV4 or AV6 on resolved scales is less than the effect of viscosity from the sub-grid scale model on these scales. The spectrum of UPW5 also has a  $5/3$  slope, but deviates considerably from the CDS2 spectrum, thus damping of the artificial viscosity in UPW5 has significant influence on resolved scales.

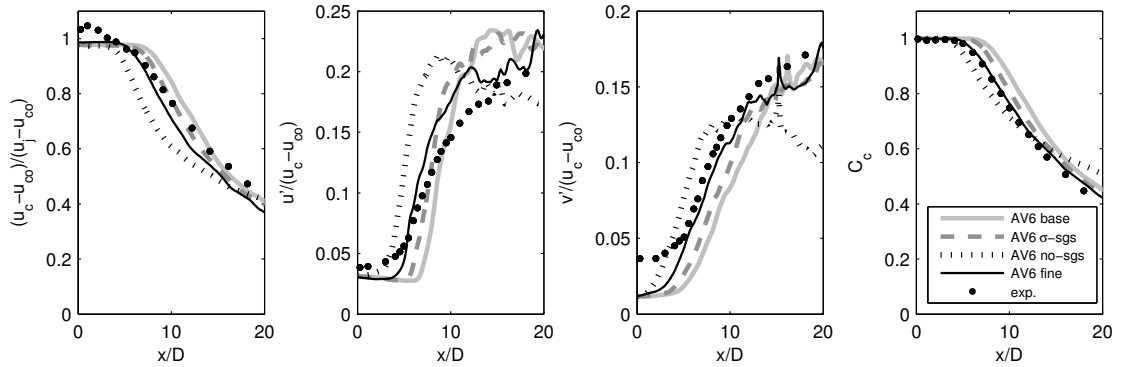


**Figure 4.17:** Comparison buoyant jet ( $Re = 32000$ ,  $\rho_{j0}/\rho_{co} = 1.52$ ) results for different grid resolutions and sub-grid scale models: WALE (base),  $\sigma$ -sgs and no sgs model. Base grid size is  $0.1D$  and fine grid size is  $0.067D$ .

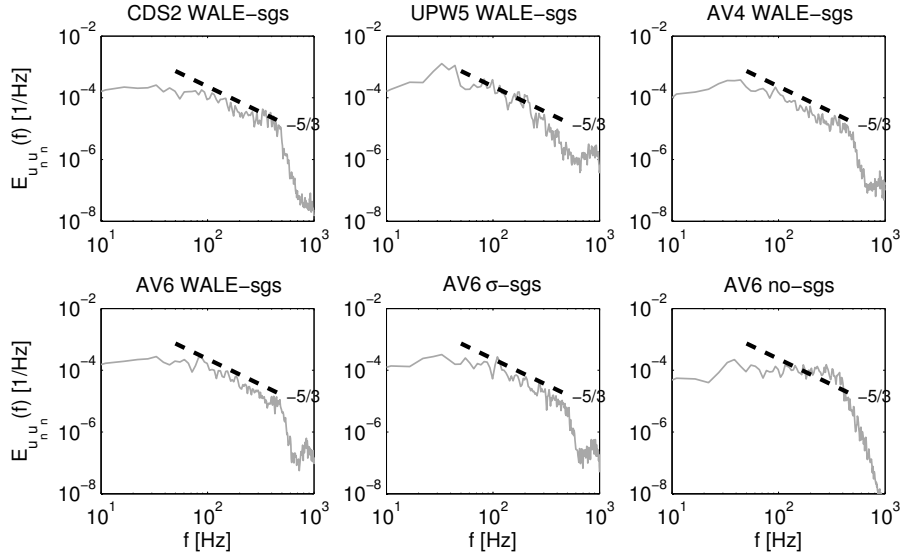


**Figure 4.18:** Spectra of normalised horizontal stream wise velocity ( $u_n = u/\bar{u}$ ) inside buoyant jet ( $Re = 32000, \rho_{j0}/\rho_{co} = 1.52$ ) at  $x/D = 11.9, y/D = 0, z/D = 0$  to compare damping of artificial viscosity from the advection scheme with damping of the sub-grid scale model. The black dashed  $-5/3$  line is only given as indication of the slope, not as a correct level of turbulent kinetic energy or length of the inertial sub range.

#### 4.5.5 Conclusions for buoyant jet in weak coflow $Re = 32000$ density ratio 1.52

In this test UPW5 fails to produce accurate results because the  $u', v'$  fluctuations are too strong which subsequently lead to incorrect spreading of the jet. The schemes CDS2, AV4 and AV6 with no or small amount of numerical dissipation give reasonably accurate results.

### 4.6 Test case buoyant JICF $Re = 4800, Ri = 1.08, \gamma = 2.1$

#### 4.6.1 Model set up

For the buoyant JICF simulation, experimental data is used from a test with  $Ri = 1.08, \gamma = 2.1, Re = 4800$  carried out at the Dredging Engineering section. A sketch of the experimental set up is given in Figure 7.2a. The simulation set up parameters are  $D = 36$  mm,  $u_{cf} = 0.062$  m/s,  $w_{j0} = 0.133$  m/s,  $\rho_{cf} = 1000$ ,  $\rho_{j0} = 1054$  kg/m<sup>3</sup>,  $\nu_{mol} = 1 \cdot 10^{-6}$  m<sup>2</sup>/s. In the experiment the buoyant jet is created with saline water. The saline water mixture is lead by a 10 mm hose into the 36 mm wide jet outflow pipe, a sponge is put inside the outflow pipe near the outflow to diverge the outflow over the full pipe diameter. The buoyant jet outflow pipe has been fitted to a scaled Trailing Hopper Suction Dredging (TSHD) vessel which is pulled through the water. Hence, the buoyant JICF is created by a

moving buoyant jet in a stagnant ambient. The downstream distances of interest in this chapter are smaller than the length of the vessel, so the under keel is simply a flat plate. The width of the vessel is  $15.6D$ , the width of the flume is  $66D$ , and the experimental results are not influenced by vessel or flume width. The conductivity of the salt jet in ambient water is measured at a fixed cross section. The presented experimental cross sections in this chapter are the average of three runs, the characteristic kidney shape is clearly visible but experimental profiles are not perfectly symmetric. There is an unresolved problem with the absolute value of the measured conductivity in the cross section. This makes a direct comparison between experimental density and CFD density impossible. Nevertheless vertical jet location and jet height/width can be clearly identified from the experimental local jet concentration contours and those are used for validation of the CFD results.

The simulation grid is shown in Figure 4.13b. The grid size in  $r$  direction is growing from  $\Delta r = 0.1D$  at the jet origin in two steps to  $\Delta r = 0.15D$  halfway and  $\Delta r = 0.2D$  at the outflow boundary. The lateral grid size in  $\phi$  direction is growing linear from  $r\Delta\phi = 0.1D$  at the jet origin to about  $r\Delta\phi = 0.3D$  at the outflow boundary. The grid size in  $z$  direction is constant  $\Delta z = 0.1D$ . The grid resolution in this simulation is 10 cells for the jet diameter at outflow and typically 30-50 cells for the jet diameter in the bend over phase. The grid dimension is  $r = -4D..26D$  in stream wise direction,  $r\Delta\phi = -6D..6D$  at the jet outflow location, and  $z = 0..30D$ . The total number of grid cells is 6.6 million. All simulations are started up for 1.7 times the model area flow through periods ( $43 \text{ times } D/u_{cf}$ ), then all turbulent and average quantities are stored 3.4 flow through periods ( $86 \text{ times } D/u_{cf}$ ).

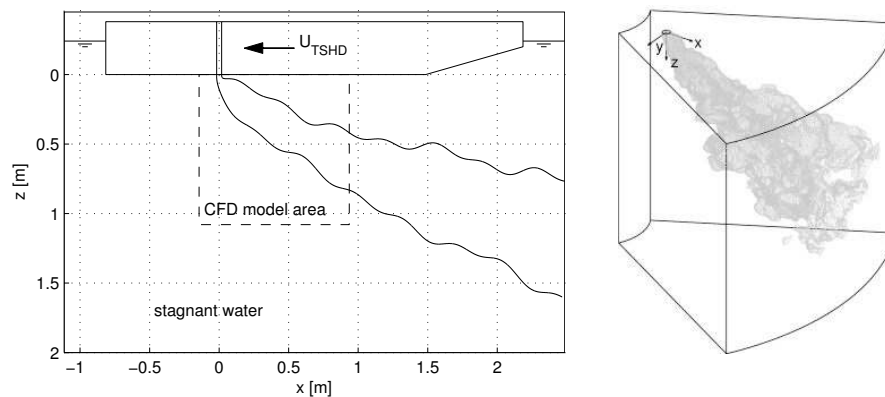


**Figure 4.19:** Experimental set up (left), CFD grid outline (right) of buoyant JICF ( $Re = 4800, Ri = 1.08, \gamma = 2.1$ )

## 4.6.2 Boundary conditions

The inflow of the jet is at the upper boundary of the grid, see Figure 4.13b. A constant 1/7th power law jet inflow velocity profile is prescribed without inflow

pipe, so there is no immersed boundary in this test. No azimuthal forcing is used in this test. These settings matches best with the almost constant jet inflow of the experiment with the sponge. A comparison of simulation results without and with azimuthal forcing ( $A = 0.5$  for  $w$ ,  $A = 0$  for  $u, v$  and  $St = 0.4$ ) is given in Figure 4.23 and shows that azimuthal forcing has little influence in this case. The cross flow velocity (the pulling velocity of the buoyant jet source  $U_{TSHD}$  in the experiment) is in the CFD model prescribed by a constant inflow velocity profile in time and space. The top wall is schematised as a free slip wall.

### 4.6.3 Results different advection schemes

Just like in the first test case, the area in front of the JICF is sensitive for wiggle formation. In Figure 4.20 the instantaneous lateral velocity is shown for the four different advection schemes. The CDS2 results clearly show wiggles. The UPW5 results show no wiggles at all, but UPW5 also shows a laminar start of the buoyant jet; only after approximately  $3D$  a transition to a turbulent jet is made. In the experiment the buoyant jet started turbulent right from the outflow. Again UPW5 has too much dissipation: not only the unwanted high frequency oscillations are damped, but also relevant larger scales are affected. In AV4 and AV6 almost all wiggles are damped, but the relevant scales are less affected than in UPW5. AV6 has slightly more damping of wiggles in front of the buoyant jet than AV4.

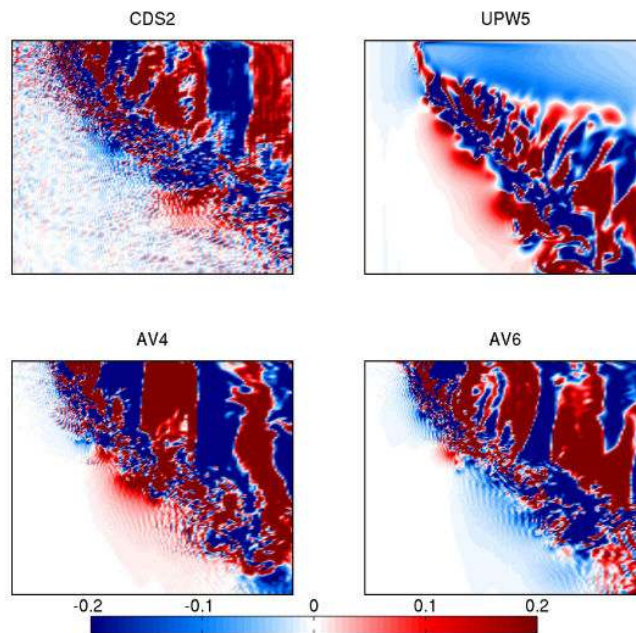


**Figure 4.20:** Instantaneous buoyant JICF ( $Re = 4800$ ,  $Ri = 1.08$ ,  $\gamma = 2.1$ ) lateral velocity field  $v/u_{cf}$  in symmetry plane of different advection schemes.

Figures 4.21 and 4.22 show the time averaged jet concentration of the CFD simulation compared to the measured jet location in the experiment at  $10D$  and  $20D$  downstream of the jet source location. Shape, width, height and vertical

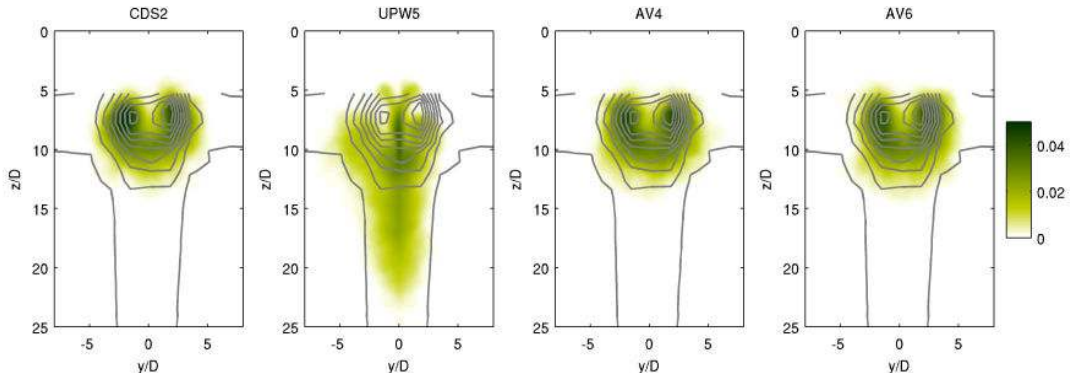


**Figure 4.21:** Comparison buoyant JICF ( $Re = 4800, Ri = 1.08, \gamma = 2.1$ ) cross sections of jet concentration (1 at jet origin) at  $x/D = 10$  of different advection schemes. The experimental results are shown as 9 iso-contours from 10 to 90% of the local maximum measured jet concentration.

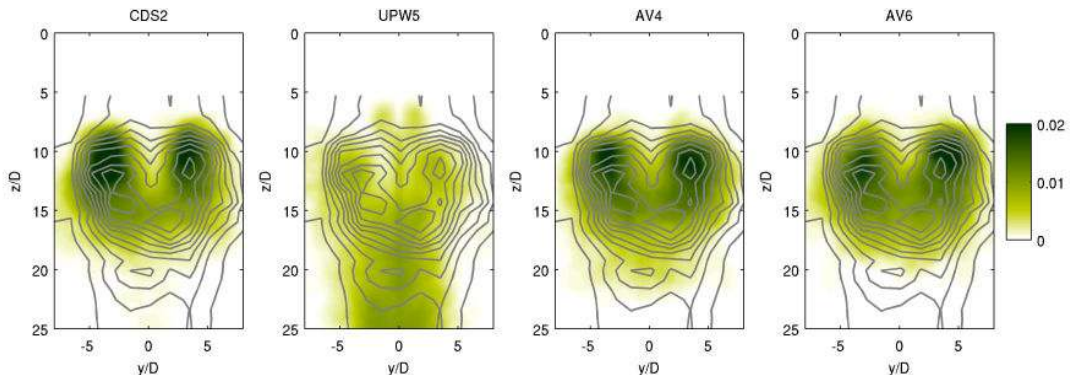


**Figure 4.22:** Comparison buoyant JICF ( $Re = 4800, Ri = 1.08, \gamma = 2.1$ ) cross sections of jet concentration (1 at jet origin) at  $x/D = 20$  of different advection schemes. The experimental results are shown as 9 iso-contours from 10 to 90% of the local maximum measured jet concentration.

position of the simulated jet concentration coincide with the experimental jet at both  $10D$  and  $20D$  for CDS2, AV4 and AV6. UPW5 clearly results in an incorrect location of the jet due to the un-physical laminarisation of the jet at the start. Despite the wiggles in instantaneous flow fields of CDS2, the time averaged profiles are similar to AV4 and AV6.

#### 4.6.4 Robustness LES results

AV6 is used to show the dependency on sub-grid scale model and grid resolution. Results obtained with the  $\sigma$ -sub-grid scale model, no sub-grid scale model and a fine simulation on a 1.5 times finer grid size in all three dimensions ( $0.067D$  at outflow, 33.4 million cells) are shown in Figure 4.23. The fine results are comparable to the results with normal grid size, therefore the results are independent of grid resolution. When only a moderate grid resolution is manageable, then the base resolution of 10 grid cells over the jet diameter at outflow and 30-50 in the bend over phase is already sufficient to obtain accurate LES of a buoyant JICF.



The run with azimuthal forcing ( $A = 0.5$  for  $w'$  and zero for  $u', v'$  in combination with  $Strouhal=0.4$ ) has the same results as the run without azimuthal forcing. The self generated turbulence from the interaction of the buoyant jet with the cross-flow is dominating the inflow turbulence mimicked by azimuthal forcing. A LES of buoyant JICF does not need azimuthal forcing at inflow. The results of the  $\sigma$ -sgs model are similar to the base case results obtained with WALE, therefore the results are independent of which sub-grid scale model is used. Results without sub-grid scale model are similar to results with the WALE or  $\sigma$ -sgs model. However the velocity spectra in Figure 4.24 show a difference between AV6 with the WALE or  $\sigma$ -sgs model or without sub-grid scale model: without sub-grid scale model there is more turbulent kinetic energy at the higher frequencies near the cut-off range than with sub-grid scale model. The effect of artificial viscosity of AV4 or AV6 on resolved scales is less than the effect of viscosity from the sub-grid scale model on these scales. The spectra of CDS2, AV4 and AV6 with WALE or  $\sigma$ -sgs model are all comparable with each other close to the expected  $-5/3$  slope. The spectrum of UPW5 does not have a  $5/3$  slope, and deviates considerably from the CDS2 spectrum, thus damping of the artificial viscosity in UPW5 has too much influence on resolved scales.

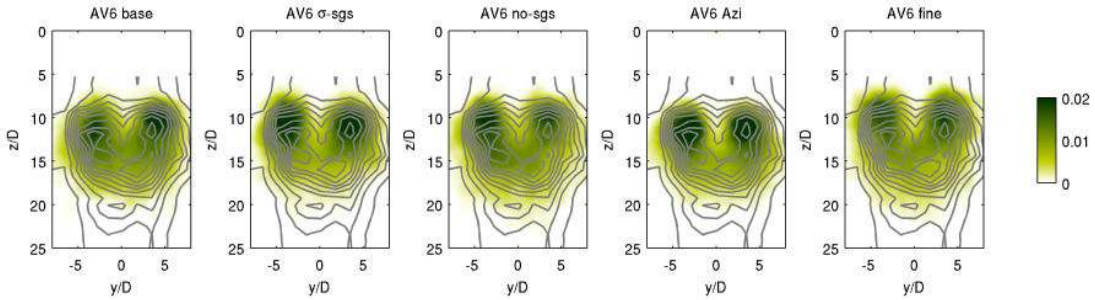


**Figure 4.23:** Comparison buoyant JICF ( $Re = 4800, Ri = 1.08, \gamma = 2.1$ ) cross sections of jet concentration (1 at jet origin) at  $x/D = 20$  for different grid resolutions, influence of azimuthal forcing and sub-grid scale models: WALE (base),  $\sigma$ -sgs and no sgs model. Base grid size is  $0.1D$  and fine grid size is  $0.067D$  at outflow. The experimental results are shown as 9 iso-contours from 10 to 90% of the local maximum measured conductivity.

#### 4.6.5 Conclusions for buoyant JICF $Re = 4800, Ri = 1.08, \gamma = 2.1$

In this test the time averaged results of UPW5 are inaccurate due to un-physical laminarisation of the jet at outflow. Time averaged results for CDS2, AV4 and AV6 are comparably accurate. Like in the first test of the non-buoyant JICF, the wiggles in CDS2 have no negative impact on the time averaged results.

## 4.7 Discussion and conclusions

This chapter has presented and tested a wiggle damping artificial viscosity advection scheme AV6 in the context of LES of buoyant JICF with  $0.5 < \gamma < 2$  and

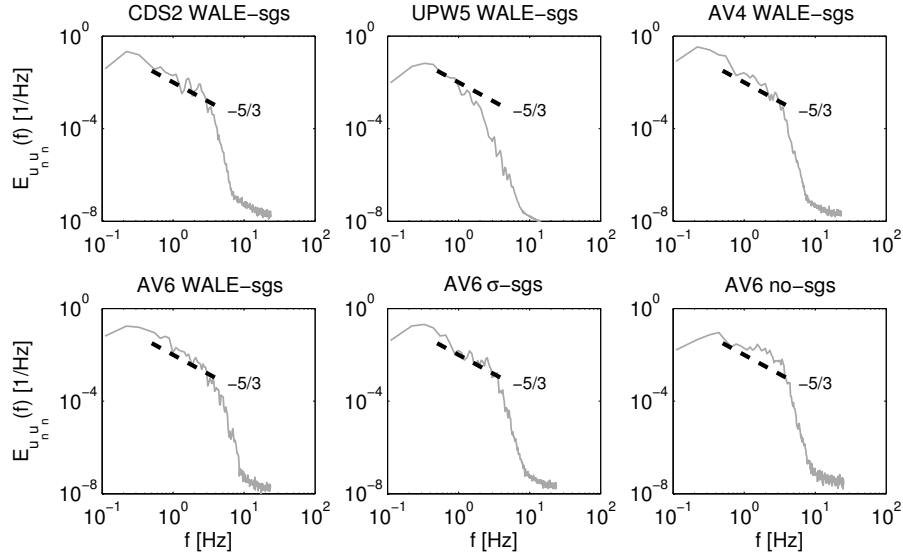


**Figure 4.24:** Spectra of normalised horizontal stream wise velocity ( $u_n = u/\bar{u}$ ) inside buoyant JICF ( $Re = 4800, Ri = 1.08, \gamma = 2.1$ ) at  $x/D = 20, y/D = 0, z/D = 17$  to compare damping of artificial viscosity from the advection scheme with damping of the sub-grid scale model. The black dashed  $-5/3$  line is only given as indication of the slope, not as a correct level of turbulent kinetic energy or length of the inertial sub range.

$Ri \approx 1$  on a staggered mesh. The intention is to apply physical LES with the sub-grid scale model responsible for adequate dissipation of turbulent kinetic energy, the artificial viscosity is not designed to take over the role of the sub-grid scale model as in MILES/ILES. In order to be able to simulate large mixing areas a moderate resolution of 10 grid cells over the diameter of the jet at outflow is used, further downstream the resolution grows rapidly to 30-50 cells over the diameter of the bend over jet. The zone in front of a buoyant JICF is sensitive for wobble formation in LES. AV6 can damp these wiggles adequately and has very limited damping on physical relevant longer scales. AV6 is a mix of, and improvement over, the original artificial viscosity scheme of Jameson et al. (1981) and UPW5 of Wicker and Skamarock (2002). For flow problems without shock waves the Jameson scheme is equal to scheme AV4 in this chapter. AV6 consists of a CDS2 flux combined with a small amount  $\epsilon$  of sixth derivative artificial viscosity. For the tests in this chapter  $\epsilon = 1/512$  was a good balance between low unwanted damping on physical relevant scales and sufficient damping on grid scale of wiggles, but for other flow problems  $\epsilon$  can be adjusted. The behaviour of AV6 is compared with a non dissipative advection scheme CDS2, and with low dissipation schemes AV4 and UPW5.

A Fourier analysis of the Advection-Diffusion equation has demonstrated the favourable damping behaviour of AV6 over AV4 and UPW5. The artificial damping is a function of the number of grid points per wave length  $ppw$ . AV6 has more wanted damping of wiggles with  $ppw = 2$  and less unwanted damping of physical relevant longer scales with  $ppw > 10$  than the original Jameson scheme AV4 or a blend of 5% UPW1 and 95% CDS2 as sometimes used for LES of engineer-

ing scale flow problems. UPW5 is unusable for physical LES as for all length scales with  $ppw < 6$  the damping of UPW5 exceeds the typical influence of sub-grid scale viscosity and for the minimum grid resolution used in this chapter ( $ppw = 10$ ) the damping of UPW5 is still 17% of typical sub-grid scale viscosity. The damping of AV6 exceeds typical sub-grid scale viscosity only up to  $ppw < 3$  and at  $ppw = 10$  it is just 2% of typical sub-grid scale viscosity, which leaves AV6 usable for physical LES.

Next, LES results obtained with AV6 are compared with CDS2, AV4 and UPW5 for three test simulations: a non-buoyant JICF, a buoyant jet in weak coflow and a buoyant JICF. The three test cases together combine all important phenomena to get accurate simulations of an overflow dredging plume: cross-flow, mixing of jet momentum, buoyancy and turbulent profiles. CDS2 suffers from strong wiggles in instantaneous velocity fields of the first and last test. In AV4, AV6 and UPW5 those wiggles are damped, but only AV4 and AV6 result in accurate time averaged results for all three tests. UPW5 shows too much damping, resulting in inaccurate concentration and velocity profiles for the second and last test. The difference in time averaged results between AV4, AV6 and CDS2 is small. Apparently, the wiggles in CDS2 for these tests have no negative impact on the time averaged LES results. Velocity spectra of all three test cases showed that the artificial viscosity in AV4 and AV6 does not replace a sub-grid scale model, but they only damp wiggles at grid scale with almost no dissipation on physical relevant longer scales. Therefore AV4 and AV6 can be used in physical LES with the sub-grid scale model responsible for sufficient dissipation at sub-grid scale. For stability reasons AV6 is preferred over CDS2 for the tests in this chapter. AV6 is preferred over AV4 because it has slightly more wanted damping of wiggles and less unwanted damping of physical relevant scales.

Azimuthal forcing is used to perturb the jet inflow velocity and trigger transition to turbulence. There is a substantial difference between the amplitude of azimuthal forcing applied for the three tests. The best azimuthal amplitude for the non-buoyant JICF is  $A = 0.5$ , for the buoyant jet it is  $A = 0.1$ , and for the buoyant JICF azimuthal forcing has negligible influence and  $A = 0$  is best. The settings used for these tests are not only different from each other, but also different from settings in literature (Menon and Rizk 1996; Chen et al. 2008; Worthy 2003). In literature a value of  $A = 0.2$  is used for buoyant and non-buoyant jets with  $Re = 1000 - 6360$ . The wide scatter in best values for  $A$  indicates that one has to be careful when using azimuthal forcing for cases where no direct comparison with measurements is possible. For LES of buoyant JICF with  $0.5 < \gamma < 2$  and  $Ri \approx 1$  no azimuthal forcing is necessary.

The tests in this chapter have demonstrated that the sixth order artificial viscosity in AV6 is an effective remedy against wiggles in moderate resolution LES, while dissipation on physical relevant scales is sufficiently low. AV6 is a robust, simple and easy to implement advection scheme and the total computational time of a simulation with AV6 is only a few percent more than with CDS2. It is anticipated that AV6 can be very useful in LES simulations on engineering scale for other problems where wiggles emerge due to interaction with obstacles, or due to a sudden change in flow profile.



# Chapter 5

## General validation CFD model

*In previous chapter a novel momentum advection scheme has been presented and tested for three jet cases relevant for simulation of a dredging plume from a moving TSHD. Now the CFD model and this momentum advection scheme are tested with some additional relevant flow benchmarks of which validation data was available. These benchmarks show the performance of the CFD model in a wide variety of turbulent flow cases: turbulent channel flow; suspended sediment transport; density current at the bed; flow near the TSHD; and air-water mixture flow. The first three flow cases are relevant for the transport of the sediment dredging plume by ambient currents and are validated with experimental and DNS data. The flow past a TSHD hull is validated by experimental data of flow past an obstacle and backward facing step tests. Propeller flow and separation of air from an air-water jet in crossflow are validated with experimental data. In this chapter the  $z$  axis is defined positive upward, which is different from the definition in Section 3.1.*

### 5.1 Turbulent channel flow

#### 5.1.1 Turbulent channel flow

Turbulent open channel flow is tested with DNS data of a  $Re_\tau = \frac{u_* H}{\nu} = 590$  ( $Re = 10900$ ) case (Moser et al. 1999) by validating the velocity and turbulent fluctuation profiles. The flow depth is  $H = 0.05$  m, the average velocity is  $U = 0.22$  m/s. A Cartesian computational domain of  $6.4H$  long and  $3.2H$  wide is used with periodic boundaries in  $x, y$  directions. The computational grid has  $128 \times 64 \times 40$  cells. All quantities are time averaged over  $19H/u_*$  ( $350H/U$ ). A hydraulic smooth bed is used.

The velocity and turbulent fluctuation profiles are validated with the DNS data in Figure 5.1. The LES velocity profile  $u$  and turbulent fluctuations  $u', w', uw'$  are simulated accurately with all LES profiles close to the DNS ones. Near the free surface the discrepancies can be explained because the free surface is lacking in the DNS data. The DNS data is taken from a simulation of a closed duct with height  $2H$ . With these results, the LES model is validated successfully for turbulent open channel flow.

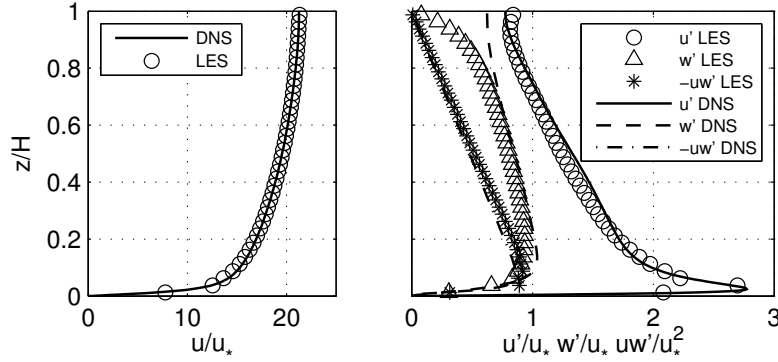


**Figure 5.1:** Time averaged velocity and turbulent fluctuations of open channel flow with  $Re_\tau = 590$  ( $Re = 10900$ ) obtained by periodic LES.

### 5.1.2 Synthetic turbulent inflow

The SEM method to generate synthetic turbulent inflow is tested for turbulent open channel flow with  $Re_\tau = 590$ . The computational settings are similar as in previous section, except now the domain is not periodic in  $x$  direction and at  $x = 0$  an inflow log velocity profile is used as a boundary condition with additional turbulent fluctuations generated by SEM. The computational domain has the following dimensions:  $20H \times 3.2H \times 1H$  with  $400 \times 64 \times 40$  grid cells.

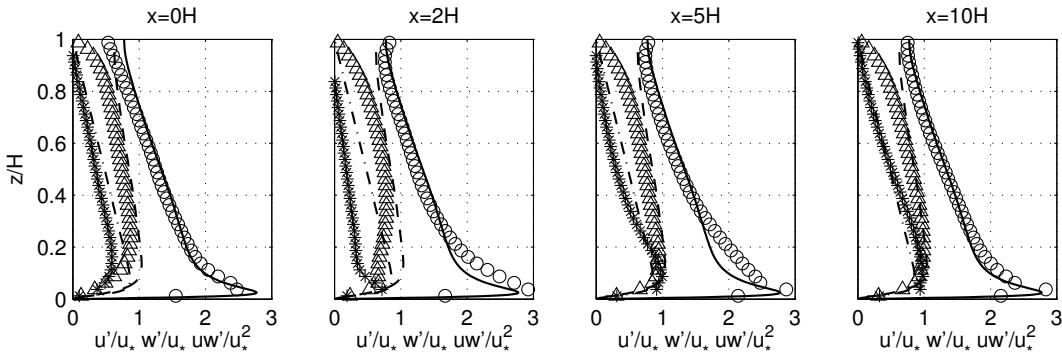


**Figure 5.2:** Time averaged turbulent fluctuations of open channel flow with  $Re_\tau = 590$  ( $Re = 10900$ ) obtained by LES steered by a SEM inflow boundary. Symbols and lines as in Figure 5.1.

The turbulent fluctuations  $u'$ ,  $w'$ ,  $u'w'$  profiles at the inflow boundary and at different distances in the interior domain are shown in Figure 5.2, the  $u$  profile is equal to the log profile at all distances and therefore not shown. At the inflow the SEM method prescribes the correct DNS  $u'$ ,  $w'$ ,  $u'w'$  profiles and the simulated profiles at the first non-boundary computational cell at  $x = 0H$  are close to the correct DNS profiles. The simulation needs some distance to adapt from the prescribed mimicked turbulent eddies to the simulated eddies and at  $x = 2H$  the  $u'$ ,  $w'$ ,  $u'w'$  profiles are not so accurate. However, the SEM method results in a rather short adaptation length and already at  $x = 5H$  the  $u'$ ,  $w'$ ,  $u'w'$  profiles are

reasonably accurate and at  $x = 10H$  the  $u', w', u'w'$  profiles are almost as accurate as the profiles in Figure 5.1 coming from a periodic simulation. The results in Figure 5.2 and an adaptation length of  $5 - 10H$  are comparable to the SEM simulation of turbulent channel flow shown in Jarrin (2008).

## 5.2 Suspended sediment transport

### 5.2.1 Low sediment concentration channel flow

The balance between settling of sediment and turbulent diffusion is tested with a low sediment concentration turbulent channel flow benchmark. A low sediment concentration in this case means there is negligible influence of the suspended sediment on the flow and hindered settling does not play a role. All sediment stays in suspension. For low suspended sediment concentrations the vertical concentration profile is given by the Rouse profile:

$$\frac{C}{C_a} = \left( \frac{z_a}{h - z_a} \frac{h - z}{z} \right)^{SP}, \quad (5.1)$$

the suspension parameter  $SP$  is given by:

$$SP = \frac{w_s}{\beta \kappa u_*}, \quad (5.2)$$

here  $\beta = 1$ ,  $C_a$  is the reference concentration at vertical level  $z_a$  from the bed. To validate the model,  $z_a$  is chosen equal to the vertical distance of the first concentration grid cell ( $0.5\Delta z$ );  $C_a$  is equal to the computed  $C$  in this grid cell. As test case the turbulent open channel flow from Section 5.1.1 is used with an average volume concentration of  $\bar{C} = 10^{-4}$  and a sediment particle size of  $32 \mu\text{m}$  with  $w_s = 0.8 \text{ mm/s}$  and flocculation not taken into account. The simulated suspended sediment concentration in Figure 5.3 is almost identical to the Rouse profile. The balance between settling and turbulent diffusion in the LES model is correct. The simulated suspended sediment concentration profile is accurate for low sediment concentration turbulent open channel flow.

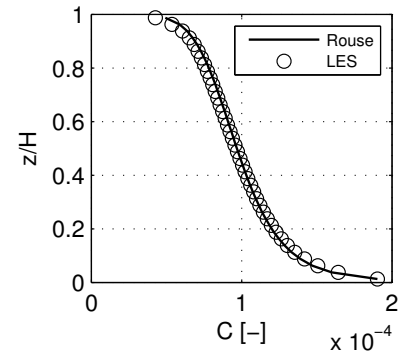


**Figure 5.3:** Time averaged suspended sediment concentration profile for low sediment concentration ( $\bar{C} = 1 \cdot 10^{-4}$ ) open channel flow.

### 5.2.2 High sediment concentration channel flow

Next step is to validate the model for a high sediment concentration case. Under high concentration conditions the influence of the suspended sediment on the

flow is significant and hindered settling is important. Mastbergen and Winterwerp (1987) performed high sediment concentration channel flow experiments with all sediment in suspension and no stationary bed, which are published in Winterwerp et al. (1990). The vertical velocity profile and suspended sediment concentration profile are measured for different flow rates and sediment concentrations. In this section experimental results for the case of an average sediment volume concentration  $\bar{C} = 0.108$  are used. The flow depth is  $H = 0.0981$  m, the average velocity is  $U = 1.53$  m/s and  $Re = 150000$ . The experimental flume was tilting with  $i = 0.0102$ . Coarse sand was glued to the bottom of the flume with  $D_{50} = 0.5$  mm, in the model this is represented by a Nikuradse roughness  $k_s = 1$  mm. In the experiment the sediment particle size distribution had a  $D_{50} = 120$   $\mu\text{m}$ , in the model this is represented with a single sediment fraction of  $120$   $\mu\text{m}$  with  $w_s = 12$  mm/s. A Cartesian computational domain of  $6.4H$  long and  $3.2H$  wide is used with periodic boundaries in  $x, y$  directions. The computational grid has  $128 \times 64 \times 40$  cells. All quantities are time averaged over  $94H/U$ .

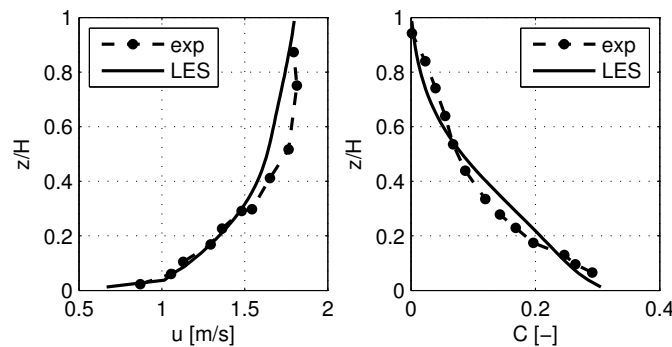


**Figure 5.4:** Time averaged velocity and suspended sediment concentration profiles for high sediment concentration ( $\bar{C} = 0.108$ ) open channel flow.

The simulated vertical velocity profile is close to the experimental one, see Figure 5.4. They are identical up to  $z/H = 0.3$ , then the experimental profile makes a small jump. This jump seems to be unrealistic as the LES velocity profile leads exactly to the desired average velocity of  $U = 1.53$  m/s. The experimental velocity profile leads to a larger average velocity. Perhaps there was a non uniform discharge distribution over the width of the flume in the experiment, or there were some measuring inaccuracies. The simulated vertical suspended sediment concentration profile is very close to the measured profile. Only near the free surface and near the bed small differences are visible; at both locations the experimental concentration is slightly larger than the simulated concentration. These small differences might be attributed to the usage of only one particle size in the simulation; in the experiment the smaller particles in the particle size distribution are expected to cause a larger concentration near the free surface and the larger particles are expected to cause a larger concentration near the bed. The particle size distribution is not documented in Winterwerp et al. (1990) and already with one sediment fraction satisfactory agreement between the measured and simulated concentration profile is obtained.

### 5.2.3 Sediment deposition at the bed

An experiment by Wang and Ribberink (1986) is used to validate the reduction of the suspended sediment concentration by deposition of sediment at the bed. In the experiment a uniform and steady flow is generated with a low sediment concentration (negligible influence of the sediment on the density). The first 45 water depths of the experimental flume have an impermeable bed, but from  $X_m = 0$  onward the bed is a perforated plate (33% holes, hole diameter 3 mm) which allows for sediment settling. Re-suspension of sediment at the perforated plate is impossible. Special care is taken to prevent exchange of momentum by turbulent eddies of the zone below the perforated plate and the zone above the plate. Sediment of  $D_{50} = 100 \mu\text{m}$  and  $w_s = 7 \text{ mm/s}$  with a narrow gradation is used, which in the model is represented by a single sediment fraction. The experimental flume is 0.5 m wide, the water depth is  $H = 0.215 \text{ m}$ , the average velocity is  $U = 0.56 \text{ m/s}$  and  $Re = 120000$ . The Nikuradse wall roughness is  $k_s = 1.1 \text{ cm}$ . At several distances  $X_m$  downstream a vertical sediment concentration profile is measured. In the simulation this case is represented by a Cartesian computational domain of  $6.4H$  long and  $3.2H$  wide with periodic boundaries in  $x, y$  directions. The computational grid has  $128 \times 64 \times 40$  cells. The simulation has a spin up time of  $914H/U$  to guarantee fully developed channel flow, then the sediment is released uniformly in the vertical and  $24H/U$  seconds later deposition at the bed is switched on in the model. The time between release of the sediment and allowing deposition at the bed was a calibration parameter:  $24H/U$  resulted in a correct starting vertical sediment profile. Each measured vertical sediment profile at distance  $X_m$  is compared with the average simulated vertical profiles in the full domain at  $t = X_m/U$ .

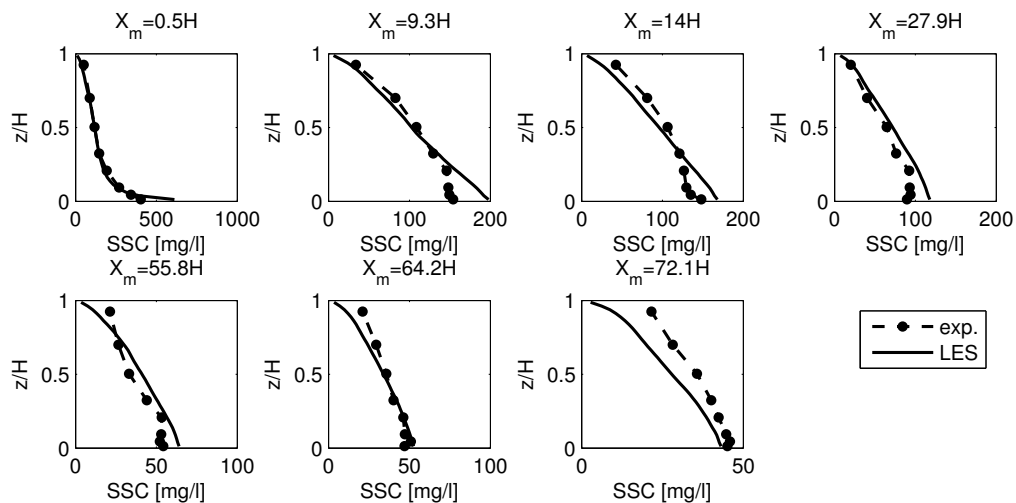


*Figure 5.5: Suspended sediment concentration profiles for channel flow with deposition at the bed.*

Figure 5.5 shows the simulated and measured vertical sediment concentration profiles at different distances  $X_m$  downstream from the start of deposition. The

simulated profiles generally agree well with the measured profiles. Most obvious difference occurs near the bed. Near the bed the simulated SSC is generally larger than the measured SSC, probably this difference originates from the perforated plate in the experiment which not only allows sediment to disappear from the flume but also permits some exchange of water. In the model the bed is simulated by a solid closed boundary where sediment can disappear by settling, but water cannot penetrate at all. Besides this explainable difference in SSC profile very close to the bed, overall the shape and magnitude of the SSC profile is simulated correctly for all distances: the model can reproduce the reduction of SSC in the water column by deposition at the bed.

## 5.3 Density currents

### 5.3.1 Density current at sloping bed

A density current at a sloping bed flows in downward direction under influence of gravity, see the sketch in Figure 5.6 (left). When the Reynolds number is sufficiently large the front velocity is constant for slopes with  $\theta \geq 5^\circ$  (Britter and Linden 1980). Friction and entrainment of ambient fluid balance the gravitational acceleration. The front speed  $u_f$  is then given by:

$$\frac{u_f}{(g\Delta\rho/\rho q)^{1/3}} = 1.5 \pm 0.2, \quad (5.3)$$

with  $q$  as the discharge per unit width. LES simulation results are shown in Figure 5.6 (right). Results for three different slopes are shown. The vertical resolution is approximately 15 cells over the height of the density current and the horizontal grid sizes are double the vertical one.  $q$  is chosen as  $0.01 \text{ m}^2/\text{s}$  and  $\Delta\rho/\rho = 0.083$ . The bed is simulated as hydraulic smooth. The simulated front speed takes some time to grow close to the expected value of Equation 5.3. For steeper slopes it takes less time to arrive at the final front speed than for less steep slopes.

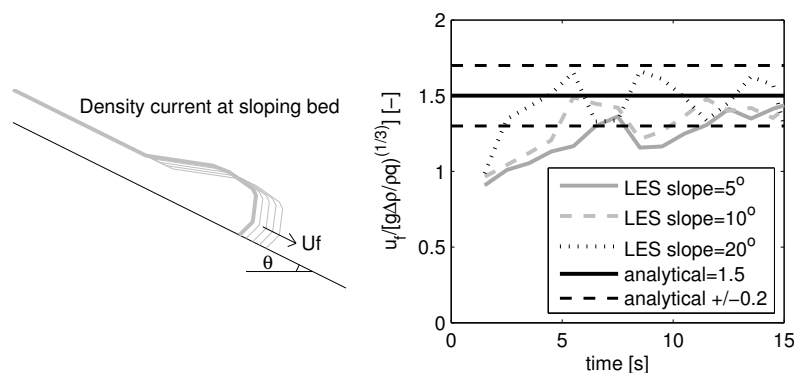
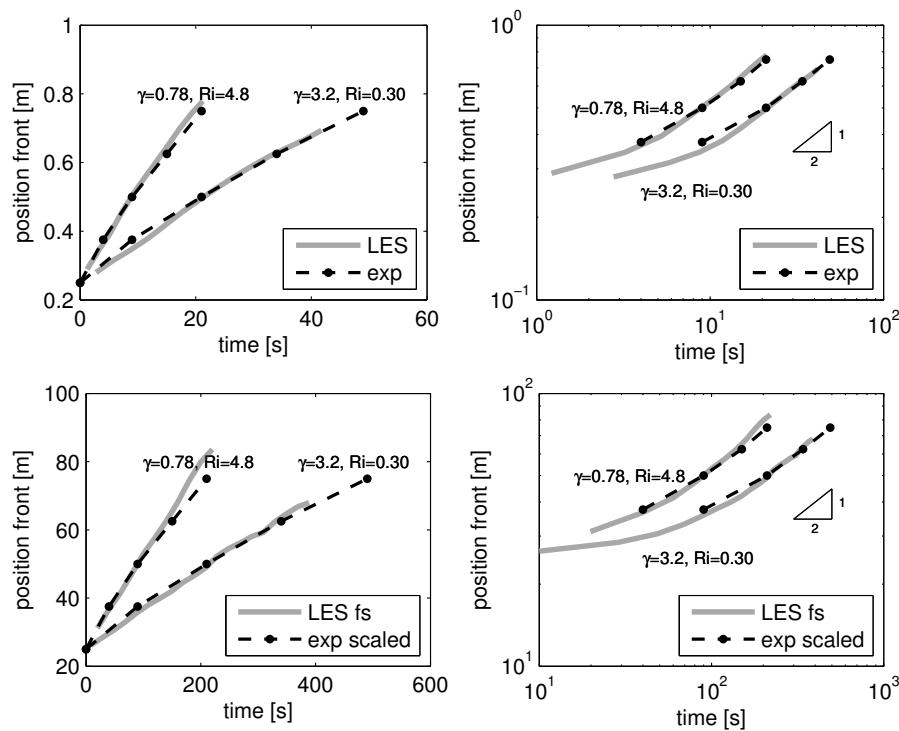


Figure 5.6: Density current at a sloping bed, sketch (left) and results (right).

### 5.3.2 Radial spreading of density driven overflow plume at bed

When an overflow plume touches the bed it will spread radially. [Boot \(2000\)](#) has studied the radial spreading of overflow plumes after impinging on a horizontal bed in an experimental set up. These experimental results are used by [Winterwerp \(2002\)](#) to derive a classification of density driven or mixing dominated behaviour of overflow plumes. Two cases in the density driven regime are used to validate the impingement of an overflow plume at the bed. First case has  $\gamma = 0.78, Ri = 4.8$  ( $\rho_{j0} = 1049 \text{ kg/m}^3, w_{j0} = 0.05 \text{ m/s}, \rho_{cf} = 1000 \text{ kg/m}^3, u_{cf} = 0.065 \text{ m/s}, D = 0.025 \text{ m}$ ) and second case  $\gamma = 3.2, Ri = 0.30$  ( $\rho_{j0} = 1049 \text{ kg/m}^3, w_{j0} = 0.2 \text{ m/s}, \rho_{cf} = 1000 \text{ kg/m}^3, u_{cf} = 0.065 \text{ m/s}, D = 0.025 \text{ m}$ ). In the experiments the density difference of the overflow plume is generated by using very fine China clay. The settling velocity is negligible ( $w_s \approx 0.02 \text{ mm/s}$ ) and thus settling is switched off in the simulations. The bed is simulated as hydraulic smooth. The horizontal spreading is traced by following the progress in time of the edge of the plume at the bed.



*Figure 5.7: Radial spreading density driven overflow plume at bed as a function of time with linear axes (left) and log-log axes (right). The top row shows results at experimental scale, the bottom row shows results at full scale with  $Ri, \gamma$  similar to the experiment.*

The LES simulations follow the experimental results of [Boot \(2000\)](#) closely, see Figure 5.7 top row. The radial spreading progresses with the square root of time (2:1 slope in the log-log diagram of Figure 5.7). Also full scale simulations are carried out where the length is multiplied by a factor 100, the velocity by a factor 10 and the density difference is kept at the experimental value to arrive at



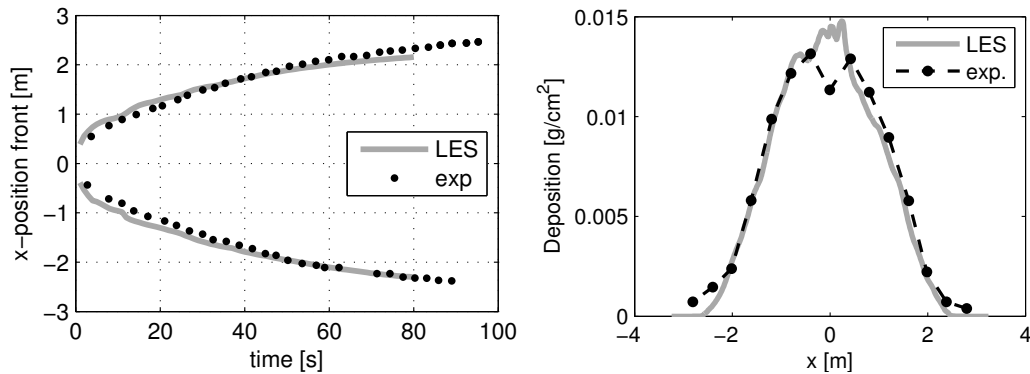
a realistic full scale TSHD with similar  $\gamma$ ,  $Ri$  values as in the experiment. In order to arrive at similar crossflow velocity profiles for the experimental scale and full scale a Nikuradse roughness of  $k_s = 0.1$  m has been applied for the full scale case. With this roughness value the log velocity profiles of full scale and experimental scale are identical. The bottom row in Figure 5.7 shows the full scale results and they are similarly accurate as the simulation results at experimental scale. This shows that even for a full scale simulation, where all turbulent scales up to the inertial sub-range cannot be resolved on the grid as much as in a simulation on experimental scale, LES is capable to simulate the correct front speed of the bed plume.

### 5.3.3 Density current at bed including deposition

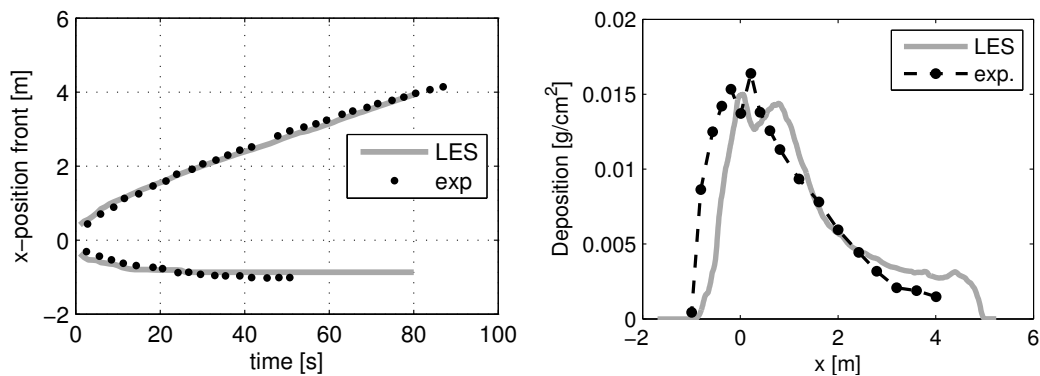
The behaviour of a density current at a horizontal bed including deposition is validated with experimental measurements by [Hallworth et al. \(1998\)](#). In the experiment a fixed amount of particle loaded water is released through a vertical pipe at the free surface of an open flume. The particle loaded water flows through the water column almost instantaneously and then spreads horizontally at the bed as a density current. The front position of the density current is tracked in time and the final deposition amounts along the experimental flume are measured. The flume length is 9.4 m, the flume width is 0.26 m and the water depth  $H = 0.287$  m. 2 l water containing 50 g/l silicon carbide particles of  $37 \mu\text{m}$  and  $\rho_s = 3217 \text{ kg/m}^3$  is released at the water surface in the flume centre within 1 s. This release time is small compared to the total spreading time of the density current of more than 80 s. Exact inflow characteristics and exact release time in the experiment are not documented; in the model the particle loaded water is released in 1 s with a constant inflow discharge. Results with and without an ambient current of  $U = 0.026$  m/s in the flume are used to validate the CFD model. The simulations are carried out on a Cartesian computational domain. The computational grid with ambient current is 6.9 m long and has  $670 \times 40 \times 40$  cells; without ambient current it is 6.5 m long and has  $645 \times 40 \times 40$  cells. The horizontal grid size  $\Delta x$  varies between  $0.02H$  and  $0.05H$  with finer cells at the origin of the density current. The settling velocity of the silicon carbide particles is  $w_s = 1.65$  mm/s. The bed is simulated as a hydraulic smooth wall and the side walls are simulated as no slip walls.

There is one important difference between the simulation set up and the experimental set up: in the experiment the release of the particle loaded water leads to an increase in the total amount of water in the flume which causes a slightly larger water depth. In the model a rigid lid approach is followed and the total volume of water in the flume stays equal. The particle loaded water released in the model therefore leads to a flow in horizontal direction out of the computational domain. In order to prevent a significant flow in positive  $x$ -direction towards the outflow boundary during the 1 s release time, 50% of the influx is sucked out of the model domain at the inflow  $x$ -boundary. This fix does not completely solve the discrepancy in volume balance between the experimental and simulation set up, but at least the density current is not biased towards the

positive  $x$ -direction in the model.



*Figure 5.8: Symmetric spreading of density current at a bed without ambient current, position front (left) and final deposition at the bed (right).*



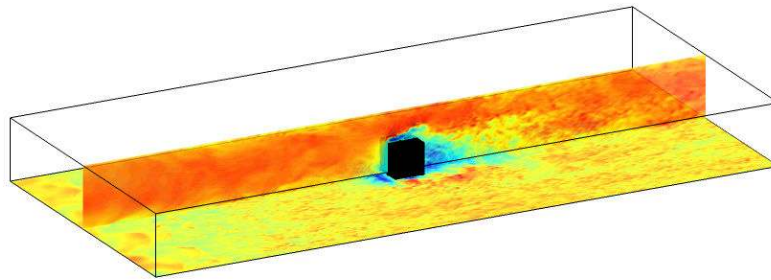
*Figure 5.9: Asymmetric spreading of a density current at a bed with ambient current, position front (left) and final deposition at the bed (right).*

Figure 5.8 shows the symmetric spreading of the density current in absence of an ambient current. The simulation results show the expected symmetric behaviour and the position of the front and deposition are close to the measurements. The results in case of a small ambient current are shown in Figure 5.9. The simulation shows the expected asymmetric spreading towards the direction of the ambient current. The simulated position of the front is close to the measured position of the front. The simulated deposition is correct in shape and magnitude, but it is shifted in positive  $x$  direction compared to the experimental one. This discrepancy might be caused by the aforementioned differences between model and experiment in volume balance and the unknown exact release characteristics of the particle loaded water in the experiment and therefore no further attempts to improve the LES results are made. Overall the model shows the correct behaviour of a density current with deposition at the bed both with and without ambient current; the front position is simulated accurately and the deposition profile has the correct shape and magnitude.

## 5.4 Flow near the TSHD

### 5.4.1 Flow past a cube

The flow past a cube benchmark is a relevant test for the immersed boundary method used to implement the TSHD hull. It consists of a square duct of height  $2H$  with a square cube of size  $H$  mounted on the floor. Although the geometry of this test is rather straightforward, complicated flow patterns are developing.



*Figure 5.10: Simulation area flow past a cube, the slices show the instantaneous velocity  $u$ .*

Numerically this test is interesting because the cube is an obstacle for the flow and the area in front of an obstacle is very sensitive for wiggles. The flow round the cube is highly unsteady, therefore LES is a better candidate to use than RANS. For this reason flow past an obstacle has often been used as a benchmark for LES codes (Rodi 1998). Experimental data by Martinuzzi and Hussein (1993) is used for validation of the CFD model. The Reynolds number defined by the average inflow velocity  $u_m$  and the cube height is  $Re = u_m H / \nu = 40000$ . The experiments are carried out in a closed duct of  $12H$  wide, the inflow section is  $104H$  long. The turbulent flow at the cube is fully developed. In the CFD model the width is  $9H$ , the inflow section is  $10H$  long, see figure 5.10.

A coordinate system with  $x, y, z = 0$  at the bottom-center of the forward side of the cube is adopted for the presentation of the results, see also Figure 5.11. The inflow velocity profile consists of a double log profile with inflow turbulence mimicked by SEM. The cube is simulated by IBM. The uniform grid size is  $\Delta x = \Delta y = 0.04H, \Delta z = 0.036H$ . Hence, a relatively coarse grid is used with only 56 cells over the vertical in the inflow duct, 28 cells over the cube height  $H$  and 25 cells over the cube width and length  $H$ . This amount of grid cells to cover the cube is comparable to the amount of grid cells available in the CFD simulations of a dredging plume to cover the TSHD vessel. Results are averaged over  $160H/u_m$  time units. Information about wall roughness in the experiment is missing. In the simulations hydraulic smooth walls are applied at the top and bottom wall of the duct and this resulted in correctly simulated velocity profiles. At the cube no shear stress is applied.

The flow patterns round the cube can be seen in the time averaged streamlines in Figure 5.11. Note that the streamlines for the experiment start at different locations as the streamlines of the simulation, but this does not harm the recognition of the general stream patterns. These general patterns in the simulation are

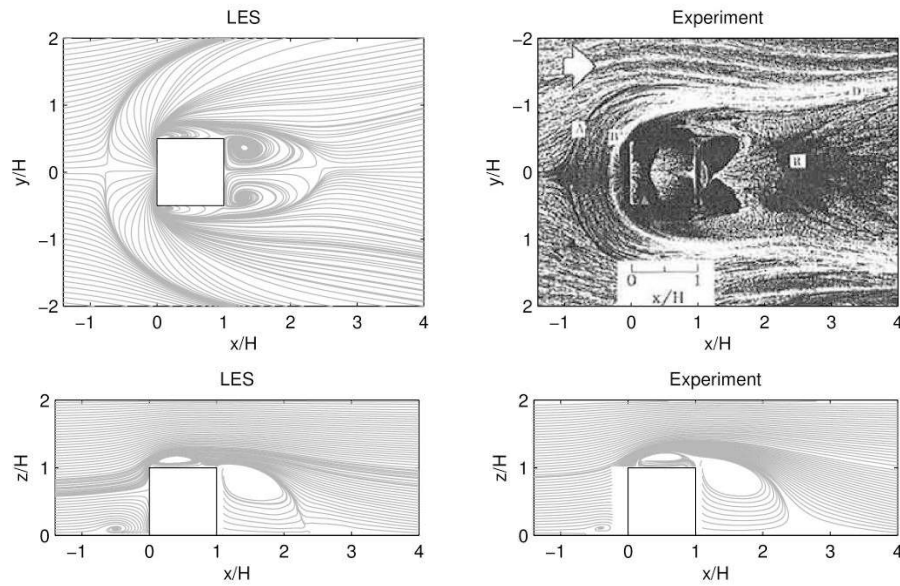


**Figure 5.11:** Time averaged streamlines of flow past a cube at the floor of the channel (top) and at the centre plane (bottom). The experimental streamlines at the floor of the channel consists of oil film visualisation, the simulated streamlines come from the velocities in the first cell at  $0.5\Delta z$  from the floor. The experimental streamlines at the centre plane are drawn using the measured flow velocities.

similar to the patterns in the experiment. At the sides and top of the cube the time averaged streamlines show narrow recirculation zones of approximately  $0.25H$ , the simulated ones agree closely with the experiment. The large front separation curve is visible in the simulation, although it is wider than in the experiment. The large recirculation zone behind the cube visible in the centre plane has a length of approximately  $1.4H$  in the simulation and  $1.5H$  in the experiment.

More detailed comparison between the experiment and simulation can be found in Figure 5.12. The time averaged profiles of velocity and turbulent quantities are compared. The vertical profiles at the center of the cube ( $x/H = 0.5, y/H = 0$ ), including turbulent energy  $u'$  and Reynolds shear stress  $u'w'$ , are reproduced reasonably accurate in the simulation; largest deviation is found for the  $w$  profile at ( $x/H = 0.5, y/H = 0$ ). Downstream at  $x/H = 1$  and  $x/H = 2$  some deviations start to occur, the strength of the recirculation is under predicted in the simulation. Further downstream at  $x/H = 4$  all profiles are reproduced correct again. These results are comparable in quality with a LES using a similar moderate grid size  $\Delta x \approx 0.04H$ , but without immersed boundaries, by [Krajnović and Davidson \(2002\)](#).

#### 5.4.2 Backward facing step

The backward facing step benchmark consists of a flow at a sudden expansion. Experimental data by [Makiola \(1992\)](#) is used for validation of the CFD model. Two cases are tested: a  $90^\circ$  expansion and a  $20^\circ$  expansion.

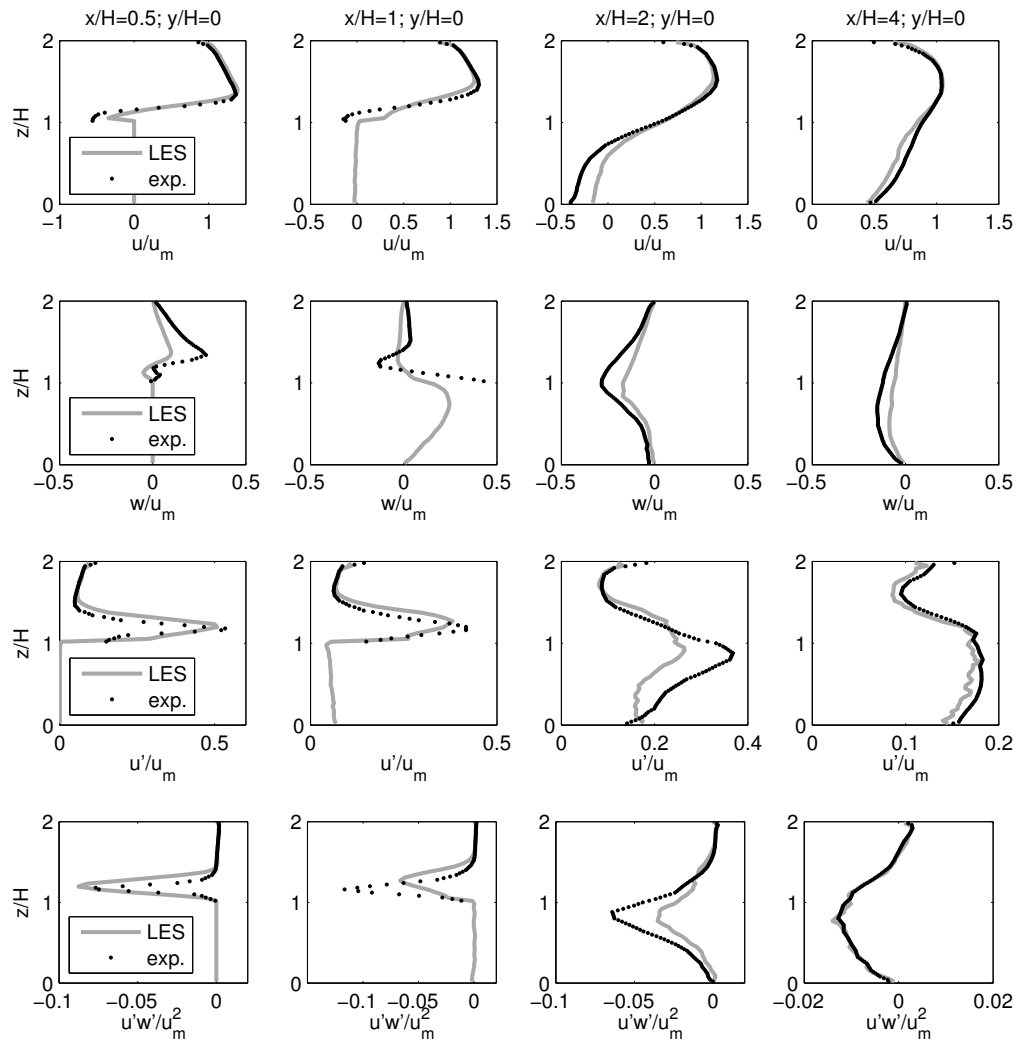


**Figure 5.12:** Time averaged results of  $u/u_m$ ,  $w/u_m$ ,  $u'/u_m$  and  $u'w'/u_m^2$  at the centre plane of flow past cube benchmark.

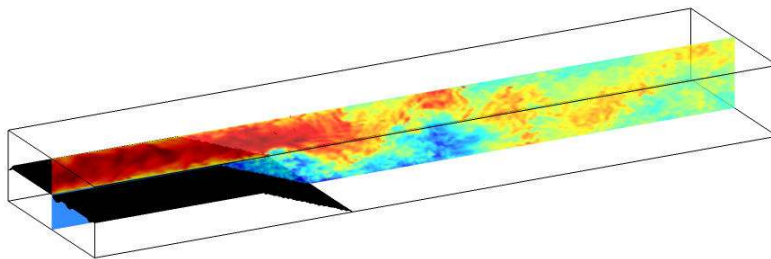


**Figure 5.13:** Simulation area backward facing step, the slice shows the instantaneous velocity  $u$  for the  $20^\circ$  case.

The step height  $H$  is equal to the flow height in front of the step and the flow height after the step is  $2H$ . The Reynolds number defined by the maximum flow velocity at the inflow  $u_m$  and the step height is  $Re = u_m H / \nu = 64000$ . The

experiments are carried out in a closed duct of  $40H$  wide, the inflow section is  $100H$  long. The turbulent flow at the step is fully developed. In the CFD model the width is  $5H$ , the inflow section is  $5H$  long, see Figure 5.13. The inflow velocity profile consists of a double log profile with inflow turbulence mimicked by SEM. The backward facing step itself is simulated by IBM. The  $20^\circ$  expansion is covered by a staircase line, the  $90^\circ$  expansion is covered more exact by a straight line. The grid size is  $\Delta x = \Delta y = \Delta z = 0.0476H$ . Only 21 cells over the step size  $H$  are used, such moderate grid resolution is comparable to the amount of grid cells which will be used in the CFD simulations of a dredging plume to cover the aft of a TSHD vessel. Also the inflow duct is covered by only 21 cells in the vertical. Results are averaged over  $256H/u_m$  time units. Information about wall roughness in the experiment is missing. In the simulations hydraulic smooth walls are applied at the top and bottom wall of the duct and this resulted in correctly simulated velocity profiles.

The CFD results of the  $90^\circ$  case are shown in Figure 5.14. Both the simulated mean stream wise velocity profiles  $u/u_m$  and the turbulent fluctuations  $u'/u_m$  are close to the experimental profiles.

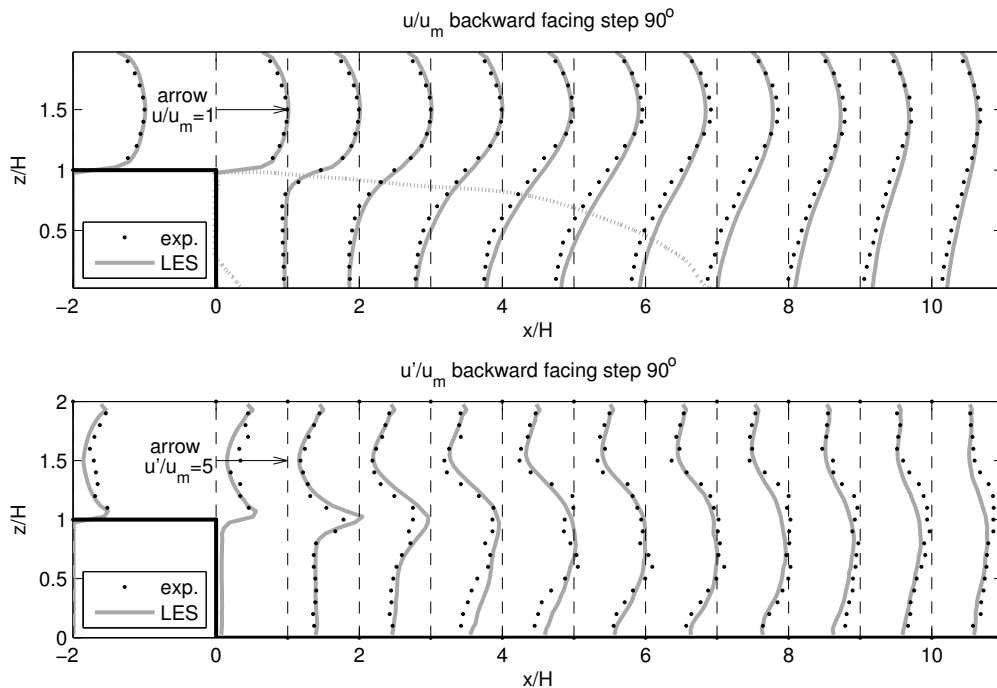


**Figure 5.14:** Time averaged results backward facing step  $90^\circ$ . The edge of the recirculation zone is indicated with a grey dotted line.

The CFD results of the more demanding  $20^\circ$  case are shown in Figure 5.15. Also these simulated  $u/u_m$  and  $u'/u_m$  profiles are close to the experimental profiles. The simulated recirculation length is  $6.9H$  for the  $90^\circ$  case and  $4.7H$  for the  $20^\circ$  case. The experiment reports values of  $8.6H$  and  $5.85H$  for  $90^\circ$  and  $20^\circ$  case respectively. Both simulated recirculation lengths are 20% too short and the staircase manner with only 21 steps covering the  $20^\circ$  slope does not harm the results



too much. A moderate resolution of only 21 cells of the step height  $H$  is sufficient to get reasonably accurate velocity and turbulent fluctuation profiles.

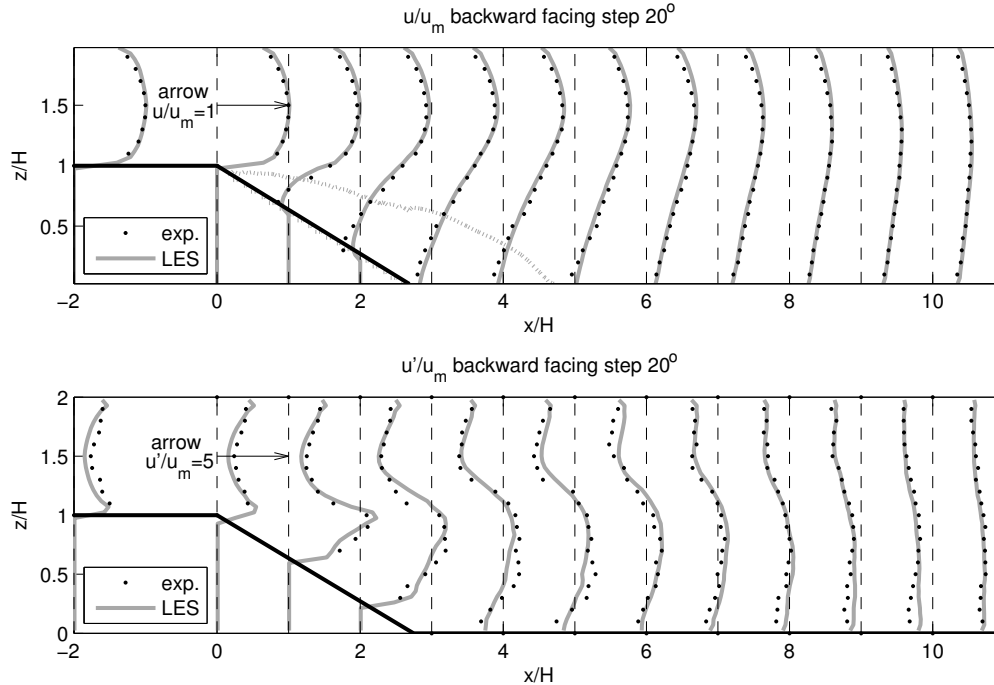


**Figure 5.15:** Time averaged results backward facing step  $20^\circ$ . The edge of the recirculation zone is indicated with a grey dotted line.

### 5.4.3 Propeller flow

The implementation of the TSHD propellers in the CFD model is tested with relations from literature and with experimentally measured propeller flow velocities. The typical resolution used in the simulations is  $\Delta x \approx D_{pr}/10$ . Propeller flow bears similarity to jet flow: high velocity flow mixes with the surroundings. Major differences are the rotational component of propeller flow caused by the propeller blades and the zero velocity behind the propeller boss. These differences lead to a smaller potential core in the order of 1-3 diameters in stead of 6.2 diameters for a round jet. The centre line velocity behind a propeller can be written as:

$$\frac{u_{pr,centre\ line}}{u_{pr0}} = a_{pr} \left( \frac{x}{D_{pr}} \right)^{-b_{pr}} \quad \text{for } x/D_{pr} > a_{pr}, \quad (5.4)$$

Lam et al. (2011) shows an overview of different velocity decay functions found in literature; values found for  $a_{pr}$  globally range between 1-2.8 and values for  $b_{pr}$  between 0.6-1. Fuehrer et al. (1987) presents values of  $a_{pr} = 2.6$  and  $b_{pr} = 1$  for propeller flow undisturbed by channel boundaries and  $a_{pr}$  ranges between 0.5-1.88 with  $b_{pr} = 0.6$  for propeller flow limited by bottom and water level. Blaauw and Kaa (1978) presents values of  $a_{pr} = 2.8$  and  $b_{pr} = 1$ . These last values are



used in this study because this velocity decay is close to the measured velocity decay from propeller experiments of a scaled TSHD conducted for this study, see Chapter 7.

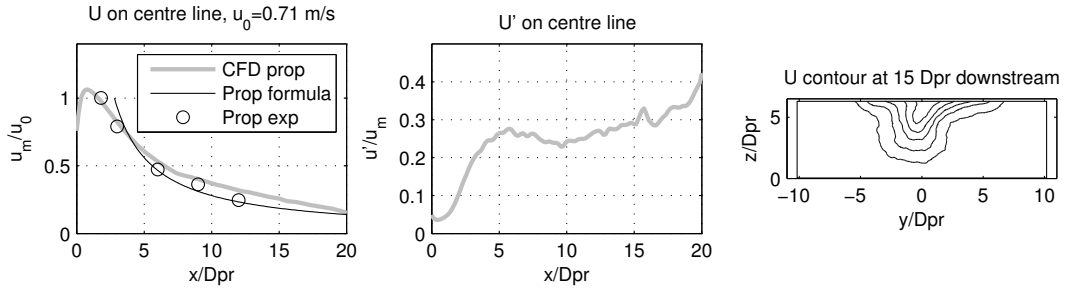


**Figure 5.16:** Time averaged results of an experimental scale propeller under a ship hull. Prop formula shows Equation 5.4 with  $a_{pr} = 2.8$  and  $b_{pr} = 1$ .

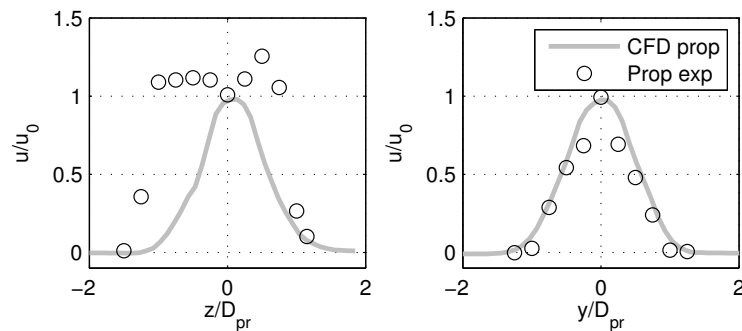


**Figure 5.17:** Time averaged  $u$ -velocity profiles at  $x = 1.8D_{pr}$  of an experimental scale propeller under a ship hull with  $u_0 = 0.71$  m/s.

Results for the propeller used in the dredge plume experiments at Deltares of  $P_{pr}=2.8W$ ,  $D_{pr} = 0.1\text{m}$  with jet tube (simulated as  $0.14\text{m}$  propeller without jet tube) are shown in Figure 5.16. The thrust applied in the LES model is calibrated to arrive at the correct propeller outflow velocity at  $x = 1.8D_{pr}$  and is kept constant. The simulated velocity decay at the centre line is close to the relation of [Blaauw and Kaa \(1978\)](#) and close to the measured velocity decay in the experiment. Figure 5.17 shows the measured and simulated  $u$ -velocity at a vertical and horizontal profile at  $1.8D_{pr}$  from the propeller. Please note that this location is still within the potential core region of the propeller jet and the self similar region is not yet reached. The vertical block profile in the experiment probably originates from the duct and the short rudder which is in place in the experimental duct. A rudder causes vertical splitting of the propeller flow and this improves mixing in vertical direction ([Prosser 1986](#); [Rhee and Kim 2008](#)). In the simulation there is no rudder and the vertical block profile is missing. The total propeller momentum in the experiment is larger than in the simulation. Hence, the propeller thrust used in the simulations without rudder results in the correct propeller centre-line velocity at  $x = 1.8D_{pr}$  and in the correct centre line velocity decay, but for

a correct total propeller momentum a larger thrust should have been applied in the simulations. Given that the centreline velocity decay is simulated accurately, the simulations are considered to be representative for the effect of a propeller without rudder on the dredging plume.

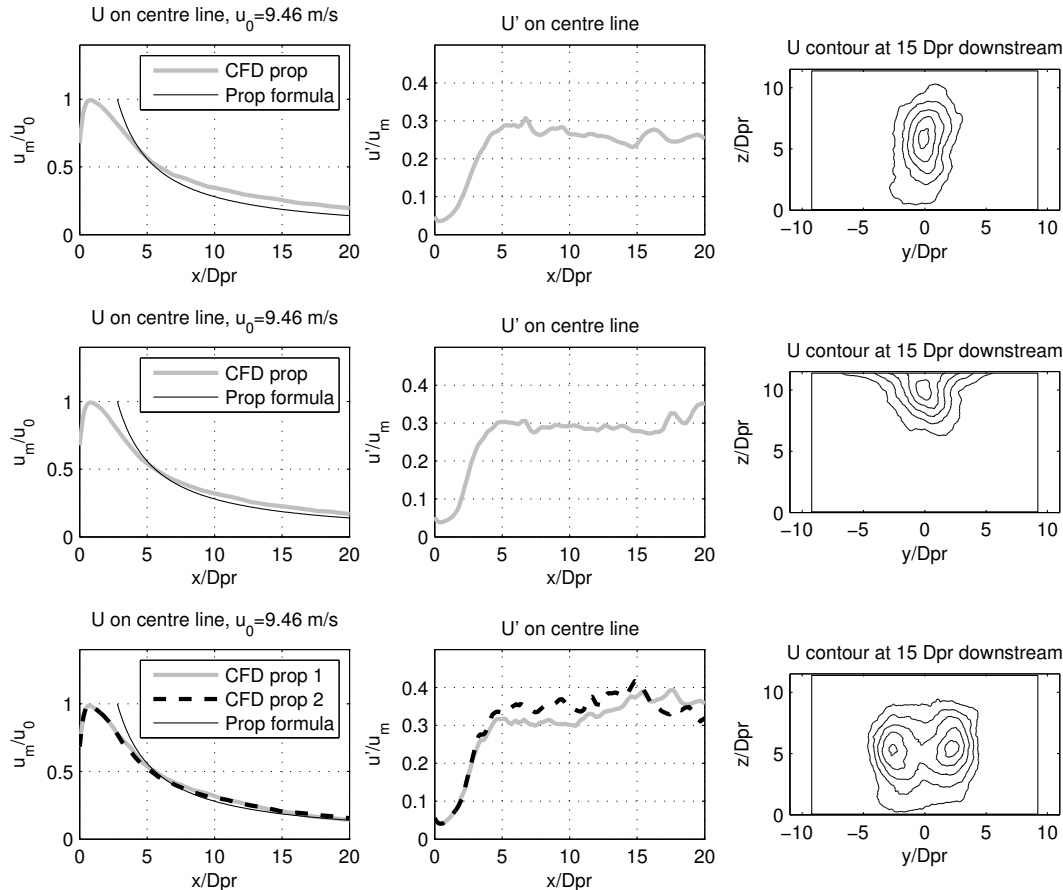


**Figure 5.18:** Time averaged results of a full scale propeller flow. One propeller at half depth (top), one propeller near the free surface (middle) and two propellers at half depth (bottom). Prop formula shows Equation 5.4 with  $a_{pr} = 2.8$  and  $b_{pr} = 1$ .

Figure 5.18 shows the simulated results for full scale propellers of  $P_{pr} = 7000$  kW per propeller,  $D_{pr} = 3.5$ m with jet tube (simulated as 5m propeller without jet tube). The simulated result for a single propeller placed halfway the water column in Figure 5.18 (top) is close to the velocity decay indicated by the relation of [Blaauw and Kaa \(1978\)](#). The simulated potential core is approximately  $1.5 D_{pr}$  long which is in the range for  $a_{pr}$  found in the literature. The simulated centre line velocity fluctuations  $u'/u_m$  are in the order of 0.25. For a propeller placed near the surface in Figure 5.18 (middle) the propeller jet tends to move towards the surface because the entrainment is blocked; this is called the Coanda effect. The centre line propeller velocity does not change much by this small deflection of the propeller jet, although the core of the propeller jet moves away from the centre line slowly. Figure 5.18 (bottom) shows the result for two propellers placed 20 m

( $5.7 D_{pr}$ ) from each other. Downstream of the two propellers the two propeller jets merge into one. In this case the merging is not yet finished at  $15 D_{pr}$ . The velocity decay of each individual propeller is almost identical to the decay of a single propeller.

Concluding, this section has shown that the CFD model produces realistic propeller flow behaviour for real scale and experimental scale situations. The centre line velocity agrees with the experimental measured velocity and the relation of [Blaauw and Kaa \(1978\)](#). When a propeller is near the free surface the propeller jet moves towards the free surface by the Coanda effect, when two propeller jets are close to each other they merge. The body force approach to implement propellers instead of implementing the propeller blades is sufficiently accurate to find the influence of propellers on the mixing behaviour of buoyant sediment dredging plumes.

## 5.5 Air-water mixture

### 5.5.1 Air-water jet in crossflow

In the CFD model air bubbles are treated as a continuous phase with an upward slip velocity (like sand particles, but then settling in upward direction). This manner of treating air bubbles is tested with a fresh water-air jet in a fresh water crossflow experiment of [Zhang and Zhu \(2013\)](#). Two cases with different volume ratios air water are used, first case has an air water ratio of 1:3 and second case has an air water ratio of 1:5. For both cases the air bubbles separate from the main water jet after certain distance. First case has  $\gamma = 17.7$ ,  $Re = 21240$ ,  $w_{j0} = 2.36$  m/s and the second case has  $\gamma = 11.8$ ,  $Re = 14160$ ,  $w_{j0} = 3.54$  m/s. In the experiment  $u_{cf} = 0.2$  m/s, the flume is 0.65 m deep with the jet nozzle of diameter  $D = 6$  mm pointing  $90^\circ$  upward at 0.12 m vertical distance from the bed and at 14 m from the start of the flume. The photographs in [Figure 5.19](#) show the experimental paths of the air-water jet in crossflow. First the air and water phase stay together, but after a certain distance the air bubbles separate from the water jet and follow a straight path towards the free surface. The angle of this straight path is determined by the local crossflow velocity and the air bubble transport velocity (sum of the vertical local carrier fluid velocity and the air bubble rise velocity). The air bubble transport velocity determined from the angle of the air path in the photographs of the experiment is 0.27 m/s. [Zhang and Zhu \(2013\)](#) themselves however, have determined are bubble rise velocities of these two cases in the order of 0.31-0.33 m/s with a vertical carrier fluid velocity of about 0.01 m/s; this leads to an air bubble transport velocity of 0.3-0.32 m/s. This air bubble transport velocity is not consistent with the angle of the air path in the photographs of the experiment. As the CFD results are compared with the photographs of the experiment, an air bubble rise velocity of 0.26 m/s is used in the simulation (0.27 m/s air bubble transport velocity minus 0.01 m/s vertical carrier fluid velocity). The reported measured air bubble diameter is 0.5-2 mm ( $0.08 - 0.3D$ ) for both cases between  $20D$  and  $100D$  from the nozzle.

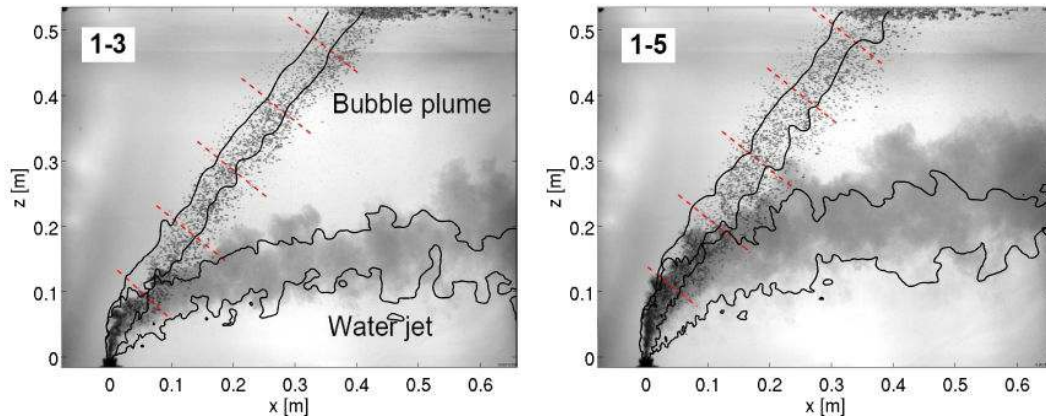


**Figure 5.19:** Experimental and LES simulation result of two cases of an air-water jet in crossflow. First case (left) has  $\gamma = 17.7$ ,  $Re = 21240$  and second case (right) has  $\gamma = 11.8$ ,  $Re = 14160$ . The photo shows the side view of the experimental jet, the black contour is the simulated  $0.01C_{max}$  contour on the centre plane at  $y = 0$ . These two things are not identical, but from both the main water-jet and air paths can be recognised.

Air bubble diameters close to the nozzle are not reported to avoid the complex bubble coalescence and breakup in this zone. The air bubble diameters between  $20D$  and  $100D$  from the nozzle are quite large compared to the nozzle diameter. The photographs in Figure 5.19 give the impression that the air bubbles close to the nozzle are finer than between  $20D$  and  $100D$  from the nozzle.

In the simulations a grid resolution of  $\Delta x = \Delta y = 0.1D$  at outflow and  $\Delta z = 0.5D$  throughout the full domain is used. The air-water jet is perturbed with azimuthal forcing ( $A = 0.5$  and  $St = 0.4$ ) to trigger the transition to turbulence. The crossflow velocity is prescribed by a logarithmic vertical distribution without turbulent fluctuations. The bottom wall of the flume is simulated as hydraulic smooth. The simulated water jet path and air bubble path for both cases are shown by the centre plane contours indicated with black lines in Figure 5.19. The two different paths of the air and water part are simulated accurately for both cases. A difference between simulation and experiment can be found in the zone close to the nozzle. In the experiment, the air plume and water jet overlap fully up to  $0.1$  m from the nozzle. In the simulation, the air plume does not overlap the water jet fully, but the air plume follows the upstream end of the water jet. This difference can be attributed to the constant air bubble diameter and rise velocity in the simulation which probably is not the case in the experiment because of the complex bubble coalescence and breakup close to the nozzle. This difference between simulation and experiment up to  $0.1$  m from the nozzle also explains the simulated water jet path being slightly too low at  $x = 0.6$  m, because in the experiment the air plume inside the water jet up to  $0.1$  m from the nozzle lifts the water jet up. Let aside this small explainable difference between simulation and experimental result, the moment of separation between the air and water part of the air-water JICF is captured well in the simulation.

# Chapter 6

## Buoyant JICF - lab scale

*The topic of this chapter is general continuous buoyant JICF flow close to the overflow, without influence of the TSHD aft or TSHD propellers. CFD results are compared with experimental results and semi-empirical solutions to verify the correct behaviour. Furthermore, some interesting observations about a buoyant JICF are made.*<sup>1</sup>

### 6.1 Introduction

CFD simulations are compared with buoyant JICF experiments for four cases with  $\gamma = 0.68 - 1.28$  and  $Ri = 0.31 - 1.83$ , see Table 6.1. The transition from initial vertical momentum or buoyancy dominated flow towards the bent over plume phase with the characteristic  $z_j \sim x_j^{2/3}$  trajectory is expected rather close to the overflow; after  $z_C$  or  $z_B = 0.79 - 2.4D$  vertical distance. In this chapter only results up to  $x/D = 30$  are used with no influence of the TSHD aft or TSHD propellers. Hence, this chapter focusses on general buoyant JICF mixing without secondary influences.

*Table 6.1: Characteristics of the buoyant JICF cases.*

run	$Ri$	$\gamma$	$\rho_{j0}$ [kg/m <sup>3</sup> ]	$w_{j0}$ [m/s]	$u_{cf}$ [m/s]	$z_M$	$z_B$	$z_C$
1	0.31	1.27	1016	0.1346	0.107	1.1D	0.49D	1.5D
2	1.08	1.28	1054	0.133	0.107	1.1D	1.6D	–
3	1.83	1.24	1089	0.133	0.11	1.1D	2.4D	–
4	1.08	0.68	1054	0.133	0.20	0.59D	0.25D	0.79D

### 6.2 Experimental set up

The buoyant JICF experiments are conducted at the large dredging flume of Deltares as part of a MSc graduation project (Liu 2013). The dredging plume

---

<sup>1</sup>A modified version of this chapter has been published as: L. de Wit, G. Keetels and C. van Rhee (2014), Turbulent interaction of a buoyant jet with crossflow, *Journal of Hydraulic Engineering*. DOI:[10.1061/\(ASCE\)HY.1943-7900.0000935](https://doi.org/10.1061/(ASCE)HY.1943-7900.0000935)

is created by injecting a saline water solution from the keel of a moving TSHD in stagnant water of  $\rho_{cf} = 1000\text{kg/m}^3$ , see Figure 6.1. The set up is scaled according to densimetric Froude, thus keeping the buoyant JICF  $Ri$  and velocity ratio  $\gamma$  constant. The length is scaled down with a factor 50, the velocity (initial jet velocity, crossflow velocity and propeller velocity) with a factor  $2\sqrt{(50)}$  and the density difference with a factor 4. The initial overflow plume is also in the experiment turbulent with  $Re = \frac{w_j D}{\nu} = 4800$ . The initial plume diameter (overflow diameter) is  $D = 36$  mm. The experimental TSHD is a scaled version of a jumbo TSHD with a typical capacity of  $16000\text{ m}^3$  of  $83.3D$  long,  $15.6D$  wide and a draught of  $6.7D$ . The shape of the experimental TSHD is schematised with a rounded bow and a sloping aft, see Figure 6.1. The width of the flume is  $66D$  which is sufficient to prevent influence from the side wall on the buoyant plume. The depth of the flume is  $40D$  under the keel which is sufficient to have hardly any influence on the buoyant plume up to  $x = 100D$  downstream. The salt water mixture is lead by a 10 mm hose into a 36 mm wide vertical pipe, a sponge is put inside the pipe near the outflow to diverge the discharge over the full pipe diameter. Without sponge, a small zone of inflow will develop at the upstream edge of the outflow pipe opening, now with sponge it can be expected that this is prevented. The sponge also prevents the existence of fully developed turbulent flow profiles at the outflow.

Measurements of the buoyant JICF are taken at a fixed cross section in the flume. In this set up, time averaging is impossible, but each run is repeated three times to get averaged plume profiles. The plume concentration in the cross section is determined by a raster of 32 vertical and 30 horizontal tensioned steel wires. A electrical current is sent through each horizontal wire and then the voltage found in each (non connected) vertical wire is a measure of the conductivity of the water at each intersection; this is repeated for all 32 vertical wires to obtain a full conductivity cross section in 1 second. The voltage from the raster scales linearly with the conductivity of the water, which is verified by measuring the conductivity at one location of the raster with a calibrated conductivity sensor (Deltares type VAZO). In such way an image of the plume concentration is obtained with a horizontal resolution of  $1.7D$  and a vertical resolution of  $0.8D$ . The measuring raster extends from  $z = 5.28D$  to  $z = 30.7D$  and from  $y = -24.44D$  to  $y = 25D$ . In order to accurately convert the conductivity to densities, each of the 960 intersection points would have to be calibrated sepa-

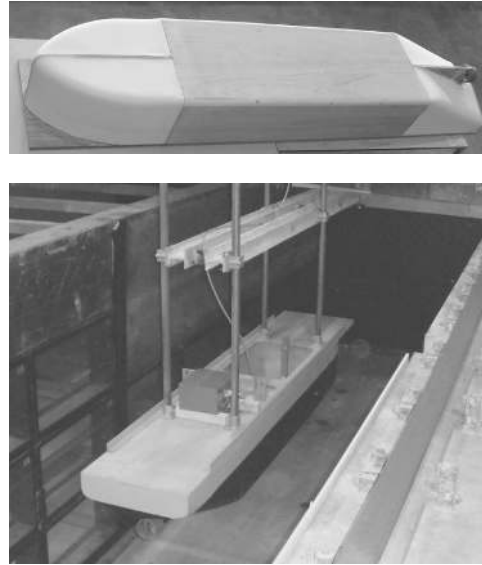


**Figure 6.1:** Images of the experimental set up of a buoyant JICF generated from a moving schematised TSHD hull (top) in a large still water flume (bottom).



*Table 6.2: Grid buoyant JICF simulations.*

run	$r_{CFD}$	$\Delta\phi$	$z_{CFD}$
1	55.6D..133.6D	0.095°	-6.7D..22.2D
2	27.8D..105.8D	0.176°	-6.7D..38.9D
3	27.8D..105.8D	0.176°	-6.7D..40D
4	55.6D..133.6D	0.095°	-6.7D..19.4D

rately, but this was not possible. However, clear plume contours appear when the measurements are scaled with the measured maximum local conductivity. This suffices for comparison with LES results. Buoyant JICF cross sections are symmetric in the  $y = 0$  axis. This symmetry is used to improve the quality of the measured concentration profiles by showing the average of the left and the right part of the cross section. In this way the number of samples used to get average profiles effectively doubles to six. Two examples of measured jet concentration cross profiles are shown in Figure 6.2. Although there is some influence of the limited number of averaging samples in the experiment, the typical kidney shape with two off-centre maxima is obvious. The vertical position, height, width and shape of the buoyant JICF are used to find the effect of different  $Ri$ ,  $\gamma$  on buoyant JICF mixing and to validate the CFD simulations.

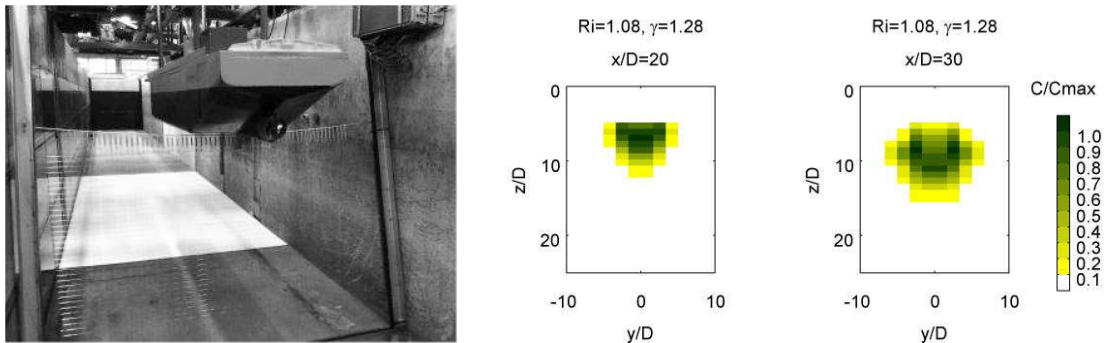


*Figure 6.2: Picture of the steel wire measurement raster under the keel of the TSHD (left) and two examples of the measured buoyant JICF cross sections.*

## 6.3 Simulation set up

The expanding flow at the sloping part of the stern of the moving vessel lifts the buoyant JICF. In this chapter, only results up to  $x/D = 30$  are considered, and up to this point the impact of the sloping back of the vessel is negligible. Simulations are carried out on a pie-shaped grid with 20-30 million grid cells (see Figure 6.3) that extends from  $x = -4D..74D$  and  $y = r\Delta\phi = -8.75D..8.75D$  at the jet outflow location. The vertical and lateral grid dimensions are dependent on the run parameters (see Table 6.2). The grid size is equidistant in  $\phi, z$  direction and



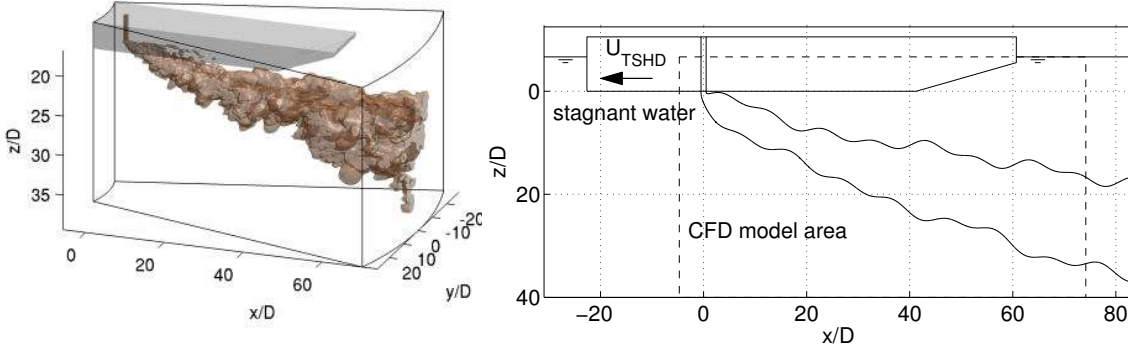


**Figure 6.3:** Pie-shaped cylindrical grid used for LES of buoyant JICF flow with TSHD hull (grid for run 2 is shown). In this chapter only results up to  $x/D = 30$  are discussed with no influence of the backward sloping part of the vessel.

variable in  $r$  direction. The grid size in  $r$  direction is  $\Delta r = 0.2D$  at  $x/D = -4$ ,  $\Delta r = 0.1D$  at the jet origin and increases in three steps to  $\Delta r = 0.15D, \Delta r = 0.2D$ , to finally  $\Delta r = 0.3D$  at  $x/D = 74$ . The grid size at the jet outflow location is  $\Delta r = r\Delta\phi = \Delta z = 0.1D$  ( $\Delta r^+ = r\Delta\phi^+ = \Delta z^+ = 31$  in inlet pipe wall units). This resolution of only 10 grid cells over the diameter of the jet is not sufficient to capture all small turbulent scales; only the largest scales are captured at outflow. Further downstream a JICF expands quickly and more and more scales are captured on the grid. Already at  $x/D = 5$  more than 30 grid cells are available to cover the diameter of the then bent over jet; at  $x/D = 30$  more than 80 cells cover the diameter of the jet. An unstructured CFD code could have been used to increase the resolution at the jet outflow region. This has not been done because unstructured codes are generally slower than structured ones and simulations with 30-80 grid cells over the diameter of the bent over jet would have been impossible given the large domain of interest and limited computational resources. In order to determine whether enough turbulent scales are covered on the LES grid, the percentage of resolved turbulent energy on the grid is determined by:

$$PERC^{res} = \frac{k^{res}}{k^{res} + k^{sgs}} \quad (6.1)$$

with the resolved kinetic energy  $k^{res} = \frac{1}{2}\overline{u'_i u'_i}$  and following Wegner et al. (2004) the kinetic sub-grid energy is estimated by  $k^{sgs} = \frac{v_{sgs}^2}{(0.086\Delta)^2}$  with grid size  $\Delta$ . The percentage of resolved turbulent energy exceeds 90% in most parts of the jet except in a very small zone near the outflow, where it drops to 40-80%. The percentage of resolved turbulent energy in most parts of the jet is greater than 80%, which qualifies it as LES (Pope 2000). A grid resolution check (described at the end of this chapter) with a 1.5 times finer grid shows that the results are independent of the chosen grid resolution.

The simulation domain starts at  $x = -4D$  and the vessel from the experiment as shown in Figure 6.1 is included without bow to save valuable computational time. Because of the rounded vessel front corner in the experiment no flow sep-

aration is expected and a constant  $u_{cf}$ , equal to the pulling velocity in the experiment, is applied as inflow boundary condition in the simulations. For the comparison between experimental results and simulation results, it introduces a small deviation. All results presented in this chapter are limited to  $x/D = 30$  in order to prevent the upward expanding flow at the sloping back of the vessel having an influence. This is verified with an extra simulation without vessel for the run with jet path closest to the keel: run 4 with  $Ri = 1.08, \gamma = 0.68$ . The wall next to the buoyant jet outflow (the keel of the vessel) is modelled as a partial slip boundary with the shear stress following from a standard hydraulic smooth logarithmic wall function (near wall resolution is  $\Delta z = 0.1D, \Delta z^+ \approx 20$  in cross flow wall units). A sufficiently long spin up time span of  $140D/u_{cf}$  and average time span of  $410D/u_{cf}$  are used to produce smoothly averaged profiles. In order to reproduce the experimental inflow conditions with a sponge near the outflow of the vertical pipe in the simulations as closely as possible, the vertical jet inflow velocity boundary condition is applied at the keel of the vessel. This means that a redistribution of the flux in the inlet pipe with more flux at the downstream part and less flux at the upstream part is not possible in the simulation. A 1/7 power law profile over the radius of the inlet pipe is applied to the jet inflow boundary condition. No perturbations to mimic turbulence are added; tests have shown that perturbations are not necessary to get accurate buoyant JICF results.

## 6.4 Buoyant JICF results

### 6.4.1 Comparison with experimental results

The comparison of simulated with measured jet concentrations at two cross sections  $x/D = 20$  and  $x/D = 30$  in Figure 6.4 shows that the vertical position, height, width and shape of the buoyant JICF are realistically simulated for all four runs. Measured and simulated profiles are close to each other; the remaining differences can be at least partly explained by the imperfectly averaged experimental contours and the vertically constant  $u_{cf}$  in the simulations and a vertically slightly varying  $u_{cf}$  under the keel in the experiment. The shown measured profiles at  $x/D = 20$  for case  $Ri = 1.08, \gamma = 0.68$  are distorted. They show the  $C/C_{max}$  contours, but in this cross section the local measured  $C_{max}$  is very low because the majority of the jet lies above the top edge of the measurement grid. The shape of all four runs clearly shows the influence of the counter rotating vortex pair. Path, height, width and therefore also dilution are different for all four runs. They are dependent on the  $Ri, \gamma$  of the buoyant JICF. Because the experimentally observed differences in the vertical position, height, width and shape of the four cases are reproduced adequately in the simulations, they can be used to investigate the influence of  $Ri, \gamma$  on the buoyant JICF behaviour.

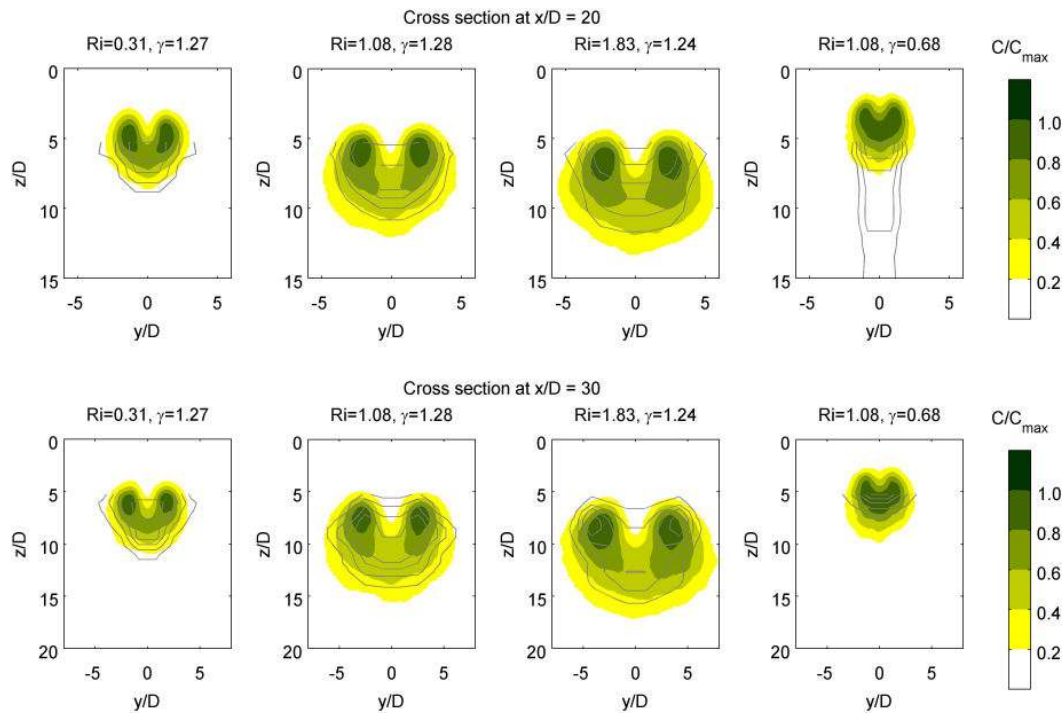


**Figure 6.4:** Comparison CFD with experimental jet concentration at cross sections  $x/D = 20$  and  $x/D = 30$  of buoyant JICF. The contours show the experimental results and the colours show the CFD results. To facilitate comparison between experiment and CFD results, both experiment and CFD results are made non dimensional with their own measured or simulated maximum jet concentration  $C_{max}$  in the cross section in hand.

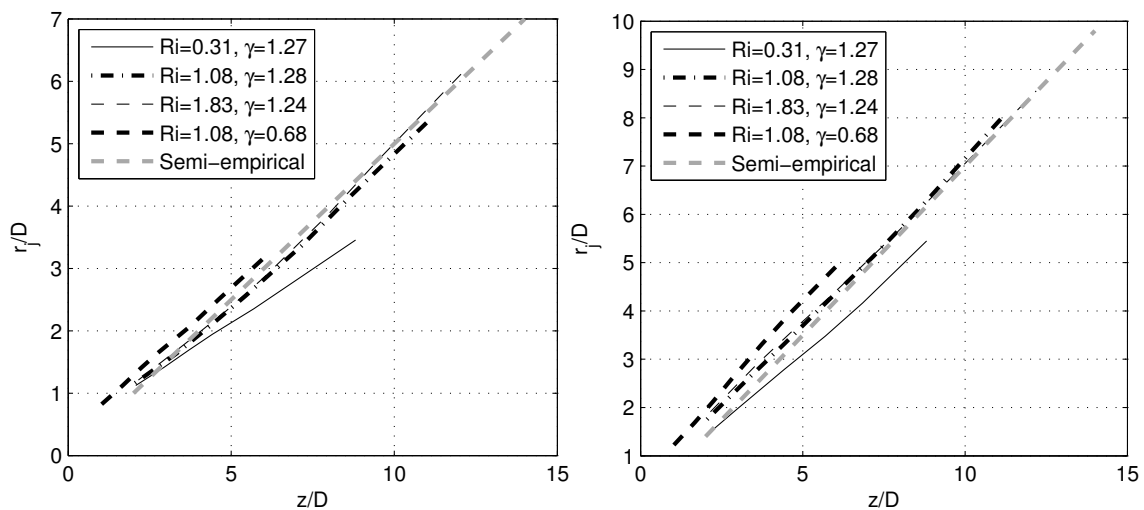


**Figure 6.5:** Simulated buoyant JICF radius based on  $0.25C_{max}$  and compared with the semi-empirical solution from Equation 2.12 with  $k_n = 1, \beta = 0.5$  (left) and based on  $0.01C_{max}, k_n = 0, \beta = 0.7$  (right).

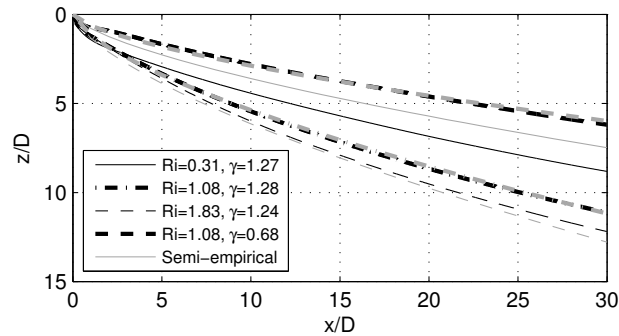


**Figure 6.6:** Simulated buoyant JICF paths compared with the semi-empirical solution from Equation 2.9 with  $k_n = 1, \beta = 0.5$  or  $k_n = 0, \beta = 0.7$ .

### 6.4.2 Comparison with semi-empirical solutions

Simulated buoyant JICF quantities are compared with the semi-empirical solutions from Equations 2.9 - 2.13. These semi-empirical solutions are valid in the bent over plume phase that for the four runs considered in this chapter is expected to take place close to the orifice at a vertical distance of maximum  $z > 2.4D$ . The simulated buoyant JICF radius is compared with  $r_j$ , which in Lee and Chu (2003) is defined with a top hat profile corresponding to  $\sqrt{RhRv}$  of the  $0.25C_{max}$  contour.  $2Rh$  is given by the horizontal distance between the two far ends of the  $0.25C_{max}$  contour and  $2Rv$  is given by the vertical distance between the two far ends of this contour. The average simulated jet quantities are based not on the  $0.25C_{max}$  contour but on the  $0.01C_{max}$  contour, because the  $0.25C_{max}$  contour labels only approximately 84% of the total jet material as inside the jet and the  $0.01C_{max}$  contour labels over 99% as inside. For the simulated JICF paths the following definition is used: the JICF path is the streamline in the centre plane starting at  $x = 0, z = 0$  (Yuan and Street 1998).

The simulated buoyant JICF radius is compared with the semi-empirical solution of Equation 2.12 in Figure 6.5. This figure shows that the assumption of a constant spreading rate  $\beta$  with a linear relation between  $z_j$  and  $r_j$  is realistic. Figure 6.5 (left) shows the simulated radius  $r_j = \sqrt{RhRv}$  based on the  $0.25C_{max}$  contour and it is described reasonably well by  $\beta = 0.5$ . The simulated buoyant JICF paths are shown in Figure 6.6. When  $\beta = 0.5$  is chosen, the semi-empirical paths in Equation 2.9 come closest to the simulated paths with  $k_n = 1$ . These values are within the range given by Lee and Chu (2003) of  $0.34 < \beta < 0.62$  with  $k_n = 1$ . The semi-empirical buoyant JICF paths of runs 2,3 and 4 are similar to the simulated paths; run 1 ( $Ri = 0.31, \gamma = 1.27$ ) deviates by  $1.3D$  vertical distance from the simulated path. Run 1 ( $Ri = 0.31, \gamma = 1.27$ ) is a run with  $z_M > z_B$  and a late transition to the bent over plume phase at  $z_C = 1.5D$  where the semi-empirical formulas are valid.

The behaviour of the simulated buoyant JICF path and vertical velocity are shown with logarithmic axes in Figure 6.7 to verify the correct asymptotic behaviour of the numerical simulations. The simulated results are also compared

with the corresponding semi-empirical solutions from Equations 2.9 - 2.13. The simulated buoyant JICF paths show a clear  $z_j \sim x_j^{2/3}$  trend and are close to the semi-empirical paths. The simulated vertical velocity of the buoyant JICF path has the same order as the semi-empirical relation from Equation 2.10 and has the correct  $w_j \sim x_j^{-1/3}$  trend.

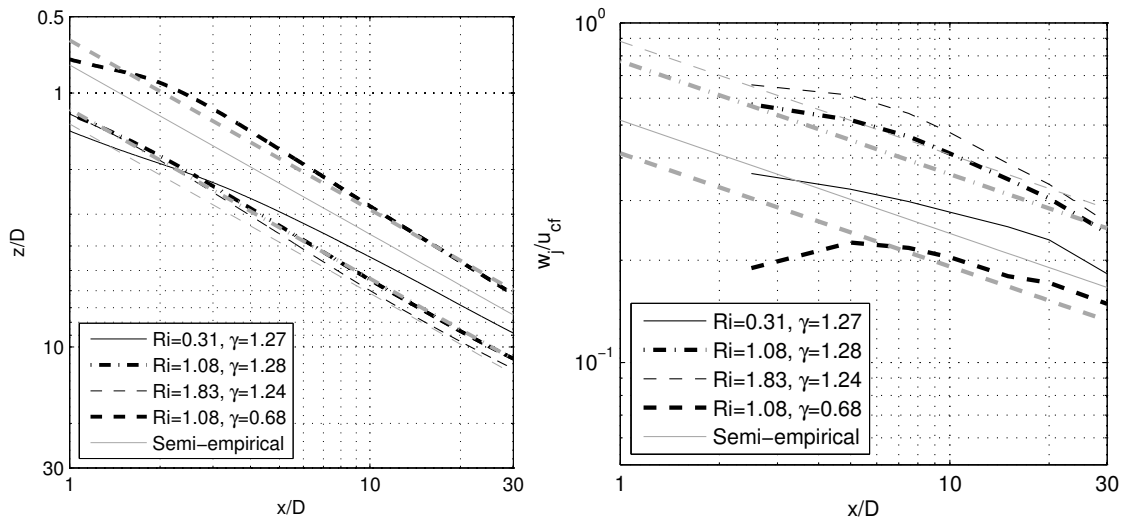


**Figure 6.7:** Simulated buoyant JICF paths (left) and simulated vertical velocity of buoyant JICF path (right). Simulated results are compared with the semi-empirical solution from Equation 2.9 (left) and Equation 2.10 (right) with  $k_n = 1, \beta = 0.5$  or  $k_n = 0, \beta = 0.7$ .

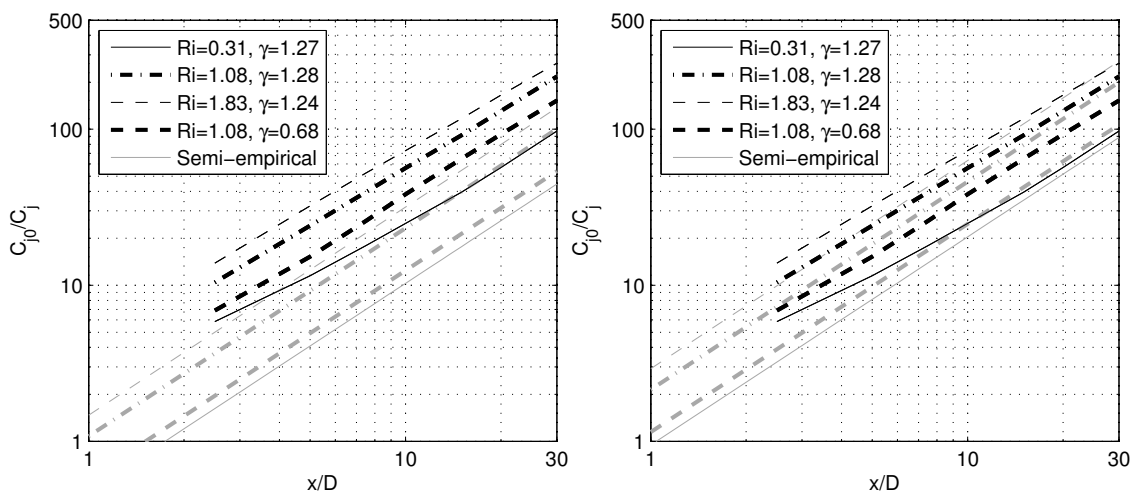


**Figure 6.8:** Simulated buoyant JICF dilution compared with the semi-empirical solution from Equation 2.13 with  $k_n = 1, \beta = 0.5$  (left) and  $k_n = 0, \beta = 0.7$  (right).

The simulated dilution in Figure 6.8 shows the expected  $C_{j0}/C_j \sim x_j^{4/3}$  slope.

But the semi-empirical solution for dilution in Figure 6.8 (left) with  $k_n = 1, \beta = 0.5$  is too low by a factor of approximately 2. This deviation between the semi-empirical dilution and the simulated dilution for buoyant JICF can be solved by choosing another definition of the contour on which  $r_j$  is based and other values for  $\beta$  and  $k_n$  that correspond to this choice. We propose to define  $r_j$  on basis of the  $0.01C_{max}$  contour instead of the  $0.25C_{max}$  contour. Then we calculate  $r_j$  by the radius of the circle with similar area as the  $0.01C_{max}$  contour:  $r_j = \sqrt{A_{0.01C_{max}}/\pi}$ . We do not use  $r_j = \sqrt{RhRv}$  as  $Rh$  based on the  $0.01C_{max}$  contour can be very wide due to some jet material near the upper boundary (see for instance Figure 6.10), leading to a  $r_j$  that is too large. When  $r_j$  is based on the  $0.01C_{max}$  contour, then the spreading of the buoyant jet is best described by  $\beta = 0.7$ , see Figure 6.5 (right). Once  $\beta = 0.7$  is chosen, the semi-empirical paths and  $w_j$  stay similar for  $k_n = 0$ . This follows directly from Equations 2.9 and 2.10 as  $(1 + k_n)\beta^2$  stays similar for either the original set  $k_n = 1$  and  $\beta = 0.5$  or for the new set  $k_n = 0$  and  $\beta = 0.7$ . Therefore Figures 6.6 and 6.7 are valid for either  $k_n = 1$  and  $\beta = 0.5$  or  $k_n = 0$  and  $\beta = 0.7$ . The semi-empirical dilution does change for this new choice in  $k_n$  and  $\beta$ . The dilution determined with  $k_n = 0$  and  $\beta = 0.7$  in Figure 6.8 (right) is very close to the simulated dilution and much more accurate than the dilution determined with  $k_n = 1$  and  $\beta = 0.5$  in Figure 6.8 (left). A buoyant JICF configuration is very effective at mixing. At  $x/D = 10$  the dilution of the four considered cases is already 20-70; at  $x/D = 30$  the dilution is between 100 and 300. The buoyant JICF run that penetrates deepest in the ambient current (run 3  $Ri = 1.83, \gamma = 1.24$ ) shows the most dilution, but the buoyant JICF that stays highest in the water column (run 4  $Ri = 1.08, \gamma = 0.68$ ) does not show the least dilution. The run with the least dilution is run 1 with  $Ri = 0.31, \gamma = 0.68$ . The semi-empirical solution for dilution in Equation 2.13 confirms this behaviour, as the dilution is dependent not only on the buoyant JICF path (through  $r_j = \beta z_j$ ), but also on the ratio  $u_{cf}/Q_{j0}$ . The second highest run has a ratio  $u_{cf}/Q_{j0}$  twice as much as the ratio of the highest run, therefore the dilution is larger.

Figures 6.5, 6.7 and 6.8 show that the simulated buoyant JICF results have the expected asymptotic behaviour  $z_j \sim x_j^{2/3}, w_j \sim x_j^{-1/3}, r_j \sim z_j, C_{j0}/C_j \sim x_j^{4/3}$  following from the semi-empirical solutions of the bent over phase. The semi-empirical solutions can predict the buoyant JICF path, radius, vertical velocity and dilution reasonably accurately, once proper values for  $\beta$  and  $k_n$  are chosen. This study found the best results using  $\beta = 0.7$  and  $k_n = 0$ . These values are slightly outside the range of values reported by Lee and Chu (2003), namely  $0.34 < \beta < 0.62$  with  $k_n = 1$ . The semi-empirical solution for the buoyant JICF paths is similarly accurate for  $\beta = 0.5$  and  $k_n = 1$ , which are inside the range of Lee and Chu (2003), but then dilution is under-predicted by a factor of two by the semi-empirical solution. The choice of  $k_n = 1$  and a lower value of  $\beta$  ( $\beta = 0.5$  in this case) corresponds to an outer edge of the buoyant JICF defined by the  $0.25C_{max}$  contour; the choice of  $k_n = 0$  and a higher value of  $\beta$  ( $\beta = 0.7$  in this case) corresponds to an outer edge of the buoyant JICF defined by the  $0.01C_{max}$  contour. Given the better results for dilution and similarly accurate results for buoyant JICF paths, the latter choice is recommended.



### 6.4.3 Concentration profiles of buoyant JICF

The simulated jet concentration contours of buoyant JICF in Figure 6.9 clearly show the effect of the double vortex, which results in a kidney-shaped profile with two off-centred maxima. The cross sections at  $x/D = 5$  show concentrations

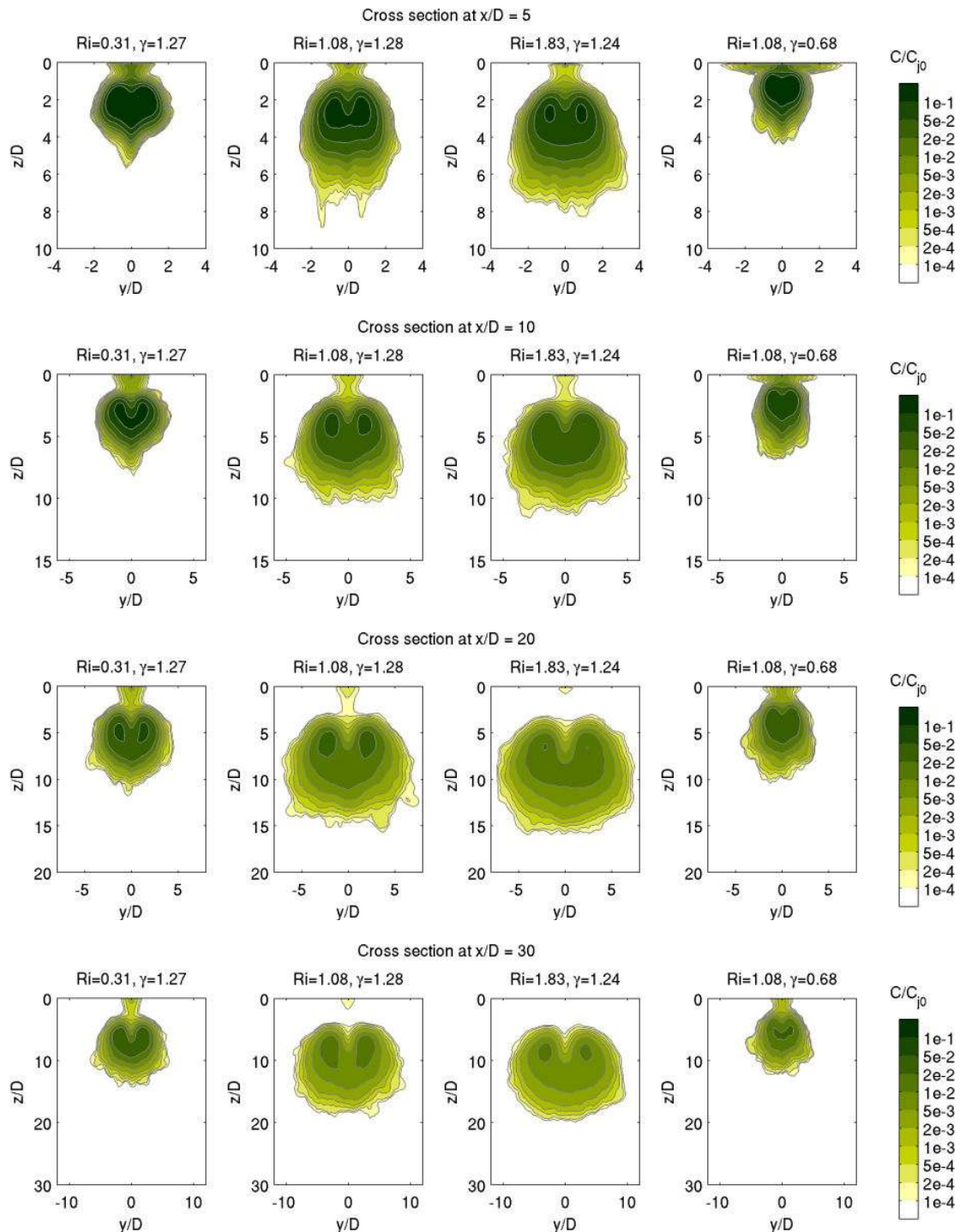
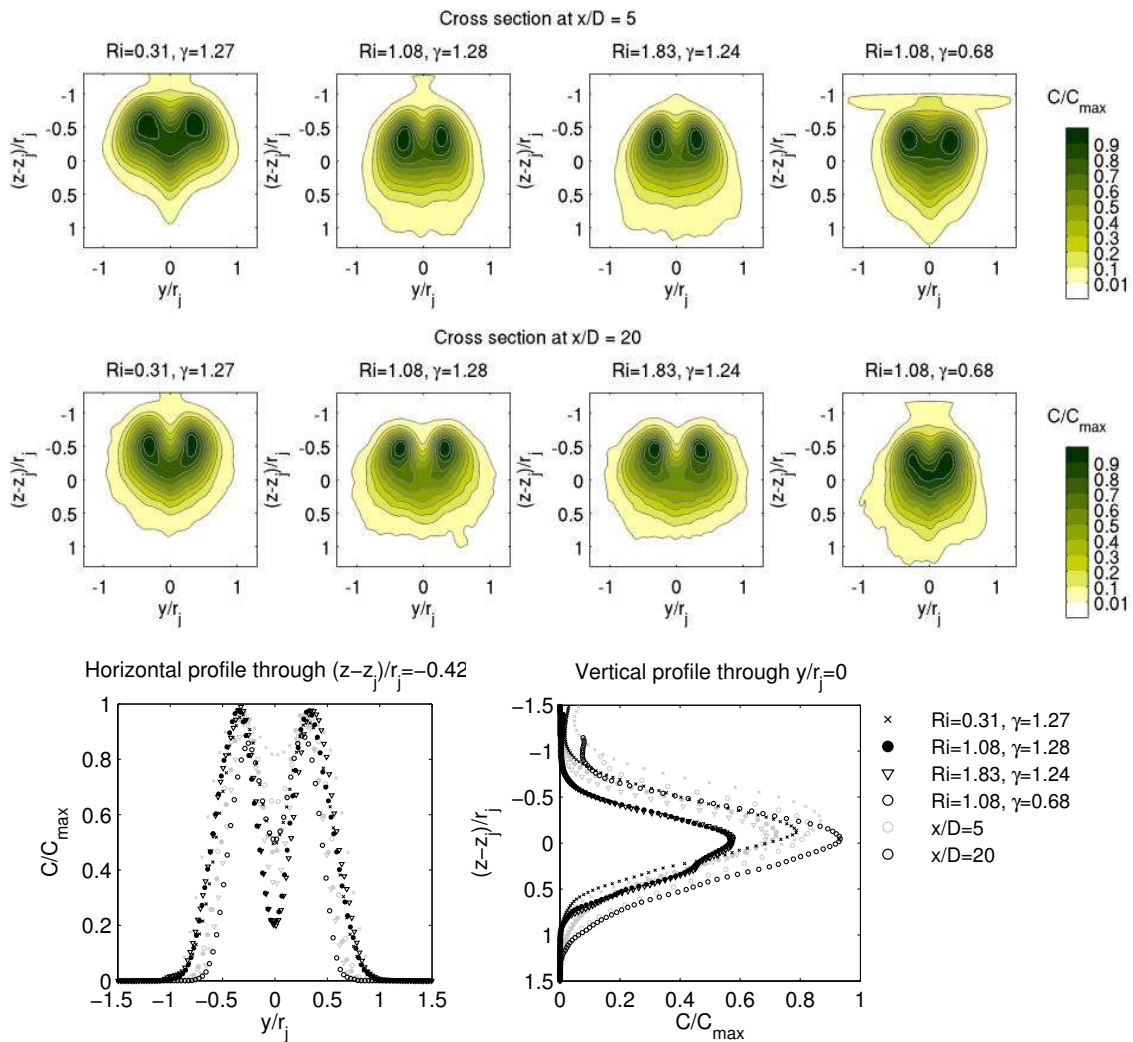


Figure 6.9: Simulated jet concentration  $C/C_{j0}$  contours.



above 10% of the source concentration  $C_{j0}$ . Cross sections further downstream are more diluted: the maximum concentration drops and the diameter of the jet increases. At  $x/D = 5$ , some jet material is trapped between the kidney-shaped jet profile and the wall next to the orifice (the vessel's keel) for all four buoyant JICF. Only for the two buoyant JICF with the highest path ( $Ri = 0.31; \gamma = 1.27$  and  $Ri = 1.08; \gamma = 0.68$ ) is the jet material near the wall visible up to  $x/D = 30$ . At  $x/D = 30$  the maximum concentration is diluted to 1-2% of the source concentration  $C_{j0}$ .



**Figure 6.10:** Simulated jet concentration  $C/C_{max}$  contours and profiles normalised with simulated jet radius  $r_j$ .  $C_{max}$  is the simulated maximum jet concentration in the cross section in hand.

Jet concentration contours and profiles normalised with  $r_j$  and  $C_{max}$  are shown in Figure 6.10.  $r_j$  is based on the  $0.01C_{max}$  contour as in Figure 6.5 (right);  $C_{max}$  is the maximum concentration in the cross section in hand. The  $0.01C_{max}$  contour is also shown in Figure 6.10. The concentration contours are approximately self-similar for all four cases with the typical kidney shape and two off-centred max-

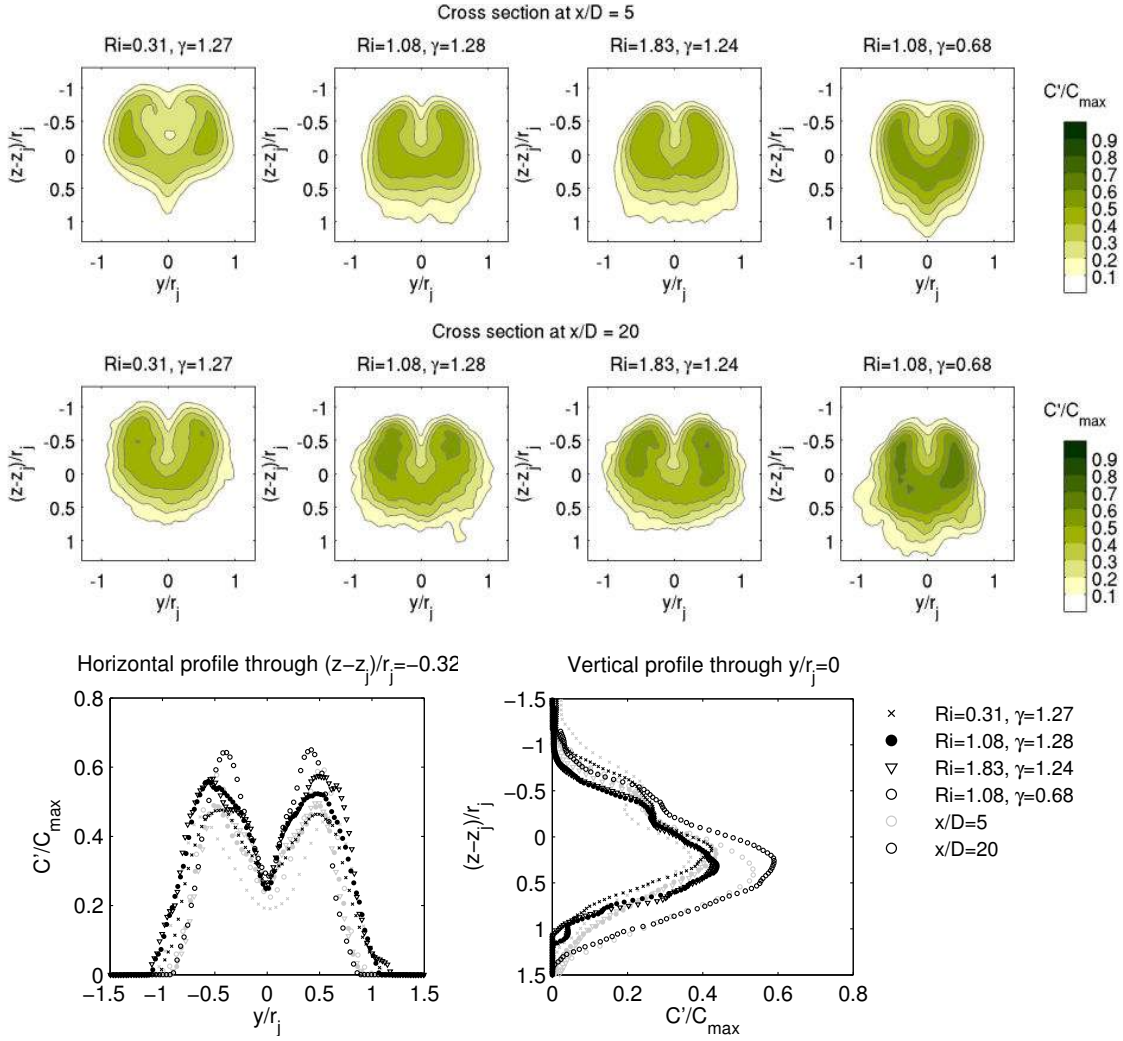


**Figure 6.11:** Simulated RMS of jet concentration  $C'/C_{max}$  contours and profiles normalised with simulated jet radius  $r_j$ .  $C_{max}$  is the simulated maximum jet concentration in the cross section in hand.

ima. The vertical profiles through  $y = 0$  are less self-similar with more deviations between the different runs and downstream distances  $x/D$  than the horizontal profiles through the average vertical location of  $C_{max}$  at  $(z - z_j)/r_j = -0.42$ .

The contours and profiles of  $C'/C_{max}$  are shown in Figure 6.11. The  $C'/C_{max}$  contours further downstream are not perfectly averaged; the averaging time should be even more than  $400D/u_c f$ , as used in this study, for perfectly smooth  $C'/C_{max}$  profiles. Nevertheless, the  $C'/C_{max}$  profiles presented in this section show that the profiles of  $C'/C_{max}$  are also approximately self-similar for the four buoyant JICF cases, with maximum values of  $C'/C_{max} = 0.45 - 0.65$ . Also for  $C'/C_{max}$ , the vertical profiles through  $y = 0$  are less self-similar with more deviations between the different runs and downstream distances  $x/D$  than the horizontal profiles through the average vertical location of the maximum  $C'/C_{max}$  at  $(z - z_j)/r_j = -0.32$ . The average vertical location  $(z - z_j)/r_j = -0.32$  of

the maximum  $C'/C_{max}$  is slightly different from the average vertical location  $(z - z_j)/r_j = -0.42$  of  $C_{max}$ . The maximum values  $C'/C_{max} = 0.45 - 0.65$  are slightly higher than the maximum values of  $C'/C_{max} = 0.4$  found for a buoyant jet in a still ambient fluid (Papanicolaou and List 1988). The increase in  $C'/C_{max}$  found for a buoyant JICF compared with a buoyant jet without crossflow is explainable by the extra turbulent vortices generated by the interaction with the crossflow, like for instance horseshoe vortices, wake vortices and the counter rotating vortex pair (Fric and Roshko 1994).

#### 6.4.4 Stream wise horizontal velocity inside buoyant JICF

The horizontal stream wise velocity contours of buoyant JICF in Figure 6.12 show an intriguing pattern: close to the origin there are zones inside the jet of jet fluid flowing both significantly faster and significantly slower in the horizontal stream wise direction than the crossflow. The zone of slower flowing fluid can be related to the fact that the buoyant jet initially contains zero velocity in stream wise direction. The buoyant jet is slowly accelerating in stream wise direction due to the velocity difference from the ambient crossflow; this phenomenon is also shown by the disappearing zone with slower fluid from  $x/D = 10$  onwards. The zone of faster flowing fluid can also be related to the fact that the buoyant jet initially contains zero velocity in the horizontal stream wise direction: the jet behaves like a vertical cylindrical-shaped obstacle, and on either side a zone with increased stream wise velocity occurs.

It is interesting that the zones of faster flowing fluid are stronger and persist further downstream than the slower flowing fluid. At  $x/D = 10$ , the minimum lower stream wise fluid velocity is  $0.9u_{cf}$ , but the maximum higher stream wise fluid velocity is  $1.3u_{cf}$ . At  $x/D = 30$ , the lower horizontal stream wise fluid velocity zone has fully disappeared, which in this case means it is more than  $0.9u_{cf}$ , but the maximum higher horizontal stream wise fluid velocity is still  $1.2u_{cf}$ . These differences in the horizontal stream wise velocity inside a buoyant JICF make clear that it is an oversimplification to say that a buoyant JICF moves with crossflow velocity in the horizontal stream wise direction in the bent over phase. It is even an oversimplification to state that *on average* a buoyant JICF moves with crossflow velocity in the horizontal stream wise direction. Figure 6.13 shows the average horizontal stream wise velocity of the jet determined in two ways, and both are larger than the crossflow velocity. What is shown in Figure 6.13 is not the jet velocity along its streamline, but the horizontal stream wise component of the jet velocity, which is higher than the crossflow velocity. A first way to determine the average horizontal stream wise velocity of the jet is the jet-concentration averaged velocity ( $\overline{uc}/\bar{c}$ ) of all grid points inside the buoyant JICF; it is shown with black lines. A second way is shown by grey lines and is determined by the horizontal stream wise velocity of the buoyant JICF path from Figure 6.6, which is approximately the centre of the jet. Both ways to determine the velocity of the buoyant JICF agree with each other and both are higher than the crossflow velocity. The difference is not very large, but with the buoyant JICF being 1-9% faster at  $x/D = 30$  the difference is not completely neg-



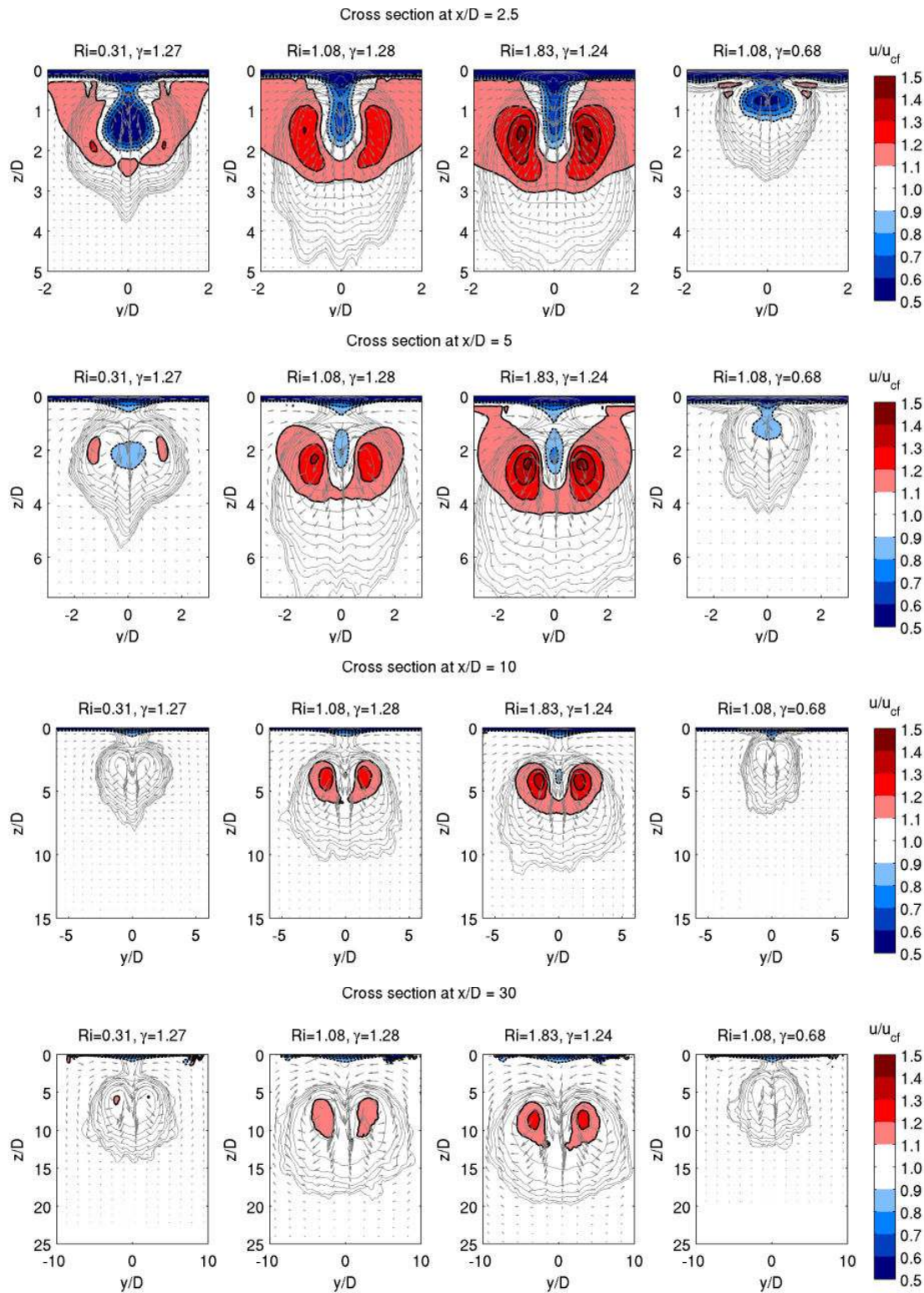


**Figure 6.12:** Horizontal stream wise velocity  $u/u_{cf}$  contours with in grey the jet concentration contours and velocity vectors  $(v/u_{cf}, w/u_{cf})$ .

ligible. Although not shown in Figure 6.13, also the average horizontal stream wise velocity of all grid points inside the buoyant JICF (not weighted with the jet concentration) is higher than crossflow: 1-4% higher at  $x/D = 30$ . The two highest buoyant JICF runs ( $Ri = 0.31, \gamma = 1.27$  and  $Ri = 1.08, \gamma = 0.68$ ) show more or less the expected behaviour, with a mean stream wise velocity of the jet that is lower than  $u_{cf}$  close to the origin and a gradual increase further downstream, but quite unexpectedly the increase continues beyond  $u_{cf}$ . The two deepest buoyant JICF runs ( $Ri = 1.08, \gamma = 1.28$  and  $Ri = 1.83, \gamma = 1.24$ ) show a completely different behaviour, with a mean stream wise velocity of the jet of 8-16% higher than  $u_{cf}$  at  $x/D = 5$  and a decrease further downstream, but still 7-9% higher than  $u_{cf}$  at  $x/D = 30$ .

Zones of faster and slower fluid in the horizontal stream wise direction are measured on the vertical slice at  $y = 0$  of a non-buoyant JICF (Andreopoulos and Rodi 1984; Crabb et al. 1981). Sykes et al. (1986) report on simulated cross slices with zones of faster and slower fluid in the horizontal stream wise direction between  $0.4u_{cf}$  and  $1.4u_{cf}$  at  $x/D = 11.5$  inside a non-buoyant JICF with  $\gamma = 8$ . Two zones of faster fluid of up to  $1.7u_{cf}$  at the lateral edges of the jet and a zone with slower fluid of  $0.1u_{cf}$  at the core of the jet is experimentally observed in a horizontal slice at  $z/D = 1.5$  through a non-buoyant JICF with  $\gamma = 4$  (Galeazzo et al. 2011). But in all those non-buoyant JICF results, there was no indication that the

zones with faster fluid are stronger or persist longer downstream than the zones with slower fluid. There was also no indication that the average stream wise velocity of the non buoyant JICF was higher than the ambient crossflow velocity. Part of this apparent difference between a non buoyant JICF and a buoyant JICF might be attributed to the different paths and different speeds of increase in jet diameter they follow. A buoyant JICF follows a  $z_j \sim x_j^{2/3}$  path with an increase in radius  $r_j \sim x_j^{2/3}$ ; a non buoyant JICF follows  $z_j \sim x_j^{1/3}$  and  $r_j \sim x_j^{1/3}$ . A wake grows with  $r_j \sim x_j^{1/2}$  and also the zones with largest horizontal stream wise direction in Figure 6.12 diverge by approximately  $x_j^{1/2}$ : this means that the widening of a wake behind an obstacle grows faster than the widening of a non

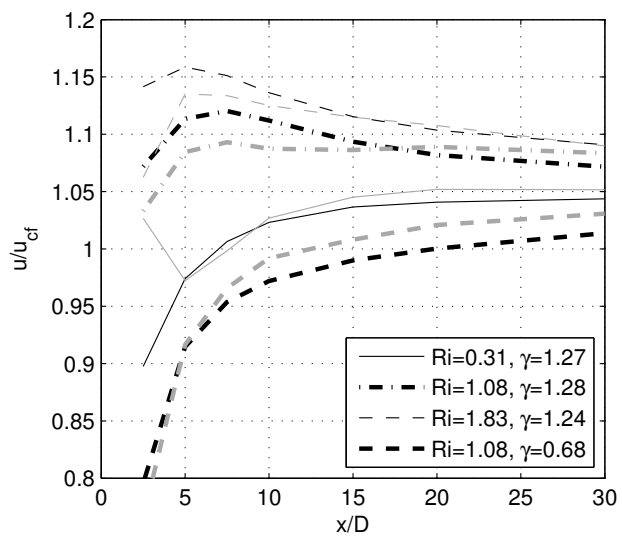


Figure 6.13: Horizontal stream wise velocity inside buoyant JICF. Black lines show the jet concentration averaged horizontal stream wise velocity ( $\overline{u\bar{c}}/\bar{c}$ ) of all grid points inside the  $0.01C_{max}$  contour of the buoyant JICF, the grey lines show the horizontal stream wise velocity of the simulated buoyant JICF path shown in Figure 6.6.

buoyant JICF, but slower than the widening of a buoyant JICF. The wake and associated zones of faster fluid get absorbed inside a buoyant JICF, but they grow out of the non buoyant JICF.

These results for the horizontal stream wise velocity inside a buoyant JICF show that the standard conceptual model of seeing a buoyant JICF as a slice of buoyant fluid that has zero horizontal stream wise velocity at the start and that is then accelerated by the crossflow up to the moment that the mean horizontal stream wise velocity inside the buoyant jet is equal to the crossflow velocity, is only approximately correct. First, the jet of a buoyant JICF moves slightly faster in the stream wise horizontal direction than its cross flow. Second, there are significant differences in horizontal stream wise velocity inside the jet of a buoyant JICF: zones with an increased horizontal stream wise velocity of  $1.2u_{cf}$  persist up to  $x/D = 30$ .

## 6.5 Accuracy of LES results

Some important numerical choices in the LES are varied in order to check that they do not determine the outcomes. In-dependency from a specific sub-grid scale model is verified by a simulation with the  $\sigma$  sub-grid scale model with  $C_s=0.5$  instead of the WALE model with  $C_s=0.325$ . In-dependency from grid resolution is verified by a 1.5 times finer grid with a total of 58 million grid cells: 15 cells cover a jet diameter at outflow at  $x/D = 0$  ( $\Delta r^+ = r\Delta\phi^+ = \Delta z^+ = 21$  in inlet pipe wall units) and 45-120 cells cover a jet diameter from  $x/D = 5$  to  $x/D = 30$ . Buoyant JICF results are strongly dependent on  $Ri, \gamma$  and as long as the flow is fully turbulent, buoyant JICF results are not dependent on  $Re$  (Jirka 2004). This is verified by a simulation with increased  $Re = 480000$  instead of  $Re = 4800$  and unchanged  $Ri, \gamma$  by increasing  $\rho_{j0}, D, g, w_{j0}$  and  $u_{cf}$  by a factor of 10.

The results of these simulations with variational input are shown in Figures 6.14-6.15. The buoyant JICF paths with different input are very close to each other, and jet concentration and RMS of jet concentration contours differ only on details. Energy spectra of the normalised stream wise velocity  $u_n = u/\bar{u}$  and the normalised jet concentration  $C_n = C/\bar{C}$  at  $x/D = 14$  inside the buoyant jet are shown in Figure 6.16. All velocity energy spectra show a  $-5/3$  slope characteristic for the inertial sub range. The jet concentration spectra show a  $-3$  slope. In the wall region the  $Re=480000$  case is not properly resolved ( $\Delta r^+ = r\Delta\phi^+ =$

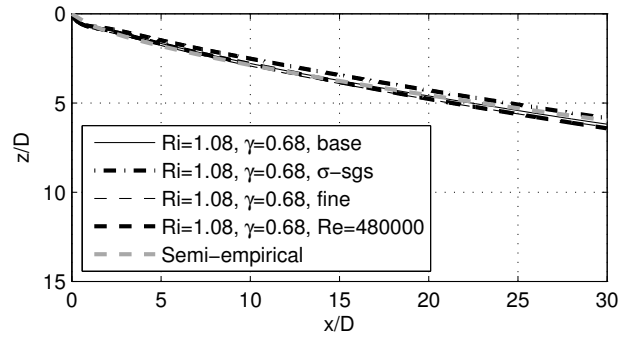


**Figure 6.14:** Buoyant JICF paths obtained with different sub-grid scale models, different grid resolutions and different  $Re$  numbers compared with semi-empirical solution from Equation 2.9 with  $k_n = 0, \beta = 0.7$ .

$\Delta z^+ = 1900$  in inlet pipe wall units) and the simulation might be less accurate, but in the jet region the  $Re = 480000$  simulation has resolved a similar part of the inertial sub range as the  $Re = 4800$  simulation with similar spectra slopes of the  $Re = 480000$  and  $Re = 4800$  cases. A slope steeper than  $-5/3$  for the concentration spectrum is associated with the inertial-diffusive sub range for buoyancy driven flows: a  $-3$  slope in the concentration spectrum and a  $-5/3$  slope in the velocity spectrum are also found in LES and experiments with buoyancy driven plumes without crossflow (Papanicolaou and List 1988; Kotsovinos 1991; Zhou et al. 2001).

This section verifies that the presented buoyant JICF results are independent of the chosen sub-grid scale model, grid resolution or  $Re$  number. The inertial sub range is covered by the chosen grid resolution, which is essential for LES, and the expected  $-5/3$  slope for the velocity spectrum and a  $-3$  slope for the buoyant jet concentration spectrum are simulated correctly.

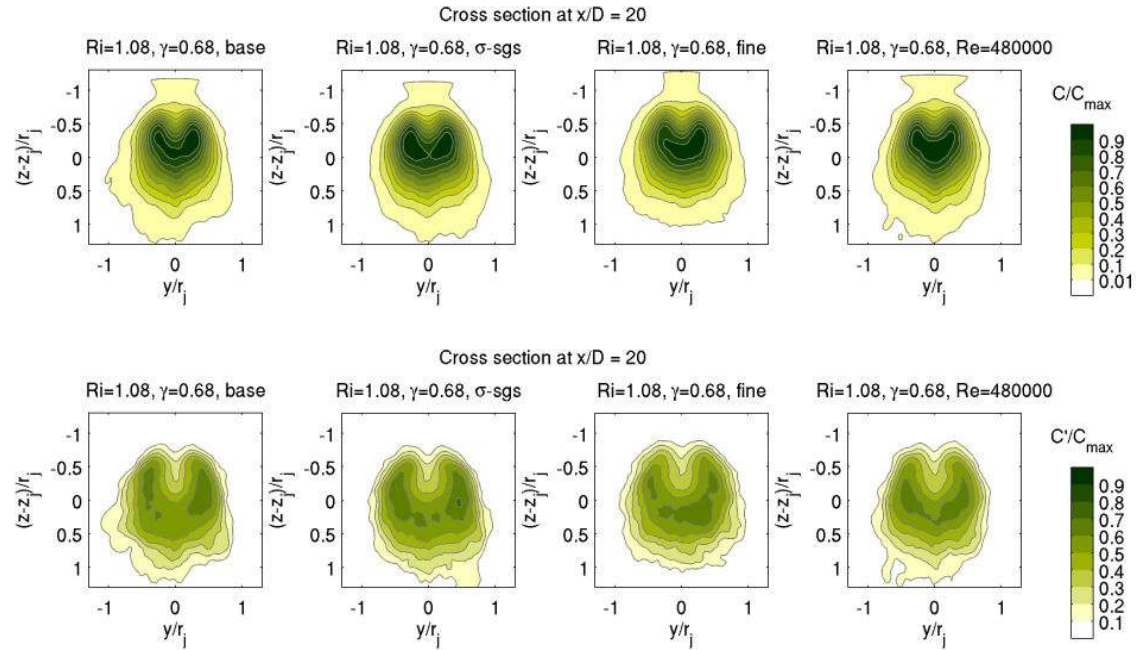


**Figure 6.15:** Self-similar jet concentration  $C/C_{max}$  contours (top) and RMS of jet concentrations  $C'/C_{max}$  contours (bottom) obtained with different sub-grid scale models, different grid resolutions and different  $Re$  numbers normalised with simulated jet radius  $r_j$ .  $C_{max}$  is the simulated maximum jet concentration in the cross section in hand.

## 6.6 Conclusions

Buoyant JICF mixing behaviour is governed by the velocity ratio  $\gamma$  and the jet Richardson number  $Ri$ . Large eddy simulations and experimental results of four buoyant JICF cases in the range  $0.68 < \gamma < 1.28$  and  $0.31 < Ri < 1.83$  are presented in this chapter. In this range, both initial momentum and initial buoyancy



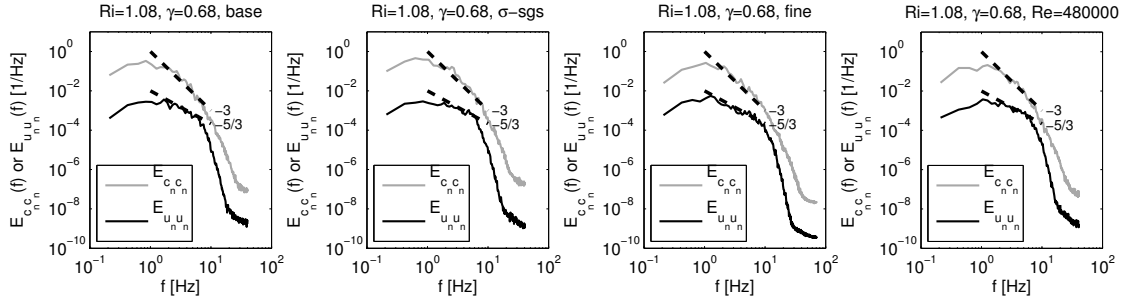


**Figure 6.16:** Energy spectra of the normalised stream wise velocity  $u_n = u/\bar{u}$  and the normalised jet concentration  $C_n = C/\bar{C}$  from time series at  $x/D = 14, y/D = 0, z/D = 4$ . The black dashed lines are only given as indication of the slope, not as a correct level of turbulent kinetic energy or length of the inertial sub range.

are important. Simulated results are found to be independent of the choice of sub-grid scale model, grid resolution or  $Re$  number, and the simulated shape, size and vertical location of the jet concentration cross sections compare well to measured ones.

Buoyant JICF path, dilution and spreading can be described reasonably well by the semi-empirical formula of [Lee and Chu \(2003\)](#) when calibration parameters  $k_n = 0$  and  $\beta = 0.7$  are used. These calibration values are different from advised values  $k_n = 1, 0.34 < \beta < 0.62$  ([Lee and Chu 2003](#)), but values inside this range ( $k_n = 1, \beta = 0.5$ ) underestimate the dilution by a factor of two. The difference in choice of  $k_n, \beta$  corresponds to a different definition of the edge of the jet. The values of [Lee and Chu \(2003\)](#) correspond to an edge at the  $0.25C_{max}$  contour, while the choice of  $k_n = 0, \beta = 0.7$  corresponds to an edge at the  $0.01C_{max}$  contour. The latter choice ( $k_n = 0, \beta = 0.7$ ) is preferred as it gives better results for dilution and equally accurate results for buoyant JICF path and spreading.

Cross contours for concentration  $C/C_{max}$  and fluctuations  $C'/C_{max}$  are approximately self-similar. The maximum value for these four buoyant JICF cases is  $C'/C_{max} = 0.45 - 0.65$ .

A close inspection of the flow fields of buoyant JICF reveals that the idea of viewing a buoyant JICF as a slice of buoyant fluid that starts with zero horizontal stream wise velocity and is then accelerated towards crossflow velocity is not entirely correct. Inside the buoyant JICF, zones with a mean horizontal stream wise velocity significantly higher and significantly lower than the crossflow are found. The faster zones persist further downstream than the slower zones. Up to  $x/D = 30$  zones that are 20% faster than the crossflow can be found inside a buoyant JICF. The origin of these zones lies in the initially vertical jet which acts as a vertical cylindrical obstacle with increased velocities on either side. These faster zones even cause the jet of a buoyant JICF to overtake the crossflow: the average stream wise horizontal velocity of the jet at  $x/D = 30$  is 1-9% higher than the crossflow velocity. This effect is found for all four buoyant JICF cases considered in this chapter, but it is strongest for the deepest buoyant JICF trajectories.

# Chapter 7

## Influence of near field processes on a dredging plume - lab scale

*A key question for the assessment of the environmental impact of an overflow dredging plume is how much ends as a surface plume and how much descends quickly towards the sea bed under influence of density and momentum. This chapter will investigate the effect of several near field processes on dredging plume mixing. Special attention is given to the generation of a surface plume and LES results will be compared with experimental results. The influences of dredging speed, propeller influence, overflow location and pulsing frequency are investigated in a systematic manner.*<sup>1</sup>

### 7.1 Introduction

In this chapter the interactions between the overflow plume and the TSHD hull / aft / propeller are investigated by LES and experimental results. The influence of pulsing on non-buoyant JICF have been studied experimentally and numerically (MCloskey et al. 2002; Narayanan et al. 2003; Muldoon and Acharya 2010), but this is the first time that the influence of pulsing on a buoyant JICF is investigated. The influence of a propeller and aft of a dredging vessel on the mixing of the dredging plume has also not been studied before.

18 simulations of near field mixing of a dredging plume under the keel of a dredging vessel are presented in this chapter with:  $Ri = 1.08$ , two different dredging speeds ( $\gamma = 1.28$  and  $\gamma = 0.68$ ), simulations with and without propeller influence, two overflow locations (front and back) and pulsing according to Equation 3.34 with three different pulsing frequencies ( $St = 0.12$ ,  $St = 0.18$ ,  $St = 0.27$ ). Table 7.1 summarises all simulations. In this chapter, the depth is chosen sufficiently large to prevent influence of the sea bed. Therefore the interaction of the dredging plume with the dredging vessel and propellers is likely

---

<sup>1</sup>A modified version of this chapter has been published as: L. de Wit, A.M. Talmon and C. van Rhee (2014), Influence of important near field processes on the source term of suspended sediments from a dredging plume caused by a Trailing Suction Hopper Dredger: the effect of dredging speed, propeller, overflow location and pulsing, *in press in Environmental Fluid Mechanics*. DOI:10.1007/s10652-014-9357-0

**Table 7.1:** LES runs buoyant dredging plume. Runs indicated with a star are compared with experimental data.

run	$Ri$	$\gamma$	overflow	prop	pulsing
1*	1.08	1.28	front	-	-
2*	1.08	1.28	back	-	-
3*	1.08	1.28	front	prop	-
4*	1.08	1.28	back	prop	-
5	1.08	1.28	front	prop	$St = 0.18$
6	1.08	1.28	back	prop	$St = 0.18$
7	1.08	1.28	front	-	$St = 0.12$
8	1.08	1.28	front	-	$St = 0.18$
9	1.08	1.28	front	-	$St = 0.27$
10*	1.08	0.68	front	-	-
11*	1.08	0.68	back	-	-
12*	1.08	0.68	front	prop	-
13*	1.08	0.68	back	prop	-
14	1.08	0.68	front	prop	$St = 0.18$
15	1.08	0.68	back	prop	$St = 0.18$
16	1.08	0.68	front	-	$St = 0.12$
17	1.08	0.68	front	-	$St = 0.18$
18	1.08	0.68	front	-	$St = 0.27$

to be underestimated. In this way low estimates of the surface plume are obtained; in (very) shallow water the surface plume could be significantly larger.

## 7.2 Experimental set up

The numerical LES simulations in this chapter are based on the experimental set up explained in Section 6.2. The simulations cover more runs and processes than the experimental runs, but the experimental subset indicated with a star in Table 7.1 is used to validate the numerical LES results. The runs in this chapter have either the overflow at  $22.6D$  from the front of the TSHD or the overflow at  $50.4D$  from the front, see Figure 7.2. In order to investigate the influence of a propeller on the saline buoyant JICF, the experimental TSHD is equipped with a propeller at the centre of the vessel. The diameter of the 4-blade propeller is 100 mm ( $D_{prop} = 2.78D$ ), and it has a duct with a short rudder. The lower end of the propeller is in line with the keel

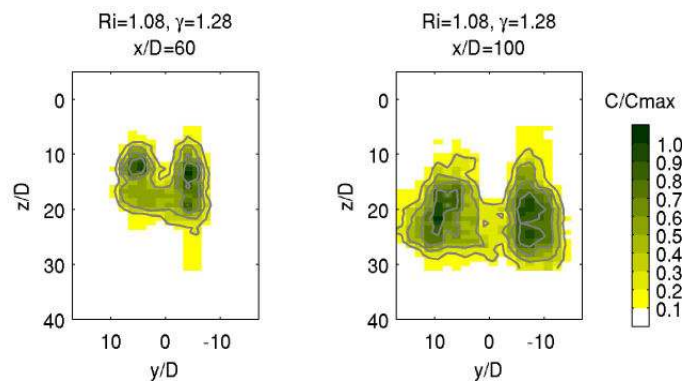


**Figure 7.1:** Two examples of the averaged experimental cross section of a dredging plume from a moving TSHD with contours at steps of  $0.2C_{max}$ .

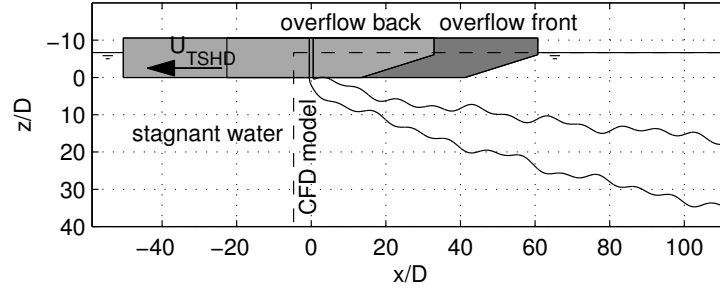


**Figure 7.2:** Schematic overview of the set up for buoyant plumes generated from a moving TSHD of  $83.3D$  long with the overflow either at the front ( $22.6D$  from front hull, TSHD shown in dark grey) or at the back ( $50.4D$  from front hull, TSHD shown in light grey).

of the TSHD and the propeller outflow is  $3.5D$  before the aft of the vessel. Because the propeller breaks the symmetry of the buoyant JICF cross section, here the experimentally measured results are not averaged over the  $y = 0$  axis and the presented experimental results come from three realisations. In Figure 7.1 an example of the measured result is shown.

### 7.3 Simulation set up

Simulations are carried out on a pie-shaped grid like shown in Figure 6.3. The grid for simulations 1-9 with a lower dredging speed extends down to  $z = 39D$  and consists of 32 million cells; the grid for simulations 10-18 with a higher dredging speed extends down to  $z = 24D$  and consists of 20 million cells. The grid size is equidistant in  $\phi, z$  direction and variable in  $r$  direction. At the plume outflow the grid size is  $\Delta r = \Delta y = 0.1D$  and  $\Delta z = 0.13D$ . Further downstream  $\Delta r$  is expanded and due to the pie-shaped grid also the effective lateral grid size  $\Delta y = r\Delta\phi$  expands further downstream of the dredging plume. This resolution of only 10 grid cells over the diameter of the plume is not sufficient to capture all small turbulent scales at outflow, only the largest scales are captured at outflow. Further downstream the dredging plume expands quickly and a broader range of turbulence scales are captured on the grid. At  $x > 5D$  already more than 45 grid cells are available to cover the width of the then bent over plume. A grid resolution check with a 1.5 times finer grid at the overflow is presented in Section 7.4.6 and shows that the results are not strongly dependent of grid resolution. In order to determine whether enough turbulent scales are covered on the LES grid, the percentage of resolved turbulent energy on the grid is determined by:

$$PERC^{res} = \frac{k^{res}}{k^{res} + k^{sgs}} \quad (7.1)$$

with the resolved kinetic energy  $k^{res} = \frac{1}{2}\overline{u'_i u'_i}$  and following Wegner et al. (2004) the kinetic sub-grid energy is estimated by  $k^{sgs} = \frac{v_{sgs}^2}{0.086\Delta}$  with grid size  $\Delta$ . The percentage of resolved turbulent energy exceeds 90% in most parts of the plume

except a very small zone near the outflow where it drops to 80%. The percentage of resolved turbulent energy is larger than 80% which qualifies it as LES by Pope (2000).

Moving along with a coordinate system fixed on the TSHD, the flow velocity near the TSHD hull is slightly different from the dredging speed because the hull is an obstacle which partly blocks the flow. As can be seen in Figure 6.3, the simulation grid starts just in front of the overflow and the bow of the TSHD is missing to save valuable computational time. In order to generate the correct inflow velocity profiles (including the blocking effect) for the dredging plume simulations an extra simulation with a domain equal to the experimental flume is carried out, see also Section 3.4.1. In this larger domain the full TSHD hull is captured and the time averaged flow profiles of this extra simulation are used as inflow boundary conditions for the dredging plume simulations.

In the simulation the plume inflow velocity is prescribed with a 1/7 power law profile at the top of the domain without turbulent fluctuations. This means that in the simulation the plume flux can redistribute inside the vertical overflow pipe. Although this is different from the experimental set up where the plume flux is injected over the full diameter of the overflow pipe at the keel of the vessel, the simulation set up is more realistic in this aspect for a dredging vessel. In reality and in the simulation it can be expected that the plume outflow focusses on the downstream end of the overflow opening. The keel of the vessel is modelled as a partial slip boundary with the shear stress following from a standard hydraulic smooth logarithmic wall function. A spin up time of  $140 D/u_{cf}$  is used to flush the full computational domain with the plume and an averaging time span of  $220 D/u_{cf}$  is used to obtain smoothly averaged profiles.

## 7.4 Results and discussions

### 7.4.1 Validation LES results

Propeller flow is validated in Section 5.4.3 for the same experimental set up as used in this chapter and the LES simulations with propeller are representative for a propeller without rudder. The simulated and measured plume concentrations are compared for two cross sections  $x/D = 60$  and  $x/D = 100$  in Figure 7.3 for the experimental runs indicated in Table 7.1. Figure 7.3 clearly shows the typical kidney shaped plume profile caused by the counter rotating vortex pair (CVP) of a buoyant JICF. The simulated plume concentration vertical position, height, width and shape are comparable with the experimental ones for both dredging speeds, overflow front and back and with/without propeller. The root-mean-square (RMS) difference of the simulated and experimental vertical position (centre of gravity) in Figure 7.3 is  $1.8D$ , the RMS difference of the height of the  $0.2C_{max}$  contour is  $3.8D$  (determined only for the  $\gamma = 1.28$  runs), the RMS difference of the width of the  $0.2C_{max}$  contour is  $3.1D$ .

Without propeller the plume concentrations do not differ much with the overflow at the front or at the back; this is true for both the experiments and the sim-

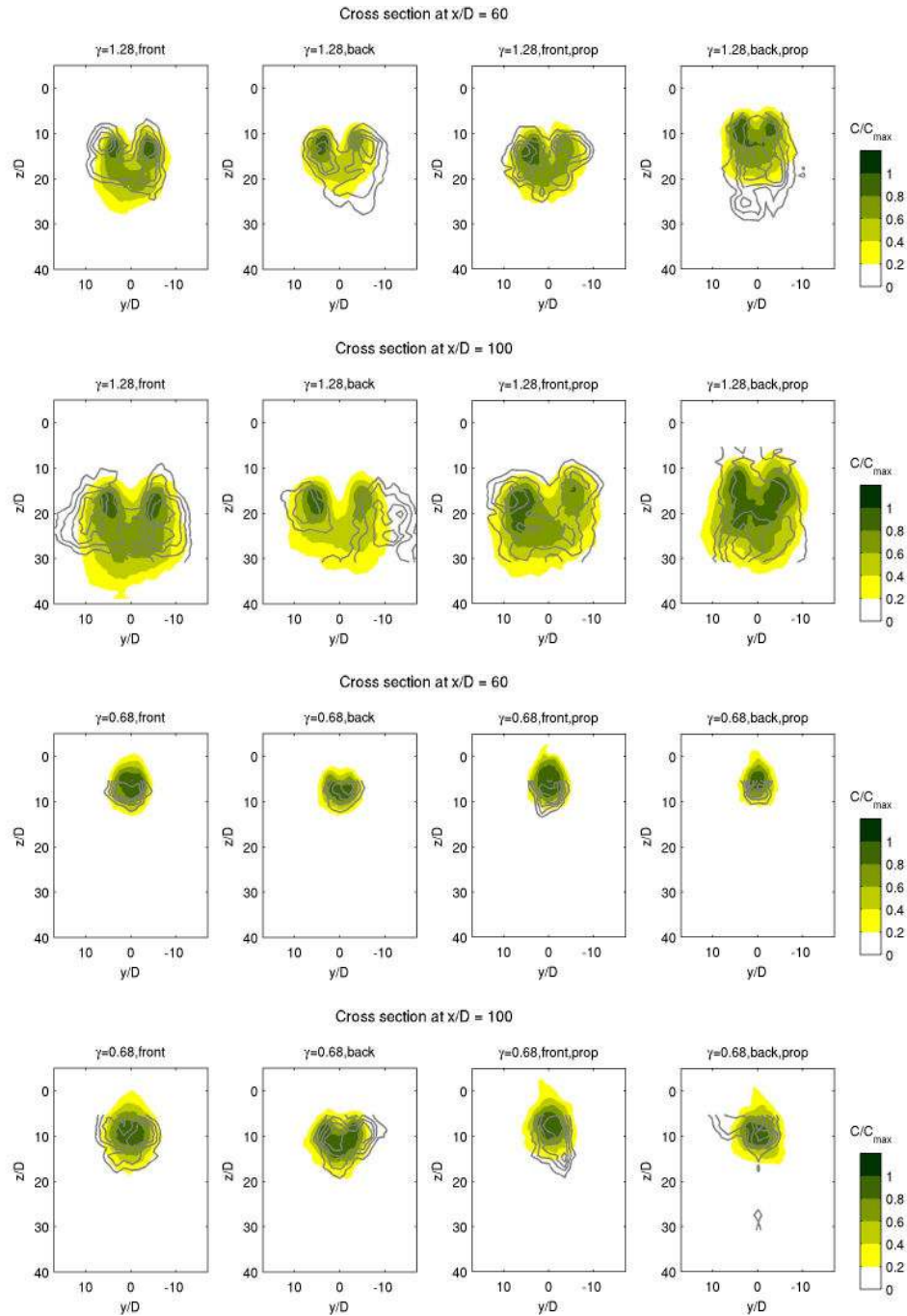


**Figure 7.3:** Comparison plume concentration cross sections of experiment (contours at steps of  $0.2C_{max}$ ) and simulation (colours). To facilitate comparison between experiment and simulations, both are made non dimensional with their own maximum plume concentration  $C_{max}$  in the cross section at hand.

ulations. With a propeller the dredging plume has moved upward a little, the plume concentration profile is narrower and more elongated in vertical direction. This effect of the propeller is caused by entrainment into the propeller jet: the dredging plume is sucked upward by this entrainment and the CVP of the



dredging plume is counteracted. More on this effect in further sections of this chapter, but it is visible in experiments and simulations. When the overflow is at the back, the influence of the propeller is larger, because of the reduced distance between outflow of the dredging plume and the propeller.

Generally, the plume profiles and influences of overflow position and propeller in the simulation are comparable with the experiment, but on details there are differences. Two most noticeable differences can be explained by differences in the set up of experiment and simulation. First difference is visible in the runs without propeller. The simulated runs without propeller show a slightly narrower and more vertically stretched simulated plume profile than the experiments. This difference is mainly caused by the different inflow condition in the experiments and the simulations. As mentioned in previous section, the inflow in the simulations is placed at the top of the domain to allow redistribution of the plume flux inside the vertical overflow pipe as can happen on a real dredging vessel. In the experiments this redistribution is prevented by injecting the plume flux over the full diameter of the overflow pipe at the keel of the vessel. Simulations with the plume flux injected over the full diameter at the keel of the vessel in Chapter 6 showed wider plume concentration profiles than in this chapter. Second difference between simulated plume profiles and experimental ones is visible in the influence of the propeller. Although the influence of the propeller in the simulations is clearly visible and in the right direction; it lifts

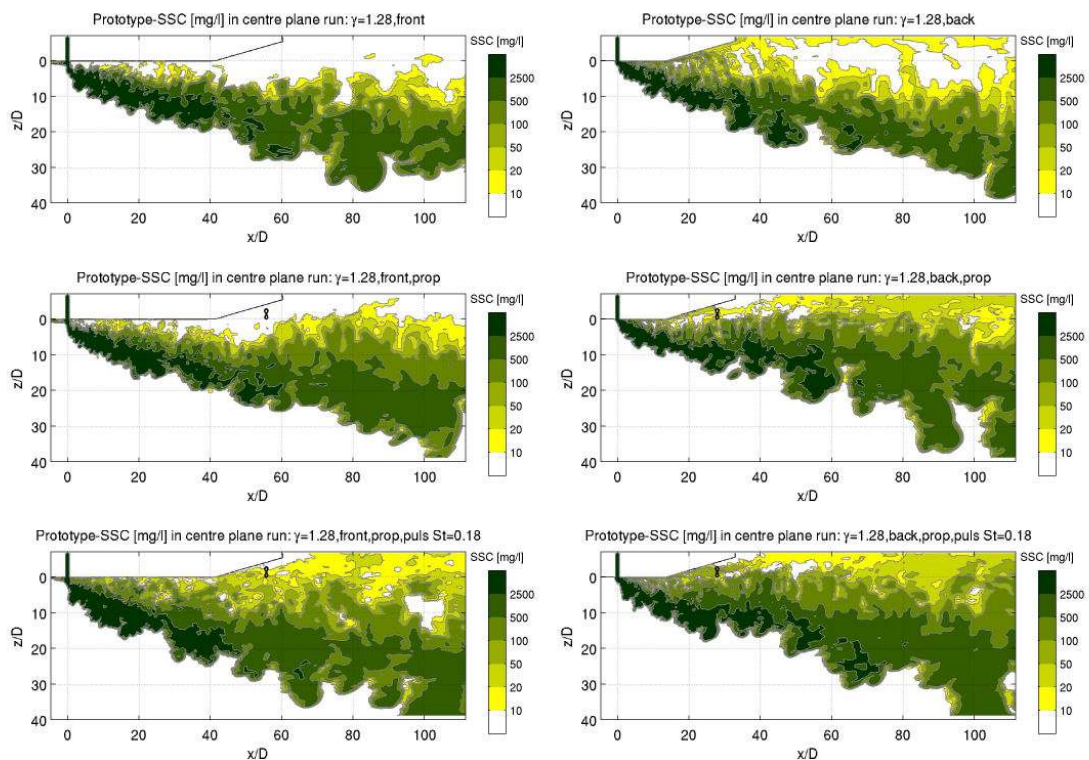


**Figure 7.4:** Simulated instantaneous prototype-SSC at the centre slice for runs with normal dredging speed.



the plume concentration profile up and makes it narrower and more elongated in vertical direction, the influence in the experiments is larger. This difference plausibly originates from the rudder influence in the experiment and the larger propeller jet momentum in the experiment compared with the simulation which also caused a difference in vertical  $u$ -velocity profile of the propeller jet in Figure 5.17.

Given that the experimental and simulated plume concentration profiles are in general agreement with each other and given that the most noticeable differences can be explained by differences in details of the set up of experiments and simulations, the simulations are validated successfully. The simulations represent the influence of a propeller without rudder realistically. Because a rudder enhances the vertical mixing of the propeller jet which probably increases the influence on the dredging plume, the simulations (without rudder) are expected to give a conservative estimation of the influence of the propeller. The simulations can now be used to find the influence of dredging speed, overflow location, propeller influence without rudder and pulsing on mixing details of a dredging plume.

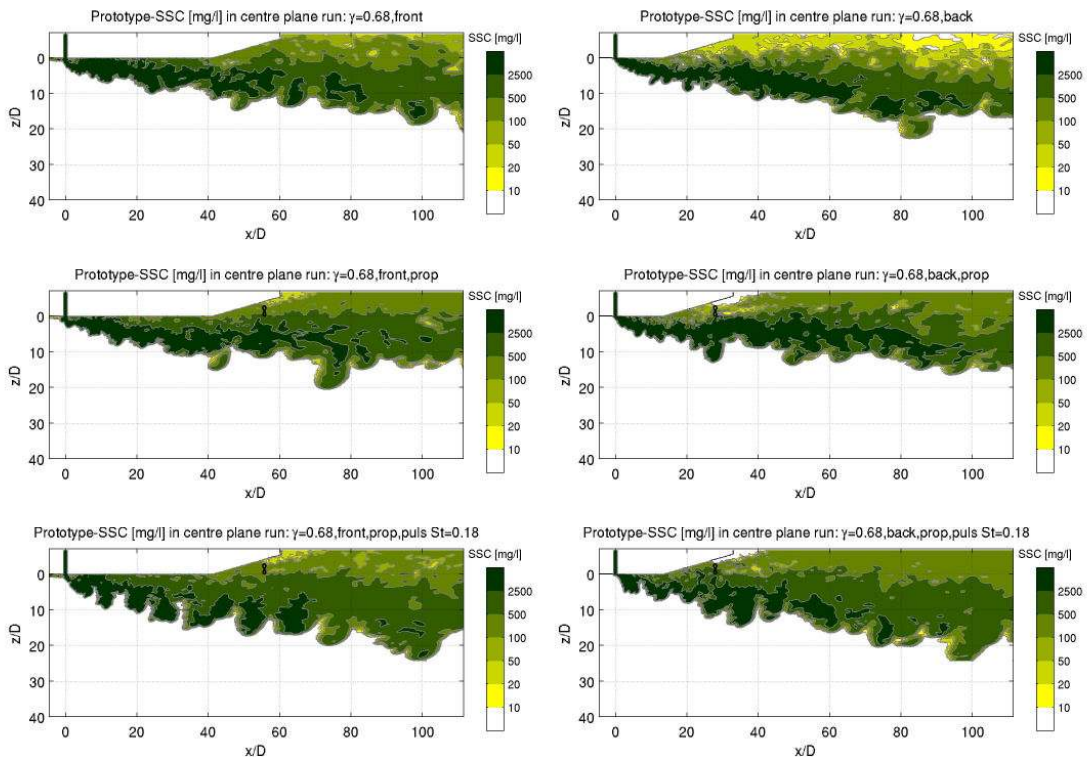


**Figure 7.5:** Simulated instantaneous prototype-SSC at the centre slice for runs with high dredging speed.

## 7.4.2 Instantaneous longitudinal sections

Figures 7.4-7.6 show instantaneous SSC (suspended sediment concentration) levels at the centre plane caused by the dredging plume for all 18 runs. All figures show prototype-SSC by scaling the simulated SSC up with the density scaling factor 4 explained in Section 6.2. For all runs, the mixing is very turbulent and the dredging plume expands quickly over the water column: at  $x = 100D$  the vertical size of the dredging plume is in the order of  $20 - 30D$ . The dredging plume mixes efficiently with the ambient water: within  $100D$  the maximum prototype-SSC has decreased under  $2.5 \text{ g/l}$ ; this is only  $0.7\%$  of the overflow concentration. Although the majority of dredging plume material moves in downward direction as one would expect under influence of the initial vertical outflow velocity and density difference, some material (prototype-SSC up to  $10\text{-}50 \text{ mg/l}$ ) from the dredging plume is lifted all the way up to the free surface forming a surface plume by the interaction with the hull, influence of the propeller and pulsing.

From the instantaneous results in Figures 7.4-7.6 some important observations about the influence of dredging speed, overflow position, propeller and pulsing can be made. With a higher dredging speed the dredging plume stays higher in the water column, leading to extra interaction with the keel and aft of the TSHD. Also the propeller has extra influence with a high dredging speed. A higher dredging speed results in a lower dilution: for  $\gamma = 1.28$  a prototype-SSC= $2.5 \text{ g/l}$  is found up to  $x/D = 70$ , for  $\gamma = 0.68$  a prototype-SSC= $2.5 \text{ g/l}$  is

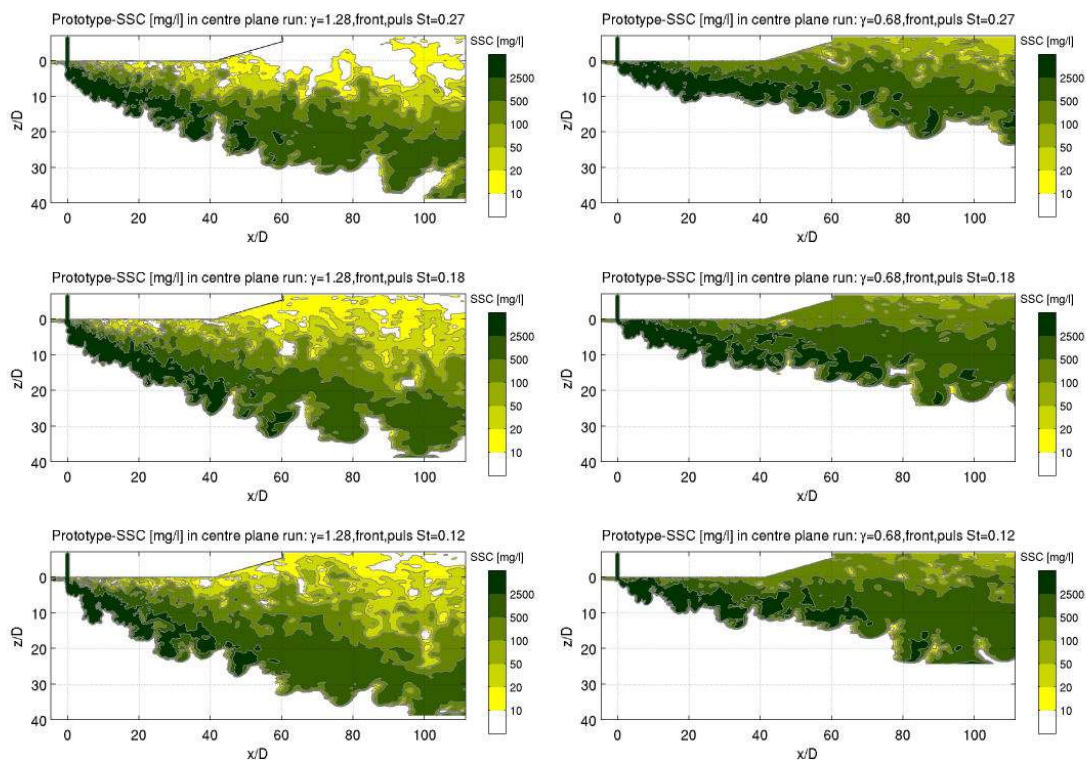


Figure 7.6: Simulated instantaneous prototype-SSC at the centre slice for runs with pulsing.

found up to  $x/D = 100$ . A free surface without sediment ( $SSC < 10$  mg/l) is only found for a low dredging speed. When the vertical distance between the dredging plume and the propeller is small enough, the dredging plume is lifted up by the propeller. This is visible for all runs with propeller and a high dredging speed ( $\gamma = 0.68$ ) and for the runs with propeller and normal dredging speed ( $\gamma = 1.28$ ) with the overflow at the back. There is no indication that significant amounts of the dredging plume are sucked directly into the propeller, even with high dredging speed ( $\gamma = 0.68$ ) and the overflow at the back, the majority of the dredging plume seems to flow under the propeller, not through the propeller. When the overflow is at the back, the influence of the aft of the TSHD and the influence of the propeller is larger because the dredging plume has not descended as much as in case of a front overflow. Pulsing is responsible for larger vertical spreading of a dredging plume: the lower end of the dredging plume descends a little quicker and near the free surface larger  $SSC$  values are found. For the largest pulsing period ( $St = 0.12$ ) the separate puffs including gaps can be recognised.

### 7.4.3 Dredging plume paths

Simulated dredging plume paths are shown in Figure 7.7. The paths are defined by the streamline on the centre slice at  $y = 0$  starting at  $x, z = (0, 0)$  (Yuan and Street 1998). At  $x/D = 100$  the difference between highest and lowest paths is  $5D$  in vertical direction for high dredging speed runs and even  $9D$  for normal dredging speed runs. The position of the overflow, propeller and pulsing can have significant influence on the main dredging plume path. The paths of dredging plumes with high dredging speed is higher than with normal dredging speed. Propeller runs are higher than non-propeller runs because of the entrainment effect into the propeller jet which lifts the dredging plume up. Pulsed runs are deeper than non-pulsed runs because of the extra vertical inflow momentum. The influence for position of the overflow is different for normal and high dredging speed. Runs with normal dredging speed and overflow at the back are higher than runs with overflow at the front. Runs with high dredging speed and overflow at the back are higher than runs with overflow at the front at  $x/D = 20 - 80$ ,

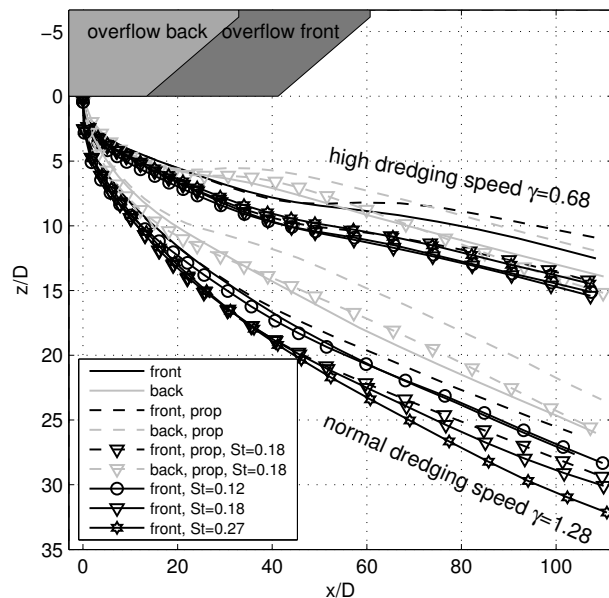


Figure 7.7: Dredging plume paths for all 18 runs.

but further downstream at  $x/D > 80$  they are deeper.

#### 7.4.4 Time averaged cross sections

Time averaged cross section results at  $x/D = 100$  are given in Figures 7.8-7.9. The CVP is clearly visible in the velocity-vectors and in the typical kidney shape of the plume concentration contours. Near the free surface a second CVP is present with the opposite direction of the dredging plume CVP. The surface CVP is caused by the flow past the aft of the TSHD. The area of the dredging plume at  $x/D = 100$  is much larger for low dredging speed than for high dredging speed, this again indicates the increased mixing and dilution obtained with lower dredging speed. With low dredging speed, without propeller and without pulsing, all sediment stays inside the main body of the dredging plume and also inside the influence zone of the CVP generated by the dredging plume. With high dredging speed, or with propeller, or with pulsing some sediment can be found above the main body of the dredging plume. This sediment is stripped off from the main dredging plume and forms a surface plume. The surface plume generated by pulsing is symmetrical, but the surface plume generated by the propeller has a tendency towards positive  $y$  direction, this is caused by the rotation direction of this single propeller. In Figure 7.8 with low dredging speed and overflow at the front, the vertical distance between the propeller and dredging plume is too large to strip off significant amounts of sediment, but with the overflow at the back the propeller generates a surface plume with time averaged prototype-SSC  $> 20$  mg/l. In Figure 7.8 with high dredging speed the propeller generates a surface plume with time averaged prototype-SSC  $> 100$  mg/l; both with the overflow at the front and at the back.

**Table 7.2:** LES results of a buoyant dredging plume at  $x/D = 100$  with infinite depth and no deposition at the bed. Presented SSC is prototype-SSC.

run	$Ri$	$\gamma$	over-flow	prop.	pulsing	max time avg. SSC dredging plume	max time avg. SSC free surface	time avg. perc. surface plume
1	1.08	1.28	front	-	-	1.2 g/l	1 mg/l	0%
2	1.08	1.28	back	-	-	1.6 g/l	5 mg/l	0%
3	1.08	1.28	front	prop	-	1.3 g/l	4 mg/l	0.3%
4	1.08	1.28	back	prop	-	1.2 g/l	31 mg/l	1.5%
5	1.08	1.28	front	prop	$St = 0.18$	1.1 g/l	12 mg/l	0.9%
6	1.08	1.28	back	prop	$St = 0.18$	1.0 g/l	30 mg/l	2.0%
7	1.08	1.28	front	-	$St = 0.12$	1.0 g/l	6 mg/l	0.4%
8	1.08	1.28	front	-	$St = 0.18$	0.9 g/l	9 mg/l	0.4%
9	1.08	1.28	front	-	$St = 0.27$	1.0 g/l	4 mg/l	0.2%
10	1.08	0.68	front	-	-	1.8 g/l	62 mg/l	1.5%
11	1.08	0.68	back	-	-	1.8 g/l	10 mg/l	0.2%
12	1.08	0.68	front	prop	-	2.0 g/l	352 mg/l	18%
13	1.08	0.68	back	prop	-	2.0 g/l	298 mg/l	17%
14	1.08	0.68	front	prop	$St = 0.18$	1.5 g/l	170 mg/l	11%
15	1.08	0.68	back	prop	$St = 0.18$	1.6 g/l	208 mg/l	12%
16	1.08	0.68	front	-	$St = 0.12$	1.4 g/l	78 mg/l	1.8%
17	1.08	0.68	front	-	$St = 0.18$	1.4 g/l	83 mg/l	2.7%
18	1.08	0.68	front	-	$St = 0.27$	1.6 g/l	44 mg/l	1.7%



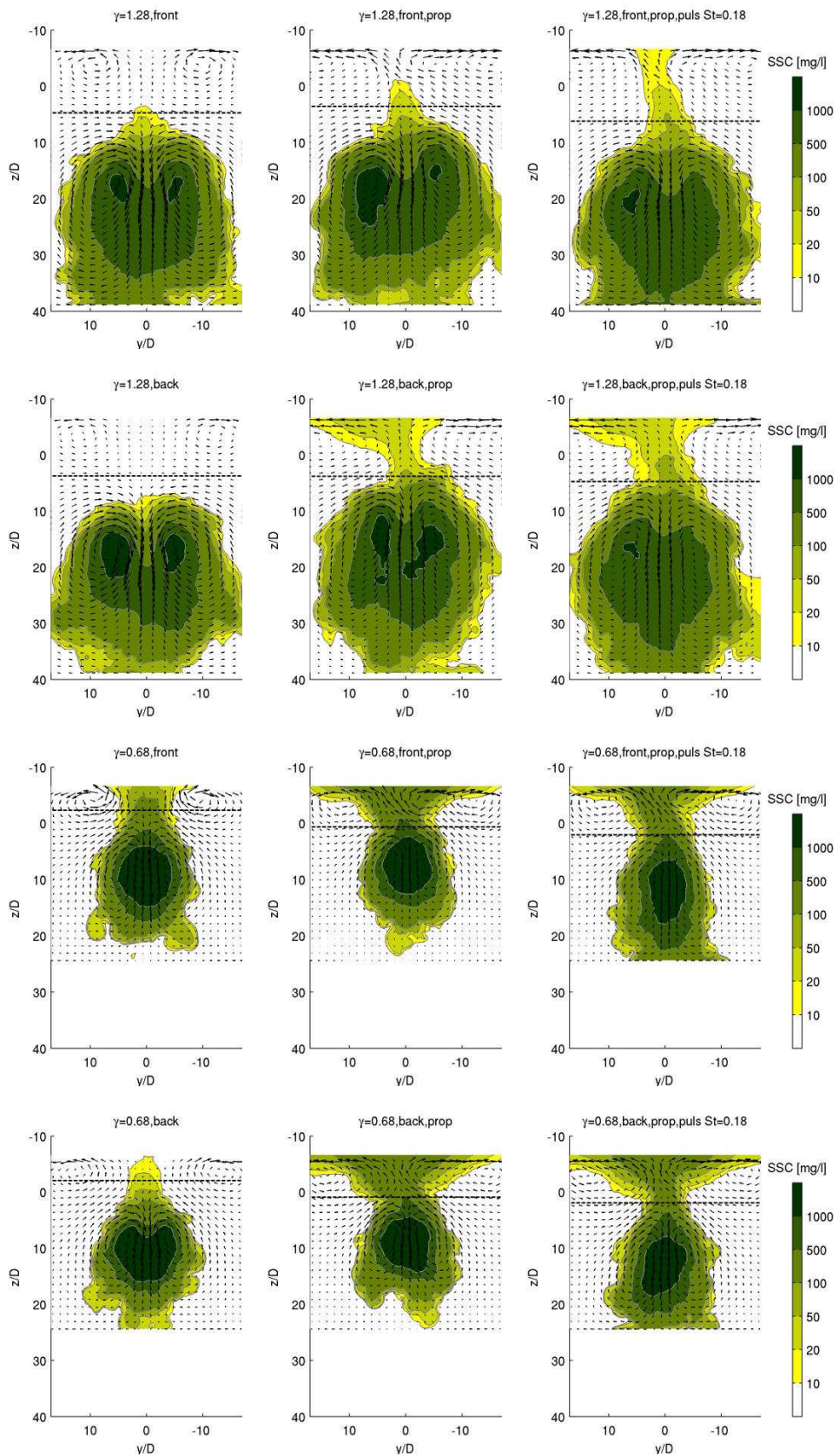


*Figure 7.8: Simulated time averaged prototype-SSC at  $x = 100D$  of different runs with normal and high dredging speed. Arrows indicate the time averaged  $v, w$  velocity; each fifth grid cell in  $y$  direction is shown and each tenth in  $z$  direction.*

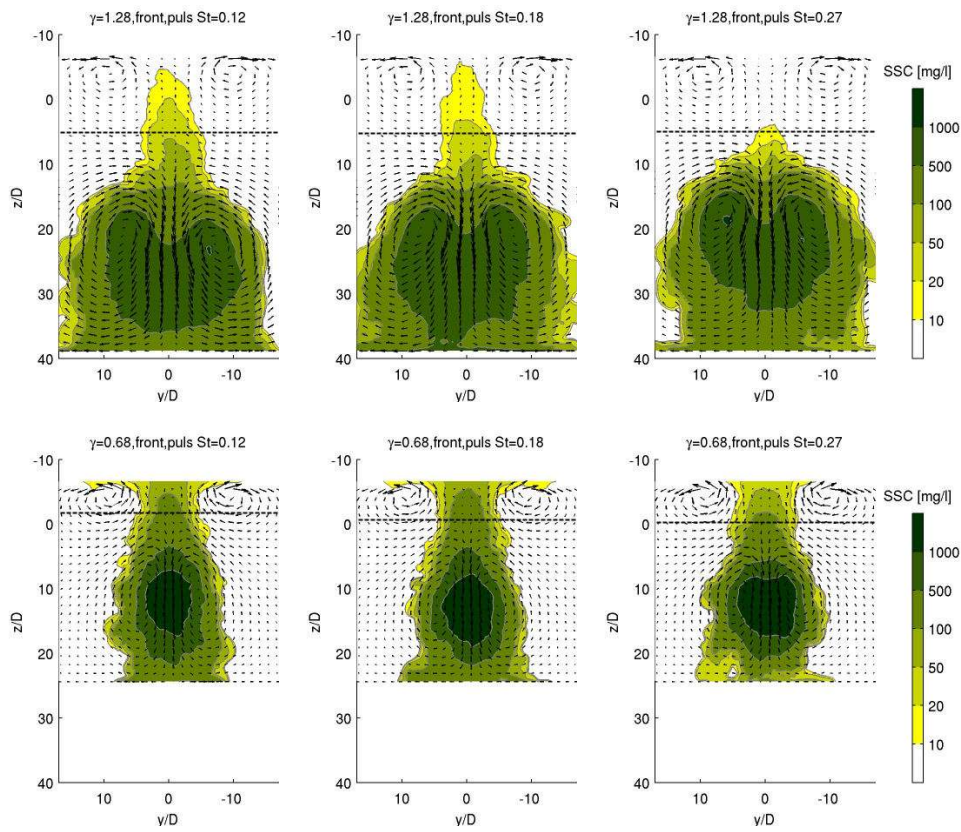


**Figure 7.9:** Simulated time averaged prototype-SSC at  $x = 100D$  for different runs with pulsing. Arrows indicate the time averaged  $v, w$  velocity; each fifth grid cell in  $y$  direction is shown and each tenth in  $z$  direction.

The sediment in the main body of the dredging plume has a downward concentration weighted velocity caused by the dredging plume CVP which is driven by the excess density. The sediment in the surface plume has an upward concentration weighted velocity caused by the surface CVP. The division between upward and downward velocity is given by the black dashed line at the vertical position where the average over the width of the plume of  $\overline{wC}/\overline{C}$  switches signs. The stripped off sediment in the surface plume is likely to stay separated from the main body of the dredging plume and can disperse as a passive dredging plume in the far field. The amount of surface plume is therefore interesting for environmental impact assessment. Table 7.2 summarises the amount of surface plume, based on the division by the black dashed line, as percentage of the total plume and the maximum time averaged prototype-SSC at the free surface and inside the dredging plume for each run. With high dredging speed ( $\gamma = 0.68$ ) the surface plume can vary between 0.2-18% of the total overflow sediment flux with a maximum time averaged prototype-SSC of 10-352 mg/l at the free surface. With normal dredging speed ( $\gamma = 1.28$ ) the surface plume is smaller: 0-2% and a maximum prototype-SSC of 1-30 mg/l at the free surface. The propeller influence is dominant over overflow position and pulsing. Maximum surface



plume percentages of 2% with normal dredging speed and 18% with high dredging speed are obtained with propeller, without propeller the maxima are only 0.4% for normal dredging speed ( $\gamma = 1.28$ ) and 2.7% for high dredging speed ( $\gamma = 0.68$ ). Pulsing in combination with propeller can have opposite effects: normal dredging speed pulsing together with propeller enhances the surface plume (with higher percentage and higher SSC at the free surface) compared to propeller alone, but high dredging speed pulsing together with the propeller reduces the surface plume (lower percentage and lower SSC at the free surface) compared to the propeller alone. Pulsing on the one hand results in a deeper dredging plume, because of the higher inflow momentum (the average inflow velocity is similar to a non-pulsed run, but the peak inflow velocity is doubled for a pulsed run), but on the other hand pulsing enhances the formation of a surface plume. For the high dredging speed the deeper dredging plume influence of pulsing is dominant and for normal dredging speed the enhanced formation of a surface plume is dominant.

Pulsing alone increases mixing, as can be seen from the lower time averaged maximum SSC levels inside the plume. Pulsing alone also generates extra surface plume, but less than the propeller. A maximum surface plume of 0.4% is found for pulsing with  $St = 0.18$  for normal dredging speed ( $\gamma = 1.28$ ) and 2.7% for high dredging speed ( $\gamma = 0.68$ ). Pulsing with  $St = 0.27$  has the smallest influence, the influence of pulsing with  $St = 0.12$  is in between  $St = 0.27$  and  $St = 0.18$ . This influence of pulsing is comparable with results previously obtained in experiments and Direct Numerical Simulation (DNS) of pulsed non buoyant JICF. The experiments of [MCloskey et al. \(2002\)](#) found: limited extra jet penetration and vertical spreading for sine wave pulsing with  $St = 0.18$ ; strong vertical splitting and a large increase in jet penetration for square wave pulsing with low duty cycles ( $< 50\%$ ) and  $0.13 < St < 0.27$ ; no big influence for  $St > 0.34$ . The experiments of [MCloskey et al. \(2002\)](#) were carried out for a non buoyant JICF with  $\gamma = 2.6$  and a pulsing amplitude of 54%. The experiments of [Narayanan et al. \(2003\)](#) showed extra vertical penetration, extra vertical spreading and extra mixing for  $St = 0.085$  and  $St = 0.19$  with sine wave pulsing for a non buoyant JICF with  $\gamma = 6$  and a pulsing amplitude of approximately 15%. The DNS ([Muldoon and Acharya 2010](#)) of a non buoyant JICF with  $\gamma = 6$  pulsed with a sine wave of amplitude 20% resulted in vertical splitting with increased penetration for  $St = 0.2$  and  $St = 0.4$  and horizontal splitting with reduced penetration for  $St = 0.6$ . For all three  $St$  numbers  $St = 0.2$ ,  $St = 0.4$  and  $St = 0.6$  the mixing was improved.

### 7.4.5 Anisotropy of turbulence

The structure of turbulence and its anisotropy can be characterised by the anisotropy tensor  $b_{ij}$ :

$$b_{ij} = \frac{\overline{u'_i u'_j}}{\overline{u'_k u'_k}} - 1/3\delta_{ij}. \quad (7.2)$$

Because the trace of  $b_{ij}$  is zero, the first invariant  $I_1$  is zero and the two remaining independent invariants  $\zeta, \eta$  of  $b_{ij}$  can be written as (Pope 2000):

$$6\eta^2 = -2I_2 = b_{ij}b_{ji}, \quad (7.3)$$

$$6\zeta^3 = 3I_3 = b_{ij}b_{jk}b_{ki}. \quad (7.4)$$

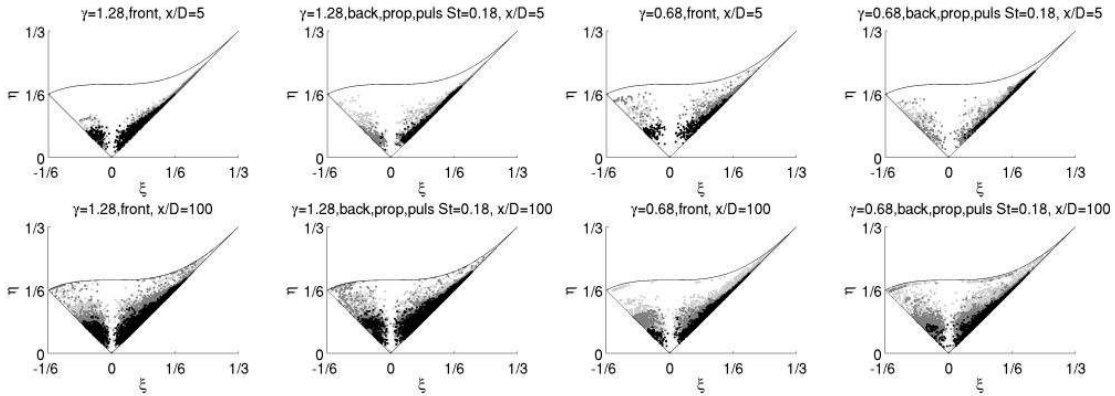


**Figure 7.10:** Lumley triangles of different dredging plume runs at two cross sections  $x/D = 5$  and  $x/D = 100$ . Black dots correspond to locations within the  $0.5C_{max}$  contour, the dark grey dots correspond to the  $0.1C_{max}$  contour and the light grey dots correspond to the  $0.01C_{max}$  contour.  $C_{max}$  is the maximum plume concentration in the cross section.

The turbulence structure can be visualised by plotting these two invariants  $\zeta, \eta$ . All realisable Reynolds stresses together form a triangular area with two straight lines and is often called the Lumley triangle (Pope 2000) after Lumley (1978), see the lines in Figure 7.10. A more detailed description of the Lumley triangle can be found in Simonsen and Krogstad (2005). For all grid points inside the dredging plume at two different cross sections, one close to the origin at  $x/D = 5$  and one further downstream at  $x/D = 100$ , values of  $\zeta, \eta$  are shown in Figure 7.10. In Figure 7.10 four runs are shown, but it could have been other runs as well, because all runs show comparable Lumley triangles. Dredging speed, position of the overflow, propeller and pulsing have not much influence on the anisotropy and structure of turbulence inside the dredging plume. For all runs at  $x/D = 5$  all points are near the bottom two edges which indicates axisymmetric turbulence. At  $x/D = 5$  most points are found near the right edge of the Lumley triangle: the turbulence inside the dredging plume starts rod-like; axisymmetric with one large eigenvalue and the shape of the Reynolds stress ellipsoid is a prolate spheroid. This state is also found for the log-law region of channel flow (Pope 2000). Some points are found near the left edge of the Lumley triangle at  $x/D = 5$ , this corresponds to disk-like turbulence; axisymmetric with one small eigenvalue and the shape of the Reynolds stress ellipsoid is an oblate spheroid. For all dredging plume runs at  $x/D = 100$   $\zeta, \eta$  are scattered over almost the entire Lumley triangle, which means that further downstream inside a dredging plume not only axisymmetric turbulence is found, but all turbulent states

**Table 7.3:** LES results buoyant dredging plume at  $x/D = 100$  with infinite depth and no deposition at the bed normal grid size and 1.5 times finer grid size. Presented SSC is prototype-SSC

run	$Ri$	$\gamma$	over-flow	prop.	pulsing	max time avg. SSC dredging plume	max time avg. SSC free surface	time avg. perc. surface plume
5	1.08	1.28	front	prop	$St = 0.18$	1.1 g/l	12 mg/l	0.9%
5f	1.08	1.28	front	prop	$St = 0.18$	1.0 g/l (fine)	12 mg/l (fine)	1.1% (fine)
14	1.08	0.68	front	prop	$St = 0.18$	1.5 g/l	170 mg/l	11%
14f	1.08	0.68	front	prop	$St = 0.18$	1.5 g/l (fine)	210 mg/l (fine)	15% (fine)

from isotropic to strongly anisotropic occur. The black dots from the core of the dredging plume are more concentrated near the origin ( $\xi = 0, \eta = 0$ ) of the Lumley triangle which corresponds to isotropic turbulence. The dark grey and light grey dots from the edges of the dredging plume are found further away from the origin which means that the turbulence at the edges of the dredging plume is more anisotropic. For other mixing flows, like mixing inside a stirred tank also strong anisotropic turbulence was found with the two invariant values all over the Lumley triangle (Hartmann et al. 2004; Lamarque et al. 2010).

Because the turbulence inside the dredging plume is found to be strongly anisotropic, especially near the edges which are most interesting for the generation of a surface plume, it can be expected that RANS models which assume isotropic turbulence will not result in accurate surface plume predictions.

#### 7.4.6 Grid resolution check

A grid resolution check is carried out for the LES results with a 1.5 times finer grid at the overflow. Two simulations with all near field processes taken into account are used (front overflow, propeller and pulsing  $St = 0.18$ ): simulation 5 with 56 million grid cells and simulation 14 with 35 million. At the plume outflow the grid size is now  $\Delta r = \Delta y = 0.067D$  and  $\Delta z = 0.13D$ . This is 15 grid cells over the plume diameter at outflow, and 68-90 grid cells over the diameter of the bend over plume from  $x/D > 5$ . Time averaged cross sections at  $x/D = 100$  in Figure 7.11 are almost identical to the normal grid resolution results in Figures 7.8. Table 7.3 compares the amount of surface plume and time averaged prototype-SSC for normal and fine grid resolution. The normal and fine time averaged prototype-SSC inside the main body of the dredging plume are within 10% of each other. The maximum time averaged prototype-SSC at the free surface and the amount of surface plume are more subtle parameters and differ up to 27% between normal and fine results. Fine grid resolution results show more surface plume than normal grid resolution results. The difference between normal and fine results is less than the influence of the investigated near field processes. Therefore the normal grid resolution results are sufficiently accurate to find the influence of these parameters on dredging plumes, but in absolute sense the presented amounts of surface plume appear to be rather low than high.

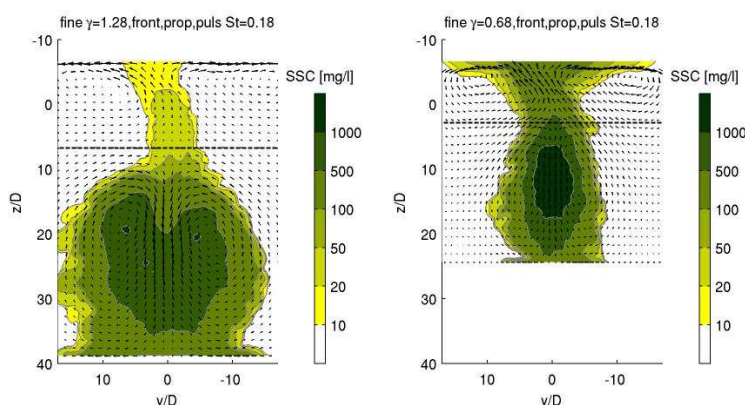


**Figure 7.11:** Simulated time averaged prototype-SSC at  $x = 100D$  of runs with fine grid. Arrows indicate the time averaged  $v, w$  velocity; each fifth grid cell in  $y$  direction is shown and each tenth in  $z$  direction.

## 7.5 Conclusions

Detailed LES results are presented on near field mixing of overflow dredging plumes generated at a TSHD. Systematically, the influence of dredging speed, overflow location, propeller and pulsing frequency is investigated with instantaneous and time averaged results. The variations had significant influence on the development of the dredging overflow plume in general and surface plume in particular. With normal dredging speed ( $Ri = 1.08, \gamma = 1.28$ ) the surface plume varied between 0 and 2% with maximum time averaged prototype-SSC levels of 1-31 mg/l at the free surface at  $x/D = 100$ . With high dredging speed ( $Ri = 1.08, \gamma = 0.68$ ) the surface plume varied between 0.2 and 18% with maximum time averaged prototype-SSC levels of 10-352 mg/l at the free surface at  $x/D = 100$ .

The LES results are close to the experimental results. A grid resolution check with a 1.5 times finer grid results in the same time averaged plume cross profiles at  $x/D = 100$ . The maximum time averaged SSC levels at the free surface and the amount of surface plume in the fine simulation are up to 27% larger than with normal resolution. The difference between normal and fine resolution is less than the influence of the investigated near field processes. Therefore the normal grid resolution results are sufficiently accurate to find the influence of those processes, but in absolute sense the presented amounts of surface plume and prototype-SSC at the free surface appear to be rather low than high.

The structure of the turbulence inside a dredging plume is not very dependent on dredging speed, overflow location, propeller or pulsing frequency. In all runs the turbulence started rod-like near the overflow and it ended very anisotropic at larger distances downstream. The edges of a dredging plume show more anisotropic turbulence than its centre which remains more isotropic. Details on the percentage of surface plume generation and surface SSC can be found in Table 7.2, but the main conclusions on the influence of the individual

processes are:

- Influence dredging speed  
Dredging speed has a large influence on the dredging plume path and determines in this way the effectiveness of the other near field processes in generating a surface plume. With high speed the overflow plume stays close to the keel and the influences of the aft of the vessel and propellers are much larger than with normal speed. The dilution at a certain distance downstream is inversely proportional to the dredging speed: higher speed results in less dilution of the dredging plume.
- Influence propeller  
A propeller lifts the dredging plume up by entrainment into the propeller jet and this entrainment partially blocks the CVP of the dredging plume. There is no indication that significant amounts of the dredging plume are sucked directly into the propeller. A propeller was found to have more influence than overflow location and pulsing on the formation of a surface plume.
- Influence position overflow  
Whether the overflow is at the front or at the back of the vessel does matter when dredging at normal speed, but does not matter much when dredging at high speed. With the overflow at the back the propeller is closer by and has more influence in generating a surface plume when dredging at normal speed. For runs with high speed combined with a propeller the difference in surface plume generation between overflow at the front or at the back is insignificant.
- Influence pulsing  
Pulsing is responsible for larger vertical spreading of a dredging plume and a deeper plume path. Pulsing alone (without propeller) enhances the formation of a surface plume. Largest influence was found for  $St = 0.18$  and smallest for  $St = 0.27$ , the influence of  $St = 0.12$  is in between the two other pulsing frequencies. Pulsing combined with propeller was found to enhance surface plume generation for normal dredging speed and to reduce surface plume generation for high dredging speed. For normal dredging speed the larger vertical spreading caused by pulsing was dominant and for high dredging speed the deeper plume path was dominant.

When dredging, a TSHD always uses propulsion to drag its drag-heads over the bed. Therefore the runs with propeller are most interesting from a practical point of view. For these runs there is always a surface plume with a variation of 0.2-2% for normal dredging speed and 11-18% for high dredging speed. This leaves the dredging speed as dominant factor of all investigated parameters to determine the amount of surface plume generated in the near field which can be available for far field dispersion to ecological sensitive areas. To reduce the surface plume it is best to have an overflow at the front instead of one at the back. There is no clear single conclusion on the influence of pulsing combined with the propeller: for normal dredging speed pulsing should be avoided in order to minimise the generation of a surface plume, but for high speed dredging pulsing can decrease the surface plume. At what dredging speed the exact transition lies

between positive and negative influence of pulsing has not not been investigated. All results are obtained without influence of a bed, hence in shallow areas the amount of surface plume could be larger. LES was found to be a useful tool to systematically investigate the influence of different processes on the near field mixing of a dredging plume.



# Chapter 8

## Validation of near field dredging plume - field scale

*CFD simulations of near field overflow dredging plume mixing are compared with field measurements from several dredging projects. Seven cases are considered with different conditions and overflow fluxes resulting in significant differences in plume behaviour.*<sup>1</sup>

### 8.1 Introduction

Seven cases from field measurements of a dredging plume close to the TSHD are used to validate the CFD model. The field measurements are carried out within the TASS framework<sup>2</sup>. CFD results are compared with the measurements in great detail on plume flux, concentrations and location in the water column.

### 8.2 Field measurements

The field measurements have been obtained in several dredging campaigns (2002, 2007 and 2011) with a variety in TSHD sizes and materials being dredged. In the 2002 campaign a ~ 6000 m<sup>3</sup> TSHD was dredging mud or sand in NW-Europe, in the 2007 campaign a ~ 15000 m<sup>3</sup> TSHD was dredging mud and fine sand in NW-Europe and in the 2011 campaign a ~ 20000 m<sup>3</sup> TSHD was dredging pre-crushed rock in NW-Australia. All measurements are taken close to the TSHD in a zone several hundred metres from the TSHD in order to find the location, extend and suspended sediment concentrations (SSC) of the dredging plume at the end of the near field. Each field trip had different details in measuring equipment and set up depending on the local project conditions and the incorporation of lessons

---

<sup>1</sup>A modified version of this chapter has been published as: L. de Wit, A.M. Talmon and C. van Rhee (2014), 3D CFD simulations of trailing suction hopper dredger plume mixing: comparison with field measurements, *Marine Pollution Bulletin*. DOI:[10.1016/j.marpolbul.2014.08.042](https://doi.org/10.1016/j.marpolbul.2014.08.042)

<sup>2</sup>TASS (turbidity assessment software) is initiated by SSB (Stichting Speurwerk Baggertechniek), which is a joint research framework of Royal Boskalis Westminster and Van Oord Dredging and Marine Contractors. The SSB is greatly acknowledged for making available the detailed and valuable data on field measurements of overflow plumes.

learnt from previous campaigns. As a starting point the protocol for the field measurements of sediment release from dredgers was used (VBKO 2003).

On all field campaigns measurements took place on board of the TSHD. TSHD location, speed, direction, total loading and suction discharge and suction density were logged with standard on-board sensors. The overflow volume flux was not measured separately but the assumption was used that, after the water level inside the hopper reaches the overflow level, the overflow volume flux is equal to the suction volume flux. In each campaign the overflow mixture was sampled to determine the sediment mixture density by either a radio active sensor or by weighting the sample bottles. The overflow samples were also used to determine a PSD. Best way to get samples from inside the overflow was by an air-lift.

From a separate survey vessel plume measurements were taken. In 2002 a side scan sonar was used from the survey vessel sailing next to the TSHD to find the lower edge of the dredging plume as it was descending towards the seabed. In the 2007 and 2011 campaigns transects were sailed through the plume with the survey vessel while measuring SSC by a combination of ADCP (acoustic Doppler current profiler) and 2 or 3 OBS (optical backscatter) sensors on a string at different depths. An ADCP gives a full vertical velocity profile of the flow and the amount of acoustic backscatter can be related to the amount of turbidity to show the extend, location and indication of SSC of the dredge plume (Wood and Boyé 2007; Smith and Friedrichs 2011) and it can be used to obtain plume fluxes. An OBS sensor gives point measurements of turbidity, and is more accurate than ADCP for turbidity. The ADCP and OBS were calibrated on site with water samples. In 2007 the OBS was calibrated with samples of  $SSC = 5 - 120$  mg/l leading to a best fit relation between  $NTU$  measured by the OBS and  $SSC$  of:

$$SSC = 1.80 \cdot NTU - 8.37 \quad \text{with } R^2 = 0.93. \quad (8.1)$$

In 2011 the OBS was calibrated with samples of  $SSC = 1 - 270$  mg/l leading to the relation:

$$SSC = 1.31 \cdot NTU + 22.8 \quad \text{with } R^2 = 0.61. \quad (8.2)$$

In 2007 the ADCP was calibrated with samples of  $SSC = 2 - 140$  mg/l, but unfortunately the best fit relation between the amount of backscatter in  $dB$  and  $SSC$  was not documented. In 2011 the ADCP was calibrated with samples of  $SSC = 1 - 270$  mg/l leading to the best fit relation:

$$\log(SSC) = 0.0338 \cdot dB + 3.148 \quad \text{with } R^2 = 0.41. \quad (8.3)$$

The chosen combination of ADCP and OBS results in more reliable dredge plume results while having large spatial coverage at the same time, but still there is considerable uncertainty because the relation between ADCP backscatter or OBS turbidity and  $SSC$  in the water depends on unknown exact local sediment characteristics like particle diameter, flocculation, sediment colour and on site conditions like constituents in the water. The ADCP and OBS  $SSC$  measurements generally agreed reasonably, but sometimes there were remarkable differences. ADCP reacts stronger on coarser particles like sand and OBS is more sensitive for fine sediment particles. An ADCP is also very sensitive for air bubbles and turbulence

(through clustering of sediment particles), for which an OBS is less sensitive. Unfortunately, the zone near a TSHD can have strong turbulence, much air from air entrainment in the overflow, from the wake of the vessel, from the propellers and from degassing (VBKO 2003). Degassing is a process in which gas sucked up from organic material in the bed is removed from the pumps of the TSHD and released in the ambient water. Close to the TSHD ADCP data has to be used with care and generally OBS data is more reliable for SSC levels.

The downward looking ADCP was fitted on the survey vessel approximately 1.1 m below the water surface to prevent disturbing influence of surface waves. The first ADCP data point lies in a blanking zone and the first usable ADCP point was approximately 1.8-1.9 m below the free surface. Near the bed an ADCP also has a blanking distance, approximately 2 m in the 2007 campaign. In the 2011 campaign a second ADCP was mounted with one beam pointing straight down to eliminate the blanking distance for SSC at the bed, the blanking distance for the velocity and suspended sediment flux is still approximately 2 m in this set up.

## 8.3 Simulations

### 8.3.1 Simulation set up

Simulations are carried out on pie-slice-shaped grids of 4-21 million grid cells of the near field zone up to  $x \approx 375\text{m}$  like depicted in Figure 3.1. The equidistant vertical grid size is  $\Delta z = 0.1D$  and at the plume outflow the horizontal grid size is  $\Delta r = \Delta y = 0.1D$ . Further downstream  $\Delta r$  is expanded and due to the pie-slice-shaped grid also the effective lateral grid size  $\Delta y = r\Delta\phi$  expands further downstream of the dredging plume. At the overflow, 10 grid cells cover the diameter of the initial dredging plume, but further downstream the plume expands quickly and approximately 30-60 grid cells cover the width of the then bent over plume. The simulation area of a dredging plume is rather large, resulting in a rather coarse grid for LES, therefore the simulations are checked for two important requirements for LES: the percentage resolved kinetic energy and resolving part of the inertial sub-range. The percentage resolved turbulent kinetic energy on the grid in LES needs to be at least 80% to qualify as LES (Pope 2000). Following the approach of Wegner et al. (2004) to determine this percentage, it is 70% inside the plume for the momentum dominated cases with a very small  $Ri$  number and it is 90% for the buoyancy dominated cases with larger  $Ri$ . For all cases there is a very small zone near the outflow where the percentage drops to 40-70%. This means that the buoyancy dominated cases in this chapter are true LES according to Pope (2000) and in the momentum dominated cases, the resolved percentage turbulent kinetic energy is just too low. The energy density spectra of the velocity inside the plume of the buoyancy dominated cases and the momentum dominated cases show the correct  $-5/3$  slopes belonging to the inertial sub-range. Resolving part of the inertial sub-range is a LES requirement which is met for both the buoyancy dominated cases and the momentum dominated

cases.

### 8.3.2 Boundary conditions

The flow velocity near the TSHD hull is slightly different from the vector sum of the trailing speed and ambient velocity because the hull is an obstacle which influences the flow. There are lateral and vertical variations in the flow velocity past the hull. The simulation grid of a plume simulation starts approximately 15 overflow diameters in front of the overflow and the front end of the bow of the TSHD is missing to save valuable computational time. In order to generate the correct inflow velocity profiles (including the blocking effect) for the dredging plume simulations, an extra simulation with much larger domain is conducted, see Figure 8.1.

In this larger domain the full TSHD hull is captured and the time averaged flow profiles of this extra simulation are used as inflow boundary conditions for the dredging plume simulations. A schematised shape of a TSHD is used in the simulations without front bulb and a straight sloping aft. The drag-heads and suction pipes are included as obstacles because they can cause extra mixing of the overflow dredging plume. The propellers are implemented with a body force resulting in realistic propeller jet flow without rudder, see Section 5.4.3. The ambient velocity  $u_a, v_a$  is defined with respect to the moving TSHD.  $u_a$  is positive when sailing with the current and  $v_a$  is positive when coming from starboard. The influence of ambient turbulence is captured by adding turbulent fluctuations to the ambient velocity component of the inflow velocity according to the Synthetic Eddy Method (Jarrin et al. 2006). A hydraulic rough wall function is used to apply the bed shear stress at the bed boundary. The bed shear stress is based on the ambient velocity only, not on  $u_{TSHD}$ . The flow from the overflow is prescribed by a 1/7th power law velocity profile at the top of the domain and the vertical overflow shaft is incorporated in the simulation domain.

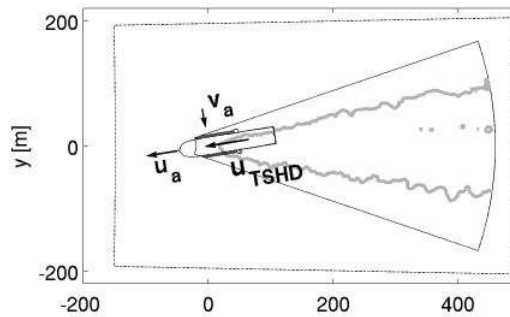


*Figure 8.1: The time averaged inflow boundary conditions around the TSHD hull at the pie-slice-shaped grid come from a second simulation on a larger grid indicated with dashed lines. The ambient velocity  $u_a, v_a$  is defined with respect to the moving TSHD.  $u_a$  is positive when sailing with the current and  $v_a$  is positive when coming from starboard.*

### 8.3.3 Simulated overflow mixture

The overflow discharge consists of a sand-mud-water mixture and sometimes air is entrained as well. When the mud concentration is large, like in the overflow mixture, flocculation is an important process. Strong flocculation has been found

for mud fractions inside an dredging overflow plume with floc diameters of 40 – 800 $\mu\text{m}$  and floc settling velocities of 0.1 – 6mm/s (Smith and Friedrichs 2011). In the simulations of this chapter flocculation is taken into account by choosing  $D_f = 5D_p$  for mud fractions. The settling velocity of flocs is determined by Equation 3.8. Air entrainment in the overflow can be modelled by including an air fraction in the overflow mixture. Air is simulated by a bubble diameter of 5 mm and an upward slip velocity of 0.25 m/s, these are realistic values for air bubbles in saline seawater (Chanson et al. 2002; Chanson et al. 2006).

## 8.4 Results

### 8.4.1 Introduction

*Table 8.1: Parameters of all cases*

case	$\gamma$	$Ri$	$\rho_{j0}$ [kg/m <sup>3</sup> ]	$w_{j0}$ [m/s]	$D$ [m]	$Q_{j0}$ [m <sup>3</sup> /s]	$S_{j0}$ [kg/s]	$\rho_{cf}$ [kg/m <sup>3</sup> ]	$u_a$ [m/s]	$v_a$ [m/s]	$u_{TSHD}$ [m/s]	depth [m]	draught [m]
1	0.33	22	1330	0.48	1.775	1.2	491	1030	-0.35	0	1.29	24.2	7.5
2	1.8	0.076	1050	2.11	1.775	5.22	171	1030	-0.31	0	0.85	25.1	7.5
3	2.7	3.9	1200	0.99	2.25	3.94	1135	1023	0	0	0.4	21.6	9.25
4	0.83	3.1	1300	1.38	2.25	5.49	2476	1023	-0.44	0.3	1.4	24	10.2
5	1.0	0.82	1100	1.58	2.25	6.28	942	1007	-0.7	0	0.9	16.5	12
6	4.0	0.01	1035.7	4.55	2	14.3	250.1	1025	0	0.8	0.8	10.5	8.2
7	2.7	0.03	1032.6	2.23	2	7.0	86.8	1025	0	-0.25	0.8	17.3	6

The measurement and simulation results of seven cases are presented. Table 8.1 summarises the most important parameters of all cases.  $Q_{j0}$  indicates the overflow mixture volume flux and  $S_{j0}$  indicates the overflow sediment flux. The cases have a wide range in  $0.33 < \gamma < 4$  and  $0.01 < Ri < 22$ . So there are cases with strong and weak crossflow and cases which are initially buoyancy or initially momentum dominated. Also the overflow sediment flux  $S_{j0}$  varies strongly with a factor 29 between the largest and smallest  $S_{j0}$ . The overflow composition of each case is given in Tables 8.2 and 8.3.

*Table 8.2: Overflow sediment composition of all cases*

case	dredged material	green valve	sediment mixture ( $D_p, D_f, w_s$ )	based on
1	mud	open	100 % mud (49 $\mu\text{m}$ ,245 $\mu\text{m}$ ,7 mm/s)	overflow sample
2	sand	open	100 % sand (114 $\mu\text{m}$ ,-,7.8 mm/s)	overflow sample
3	mud	open	100 % mud (32 $\mu\text{m}$ ,160 $\mu\text{m}$ ,3.3 mm/s)	assessment
4	mud and fine sand	closed	60% sand (130 $\mu\text{m}$ ,-,10 mm/s) 40% mud (32 $\mu\text{m}$ ,160 $\mu\text{m}$ ,3.3 mm/s)	hopper model (Spearman et al. 2011)
5	mud and fine sand	closed	43% sand (118 $\mu\text{m}$ ,-,8.6 mm/s) 57% mud (32 $\mu\text{m}$ ,160 $\mu\text{m}$ ,3.3 mm/s)	(Spearman et al. 2011)
6	pre-crushed rock	partly closed	50% sand (400 $\mu\text{m}$ ,-,60 mm/s) 50% mud (15 $\mu\text{m}$ ,80 $\mu\text{m}$ ,1 mm/s)	overflow sample
7	pre-crushed rock	partly closed	100% mud (15 $\mu\text{m}$ ,80 $\mu\text{m}$ ,1 mm/s)	overflow sample

All presented measurements and simulated results are instantaneous. This means that when a slice had been taken some seconds later or earlier already a

*Table 8.3: Overflow air/pulsing of all cases*

case	dredged material	green valve	air/pulsing	based on
1	mud	open	no air, no pulsing	assessment
2	sand	open	no air, no pulsing	assessment
3	mud	open	4% air, no pulsing	calibration (1m drop in overflow)
4	mud and fine sand	closed	no air, no pulsing	closed green valve
5	mud and fine sand	closed	7% air, no pulsing	calibration (2m drop in overflow)
6	pre-crushed rock	partly closed	1% air, no pulsing	overflow video recordings
7	pre-crushed rock	partly closed	10% air, no pulsing	overflow video recordings

different turbidity pattern would have been found. It will therefore be impossible to simulate the exact shape and location of the cauliflower shaped sediment puffs measured this close to the TSHD. In fact, it is even impossible to reproduce the exact measured shape and location of the sediment puffs in another measurement. Detailed comparison between simulations and measurements will therefore be done on more general characteristics as maximum SSC inside the plume, plume flux, plume width and vertical location of the maximum SSC inside the plume. Those characteristics also have an instantaneous character, but often they are a bit less instantaneous as the exact shape and location of individual sediment puffs. For each case the instantaneous slice is chosen from the simulation which resembles the measured slice as best. For cases where a cross slice has been measured through the plume the difference between different instantaneous slices is small, but for cases where a longitudinal slice has been measured through the edge of the plume the difference between different instantaneous slices can be large. The location of a measured slice in TSHD-fixed coordinates is corrected for the movement of the TSHD during the time it took to take the measured slice.

#### 8.4.2 Case 1 from 2002 campaign

Case 1 is the condition associated with a side scan sonar image from the 2002 campaign. The side scan sonar image shows the lower edge of the dredge plume, but the upper edge of the plume is missing. It can be used to show the fast descending behaviour of the plume towards the bed. Figure 8.2a shows the processed side scan sonar image and the simulated CFD result. The simulated lower edge of the plume from an instantaneous flow field compares well with the lower plume edge from the also instantaneous side scan sonar image. The x-distance of touch down of the dredge plume at the bed in the simulation  $x_{td} = 34$  m is equal to  $x_{td} = 34$  m in the side scan sonar image.

#### 8.4.3 Case 2 from 2002 campaign

Case 2 is a side scan sonar image from the 2002 campaign of the lower edge of the dredge plume under the keel of the TSHD. Figure 8.2b shows that the simulated lower edge of the plume is comparable with the lower plume edge from the side



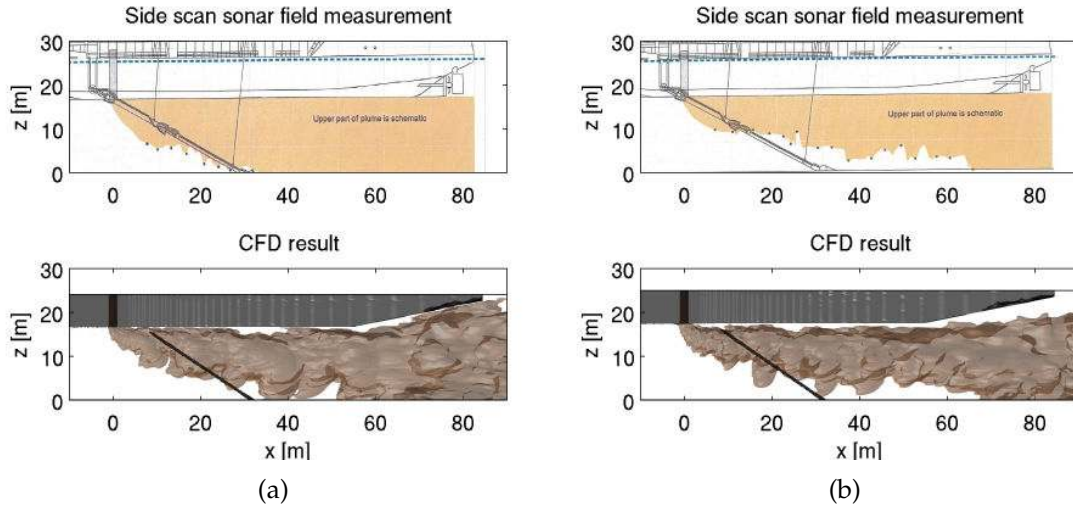


**Figure 8.2:** Processed side scan sonar image of overflow plume Case 1 2002 campaign (a) and Case 2 2002 campaign (b) under keel of TSHD (top) and simulated result (bottom). The upper part of the processed side scan sonar image is schematic.

scan sonar image. The simulated  $x$ -distance of touch down of the plume  $x_{td} = 66$  m is almost equal to  $x_{td} = 65$  m in the side scan sonar image (difference -1.5%).

#### 8.4.4 Case 3 from 2007 campaign

Case 3 consists of two measured cross slices through an overflow plume. Both slices are taken four minutes from each other at similar (earth fixed) coordinates. In this case there was no ambient current, therefore both slices show the time development of the same plume. First slice (Case 3a) is taken 180 m behind the overflow of the TSHD and second slice (Case 3b) is taken 276 m behind the overflow, see Figure 8.3c and Figure 8.4c. The difference of 96 m between both slices is four minutes movement of the TSHD at  $u_{TSHD} = 0.4$  m/s.

In Figures 8.3a and 8.4a the measured cross section through the plume at  $x = 180$  m and  $x = 276$  m is shown. From ADCP and OBS a background value  $SSC = 4$  mg/l is subtracted. At  $x = 180$  m the ADCP shows a plume of about 60 m wide with highest  $SSC = 100$  mg/l. There is a huge discrepancy between the ADCP and OBS measurement, because the OBS sensors have not detected any significant turbidity. At  $x = 276$  m both the ADCP and the OBS detect a plume. The maximum  $SSC$  detected by OBS is 30 mg/l and the maximum  $SSC$  detected by ADCP is 50 mg/l. The plume is about 50 m wide. The ADCP measurement at  $x = 180$  m seems to be realistic because it is consistent with the ADCP and OBS measurement at  $x = 276$  m. Although in general an OBS is more accurate than an ADCP for turbidity measurements, as an exception for this case we ignore the OBS measurement at  $x = 180$  m that has missed the plume and we use the ADCP measurement.

The simulated slices at  $x = 180$  m and  $x = 276$  m are shown in Figures 8.3b and 8.4b. Just as the measured plume, the simulated plume is wider at the free surface

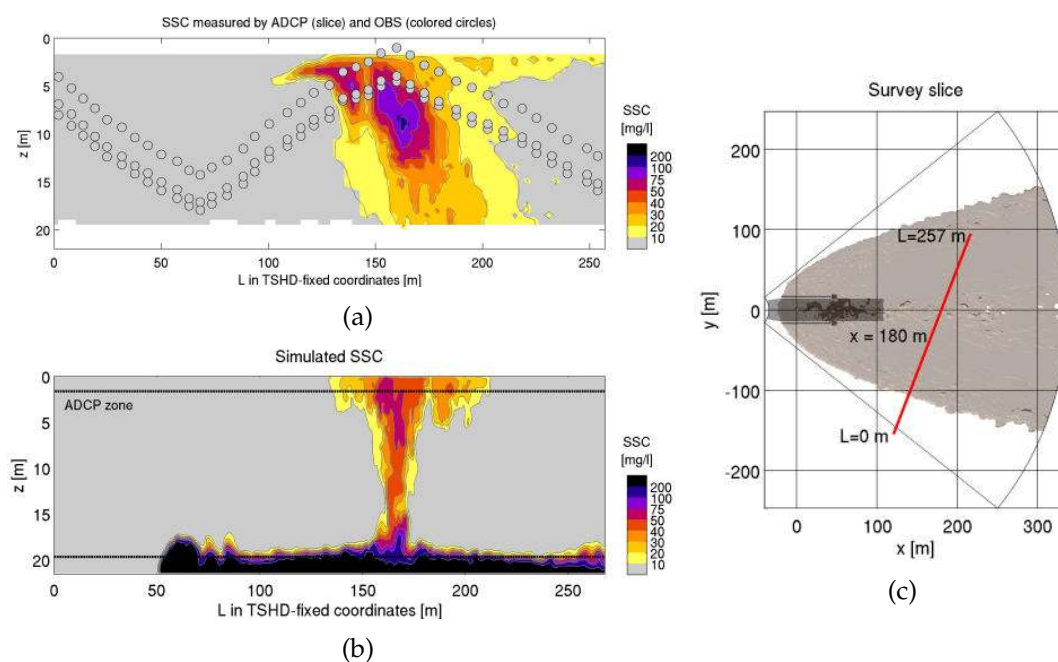


**Figure 8.3:** Cross slice Case 3a; measurement (a), simulation (b) and location of the slice with respect to the moving TSHD (c).

than halfway the water column. The simulated width halfway is only about 20-30 m, which is narrower than the measured width of 50-60 m. The simulated zones of maximum SSC are similar in vertical level and area as the measurements at  $x = 180$  m and  $x = 276$  m. At  $x = 180$  m the simulated maximum of SSC = 50 mg/l is half the ADCP maximum SSC = 100 mg/l. At  $x = 276$  m the simulated maximum of SSC = 50 mg/l equal to the ADCP maximum of SSC = 50 mg/l. At the vertical level of the OBS the simulated maximum of SSC = 40 mg/l is slightly higher than the OBS maximum SSC = 30 mg/l. A striking feature of the simulated plume is a zone with high SSC close to the bed. In this zone the majority of the plume can be found, but because of the blanking zone of the ADCP near the bed, it has missed it completely. Table 8.5 shows the measured and simulated fluxes. The measured ADCP fluxes for case3a and 3b are only 1.4 and 0.72% of the total overflow flux. The simulated fluxes for Case 3a and 3b in the ADCP zone are 1.6 and 1.1%; this is close to the measured fluxes.

#### 8.4.5 Case 4 from 2007 campaign

Figure 8.5 shows the plume cross slices of Case 4. A background value SSC = 4 mg/l is subtracted from the ADCP and OBS measured SSC values. The OBS location is shifted 20 m to correct for flaring of the OBS string; this leads to a very good agreement between the ADCP and OBS location of the plume. The ADCP data shows a plume of approximately 80 m wide extending all the way to the free surface. The SSC as measured by the ADCP is 2-20 mg/l. The OBS shows similar contours of the plume as the ADCP, but the SSC as measured by OBS is 10-50 mg/l inside the plume. In this case SSC measured by OBS is approx-

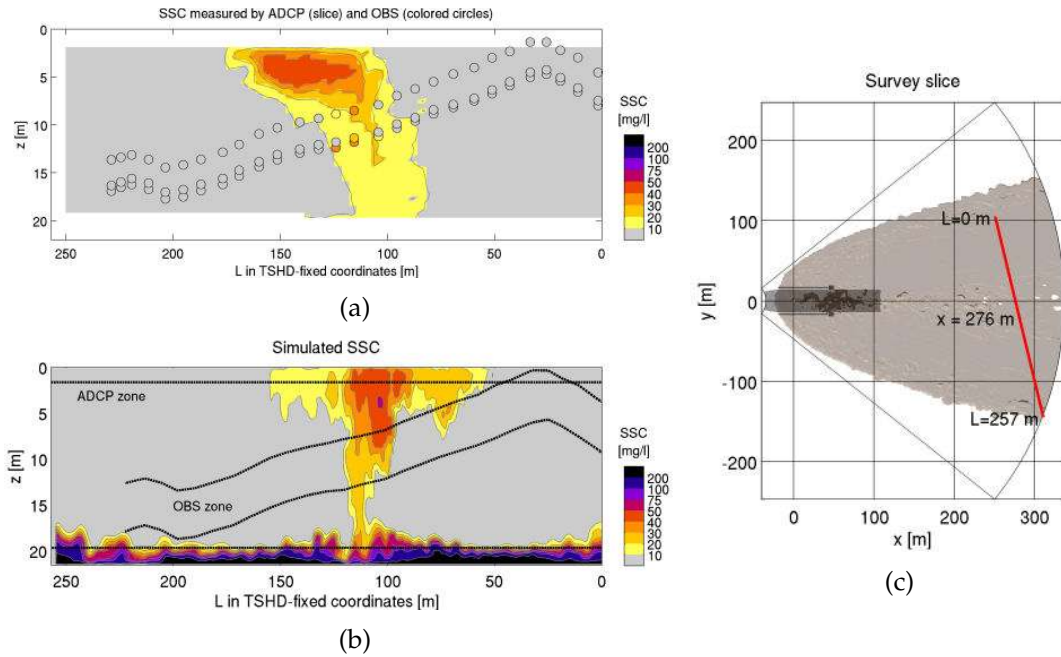


**Figure 8.4:** Cross slice Case 3b; measurement (a), simulation (b) and location of the slice with respect to the moving TSHD (c).

imately 5 times larger than SSC measured by ADCP at the same location. The reason for the large discrepancy between OBS and ADCP SSC is unknown; for instance there is no indication of air which could have corrupted the ADCP measurements. Because OBS is generally more accurate than ADCP in measuring turbidity, the OBS SSC values are used and the ADCP is used for plume edges and velocities.

The simulated plume is shown in Figure 8.5b. The shape of the simulated plume resembles the shape of the plume obtained by ADCP with a narrow zone of sediment all the way up to the free surface. In the simulation the width of this zone is 50m compared to 80m in the measurement. The simulated maximum  $SSC = 50$  mg/l in the OBS zone agrees with the OBS maximum  $SSC = 50$  mg/l. Because the ADCP SSC values differed so much from the OBS values, for this case a flux is determined from the three OBS sensors by  $\sum_1^3 (u_{\perp ADCP} + u_{\perp TSHD}) \cdot SSC_{OBS} \cdot \Delta z_{OBS} \cdot \Delta L_{OBS}$ , where  $(u_{\perp ADCP} + u_{\perp TSHD})$  is the ADCP velocity combined with TSHD speed perpendicular to the slice. The vertical distance  $\Delta z_{OBS} = 2$  m is chosen equal to the vertical distance between the three OBS sensors. Table 8.5 shows the measured and simulated fluxes. The measured flux in the OBS zone is 1.5% of the overflow flux and the simulated flux in this zone is 0.6%.

In the lower part of the plume there are huge discrepancies between the simulation and measurement. The ADCP measurement indicates a zone of more than 300m wide with low SSC up to 3-6 m above the blanking zone (5-8 m from bed). At  $L=250$  m the bed layer of suspended sediment detected by the ADCP is also found by the OBS with  $SSC = 30$  mg/l at 5-8m from the bed. The simulation shows a 175 m wide zone with  $SSC > 1000$  mg/l up to 8m from the bed (up

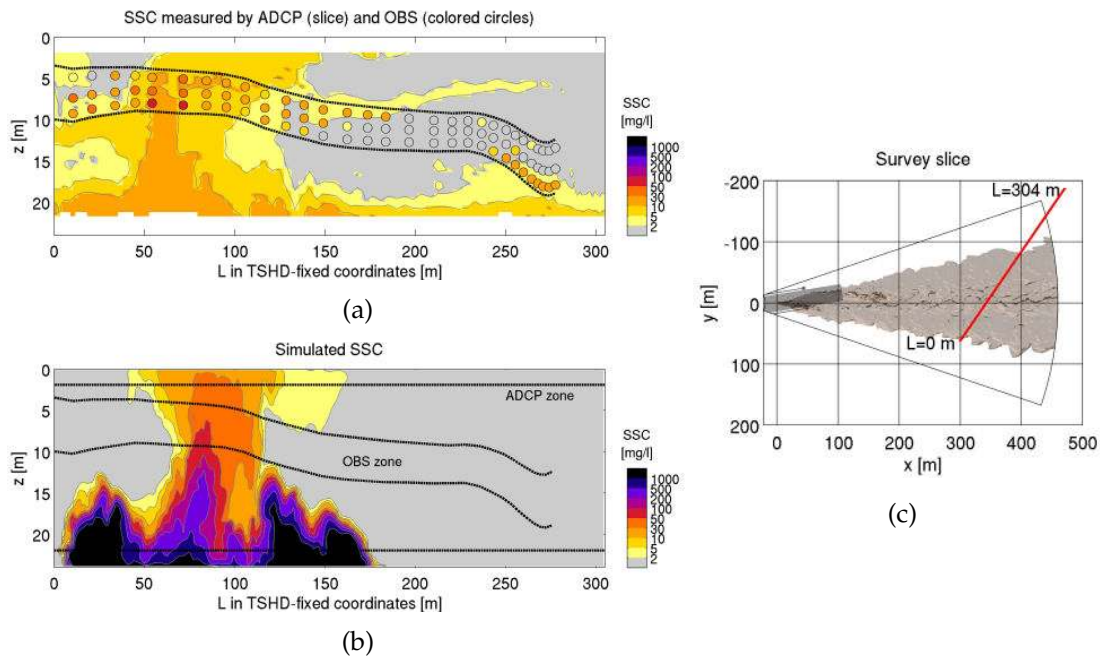


**Figure 8.5:** Cross slice Case 4; measurement (a), simulation (b) and location of the slice with respect to the moving TSHD (c).

to 6m above blanking zone ADCP). In Case 3a and 3b the simulation showed a thin density current near the seabed below the blanking zone of the ADCP, but in Case 4 the combination of ambient velocity and TSHD velocity is too large causing too much mixing for development of such thin layer in the simulation. The CFD model is validated for density currents at the bed (Brunner and Linden 1980; Hallworth et al. 1998; Boot 2000), therefore there is no obvious reason why the model would simulate the near bed density driven behaviour for Case 4 incorrectly. Case 4 is located in the Rotterdam harbour in the combined outflow of the Rhine-Meuse and took place at the start of flood. Hence, stratification is likely and a speculative explanation could be that this stratification has damped the up-mixing of the near bed sediment plume as simulated for an unstratified situation. Unfortunately, there were no conductivity measurements taken to verify the presence of stratification. Therefore, the end conclusion for Case 4 is that the simulated upper part of the plume agrees with the OBS measurements for both SSC and flux, but for unknown reasons the simulated bottom part of the plume differs strongly from the measurement.

#### 8.4.6 Case 5 from 2007 campaign

Case 5 consists of a measured cross slice through an overflow plume at  $x = 320$ m, see Figure 8.6. The ADCP data (velocity and turbidity) was influenced heavily by air from the overflow and gas bubbles from degassing from the TSHD. Therefore the ADCP data is not trustworthy and in Figure 8.6a only OBS data is shown. A background value  $SSC = 5$  mg/l is subtracted. The OBS detects a zone of very turbid water of about 60 m wide with  $SSC = 100 - 500$  mg/l. The ambient



velocity of  $u_a = -0.7$  m/s,  $v_a = 0$  m/s as used in the simulation comes from the ADCP data in this slice outside the plume where it is not corrupted by air/gas.

By accident, Case 5 is comparable to a case in literature by [Nichols et al. \(1990\)](#). The overflow discharge, overflow density, dredged material, combination of TSHD speed and ambient velocity and ambient depth are all comparable. The most obvious differences are the overflow pipe diameter and outflow direction. In Case 5 the overflow diameter is 2.25m and the outflow is vertical downwards, as in [Nichols et al. \(1990\)](#) the overflow is discharged horizontally from a pipe with diameter 0.67m. Therefore  $\gamma, Ri$  are different, but nevertheless it is interesting to note that  $SSC = 120 - 840$  mg/l measured at mid-depth at a distance of less than 300 m from the TSHD by [Nichols et al. \(1990\)](#) is the same order as  $SSC = 100 - 500$  mg/l measured at  $x = 320$ m in Case 5.

The simulated slice at  $x = 320$ m is shown in Figure 8.6b. The simulated plume is 50-70 m wide which agrees with the measured width. The maximum simulated  $SSC$  inside the OBS zone  $SSC = 500 - 600$  mg/l agrees with the maximum measured  $SSC = 400 - 600$  mg/l. A 10-20 m wide zone of  $SSC = 500 - 600$  mg/l extends all the way up to the free surface. These high  $SSC$  values inside the surface plume are caused by the air entrainment in the overflow and the rather small keel clearance of only 4.5 m: under the keel of the vessel the plume cannot spread gently over the bed but it stays in suspension up to the end of the TSHD where the upward motion of the flow around the TSHD hull and the propellers mix up the plume towards the free surface. The corrupt ADCP data was unusable to calculate a sediment flux, therefore the OBS data is used for this. The flux from the three OBS sensors is obtained by  $\Sigma_1^3 (u_{\perp TSHD} - u_{\perp a}) \cdot SSC_{OBS} \cdot \Delta z_{OBS} \cdot \Delta L_{OBS}$ . The vertical distance  $\Delta z_{OBS} = 2$ m is chosen equal to the vertical distance between the three OBS sensors. The measured flux in the OBS zone is 16% of the overflow flux and the simulated flux in the OBS zone is 14%, see Table 8.5.

#### 8.4.7 Case 6 from 2011 campaign

Case 6 consists of a measured slice along the path of the TSHD, see Figure 8.7. A background value  $SSC = 40$  mg/l is subtracted from OBS and ADCP; this large background value is caused by previous dredge plumes in this area. The overflow plume is mixed over the full water column with  $SSC = 100$  mg/l over the full depth. Largest  $SSC = 150 - 200$  mg/l can be found at the free surface. The ADCP and OBS turbidity measurements agree well. The measured plume is 170m wide.

The simulated slice is shown in Figure 8.7b. Also in the simulation the plume is mixed over the full water column with  $SSC = 100$  mg/l over the full depth. The maximum value of the simulation of  $SSC = 150$  mg/l is equal to the maximum  $SSC = 150$  mg/l detected by OBS and close to the maximum  $SSC = 200$  mg/l detected by ADCP. The simulated plume width is only 120 m which is 70% of the measured width. Table 8.5 shows the measured and simulated fluxes. The measured flux in the ADCP zone is 20% of the overflow flux and the simulated flux in the ADCP zone is 29%.

Case 6 is a challenging case because the TSHD is dredging in a very shallow

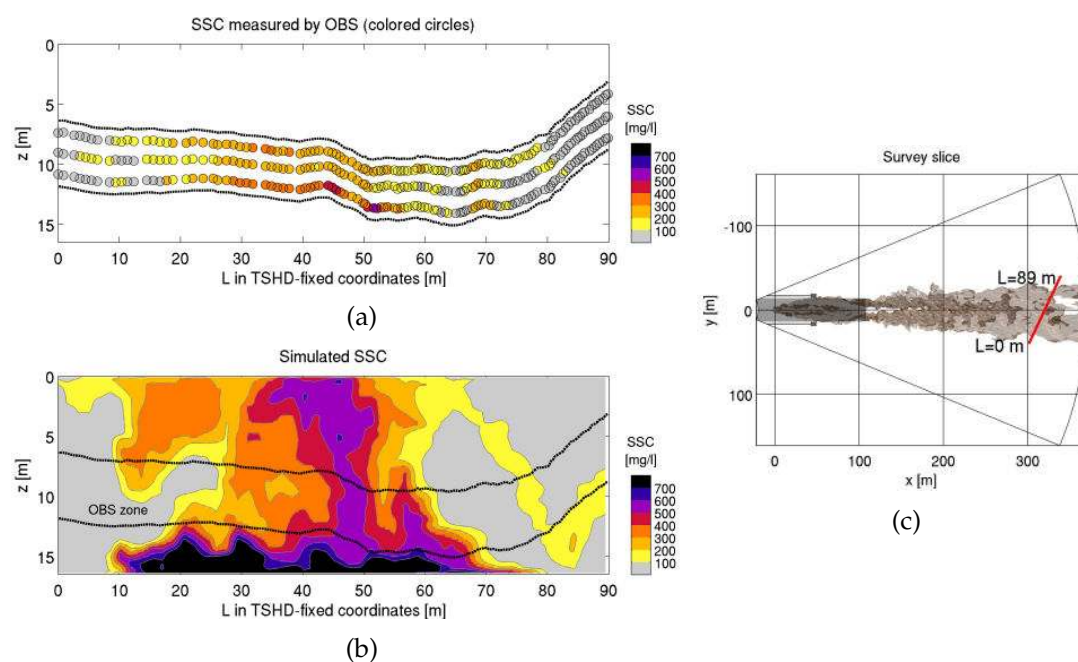


**Figure 8.6:** Cross slice Case 5; measurement (a), simulation (b) and location of the slice with respect to the moving TSHD (c).

area of 10.5 m deep with only 2.3 m keel clearance. The ambient current comes from starboard at an angle of  $90^\circ$ . The ambient current pushes the plume to the side of the TSHD which is sheltered by the 8.2m draught of the TSHD resulting in a very low velocity in this zone. In this sheltered zone the simulated plume behaves very transient: the full plume swings from flowing downstream in line with the TSHD to flowing perpendicular to the TSHD like visible in Figure 8.7c. The best simulated result in Figure 8.7b is found when the measured slice touches the edge of the plume. At other moments in the simulation there can be either a plume with much higher SSC and flux at the location of the measured slice than in the measurement or no plume at all. Although the plume is very transient, Figure 8.7 shows that the model can reproduce the correct measured plume  $x, y$  location, vertical distribution and SSC, albeit with a smaller plume width.

#### 8.4.8 Case 7 from 2011 campaign

Case 7 consists of a measured slice through the edge of the plume (a longitudinal section instead of a cross section) very close to the TSHD, see Figure 8.8. The slice is measured by overtaking the TSHD at a distance of only about 40 m from the side of the TSHD. A background value  $SSC = 40$  mg/l is subtracted from OBS and ADCP; this large background value is caused by previous dredge plumes in this area. This plume is a true surface plume with highest SSC at the free surface and lower SSC values or even zero SSC at the bed. The plume started at the keel 6 m below the free surface, but first it is pushed to the side by the ambient current flowing from  $90^\circ$  port side and then directly next to the TSHD hull air lifts the plume towards the free surface. The plume has separate surface blobs of



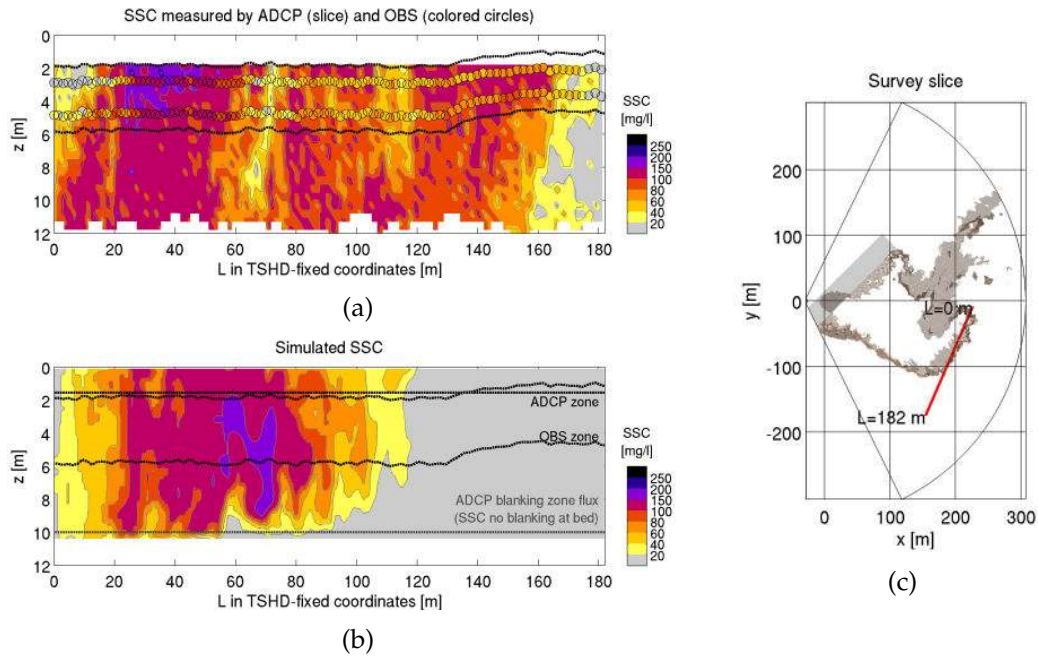


**Figure 8.7:** Cross slice Case 6; measurement (a), simulation (b) and location of the slice with respect to the moving TSHD (c).

sediment with zero SSC in between comparable to Rayleigh Taylor finger type of flow structures which are caused by the inverse density gradient (dense fluid on top of less dense fluid). The ADCP and OBS turbidity measurements agree well. The OBS finds maximum values of  $SSC = 100$  mg/l 8 to 10 m from the free surface. The ADCP shows values of  $SSC = 200 - 250$  mg/l at the upper blanking zone.

The simulated slice is shown in Figure 8.8a. Also the simulated plume shows surface blobs of sediment with clear water in between and below. The exact location of the simulated sediment blobs is different, but that is caused by the instantaneous character of both measured and simulated slices. The typical maximum SSC values simulated at the vertical level of the OBS is  $SSC = 100$  mg/l, which agrees with the OBS measurement. The ADCP measurement shows largest SSC values of  $SSC = 200 - 250$  mg/l at the upper blanking zone, but that is missing in the simulation where maximum values at the free surface are only  $SSC = 150$  mg/l. The simulation also has a maximum  $SSC = 200 - 250$  mg/l, but in the simulation this zone is halfway the water column. Table 8.5 shows the measured and simulated fluxes. The simulated flux in the ADCP zone is 7.1% which is almost exactly equal to the measured flux of 7.0%.

#### 8.4.9 Synthesis all 7 cases

The measured touchdown distances of the plume at the seabed of Case 1 and 2 of  $x_{td} = 34$  m, respectively  $x_{td} = 67$  m are simulated within  $\pm 1.5\%$  by the CFD model. The maximum SSC inside the plume and the flux are used to compare the measurements and simulations for Case 3-7 in Tables 8.4-8.5. The presented

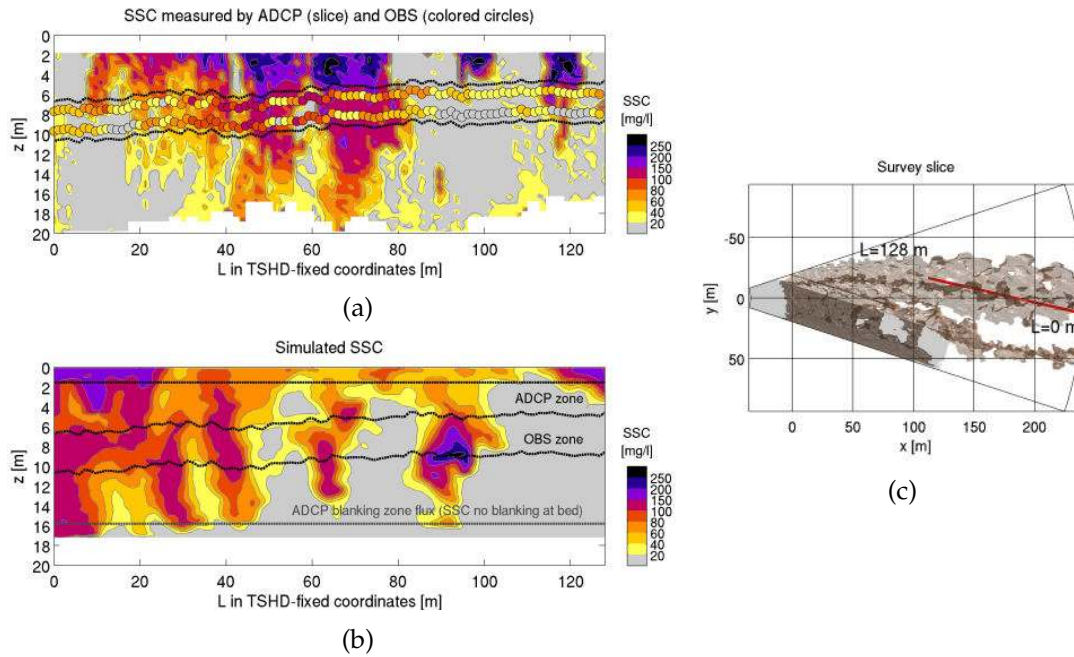


**Figure 8.8:** Cross slice Case 7; measurement (a), simulation (b) and location of the slice with respect to the moving TSHD (c).

plume distance is taken as the location where the slice crosses the  $y = 0$  line and the plume age is the plume distance divided by the effective plume velocity in downstream direction  $u_{cf} = \sqrt{(u_{TSHD} - u_a)^2 + v_a^2}$ .

In Table 8.4 the peak OBS SSC value inside the plumes are compared with the peak simulated SSC value in the OBS zone indicated in the simulation result figures. The OBS measured SSC value is used because in general an OBS is more accurate than an ADCP in measuring turbidity. Only for Case 3b ADCP data is used, as the OBS did not detect a plume at all. The measured peak SSC value varied considerably between 34 and 519 mg/l and the CFD model is able to reproduce the correct SSC value within +/-50% of the measured SSC value, with an exception for case 7 where one sediment puff with  $SSC = 267$  mg/l in the OBS zone leads to a large error of +130% compared to the measured peak SSC (without this puff the peak SSC is 129 mg/l, an error of only +11%).

Measured and simulated fluxes are shown in Table 8.5. Measured fluxes are obtained from the SSC and velocity measured by the ADCP with corrections for  $u_{TSHD}$ , angle of the slice with respect to the TSHD and the movement of the TSHD during the time an ADCP slice was measured. The measured fluxes of Case 4 and 5 are obtained from OBS measurements because the ADCP signal cannot be trusted to determine a flux. All plume fluxes are related to the total sediment flux flowing through the overflow. The measured fluxes vary greatly between 0.7 and 20% of the overflow flux for these 6 plumes. The CFD model is able to reproduce this large variation by simulating the fluxes within +/-60% of the measured flux. The large difference between the simulated flux in the full slice and in the ADCP zone indicates how inaccurate it can be to use ADCP in measuring plume fluxes this close to a TSHD because a substantial part of the

**Table 8.4:** Comparison simulated and measured typical peak SSC inside overflow plume. <sup>A</sup>SSC measured by ADCP instead of OBS.

case	Distance plume [m]	Age plume [min]	Measured SSC [mg/l]	Simulated SSC [mg/l]	Difference
3a	180	7.5	111 <sup>A</sup>	59	-47%
3b	276	11.5	34	47	+38%
4	342	3.9	57	69	+21%
5	320	3.3	519	640	+23%
6	230	3.4	159	173	+9%
7	183	3.6	116	267	+130%

plume can be found in the blanking zones of the ADCP. Fortunately the majority of missed plume flux is in the ADCP blanking zone close to the bed and this plume material will deposit quickly. A note by Case 4 is that the results presented in Tables 8.4-8.5 consider the flux and SSC measured by OBS at the top half of the water column and there the simulation agrees well with the measurement, but for unknown reasons the simulated bottom part of the plume differs strongly from the measurement.

Please note that the presented fluxes in this study are too close to the dredger to be used as a proper far field source flux of suspended sediment. The density differences and vertical distribution of the plume with typically a large part of the plume close to the bed which will deposit quickly, cannot be handled in a far field model without simplification and schematisation. For a far field source flux of suspended sediments the plume characteristics at a larger distance of the TSHD must be used, Chapter 9 elaborates more on this.

Part of the differences between simulations and measurements come from schematisation and simulation inaccuracies. Another part can be explained by the instantaneous character of both simulated and measured results and lacking information like the exact 3D flow field round the TSHD at the moment of measuring, the exact instantaneous overflow fluxes which now are being estimated as equal to the measured suction discharge and the exact composition of the sand-mud-water-air mixture flowing through the overflow. This exact information is very hard or even impossible to measure accurately in a field campaign. However, perhaps the biggest uncertainty comes from the measurement inaccuracies of plume SSC levels and fluxes this close to a TSHD because of air bubbles, turbulence and the influence of the unknown exact sediment particle size on the measured SSC levels. Given these notes, altogether the CFD model can reproduce the measured near field mixing behaviour of overflow dredging plumes in a satisfactory way.

## 8.5 Conclusions

A 3D CFD model is used to simulate near field mixing of an overflow dredging plume within 400 m from the TSHD. The simulations are compared with new field measurements of the plume under the keel of and close to the TSHD. It is the first time full scale near field simulations of overflow dredging plumes are

**Table 8.5:** Comparison simulated and measured overflow plume fluxes as percentage of total overflow flux. <sup>A</sup>Measured flux not from ADCP, but from OBS with ADCP velocity corrected for TSHD velocity; simulated flux in OBS zone. <sup>B</sup>Measured flux not from ADCP, but from OBS with velocity ( $u_{TSHD} - u_a$ ); simulated flux in OBS zone.

case	Distance plume [m]	Age plume [min]	Simulated flux full slice	Simulated flux ADCP zone	Measured flux ADCP	Difference
3a	180	7.5	17%	1.6%	1.4%	+14%
3b	276	11.5	5.5%	1.1%	0.72%	+53%
4	342	3.9	56%	0.6% <sup>A</sup>	1.5% <sup>A</sup>	-60%
5	320	3.3	58%	14% <sup>B</sup>	16% <sup>B</sup>	-13%
6	230	3.4	33%	29%	20%	+45%
7	183	3.6	9.3%	7.1%	7.0%	+1%

compared in such detail to field measurements this close to a TSHD.

The LES technique is used to capture the highly turbulent and unsteady plume behaviour. The CFD model uses a variable density to capture the general buoyant JICF behaviour of the overflow plume under the keel of the TSHD. Other essential near field processes as interaction of the plume with TSHD hull/aft, interaction with propellers, air entrainment and pulsing are implemented as well in the CFD model.

Seven different dredging cases with a large variety in overflow flux and buoyant JICF characteristics  $\gamma$ ,  $Ri$  are used to compare simulations with field measurements. The CFD model simulates the correct touchdown distance of the plume. The measured maximum SSC levels inside these plumes vary between 30-400 mg/l. The measured plume fluxes vary between 0.7 and 20% of the overflow flux. Simulated fluxes (in the measurement zone) and SSC levels for all these very different cases have the correct order of magnitude compared with the measurements. The simulations reveal that this close to a TSHD a substantial part of the plume can be found in the blanking zones of an ADCP, therefore measuring the plume flux with ADCP can underestimate the plume flux substantially. Please note that the fluxes presented in this study are too close to the dredger to be used as a proper far field source flux of suspended sediment. Remaining differences between simulation and measurement can at least partly be explained by the instantaneous character of the measured slices, and unknown information as the exact 3D flow field round the TSHD during the measurement and the exact flux/composition of the sand-mud-water-air mixture inside the overflow. There is also a large uncertainty involved in measuring plume SSC levels and fluxes this close to a TSHD because of air bubbles, turbulence and the influence of sediment particle size on the measurements.

The CFD model has, subject to the limitations of the field data, been shown to reproduce the field measurements of very different overflow dredging plumes in a satisfactory way; this provides evidence that the most important near field processes are incorporated adequately. The near field model gives better understanding of the plume mixing close to the dredger which helps to assess the frequency, duration and intensity of stresses like turbidity and sedimentation needed to find the environmental impact of dredging projects.

## Chapter 9

# Influence of near field processes on a dredging plume - field scale

*After the comparison between field measurements and CFD results for specific cases in previous chapter, now a parameter study is carried out with systematic variation in important near field conditions which influence the mixing and deposition behaviour of a dredging plume. The results are translated into mathematical relations to quantify the sediment plume characteristics without computational effort and practical guidelines are provided to assess a proper far field source flux from a TSHD while dredging in case measurements are lacking.*<sup>1</sup>

### 9.1 Introduction

CFD simulations of 30 minutes TSHD overflow dredging plume mixing and deposition are conducted to determine the suspended sediment source flux from the dredging plume for 136 near field conditions. First near field simulations determine the sediment flux 350 m downstream of the overflow, then these results are plugged into a mid field model covering an area up to 5.4 km downstream of the overflow, which corresponds to 30 minutes plume development for the largest crossflow velocity included in the 136 runs. In the near field, plume mixing is dominated by density differences and interaction with the vessel. In the mid field density differences of the plume (up to  $\Delta\rho = 3 \text{ kg/m}^3$ ) still have influence, but there is no interaction with the vessel.

---

<sup>1</sup>A modified version of this chapter has been published as: L. de Wit, A.M. Talmon and C. van Rhee (2014), 3D CFD simulations of trailing suction hopper dredger plume mixing: a parameter study of near field conditions influencing the suspended sediment source flux, *Marine Pollution Bulletin*. DOI:[10.1016/j.marpolbul.2014.08.043](https://doi.org/10.1016/j.marpolbul.2014.08.043)



## 9.2 Simulations

### 9.2.1 Near field set up

The near field simulations are carried out on pie-slice-shaped grids of 6-25 million grid cells of a zone up to  $x \approx 375\text{m}$  like depicted in Figure 9.2. The equidistant vertical grid size is  $\Delta z = 0.1D$  and at the plume outflow the horizontal grid size is  $\Delta r = \Delta y = 0.1D$ . Further downstream  $\Delta r$  is expanded and due to the pie-slice-shaped grid also the effective lateral grid size  $\Delta y = r\Delta\phi$  expands further downstream of the dredging plume. At the overflow, 10 grid cells cover the diameter of the initial dredging plume, but further downstream the plume expands quickly and approximately 30-60 grid cells cover the width of the then bent over plume.

The simulation area of the near field zone is rather large for LES, resulting in a rather coarse grid for LES, but nevertheless the simulations meet two important requirements for LES: a sufficient percentage resolved kinetic energy and resolving part of the inertial sub-range. The percentage resolved turbulent kinetic energy on the grid in LES needs to be at least 80% (Pope 2000). Following the approach of Wegner et al. (2004) to determine this percentage, it is 80% inside the plume. For all cases there is a very small zone near the outflow where the percentage drops to 70%. The energy density spectrum of the velocity inside the plume in Figure 9.1 shows the correct  $-5/3$  slope which shows that part of the inertial sub-range is resolved on the computational grid. A grid refinement test simulation is presented in Section 9.4.4.

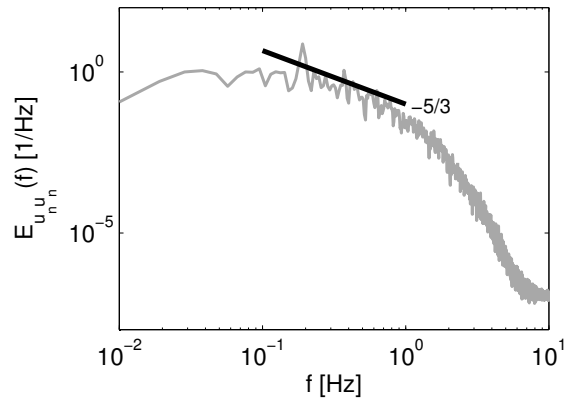


*Figure 9.1: Energy density spectrum of the normalised stream wise velocity  $u_n = u / \bar{u}$  from time series at  $x/D = 12$  inside the dredging plume. The black line is only given as an indication of the  $-5/3$  slope, not as a correct level of turbulent kinetic energy or length of the inertial sub range.*

### 9.2.2 Near field boundary conditions

Near the TSHD hull there are lateral and vertical variations in the flow velocity which make the velocity slightly different from the vector sum of the trailing speed and ambient velocity, because the hull acts as an obstacle which influences the flow. In the simulation grid of a plume simulation the front end of the bow of the TSHD is missing to save valuable computational time. In order to generate the correct inflow velocity profiles (including the blocking effect) for the dredging plume simulations, an extra simulation with much larger domain is conducted, see Figure 9.2. In this larger domain the full TSHD hull is captured



and the time averaged flow profiles of this extra simulation are used as inflow boundary conditions for the dredging plume simulations.

A schematised shape of a TSHD is used without front bulb and a straight sloping aft. The drag-heads (schematised as a rectangular shape of 5.4x1.8x1.8 m) and suction pipes of 1.8m outer-diameter are included as obstacles because they can induce extra mixing of the overflow dredging plume. The propellers are implemented with a body force resulting in realistic propeller jet flow without rudder, see Section 5.4.3. The ambient velocity  $u_a, v_a$  is defined with respect to the TSHD.  $u_a$  is positive when sailing with the current and  $v_a$  is positive when coming from starboard. The Synthetic Eddy Method of Jarrin et al. (2006) is used to add turbulent fluctuations to the ambient inflow velocity to capture the influence of ambient turbulence. The bed shear stress at the bed is determined by a hydraulic rough wall function with a Nikuradse roughness of 0.1 m based on the ambient velocity only, not on  $u_{TSHD}$ . The influx from the overflow is prescribed at the top of the domain by a 1/7th power law velocity profile and the vertical overflow shaft is incorporated in the simulation domain.

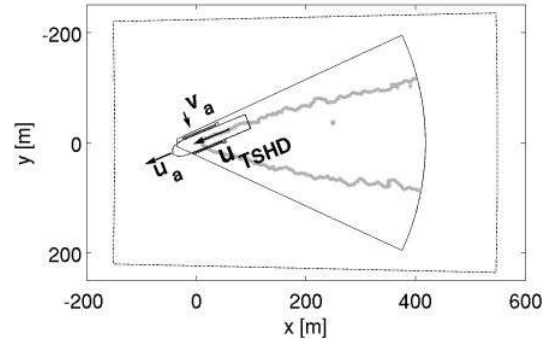


**Figure 9.2:** The time averaged inflow boundary conditions around the TSHD hull at the pie-slice-shaped grid come from a second simulation on a larger grid indicated with dashed lines. The ambient velocity  $u_a, v_a$  is defined with respect to the moving TSHD.  $u_a$  is positive when sailing with the current and  $v_a$  is positive when coming from starboard.

### 9.2.3 Mid field set up

The mid field flow solver is identical to the near field solver and includes variable density. However, in the mid field model a Cartesian orthogonal grid is used, a fifth order upwind scheme is used for the advection of momentum, see Section 4.2.2 and a RANS type mixing length turbulence model is used instead of the LES type WALE sub-grid model. The mixing length is based on the Bakhmetev profile. Turbulence damping by the sediment induced density gradients are taken into account by damping functions with coefficients determined in the COSINUS project (Berlamont and Toorman 2000; Violeau et al. 2002):

$$Ft = (1 + 100Ri_g)^{-1/3} \text{ for } Ri_g > 0, Ft = 1 \text{ for } Ri_g \leq 0, \quad (9.1)$$

$$Fs = Ft(1 + 21Ri_g)^{-0.8} \text{ for } Ri_g > 0, Fs = 1 \text{ for } Ri_g \leq 0, \quad (9.2)$$

with  $Ri_g = \frac{-g/\rho\partial\rho/\partial z}{(\partial u/\partial z)^2 + (\partial v/\partial z)^2}$ .  $Ft$  is used to restrict the eddy viscosity and  $Fs$  is used to restrict the diffusion coefficient.

The mid field model extends up to 5.85 km downstream from the TSHD overflow, which is sufficient to cover up to 30 minutes of plume development for all

cases. The mid field model assumes uniform depth and covers a rectangular domain of 5.5 km long and 840m wide, starting at the end of near field at  $x = 350$  m downstream of the overflow. The grid size is  $\Delta x = 50\text{m}$ ,  $\Delta y = 5\text{m}$ ,  $\Delta z = 0.5\text{m}$ . The simulation time of the mid field model is 1.5 times the flow through time.

The inflow boundary conditions of the mid field model are the time averaged velocity and sediment concentration conditions at the end of near field at  $x = 350\text{m}$  downstream from the overflow. The lateral size of the mid field model is larger than the lateral size of the near field model and outside the near field model a  $SSC = 0$  and extrapolated velocity profile is used as inflow boundary for the mid field model. The Nikuradse bed roughness is 0.1 m.

### 9.3 Conditions parameter study

To investigate the influence of near field mixing on the far field source flux of a TSHD overflow plume in a systematic manner, 136 runs are composed with different near field conditions. Realistic input is chosen for overflow density, air entrainment, pulsing, ambient velocity/dredging speed, angle between ambient and dredging velocity and ambient depth. The first 128 different runs cover a selection in conditions. This selection is aimed at obtaining a maximum surface plume in order to learn how the largest far field source fluxes are generated. Therefore, the 128 runs are biased, but they cover all possible combinations of the selected input conditions. The remaining input conditions are used in eight additional runs which do not cover all possible combinations, but they are not biased towards a maximum surface plume. In total there are 136 unique combinations of input.

#### 9.3.1 Overflow density and particle sizes

The measured sediment-water mixture densities in the overflow presented in [Nichols et al. \(1990\)](#) vary between  $\rho_{j0} = 1047 - 1177 \text{ kg/m}^3$ ,  $\rho_{j0} = 1060 - 1160 \text{ kg/m}^3$  in [Whiteside et al. \(1995\)](#) and  $\rho_{j0} = 1033 - 1330 \text{ kg/m}^3$  in Chapter 8. The time development of measured sediment-water mixture densities inside the overflow in [Spearman et al. \(2011\)](#) show a steadily growing overflow mixture density: at the start of overflowing the overflow mixture contains almost no sediment (clear water mixture density) and at the end of overflowing the largest sediment concentrations are found with mixture densities between  $\rho_{j0} = 1210 \text{ kg/m}^3$  and  $\rho_{j0} = 1340 \text{ kg/m}^3$ . At the start of overflowing mainly fine sediment fractions flow through the overflow because they settle slowest inside the hopper, but at the end of overflowing also coarser fractions flow through the overflow. For the simulations in this study, three schematised overflow mixtures are composed containing very large percentages of fines:

- Begin phase overflow:  $\rho_{j0} = 1100\text{kg/m}^3$ , 100% fines
- Middle phase overflow:  $\rho_{j0} = 1200\text{kg/m}^3$ , 75% fines + 25% sand
- End phase overflow:  $\rho_{j0} = 1300\text{kg/m}^3$ , 50% fines + 50% sand (not in 128 runs)

Although these three schematised overflow sediment-water mixture compositions cover quite a range of possible compositions, obviously the overflow mixture can be different for a specific dredging project. The overflow mixture depends on the dredged material, the working method of the TSHD and hopper characteristics as vertical level of the overflow edge and the horizontal distance between the production pipe in the hopper and the overflow shaft. There exist some practical limits in possible overflow compositions. The large percentages of fines in the overflow used in this study, can only exist when the dredged source material contains large amounts of fines as well. The combination of mixture density and percentage fines must always be smaller than the percentage fines in the dredged material multiplied with the production rate of the TSHD, because part of the fines from the dredged material will be buried inside the hopper. And it is unlikely for the overflow mixture density to be larger than the suction mixture density for long periods, otherwise the TSHD would not fill with sediment.

Only the begin and middle phase of overflow are incorporated into the 128 runs, because the end phase overflow density is larger and generates less surface plume. The fine fraction is simulated as mud with particle size  $D_p = 32\mu\text{m}$ , with a floc size  $D_f = 160\mu\text{m}$  and floc settling velocity  $w_s = 3.5\text{mm/s}$  which corresponds to the strong flocculation and settling velocities found for mud in a dredging overflow plume (Smith and Friedrichs 2011). The sand fraction is simulated as  $D_p = 220\mu\text{m}$ , with  $w_s = 22.6\text{mm/s}$ . Mud can deposit on the sea bed and erode, but sand can only deposit and erosion of sand is neglected.

### 9.3.2 Overflow pulsing and air entrainment

Three different options for pulsing are used in the runs of this chapter: no pulsing,  $T_p = 5.5\text{s}$  and  $T_p = 11\text{s}$ .  $T_p = 5.5\text{s}$  has been measured in a near-empty jumbo-TSHD and was equal to the ambient wave period,  $T_p = 11\text{s}$  is the typical rolling period of a loaded jumbo-TSHD (Hannot 2014). Three different amounts of air entrainment in the overflow are used: 0%, 4% and 12% air. 4% air entrainment is a realistic expected amount according to the assessment in Section 2.4 and 12% air entrainment is a large amount. Air is simulated by a bubble diameter of 5 mm and an upward slip velocity of 0.25 m/s, these are realistic values for air bubbles in saline seawater (Chanson et al. 2002; Chanson et al. 2006). Four combinations of pulsing and air are selected from the nine possible combinations:

- 0% air, no pulsing
- 4% air,  $T_p = 5.5\text{s}$
- 4% air,  $T_p = 11\text{s}$
- 12% air,  $T_p = 5.5\text{s}$ .

Because pulsing and air entrainment are only likely with a open green valve and a low water level in the overflow shaft, they are combined with each other. The influence of the pulsing period  $T_p = 5.5\text{s}$  or  $T_p = 11\text{s}$  is investigated for 4% air only.

### 9.3.3 Ambient velocity and sailing speed

Typical dredging sailing speeds are 0.5-1.5 m/s with typical ambient velocities in the range of 0-1.5 m/s. Combining this and omitting negative  $u_{cf}$  values because then the TSHD is not manoeuvrable, leads to a possible range of  $u_{cf} = 0$  m/s to  $u_{cf} = +3$  m/s depending on whether dredging takes place with or against the ambient current. The seven cases in Chapter 8 have  $u_{cf} = +0.4$  m/s to  $u_{cf} = +1.9$  m/s. In this study, four combinations of dredging speed and ambient current are considered:

- $|U_a| = 0$  m/s,  $u_{TSHD} = 0.5$  m/s ( $u_{cf} = 0.5$  m/s for  $\Psi = 0^\circ$ ) (not in 128 runs)
- $|U_a| = u_{TSHD} = 0.5$  m/s ( $u_{cf} = 1$  m/s for  $\Psi = 0^\circ$ ) (not in 128 runs)
- $|U_a| = u_{TSHD} = 0.75$  m/s ( $u_{cf} = 1.5$  m/s for  $\Psi = 0^\circ$ )
- $|U_a| = u_{TSHD} = 1.5$  m/s ( $u_{cf} = 3$  m/s for  $\Psi = 0^\circ$ ).

First two options with the lowest dredging and ambient velocity are omitted from the 128 runs because the lower  $u_{cf}$ , the smaller the surface plume and the smaller the far field source flux. First option consists of dredging in an ambient water without current, which can happen when dredging during slack tide or inside a sheltered area. The lack of ambient current prevents transport of a dredging plume towards environmental sensitive areas somewhere away from the dredging location, therefore this situation seems to be less important for the determination of a far field source flux. It is however included in the twelve unbiased simulations because it gives valuable extra information on the time development of a dredging plume at low  $u_{cf}$  and it is possible that dredging takes place at slack water. Dredging takes place against the ambient current with two possible angles of the ambient velocity:

- $\Psi = 0^\circ$
- $\Psi = 22.5^\circ$ .

First option of  $\Psi = 0^\circ$  corresponds to dredging in line with the ambient current and second option corresponds to dredging with the ambient current  $|U_a|$  coming from  $45^\circ$  starboard ( $v_a = |U_a| \sin(45^\circ)$  and  $u_a = -|U_a| \cos(45^\circ)$ ) with an effective angle  $\Psi = 22.5^\circ$ . The effective angle  $\Psi$  is the angle between the effective crossflow velocity  $u_{cf} = \sqrt{v_a^2 + (u_{TSHD} - u_a)^2}$  and the ship sailing direction:  $\Psi = \text{atan}(v_a / (u_{TSHD} - u_a))$ .

### 9.3.4 Dredging depth

Four different dredging depths are considered:

- depth=12 m
- depth=17 m
- depth=25 m
- depth=35 m.

### 9.3.5 Combinations of input

Two overflow densities, four air/pulsing combinations, two ambient/dredging velocities, two angles between ambient and dredging velocity and four depths

combined gives  $2 \times 4 \times 2 \times 2 \times 4 = 128$  combinations of input. The end phase of overflow ( $\rho_{j0} = 1300 \text{ kg/m}^3$ ) and two  $u_{cf}$  options ( $u_{cf} = 0.5 \text{ m/s}$  and  $u_{cf} = 1 \text{ m/s}$ ) are not used in the 128 runs. They are used in twelve extra input combinations without bias towards large surface plumes with three different overflow densities and four different ambient/dredging velocities combined with 0% air, no pulsing,  $\Psi = 0^\circ$ , depth=25 m. Four of these twelve combinations are already incorporated in the 128 runs and the additional eight runs are simulated separately. In total there are 136 unique combinations of input. The total computational effort of these 136 CFD runs counted up to 7000 hours on 8-core computers, mostly performed on the SARA LISA supercomputer facilities<sup>2</sup>.

All 136 simulations are conducted with a schematised jumbo-TSHD of  $150 \times 28 \text{ m}$  with a draught of 8m and 2 propellers. The overflow diameter is  $D = 2.25 \text{ m}$ , the overflow volume flux is  $7 \text{ m}^3/\text{s}$  ( $w_{j0} = 1.77 \text{ m/s}$ ) for all runs. Each simulation has a start up time sufficient to flush the near field domain 1.5 times, then the results are time averaged for 3 minutes which is more than  $80D/u_{cf}$  or more than  $140D/w_{j0}$ .

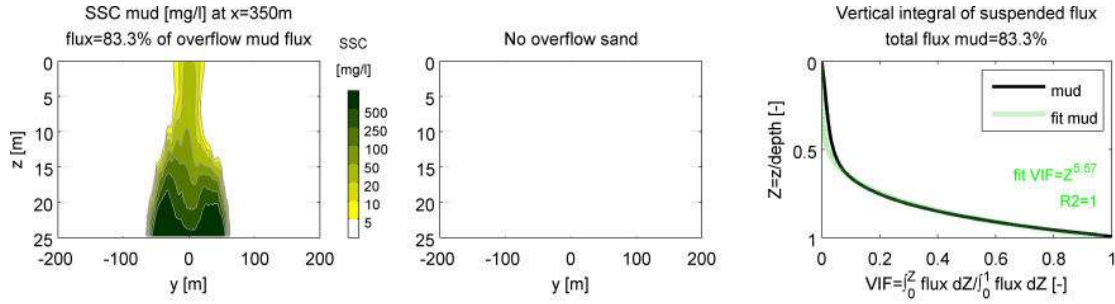
## 9.4 Results

### 9.4.1 Example individual results near field plume

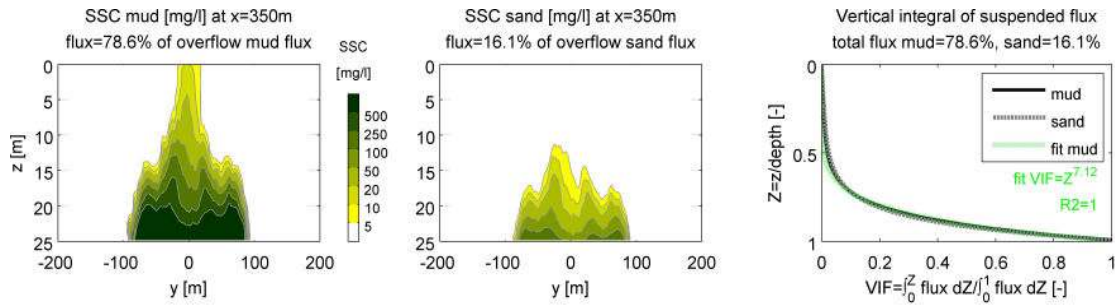
In this section some individual results are discussed to illustrate the characteristic influence of the different near field conditions in the 128 runs. Figures 9.3-9.4 show six results at the end of near field at  $x = 350 \text{ m}$ . The SSC of the mud fraction and of the sand fraction are shown separately; they have to be added to get the total SSC. For the simulations in Figures 9.3 and 9.4 with depth=25m, the majority of the plume can be found in a 65-175m wide zone near the bed with the  $\text{SSC} = 500 \text{ mg/l}$  contour approximately 5m from the bed. The 25m depth simulations with  $u_{cf} = 1.5 \text{ m/s}$  typically show a narrow surface plume of about 50m wide and  $\text{SSC} = 10 - 20 \text{ mg/l}$ , also without air entrainment and without pulsing. The vertical distributions of the plume flux still in suspension, in the third panels of Figures 9.3 and 9.4, reveal that for runs without air entrainment and large depth there is only a very small percentage of the plume flux in the surface plume. Typically 75% of the fines (mud) flux still in suspension can be found in the bottom 20% of the water column and less than 5% can be found in the top half of the water column for situations with large depth and without air entrainment. At  $x = 350 \text{ m}$  about 25% of the flux of fines through the overflow has deposited for runs with  $u_{cf} = 1.5 \text{ m/s}$ , depth=25m and about 75% is still in suspension. More air entrainment, a larger  $u_{cf}$  and a smaller depth lead to a larger surface plume with larger SSC and more flux in suspension in the higher parts of the water column. An increase in  $\rho_{j0}$  from  $\rho_{j0} = 1100 \text{ kg/m}^3$  to  $\rho_{j0} = 1200 \text{ kg/m}^3$  leads to a wider bed plume due to the increased driving force of the

<sup>2</sup>This work was sponsored by NWO Exacte Wetenschappen (Physical Sciences) for the use of supercomputer facilities, with financial support from the Nederlandse organisatie voor Wetenschappelijk Onderzoek (Netherlands Organization for Scientific Research, NWO).

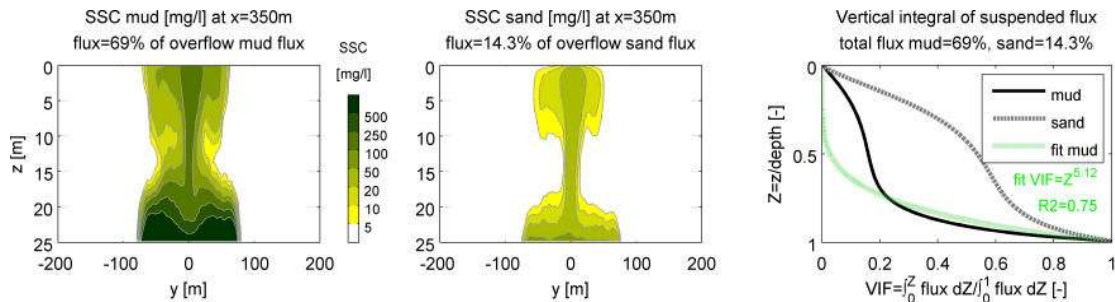




(a)  $\rho_{j0} = 1100 \text{ kg/m}^3$ , 0% air/no pulsing,  $|U_a| = U_t = 0.75 \text{ m/s}$ ,  $u_{cf} = 1.5 \text{ m/s}$ ,  $\Psi = 0^\circ$ , depth=25m



(b)  $\rho_{j0} = 1200 \text{ kg/m}^3$ , 0% air/no pulsing,  $|U_a| = U_t = 0.75 \text{ m/s}$ ,  $u_{cf} = 1.5 \text{ m/s}$ ,  $\Psi = 0^\circ$ , depth=25m



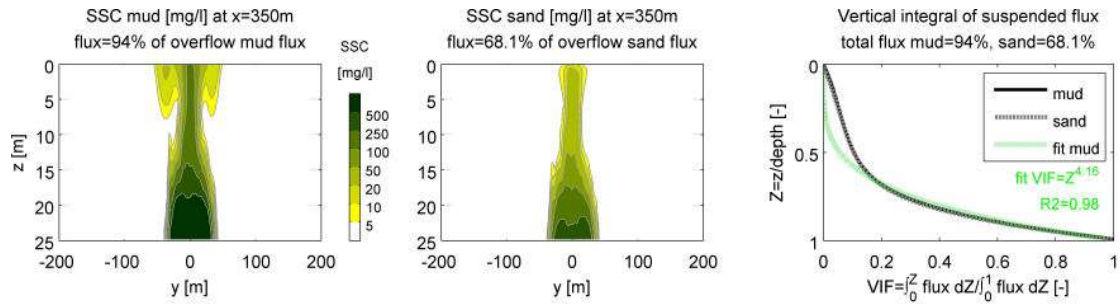
(c)  $\rho_{j0} = 1200 \text{ kg/m}^3$ , 12% air/ $T_p = 5.5 \text{ s}$ ,  $|U_a| = U_t = 0.75 \text{ m/s}$ ,  $u_{cf} = 1.5 \text{ m/s}$ ,  $\Psi = 0^\circ$ , depth=25m

Figure 9.3: Simulated result at end near field  $x = 350 \text{ m}$ .

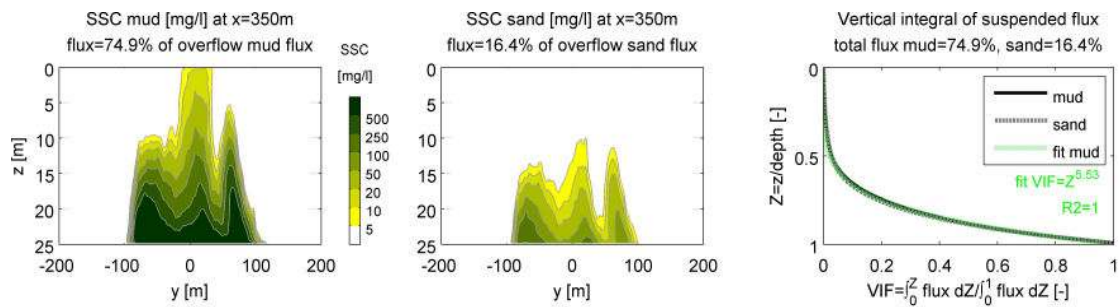
density difference. Dredging under an angle to the ambient current of  $\Psi = 22.5^\circ$  results in an asymmetric plume. A small depth of only 12 m leads to a vertically fully mixed plume with almost uniform SSC values over the water column and a linear vertical distribution of the flux instead of a concave one.

Due to its larger settling velocity the sand flux decreases much faster than the mud flux: only about 15% of the sand flux is still in suspension at  $x = 350 \text{ m}$  for  $u_{cf} = 1.5 \text{ m/s}$  and depth=25m, compared to about 75% for the mud flux. Because the sand fraction of the overflow deposits so close to a dredging site, this chapter will not discuss the sand fraction any further and will focus on the fine fractions.

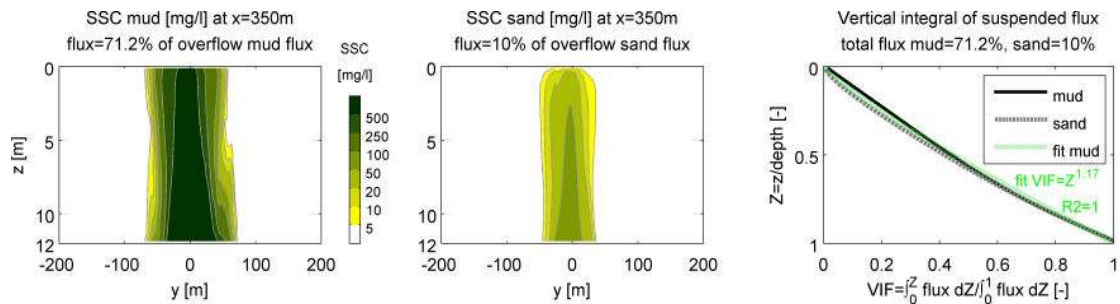




(a)  $\rho_{j0} = 1200 \text{ kg/m}^3$ , 0% air/no pulsing,  $|U_a| = U_t = 1.5 \text{ m/s}$ ,  $u_{cf} = 3 \text{ m/s}$ ,  $\Psi = 0^\circ$ , depth=25m



(b)  $\rho_{j0} = 1200 \text{ kg/m}^3$ , 0% air/no pulsing,  $|U_a| = U_t = 0.75 \text{ m/s}$ ,  $u_{cf} = 1.39 \text{ m/s}$ ,  $\Psi = 22.5^\circ$ , depth=25m



(c)  $\rho_{j0} = 1200 \text{ kg/m}^3$ , 0% air/no pulsing,  $|U_a| = U_t = 0.75 \text{ m/s}$ ,  $u_{cf} = 1.5 \text{ m/s}$ ,  $\Psi = 0^\circ$ , depth=12m

*Figure 9.4: Simulated result at end near field  $x = 350 \text{ m}$ .*

### 9.4.2 Near field plume results for all conditions

Figures 9.5-9.7 show some important results at the end of the near field at  $x = 350 \text{ m}$  of the 128 runs.

Figure 9.5 shows the maximum time averaged SSC inside the surface plume at the free surface at  $x = 350 \text{ m}$ . The surface SSC varies strongly for the 128 runs: the largest values are nearly  $1000 \text{ mg/l}$  for the small depth runs and the lowest values are near  $10 \text{ mg/l}$  for the large depth in combination with low  $u_{cf}$ , 0% air, no pulsing runs. Large surface SSC values are found for all runs with low depth *or* with large  $u_{cf}$ , independent of air entrainment and pulsing. A large depth *and* a small  $u_{cf}$  are necessary for a low surface SSC. 4% air and pulsing is sufficient to let the surface SSC rise significantly, but only when  $u_{cf}$  is small and the depth is

large. The SSC at the free surface is not dependent on whether the pulsing period is  $T_p = 5.5$  s or  $T_p = 11$  s. 12% air and pulsing gives larger SSC at the free surface than 4% air and pulsing, but again largest difference is found for larger depths and smaller  $u_{cf}$ .  $\rho_{j0} = 1100 \text{ kg/m}^3$  instead of  $\rho_{j0} = 1200 \text{ kg/m}^3$  only increases the surface SSC for larger depths; for smaller depths it has no influence or it even causes a decrease in SSC. The latter is caused by the lower total sediment flux through the overflow when  $\rho_{j0} = 1100 \text{ kg/m}^3$  instead of  $\rho_{j0} = 1200 \text{ kg/m}^3$ .

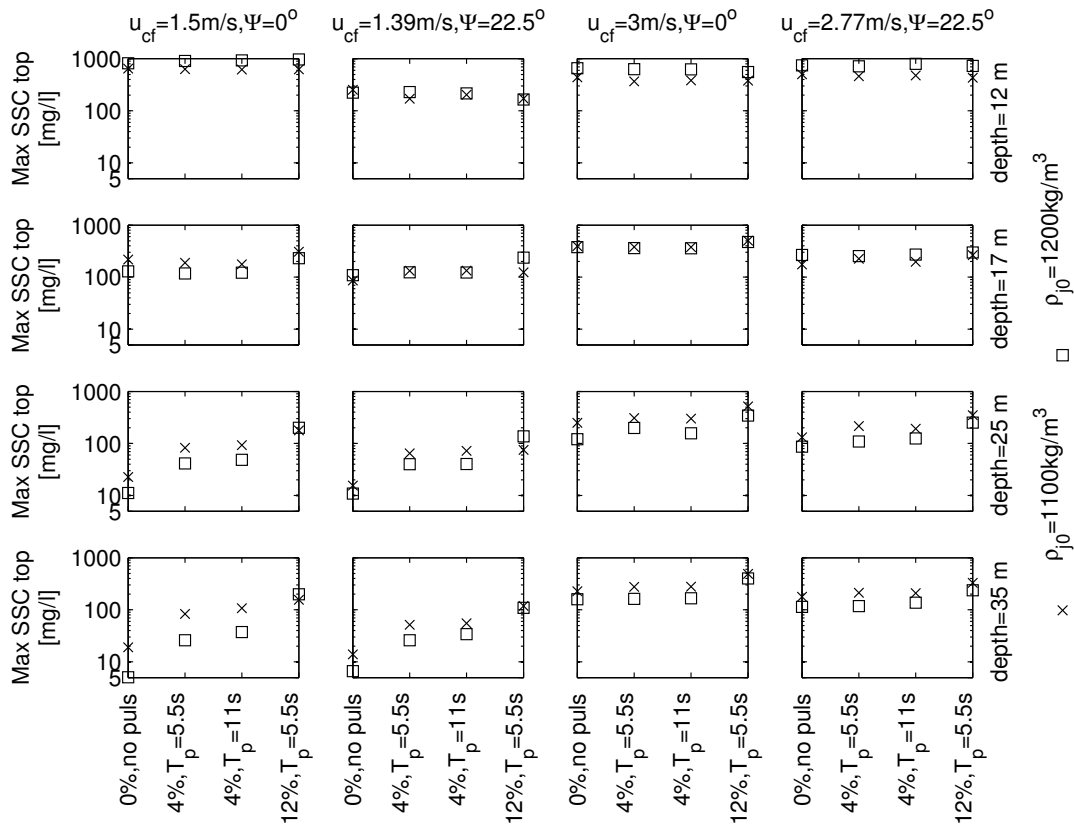


**Figure 9.5:** Maximum time averaged surface plume SSC at the free surface (highest computational cell) at the end of near field at  $x = 350 \text{ m}$  shown for each of the 128 individual input combinations with bias towards a large surface plume.

The different vertical distributions of the flux of fines in suspension in Figure 9.6 illustrate the impact of all variations in near field conditions. All vertical distributions for situations with low  $u_{cf}$  and large depth are strongly concave with the majority of the flux near the bed. For runs with large  $u_{cf}$  or smaller depth the curves are less concave. For the smallest depth=12m all curves are near linear, independent of air, pulsing or  $u_{cf}$ . A linear curve indicates a vertically fully mixed plume. Most  $\rho_{j0} = 1100 \text{ kg/m}^3$  cases have a vertical distribution profiles lying above the  $\rho_{j0} = 1200 \text{ kg/m}^3$  profiles, which indicates that a larger part of the plume is found higher in the water column. Air with pulsing lifts the vertical distribution profile up with a small effect of 4% with  $T_p = 5.5$  s or  $T_p = 11$  s pulsing and a big effect of 12% air with  $T_p = 5.5$  s. The runs with

depth=25m or 35m,  $\rho_{j0} = 1100\text{kg/m}^3$  and 12% air with pulsing even show convex curves: more than 50% of the fines flux still in suspension can be found in the upper half of the water column and the plume is floating above the bed without touching it. Dredging under an angle  $\Psi = 22.5^\circ$  to the ambient velocity gives lifted vertical distribution profiles with more material in the upper parts of the water column than for  $\Psi = 0^\circ$ . The one exception is the case with depth=12m where  $u_{cf} = 1.39\text{m/s}, \Psi = 22.5^\circ$  has a lower vertical distribution profile than  $u_{cf} = 1.5\text{m/s}, \Psi = 0^\circ$ .

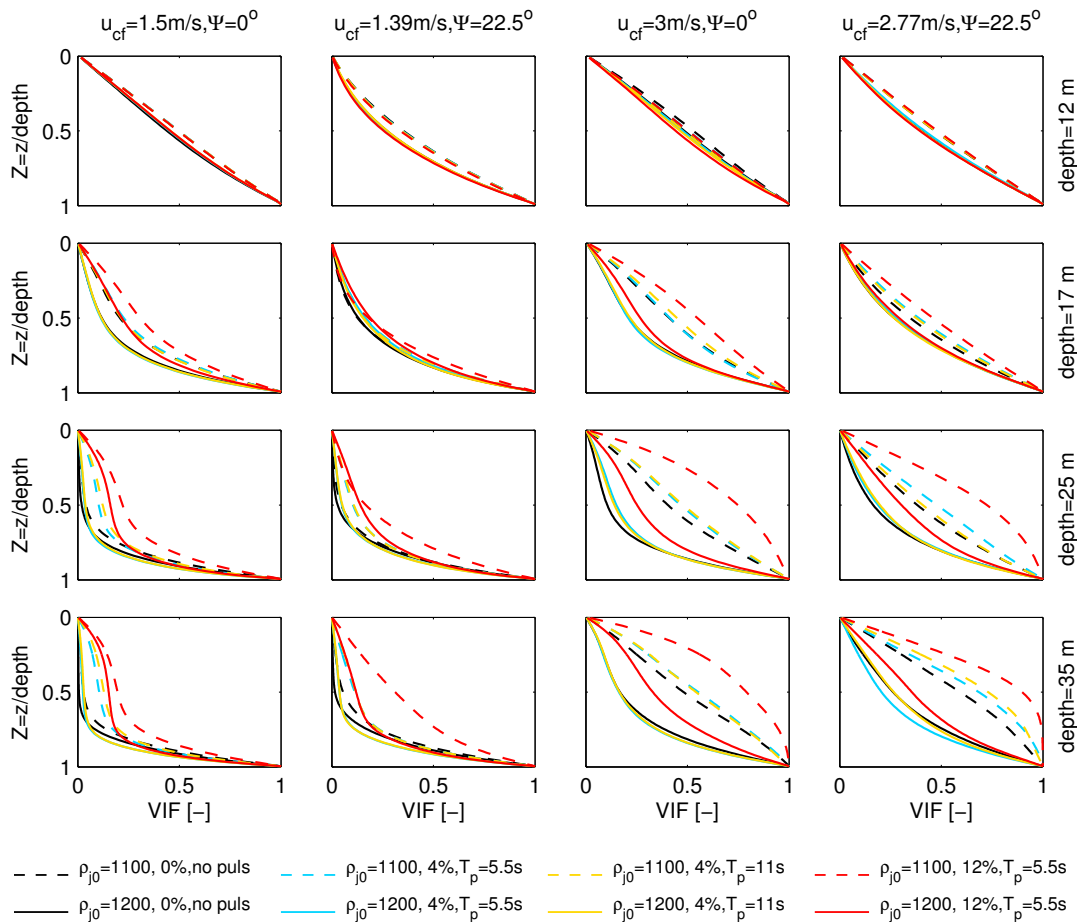


**Figure 9.6:** Vertical distribution of the flux of fines ( $VIF = \int_0^Z \text{flux } dZ / \int_0^1 \text{flux } dZ$ , with  $Z = z/\text{depth}$ ) at the end of near field  $x = 350\text{m}$  shown for each of the 128 individual input combinations with bias towards a large surface plume.

$FF_{nf}$ , the flux of fines still in suspension at the end of near field at  $x = 350\text{m}$  indicated as the ratio of the flux of fines through the overflow, varies between 50% to near 100% for the 128 runs in Figure 9.7. Please keep in mind that the 128 runs are biased towards large surface plumes with large percentages still in suspension and they are aimed for the investigation of the influence of different conditions. Air and pulsing have virtually no influence on  $FF_{nf}$  for larger  $u_{cf}$ : it is near 100% for large  $u_{cf}$  and large depth and it decreases to approximately 80% for large  $u_{cf}$  and depth=12m, independent of air and pulsing. 4% air with pulsing

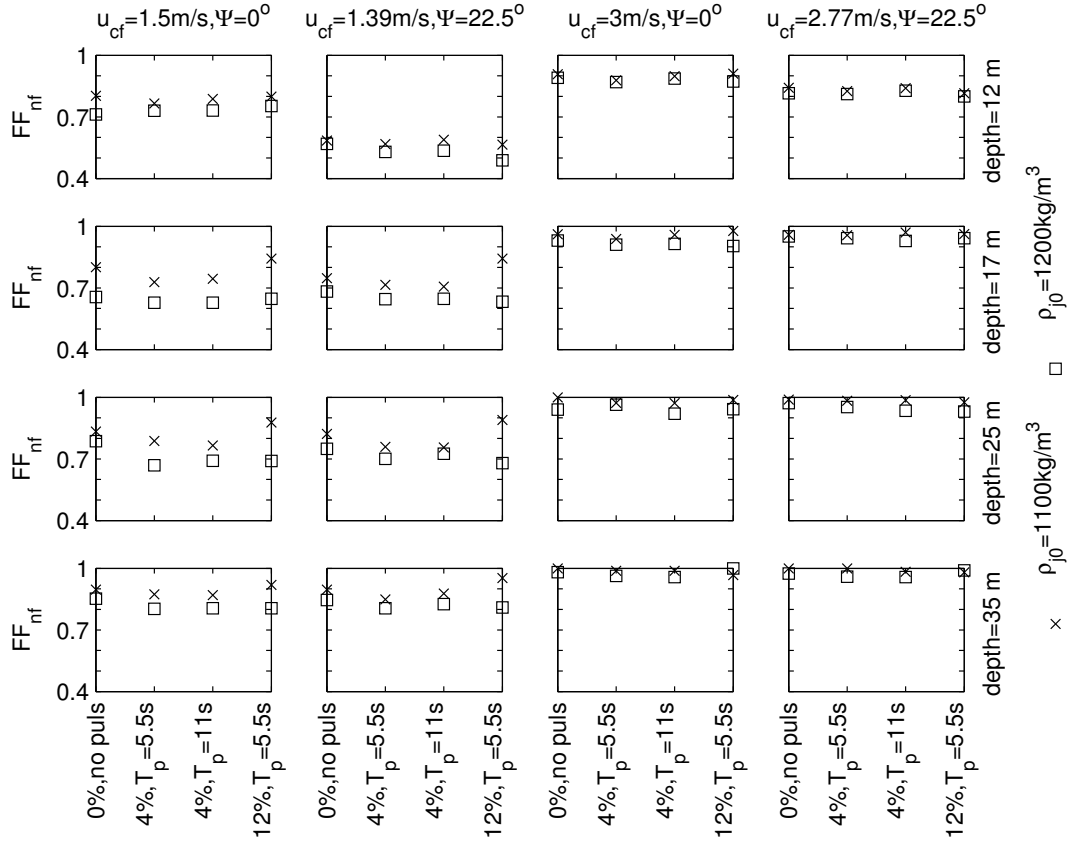


**Figure 9.7:**  $FF_{nf}$  shown for each of the 128 individual input combinations with bias towards a large surface plume.

has limited influence on  $FF_{nf}$ , in some cases it is slightly more and in some cases it is slightly less than 0% air without pulsing. The difference in pulsing period  $T_p = 5.5s$  or  $T_p = 11s$  has no influence on  $FF_{nf}$ . 12% air and pulsing only increases  $FF_{nf}$  significantly for the two smaller  $u_{cf}$  options when  $depth \geq 17m$  and  $\rho_{j0} = 1100kg/m^3$ ; with  $\rho_{j0} = 1200kg/m^3$  12% air and pulsing even decreases  $FF_{nf}$ .  $\rho_{j0} = 1100kg/m^3$  instead of  $\rho_{j0} = 1200kg/m^3$  increases  $FF_{nf}$  only for the two low  $u_{cf}$  options and  $depth \geq 17m$ .

The results of the twelve additional cases without bias towards a large surface plume of three different  $\rho_{j0}$  and four different  $u_{cf}$  are shown in Figure 9.8.  $u_{cf} = 0.5m/s$  and  $u_{cf} = 1m/s$  were missing in the 128 runs, but they lead to comparable vertical distribution profiles and max surface plume SSC values as for  $u_{cf} = 1.5m/s$  which was included in the 128 runs.  $FF_{nf}$  however, is reduced significantly for these lower  $u_{cf}$  values, with only 25% and 61% still in suspension at  $x = 350m$  for  $u_{cf} = 0.5m/s$  and  $u_{cf} = 1m/s$  respectively compared to approximately 78% for the lowest velocity  $u_{cf} = 1.5m/s$  included in the 128 runs. The difference between  $FF_{nf}$  with  $\rho_{j0} = 1300kg/m^3$  not included in the 128 runs and  $FF_{nf}$  with  $\rho_{j0} = 1200kg/m^3$  which was included is not striking and smaller than the difference between  $u_{cf} = 0.5m/s$ ,  $u_{cf} = 1m/s$  and  $u_{cf} = 1.5m/s$ .

### 9.4.3 Translation results beyond the near field

The time averaged velocity, mud SSC, and sand SSC distributions at the end of near field at  $x = 350\text{m}$  for all 136 runs are plugged into the mid field model to find the impact of the different near field conditions on the plume fluxes at distances beyond the near field. An illustrative example of the mid field result is shown in Figure 9.9. The maximum SSC values are reduced considerably from about  $\text{SSC} \approx 3000 \text{ mg/l}$  near the bed at the end of near field at  $x = 350\text{m}$  to  $\text{SSC} \approx 100 - 250 \text{ mg/l}$  after 15 minutes and  $\text{SSC} \approx 50 - 100 \text{ mg/l}$  after 30 minutes for this case. The fines (mud) flux after 30 minutes is reduced by a factor of approximately 2.5 compared to the end of near field at  $x = 350\text{m}$  for this case.

The 136 near and mid field runs are used to find mathematical relations via curve fitting which describe the simulation results without the need for long CFD calculations. The curve fitting is based on optimising coefficients to get the smallest Least Square Error (LSE) of the predictions compared to the actual simulated results. As a first step the vertical distribution and amount of flux at the end of near field will be predicted, and then, using these outcomes, also the mid field flux will be predicted. The curve fitting for the fluxes uses relations based on the differential equation describing the deposition of sediment from a cloud of uniform concentration  $C$  with height  $z_s$ :  $\frac{d(C)}{dt} = -C(t) \frac{w_s}{z_s}$  which has the solution  $C(t) = C(0) \cdot \exp(-w_s \cdot t/z_s)$  with the time given by  $t = x/u_{cf}$ . The relations found on the basis of the 136 CFD runs are:

$$PC = 1.3 \cdot Ri^{0.29} \cdot \gamma^{0.75} \cdot (1 + \sin |\Psi|)^{-0.58} \cdot (1 + p_{air})^{-2.5} \cdot ((\text{depth} - \text{draught})/D)^{0.62}, \quad (9.3)$$

$$FF_{nf} = \exp\left(-1.5 \cdot \frac{x_{nf}}{u_{cf}} \cdot \frac{w_s}{(\text{depth} - \text{draught}) \cdot PC^{-0.79}}\right), \quad (9.4)$$

$$FF_{mf} = FF_{nf} \cdot \exp\left(-1.7 \cdot (t - \frac{x_{nf}}{u_{cf}}) \cdot \frac{w_s}{\text{depth} \cdot PC^{-0.72}}\right), \quad (9.5)$$

where  $PC$  is the power of the fit through the vertical distribution of the sus-

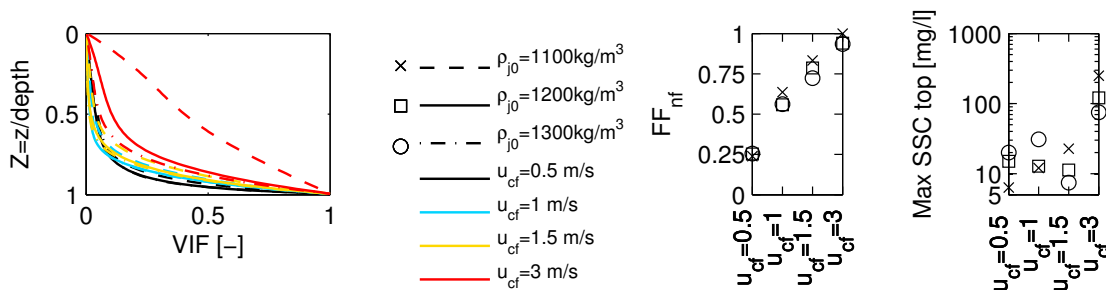


**Figure 9.8:** Vertical distribution flux of fines ( $VIF = \int_0^Z \text{flux } dZ / \int_0^1 \text{flux } dZ$ , with  $Z = z/\text{depth}$ ),  $FF_{nf}$  and maximum time averaged SSC at the free surface at the end of near field  $x = 350\text{m}$  shown for each of the additional 12 individual input combinations without bias towards a large surface plume. The parameters equal for all 12 runs are: 0% air/no pulsing,  $\Psi = 0^\circ$ ,  $\text{depth}=25\text{m}$ .

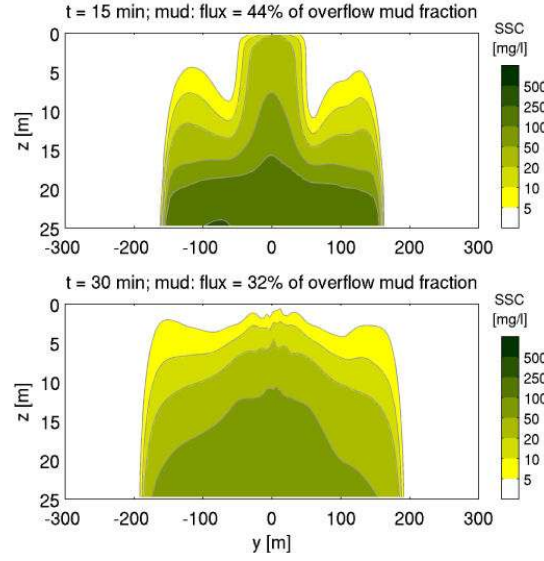


**Figure 9.9:** Simulated mid field result for plume ages  $t = 15\text{min}$  and  $t = 30\text{min}$ . Only the mud fraction is shown because the sand fraction has deposited completely with  $< 1\%$  still in suspension after  $t = 15\text{min}$ . Parameters:  $\rho_{j0} = 1200 \text{ kg/m}^3$ , 0% air/no pulsing,  $|U_a| = U_t = 0.75\text{m/s}$ ,  $u_{cf} = 1.5\text{m/s}$ ,  $\Psi = 0^\circ$ ,  $\text{depth} = 25\text{m}$ .

pendent fines flux:  $VIF = (z/\text{depth})^{PC}$  as for example can be seen in the third column of panels in Figures 9.3-9.4.  $FF_{nf}$  is the flux of fines still in suspension at the end of near field ( $x_{nf} = 350\text{m}$ ).  $FF_{mf}$  is the mid field flux of fines still in suspension after time  $t$ . Both  $FF_{nf}$  and  $FF_{mf}$  are a ratio of the flux of fines flowing through the overflow.  $p_{air}$  is the volume fraction of air, i.e.  $p_{air} = 0.1$  for 10% air.  $x_{nf} = 350\text{m}$  is the downstream distance from the overflow at the end of near field.

Figure 9.10 shows the results of Equations 9.3-9.5 for the 136 runs used to find the coefficients of the relations. First Equation 9.3 is used to predict the vertical distribution  $VIF = (z/\text{depth})^{PC}$  of the flux of fines at the end of near field at  $x = 350\text{m}$ . Then Equation 9.4 is used to predict the flux of fines at the end of near field and subsequently Equation 9.5 predicts the flux of fines after time  $t > x/u_{cf}$ . Equations 9.4 and 9.5 in essence both are describing the reduction of the fines flux by deposition. For  $FF_{nf}$  the settling height is  $[(\text{depth} - \text{draught}) \cdot PC^{-0.79}]$  and for  $FF_{mf}$  it is  $[\text{depth} \cdot PC^{-0.72}]$ . Hence, for both fluxes the settling height decreases for increasing  $PC$ , which makes sense because a larger  $PC$  belongs to a more concave vertical distribution curve with more material close to the bed. Pulsing is taken into account in Equation 9.3 by adjusting  $\gamma$  and  $Ri$  for the increased inflow momentum:  $\overline{w_{j0}^2}(t) = 1.5w_{j0}^2$  for the sine-shaped periodic pulsing with mean and amplitude  $w_{j0}$ . Therefore  $\gamma$  increases by a factor  $\sqrt{1.5}$  in case of pulsing and  $Ri$  decreases by a factor 1.5.

Equations 9.3-9.5 can reproduce the 136 results they are based upon with a maximum error of  $RMS = 1.1$  for  $PC$ ,  $RMS = 0.13$  for  $VIF$  at  $z/\text{depth} = 0.25$  and  $RMS = 0.09$  (maximum average of the absolute error is 19%) for the fluxes



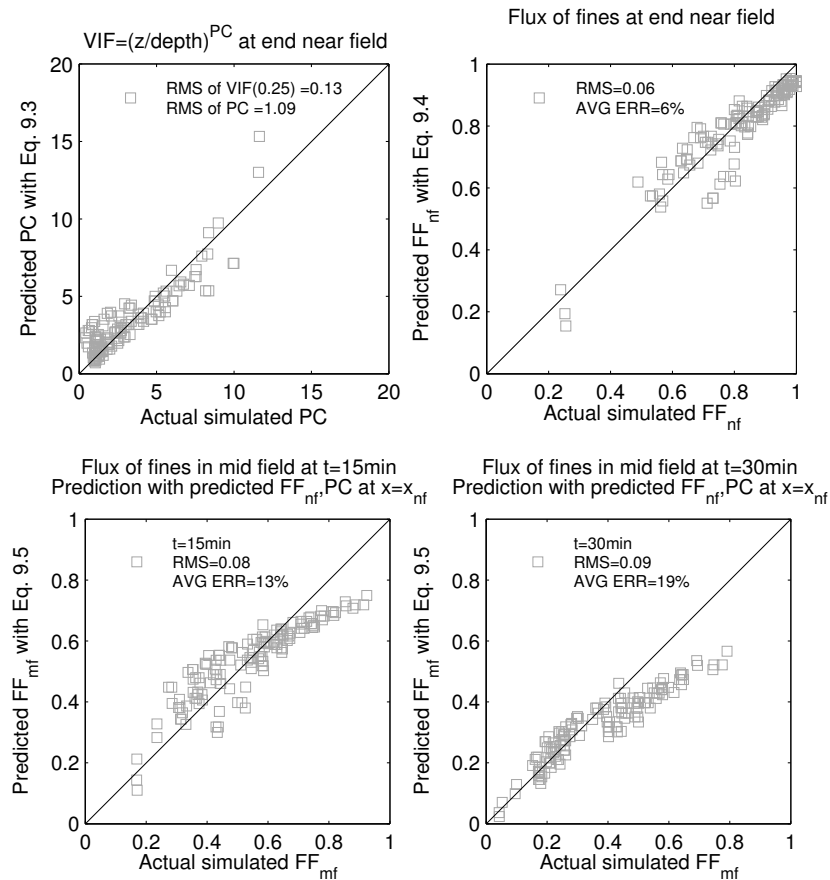


**Figure 9.10:** Predicted  $PC$ ,  $FF_{nf}$  and  $FF_{mf}$  with Equations 9.3-9.5 compared to the actual simulated  $PC$ ,  $FF_{nf}$  and  $FF_{mf}$  for the 136 runs used to find the coefficients in the relations.

of fines, see Figure 9.10. Next step is to verify the relations for situations not used to determine the coefficients. Table 9.1 describes the parameters of 22 extra runs which are conducted in order to check the accuracy and robustness of Equations 9.3-9.5. The last three runs in Table 9.1 are taken from Chapter 8 where near field simulations of overflow dredging plumes are compared with field measurements. Figure 9.11 shows the results of Equations 9.3-9.5 for these 22 verification cases. The relations can reproduce these 22 results with a maximum error of  $RMS = 2.8$  for  $PC$ ,  $RMS = 0.08$  for  $VIF$  at  $z/\text{depth} = 0.25$  and  $RMS = 0.12$  (maximum average of the absolute error is 27%) for the fluxes of fines. Hence, Equations 9.3-9.5 are reasonably accurate also for different cases than the ones they are based upon and maybe even more important: the relations are robust as there is not one of these 22 cases where the relations give complete wrong order in  $PC$  or flux of fines.

Equations 9.3-9.5 are only valid for finer particle fractions in the overflow with a settling velocity in the range of approximately  $w_s = 0 - 8$  mm/s. When the settling velocity is much larger, then the vertical distribution of the suspended sediment flux can alter significantly as illustrated by the difference in vertical distribution of the sand and mud fraction in the right panel in Figure 9.3c.

**Table 9.1:** Parameters of 22 verification cases of Equations 9.3-9.5. The input parameters  $u_{cf}$  and  $\Psi$  in these equations can be calculated by  $u_{cf} = \sqrt{v_a^2 + (u_{TSHD} - u_a)^2}$  and  $\Psi = \text{atan}(v_a / (u_{TSHD} - u_a))$ . <sup>A</sup>Input parameters  $\gamma$  and  $Ri$  are corrected for  $w_{j0}^2(t) = 1.5w_{j0}^2$  for the periodic sine-shaped pulsing with mean and amplitude  $w_{j0}$ .

#	$\gamma^A$	$Ri^A$	$\rho_{j0}$	mud	$w_s$	mud	$w_{j0}$	$D$	$\rho_{cf}$	$u_a$	$v_a$	$u_{TSHD}$	depth	draught	$p_{air}$	$T_p$	$x_{nf}$
-	-	-	[kg/m <sup>3</sup> ]	[%]	[mm/s]	[m/s]	[m]	[kg/m <sup>3</sup> ]	[m/s]	[m/s]	[m/s]	[m]	[m]	[-]	[s]	[m]	
1	1.6	1.2	1300	50	3.5	1.77	2.25	1030	-0.75	0	0.75	25	8	0.04	5.5	350	
2	1.6	0.78	1200	75	3.5	1.77	2.25	1030	-0.75	0	0.75	25	8	0.04	2.75	350	
3	2.3	0.78	1200	75	3.5	1.77	2.25	1030	-0.5	0	0.5	25	8	0.04	5.5	350	
4	1.6	0.78	1200	75	3.5	1.77	2.25	1030	-0.75	0	0.75	50	8	0.04	5.5	350	
5	1.2	0.64	1100	100	3.5	1.77	3	1030	-0.75	0	0.75	25	8	0	-	350	
6	1.3	1.6	1200	75	3.5	1.77	3	1030	-0.75	0	0.75	25	8	0	-	350	
7	1.3	2.5	1300	50	3.5	1.77	3	1030	-0.75	0	0.75	25	8	0	-	350	
8	1.2	0.29	1100	100	3.5	1.77	1.35	1030	-0.75	0	0.75	25	8	0	-	350	
9	1.3	0.70	1200	75	3.5	1.77	1.35	1030	-0.75	0	0.75	25	8	0	-	350	
10	1.3	1.1	1300	50	3.5	1.77	1.35	1030	-0.75	0	0.75	25	8	0	-	350	
11	1.8	1.2	1200	75	3.5	1.77	2.25	1030	0	0.75	0.75	25	8	0	-	350	
12	1.3	1.2	1200	75	3.5	1.77	2.25	1030	-0.69	0.29	0.75	25	8	0	-	350	
13	1.3	1.2	1200	75	3.5	1.77	2.25	1030	-0.75	0	0.75	25	8	0.08	-	350	
14	1.3	1.2	1200	75	3.5	1.77	2.25	1030	-0.75	0	0.75	25	8	0.2	-	350	
15	1.6	0.78	1200	75	3.5	1.77	2.25	1030	-0.75	0	0.75	25	8	0	5.5	350	
16	1.3	1.2	1200	75	1	1.77	2.25	1030	-0.75	0	0.75	25	8	0	-	350	
17	1.3	1.2	1200	75	6	1.77	2.25	1030	-0.75	0	0.75	25	8	0	-	350	
18	1.3	1.2	1200	75	1	1.77	2.25	1030	-0.75	0	0.75	12	8	0	-	350	
19	1.3	1.2	1200	75	6	1.77	2.25	1030	-0.75	0	0.75	12	8	0	-	350	
20	2.7	3.9	1200	100	3.3	0.99	2.25	1023	0	0	0.4	21.6	9.25	0.04	-	250	
21	0.83	3.1	1300	40	3.3	1.38	2.25	1023	-0.44	0.3	1.4	24	10.2	0	-	350	
22	1.0	0.82	1100	57	3.3	1.58	2.25	1007	-0.7	0	0.9	16.5	12	0.07	-	300	

Another note must be made regarding the predicted factor  $PC$  of the vertical distribution  $VIF = (z/\text{depth})^{PC}$ . The right panel in Figure 9.3c shows the vertical distribution for a run with much air and the fitted distribution  $VIF = (z/\text{depth})^{5.12}$  misses the surface part of the plume caused by the air. The average RMS error of the missing surface plume in the predicted  $VIF = (z/\text{depth})^{PC}$  distributions is 0.13 at  $z/\text{depth} = 0.25$  for the basis 136 runs which often show a surface plume, see Figure 9.10. The only influence of the large amount of suspended flux in the upper parts of the water column in Equations 9.3-9.5 is a reduction of the  $PC$  fit parameter. This reduction of  $PC$  for plumes with much air leads to a slower reduction of the flux of fines in Equations 9.4 and 9.5 by an increased settling height, and Figures 9.10-9.11 demonstrate that reliable predictions of the flux of fines can be obtained even without taking into account the surface plume separately. It is easily possible to include the surface plume in the fit of  $VIF$  for example by fitting a curve of the shape  $VIF = SP + (1 - SP) \cdot (z/\text{depth})^{PC}$ . Attempts to include the surface plume in this way were unsuccessful because it turned out to be impossible to get reliable predictions of the amount of  $SP$  by relations based on the input parameters. Hence, we stick to Equations 9.3-9.5 as predictions of the amount and vertical distribution of the flux of fines as they are robust and sufficiently accurate for a first estimate. But one needs to keep in mind that the prediction of the vertical distribution of the fines flux at the end of near field by Equation 9.3 never shows a surface plume even for cases with much air entrainment and a large surface plume is plausible; the only influence of air is a slightly reduced  $PC$  factor. When a more accurate prediction is needed of the surface plume then detailed near field simulations or measurements still

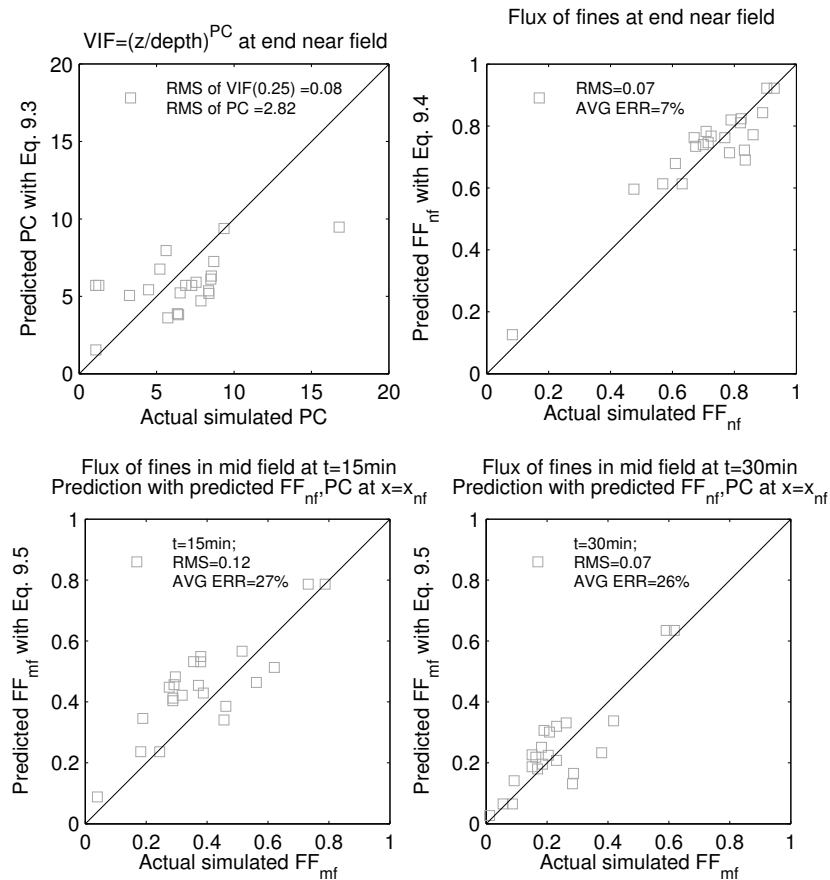


**Figure 9.11:** Predicted PC,  $FF_{nf}$  and  $FF_{mf}$  with Equations 9.3-9.5 compared to the actual simulated PC,  $FF_{nf}$  and  $FF_{mf}$  for 22 verification runs which were not used to find the coefficients in the relations.

are necessary.

Finally, Equations 9.3-9.5 are used to illustrate the influence of some reasonable variations within dredging practice of  $\rho_{j0}$ , air/pulsing,  $\Psi$ ,  $w_{j0}$  and  $w_s$  on the flux of fines for a range of  $0.4\text{m/s} < u_{cf} < 3\text{m/s}$ . Figure 9.12 shows the results for depth=25m, Figure 9.13 shows the results for depth=12m. In case CFD simulation results are available they are shown with filled markers. These figures therefore also show the performance of Equations 9.3-9.5 for individual runs compared to the CFD results. The significant influence of  $u_{cf}$  on the flux of fines in the mid field after a fixed time of 15 or 30 minutes is striking as it is caused purely by influence on vertical plume distribution and not by a difference in settling time. Also the variations in  $\rho_{j0}$ , air/pulsing,  $\Psi$  and  $w_{j0}$  have influence on the flux of fines, but less than the influence of  $u_{cf}$ . The influence of reasonable variations in  $w_s$  is larger than the influence of  $\rho_{j0}$ , air/pulsing,  $\Psi$  and  $w_{j0}$ , which is caused by the very large variation in reasonable  $w_s$  of the finer fractions in a dredging plume (Smith and Friedrichs 2011). Hence, most important factors determining the amount of the TSHD overflow plume flux still in suspension after a given settling time are the settling velocity and the vertical distribution of the dredging plume. The settling velocity of the sediment particles in the over-

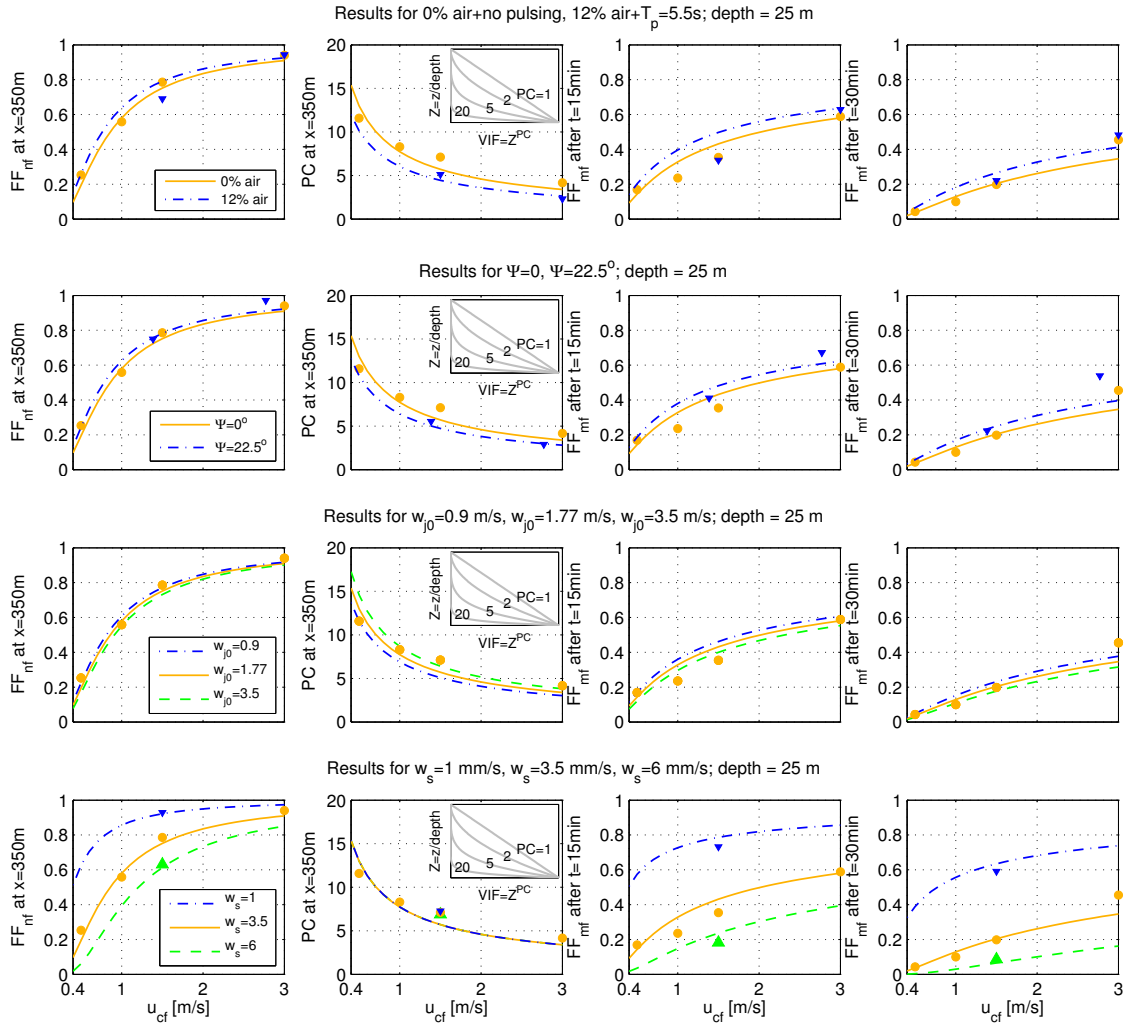


**Figure 9.12:** Influence of variation in air/pulsing,  $\Psi$ ,  $w_{j0}$  and  $w_s$  on  $FF_{nf}$  and the vertical distribution  $VIF = (z/\text{depth})^{PC}$  at  $x = 350\text{m}$  and  $FF_{mf}$  after  $t = 15\text{ min}$  and  $t = 30\text{ min}$  for  $25\text{m}$  depth. Coloured lines show the results based on Equations 9.3-9.5; filled markers show the CFD results of the basis runs and, if available, the CFD results of the variation in air/pulsing,  $\Psi$ ,  $w_{j0}$  and  $w_s$ . The parameters of the basis run are:  $\rho_{j0} = 1200\text{ kg/m}^3$ , 0% air+no pulsing,  $w_{j0} = 1.77\text{ m/s}$ ,  $w_s = 3.5\text{ mm/s}$ ,  $D = 2.25\text{ m}$ ,  $\rho_a = 1030\text{ kg/m}^3$ ,  $\Psi = 0^\circ$ ,  $\text{depth} = 25\text{ m}$ ,  $\text{draught} = 8\text{ m}$ .

flow depends mainly on the material being dredged. The vertical distribution is determined by the depth, which is a given and by near field mixing which is influenced by  $\rho_{j0}$ , air/pulsing,  $\Psi$ ,  $w_{j0}$  and mostly by  $u_{cf}$  which are factors that, to some extent, can be influenced during dredging.

#### 9.4.4 Practical guidelines to determine a far field source flux

The presented results at the end of near field at  $x = 350\text{ m}$ , just  $250\text{ m}$  behind the *moving* TSHD aft, are too close to the dredger to be used as a proper far field source flux of suspended sediment from a TSHD. At  $x = 350\text{ m}$  the plume

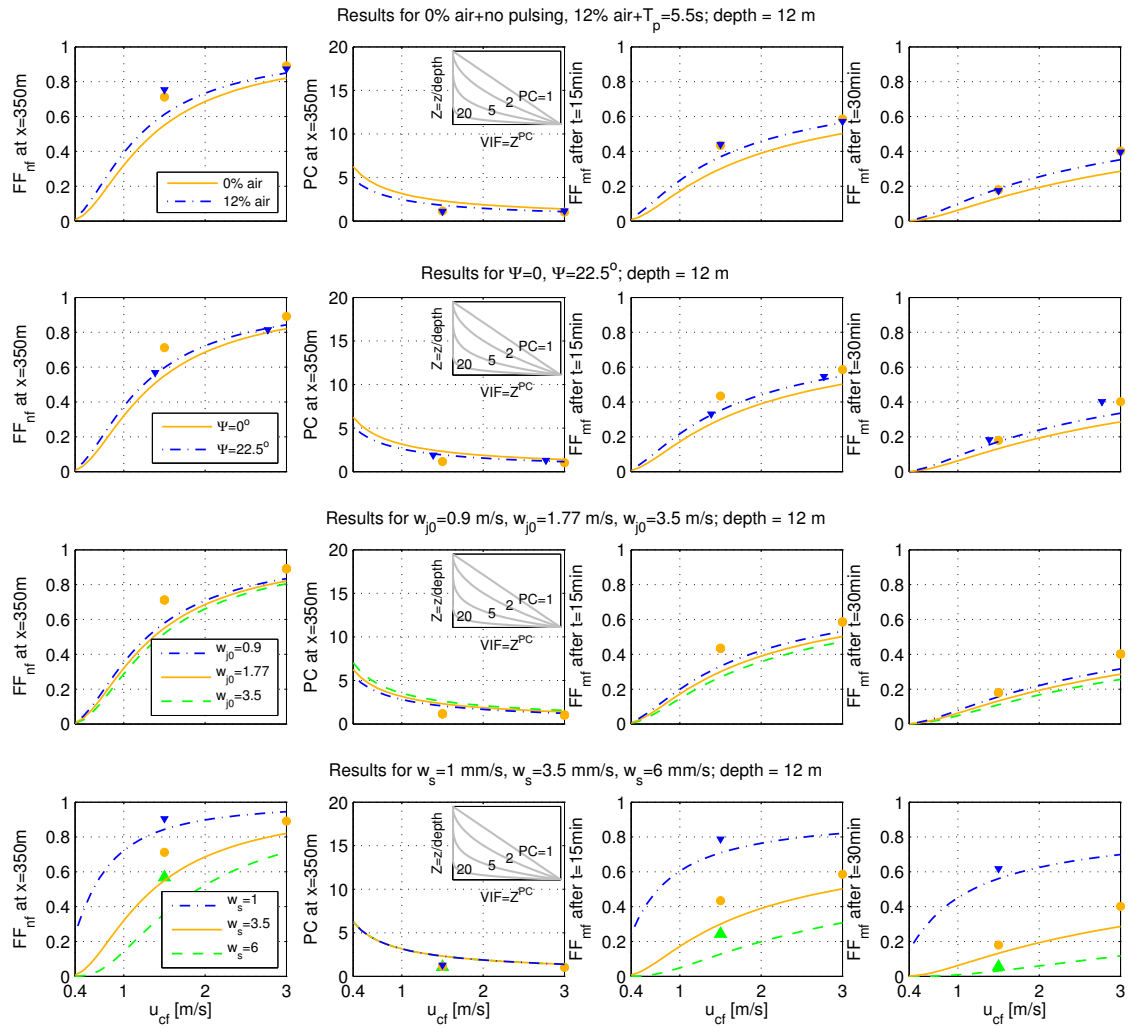


**Figure 9.13:** Influence of variation in air/pulsing,  $\Psi$ ,  $w_{j0}$  and  $w_s$  on  $FF_{nf}$  and the vertical distribution  $VIF = (z/\text{depth})^{PC}$  at  $x = 350\text{m}$  and  $FF_{nf}$  after  $t = 15\text{ min}$  and  $t = 30\text{ min}$  for  $12\text{m}$  depth. Coloured lines show the results based on Equations 9.3-9.5; filled markers show the CFD results of the basis runs and, if available, the CFD results of the variation in air/pulsing,  $\Psi$ ,  $w_{j0}$  and  $w_s$ . The parameters of the basis run are:  $\rho_{j0} = 1200\text{ kg/m}^3$ , 0% air+no pulsing,  $w_{j0} = 1.77\text{m/s}$ ,  $w_s = 3.5\text{mm/s}$ ,  $D = 2.25\text{m}$ ,  $\rho_a = 1030\text{kg/m}^3$ ,  $\Psi = 0^\circ$ ,  $\text{depth}=12\text{m}$ ,  $\text{draught}=8\text{m}$ .

induced density difference of typically  $\Delta\rho \approx 3\text{kg/m}^3$  is still important and typically 75% of the plume flux can be found in the bottom 25% with typically over 50% in the bottom 5 m; this large near bottom part of the plume will deposit quickly. In our opinion, mid field results after about 15 minutes plume development are a good candidate to use as a far field source flux, because then the plume density difference with a typical maximum of  $\Delta\rho \approx 0.1 - 0.25\text{kg/m}^3$  is not so important any more and 15 minutes transport with a common ambient current of less than 1 m/s still is within 1 km from the original sediment release location. Obviously, for an individual project there can be good reasons to define the far field source flux after a longer or shorter period of plume development.

Besides, when the correct vertical distribution of the sediment plume is used as source flux in a far field model which can cope with density differences and has sufficient horizontal and vertical resolution, the choice where to exactly define your far field source term is less important as the density driven dispersion is taken care of in the far field model. On the other hand, when a depth averaged far field model is used, it can be wise to choose the source flux after a longer period of time than 15 minutes, because the near bed plume behaviour with quick deposition is completely lost in a depth averaged far field model.

In case no measurements are available to determine a far field source flux of suspended sediment, the source flux must be assessed based on local conditions. Simply using a source flux from a different project with different conditions will lead to erroneous results. Using the total amount of fines in the dredged material as far field source flux will be an overestimation because it neglects the burial of fines in the hopper and using the total amount of fines flowing through the overflow will also be an overestimation because it neglects the fines which deposit close to the dredger due to the density driven spreading of the overflow plume. The following steps can be identified for a correct determination of a far field source flux of suspended sediment from a TSHD while dredging:

1. Assess the PSD of the dredged material: fine sediment fractions with low settling velocity will stay suspended for significant periods, coarser fractions will deposit very close to the dredger (see for example Figures 9.3 and 9.4) and determine  $w_s$  of the fine fraction(s) with the possibility of flocculation taken into account.
2. Assess the amount of fines from the dredged material which will be buried in the hopper and the amount of fines flowing through the overflow, a dedicated hopper CFD model can be helpful (Rhee 2002; Spearman et al. 2011). Reduce the total amount of fines in the dredged material with the amount staying behind in the hopper to arrive at the total amount of fines released through the overflow.
3. Assess the near field conditions as  $u_{cf}$ , depth, draught,  $\rho_{j0}$ , air/pulsing,  $\Psi$  and  $w_{j0}$  in order to determine plume mixing and deposition of fines near the TSHD, for example by using dedicated near field plume simulations which take all important processes as identified in Section 2.4 into account or by using Equations 9.3-9.5. Multiply the overflow flux of fines from step 2 with the reduction factor accounting for deposition near the dredger to get the source flux of suspended sediments usable for a far field simulation. Take into account the vertical distribution of the suspended sediment plume, because this determines the rate of deposition in the far field to a far extent. When re-suspension of already deposited sediment due to wave action or ambient currents is expected to be important, the deposited sediment near the dredger needs to be included as a bed source in the far field model.
4. Assess the horizontal release location and source flux over time based on the (expected) project planning and TSHD trails during dredging.

Not all these steps can be executed easily, because quite some information is needed, but they all are essential to arrive at a proper source flux. To account for uncertainty in the input a sensitivity analysis can help, Equations 9.3-9.5 for



example do not demand computational effort and can be repeated for different conditions to find how sensitive the outcome is to the unknown exact input. For the source of suspended sediments from a TSHD while discharging, similar steps can be derived, but that is not the topic of this chapter. This chapter aims at assisting in step 3 of the determination of a source flux of suspended sediments from a TSHD while dredging.

### Uncertainty CFD results

The results presented in this chapter are based on CFD simulations. They are a schematised version of reality and therefore have a degree of uncertainty for several reasons. First of all the time averaged results are not perfectly smooth. For perfectly smooth results the simulation period should be extended by a factor 2 or 3, but this was impossible because of limited resources on the super computer facilities. The ambient turbulence is imposed on the inflow boundaries by the Synthetic Eddy Method of (Jarrin et al. 2006) which uses a randomiser. Therefore doing a second simulation with identical input does not give identical results, and a test with identical input resulted in 1% difference in time averaged flux of fines at the end of near field, 0% difference in fitted vertical distribution factor  $PC$  and 5% difference in maximum time averaged  $SSC$  at the free surface. The influence of grid resolution is verified by a simulation with the grid refined a factor 1.5 in all three dimensions. This refined simulation differed 1% in flux of fines at the end of near field, 5% in  $PC$  and 3% in maximum time averaged  $SSC$  at the free surface.

Unfortunately, it turned out that there was an error in the propellers locations in the CFD simulations: the port side propeller was placed 3 m more to the front than the starboard propeller. For the simulations with  $\Psi = 22.5^\circ$  the propellers are also erroneously placed 7 m shifted towards port side. The 3 m shift between starboard and port side propeller causes the small asymmetry in the time averaged results in Figures 9.3 and 9.4. Three extra simulations with the propellers at the correct location for  $\Psi = 0^\circ$  with depth=25 or 12m, and  $\Psi = 22.5^\circ$  with depth=25m give a difference of maximum 2% in fines flux, 10% in  $PC$  and 18% in maximum time averaged  $SSC$  at the free surface. Given the total computational effort of 7000 hours on 8-core computers, it is not possible to re-run all 136 CFD simulations with the correct propeller location. But as the influence of the investigated near field conditions is much larger than the influence of the incorrect propeller placement, the conclusions in this chapter are not harmed by the errors caused by the incorrect propeller placement.

Altogether the uncertainty of the CFD results (determined with quadratic addition) is 4% in flux of fines, 11% in  $PC$  and 19% in maximum time averaged  $SSC$  at the free surface. All presented results in this chapter must be used with these uncertainties kept in mind.

## 9.5 Conclusions

The influence of several near field conditions on the far field source flux of a TSHD overflow plume is investigated by 136 CFD model runs. The amount of dredging plume flux still in suspension after a given time is determined by the settling velocity and the vertical distribution of the plume resulting from the near field mixing. The settling velocity of the sediment particles in the overflow depends mainly on the material being dredged. The following factors are varied in the 136 near field runs: the overflow sediment mixture density; the amount of entrained air in the overflow, a pulsing overflow discharge; an angle between the TSHD path and ambient current; the crossflow velocity (the vector sum of trailing speed and ambient velocity); the ambient depth. The dredging plume source flux at the end of near field is plugged into a mid field model to find the impact of the near field variations on the plume dispersion beyond the near field.

The largest influences on the near field mixing were found to be the crossflow velocity and depth. A higher crossflow velocity or a smaller depth lead to more surface plume, with a vertical distribution of the overflow plume that shows more material at large distance from the bed. A higher crossflow velocity leads to a larger ratio of fines still in suspension (the ratio of fines still in suspension compared to the fines flowing through the overflow) due to the increased amount of surface plume, but although a smaller depth also leads to more surface plume, the ratio of fines still in suspension is lower due to the reduced vertical settling distance. A lower overflow density, more air entrainment combined with pulsing, or dredging under an angle with the ambient current all lead to more surface plume and a larger ratio of fines still in suspension. But the influence of these factors is conditional: only with a low crossflow velocity and a large depth they have significant influence. With a high crossflow velocity or a small depth the plume is mixed over the water column independent of the other factors.

These findings can be applied to dredging practice as follows. A low crossflow velocity promotes settling of the dredging overflow plume close to the TSHD. Air entrainment/pulsing and dredging at an angle with the ambient current should be avoided if possible, but a low crossflow velocity is more important. A larger overflow density and higher overflow velocity are beneficial as they bring the overflow plume quicker to the bed, but the total sediment flux becomes larger. Ambient depth and the settling velocity of the sediment in the overflow plume have major influence, but cannot be influenced easily during dredging.

The findings of the 136 CFD runs are translated in mathematical relations which predict, without computational effort, the vertical distribution and flux of the overflow plume of a TSHD. These relations can be used when accurate measurement or model results are not available. They implicitly incorporate all investigated near field processes and are robust and reasonably accurate, which is verified with 22 extra CFD simulations. Practical guidelines are provided to assess a proper far field source flux of suspended sediments from a TSHD while dredging in case detailed measurements are lacking.

# Chapter 10

## IMPROVE: IMPact Reducing OVerflow Extension

*The simulation set up from previous chapter is used to test the novel concept IMPROVE to reduce the environmental impact of the overflow plume. IMPROVE consists of an extended overflow pipe which releases the overflow mixture close to the seabed. With CFD simulations a systematic comparison is carried out between different overflow extension lengths, overflow positions and the base case without extension.*

### 10.1 Introduction

After the improved insight obtained in previous chapters on near field TSHD overflow plume mixing, this chapter focusses on manners to influence the mixing process with as aim to reduce the environmental impact of the overflow plume. Most fundamental manner to reduce the environmental impact would be to reduce the amount of (fine) sediments spilled during dredging. This can be achieved in many different ways, but they all have in common that they either are expensive (e.g. separating the (fine) sediment from the overflow water) or hinder production seriously resulting in increased dredging costs (e.g. dredging without overflow). Re-using the overflow mixture as jetting water in the drag-head, like tested in [Parys et al. \(2001\)](#), can reduce the overflow sediment spill, but in general the jetting water flux is (much) smaller than the overflow flux.

A potentially easier manner to reduce the environmental impact than reducing the spill could be to promote settling of the overflow sediment at the seabed and to reduce the generation of a surface plume. For example a green valve which reduces overflow pulsing and air entrainment in the overflow is designed for this purpose. The influence of air entrainment and pulsing is investigated in [Chapter 9](#) and these findings can also be used to assess the potential positive influence of a green valve: the influence of air and pulsing was found to be significant on the surface plume SSC, but only limited on the amount of fine sediment still in suspension. Therefore, the positive effect of a green valve is expected to be mainly in reducing the surface plume SSC and not so much in reducing the amount of fine sediment still in suspension. Another manner to promote settling

of fine sediment from the overflow plume and reduce the generation of a surface plume is to release the overflow mixture closer to the seabed. When the overflow is released closer to the seabed, less mixing occurs, resulting in larger concentrations near the bed which can deposit close to the TSHD. Because the overflow mixture is released deeper in the water column, at a larger distance from the free surface, it is expected that also the SSC in the surface plume are reduced. Releasing the overflow mixture closer to the seabed can be realised by an overflow extension: instead of releasing the overflow sediment-water-air mixture at the keel of a TSHD, the overflow shaft is extended below the keel. It was Building with Nature partner IHC who asked for CFD tests of the concept of an extended overflow, and in this chapter these tests are presented.

## 10.2 Extended overflow test runs

Three overflow extensions are tested for a situation of dredging in a depth of 25m:

- Short extension of 3m long
- Medium long extension of 8m long
- Long extension of 16m long (1 m above seabed)

All overflow extensions are compared with a base run with the following parameters:  $\rho_{j0} = 1200 \text{ kg/m}^3$ , 75% mud + 25% sand, sand:  $w_s = 22.6 \text{ mm/s}$ , mud:  $w_s = 3.5 \text{ mm/s}$ , 4% air+pulsing  $T_p = 5.5 \text{ s}$ ,  $w_{j0} = 1.77 \text{ m/s}$ ,  $D = 2.25 \text{ m}$ ,  $\rho_a = 1030 \text{ kg/m}^3$ , depth=25m, draught=8m. The parameters are identical to a run in Chapter 9 and also the model settings are similar. For computational reasons, the overflow extension is not round, like the overflow itself, but the extension is a square pipe of 2.5m internally. Hence, the overflow extension has a slightly larger flow through area than the overflow itself. The 16m overflow extension releases the sediment overflow mixture horizontally backwards at 1m from the seabed through a 2.5m wide and 2m high gap. To investigate the interaction between the influence of the TSHD sloping aft and propellers and the influence of the overflow extension, two overflow locations are tested: 100m (base) and 40m (back) in front of the TSHD aft.

Because the extended overflow pipe has strong interaction with the flow, the standard immersed boundary method (IBM) from Sections 3.4.1 and 3.6 to simulate obstacles in the computational domain is not adequate any more to simulate the pipe walls as the velocity through the pipe wall gets in the range of cm/s and the extension of the overflow pipe is leaking. Therefore, at the end of each time step the IBM body force is reapplied ten times with a subsequent pressure correction. This doubles the computational time of each simulation, but now the velocity through the pipe wall gets under mm/s which is a factor 1000 times less than the velocities inside the pipe and results in an extended overflow pipe with not much leaking. The runs without overflow extension have 100% overflow sediment flux directly downstream of the overflow at  $x = 2 \text{ m}$  (where there is no deposition yet), but the runs with overflow extension only have 89-98% left of the overflow sediment flux. The lowest flux is found for the longest overflow

extension and the missing part of the flux is numerically destructed because the sediment concentration in each pipe wall grid cell is put to zero. To correct for this numerical loss in overflow sediment flux, all presented overflow fluxes  $FF_{nf}$  at  $x = 350\text{m}$  are compared with the sediment flux at  $x = 2\text{m}$  instead of the sediment flux flowing into overflow.

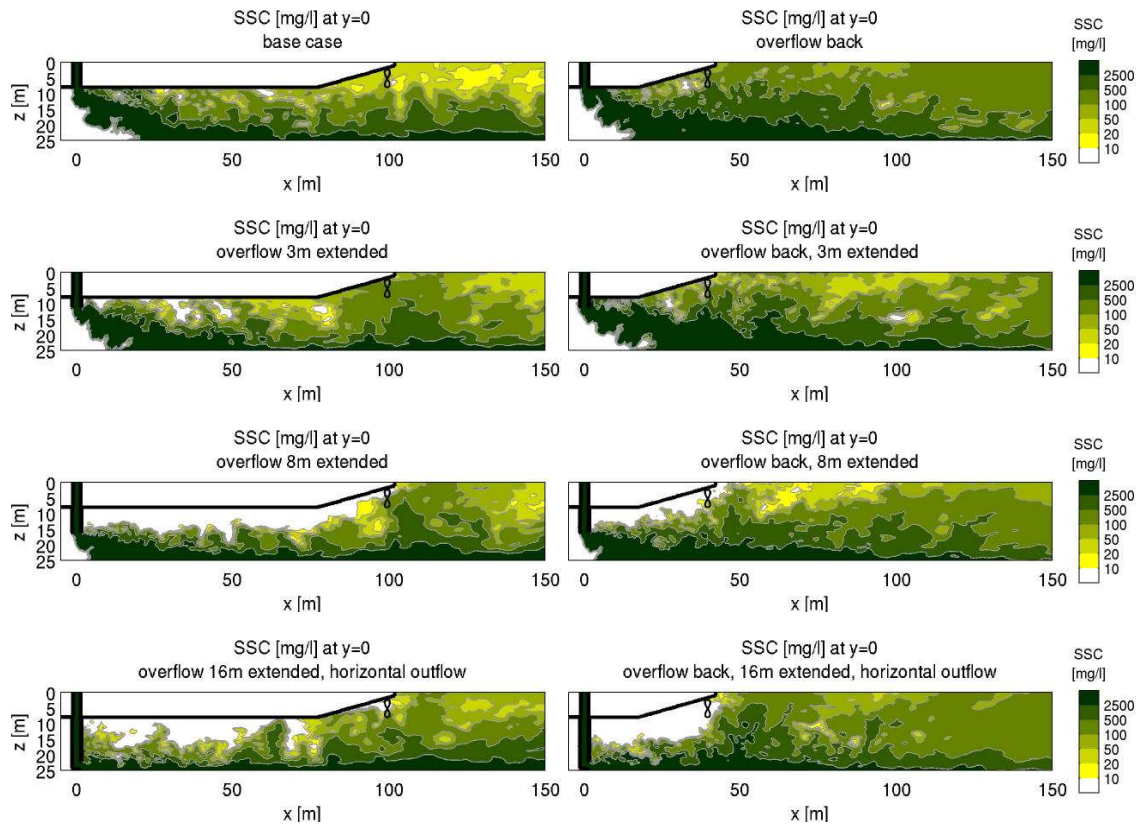


Figure 10.1: Instantaneous SSC at centre slice for different overflow adjustments.

## 10.3 Extended overflow results

The instantaneous SSC through the centre slice at  $y = 0$  are shown in Figure 10.1 to have an indication of the vertical mixing of the suspended sediment towards the free surface after it has been released close to the sea bed. In the base case, without overflow extension, the plume spreads over the complete zone below the keel and suspended sediment clouds of  $SSC > 100 \text{ mg/l}$  touch the keel. A 3m extended overflow has limited influence on the instantaneous SSC distribution at  $y = 0$ , but a 8m extension results in a zone free of suspended sediment below the keel of the TSHD. The 16m overflow extension brings the sediment right at the bed without mixing, but then the sediment is re-suspended up in the water column by the air fraction from the overflow mixture and the turbulent interaction between the vertical overflow extension and the crossflow. This re-suspension is so strong that some puffs of suspended sediment reach the keel of

the TSHD before the sloping aft of the TSHD. The re-suspension caused by air of the 16m overflow extension is larger than the re-suspension by air of the 3m and 8m extensions as the outflow of the 3m and 8m extensions has downward momentum leading to more separation of the air from the sediment-water mixture than with the 16m extension which has horizontal outflow. At the sloping aft, the flow expansion and entrainment into the propeller jet even brings suspended sediment to the free surface. With the overflow at the back the plume spreads more in vertical direction and larger SSC values are found at the free surface than with the overflow at the front. This holds for all cases, with and without overflow extension, and is caused by the shorter distance from the overflow to the TSHD aft and propellers.

Time averaged separate mud and sand SSC cross contours at  $x = 350\text{m}$  are given in Figure 10.2. With and without overflow extension, only a few percent of the sand fraction at  $x = 350\text{m}$  is still in suspension and the majority of the mud fraction forms a bed plume of 150-200 m wide. All runs show a surface plume of 40-60 m wide. Table 10.1 summarises the most important results at  $x = 350\text{m}$ . In the base case the mud flux at  $x = 350\text{m}$  is  $FF_{\text{nf}} = 0.65 - 0.69$ , which means that 0.35-0.31 of the overflow mud flux has deposited before  $x = 350\text{m}$  with respect to the moving TSHD. The 3m overflow extension is too short to have any significant influence on  $FF_{\text{nf}}$  at  $x = 350\text{m}$ , but the 8m extension reduces the mud flux to  $FF_{\text{nf}} = 0.56 - 0.57$  and the 16m extension even reduces the mud flux to  $FF_{\text{nf}} = 0.45 - 0.5$ . Largest reduction in  $FF_{\text{nf}}$  of 35% is found for a 16m extended overflow at the back, because in this case the upward mixing at the sloping aft of the TSHD and upward entrainment in the propeller jet is less than with the overflow at the front. For this case more than half of the overflow mud flux has deposited before  $x = 350\text{m}$  from the moving TSHD.

Hence, an overflow extension of sufficient length can have significant influence on the mud flux still in suspension. The time averaged mud-SSC values at the free surface in Table 10.1 however, are hardly influenced by an overflow extension; the only significant influence is found for the overflow at the back which results in a considerable increase of the SSC value at the free surface.

**Table 10.1:** Mud flux still in suspension and maximum time averaged SSC at the free surface at  $x = 350\text{m}$  for the extended overflow runs.

run	$FF_{\text{nf}}$	$FF_{\text{nf}}/FF_{\text{nf}}^{\text{base case}}$	max SSC top [mg/l]
base run	0.69	100%	27
overflow back	0.65	95%	84
overflow 3m extended	0.68	99%	32
overflow back, 3m extended	0.66	96%	72
overflow 8m extended	0.57	83%	23
overflow back, 8m extended	0.56	82%	51
overflow 16m extended, horizontal outflow	0.50	73%	37
overflow back, 16m extended, horizontal outflow	0.45	65%	67



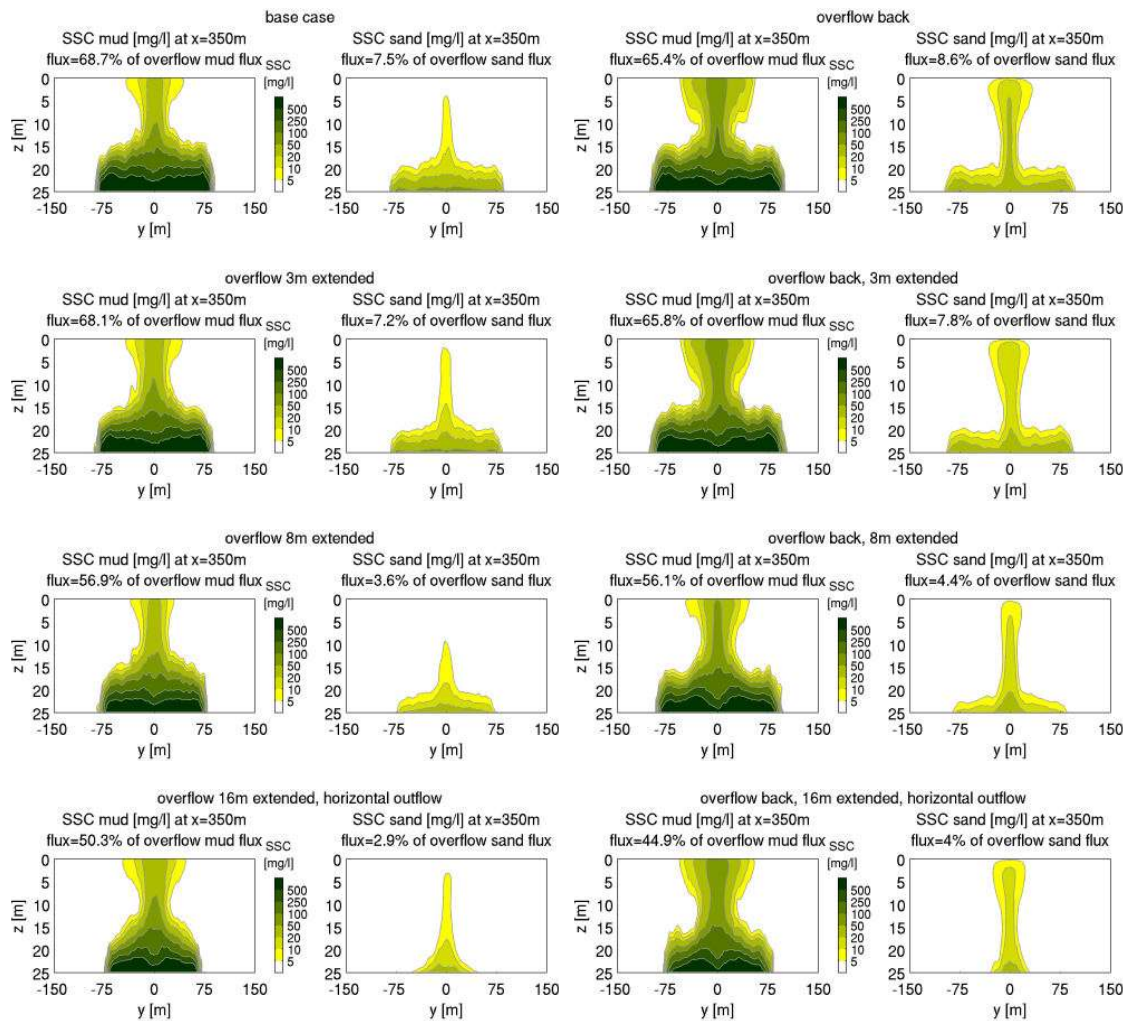


Figure 10.2: Simulated results at end near field  $x = 350\text{m}$  for different overflow extensions.

## 10.4 Conclusions on overflow extension

The CFD results show that an overflow extension of sufficient length can reduce the mud flux still in suspension at  $x = 350\text{m}$  significantly up to 35%, but the SSC in the surface plume are not reduced by an overflow extension. For the investigated dredging depth of 25m an overflow extension of just 3m has no effect, an extension of 8m already has some positive effect and largest positive influence is found when the overflow flux is released at the seabed near the aft of the TSHD. Latter case is investigated by a vertical overflow extension and a simple square shaped outflow gap for computational reasons, but a more realistic design could be to have a sloping overflow pipe starting in front of the hopper and ending near the aft of the TSHD with a diffuser at the seabed. A diffuser with gentle outflow might reduce the re-suspension of the sediment bed plume up in the water column and lead to even more reduction in mud flux than found for the investigated 16m overflow extension. The concept of releasing the overflow

mixture closer to the seabed by an IMPROVE (IMPact Reducing OVerflow Extension) looks promising for a reduction in the potential environmental impact of a dredging overflow plume.

# Chapter 11

## Conclusions and recommendations

### 11.1 General

In the introduction, the aim of this study was defined as *"...to provide insight in the overflow dredging plume mixing in the near vicinity of the TSHD and under its keel resulting in a practical translation to assess the plume deposition and flux without the necessity of long computer simulations. Specific attention is paid to processes which generate a surface plume and under which conditions this happens."*

The conducted LES CFD simulations give valuable insight in the mixing of an overflow dredging plume close to a TSHD and under its keel. Three dimensional information on concentrations and velocities is available to analyse the plume path and dilution. Experiments and field measurements have validated and supplemented the CFD findings. Better understanding is obtained for the conditions when a surface plume is generated with increased turbidity near the free surface and which processes cause a surface plume. Practical guidelines and mathematical relations are presented to assess the dredging plume deposition and flux which can be used in far field simulations to determine the frequency, duration and intensity of stresses like turbidity and sedimentation needed to find the environmental impact of dredging.

The CFD model is tested for a wide variety of turbulent benchmark cases and accurate results are obtained. The benchmarks include buoyant JICF (jet in cross-flow), non-buoyant JICF, plume without crossflow, turbulent channel flow with and without suspended sediment, density current at a bed, deposition of sediment at the bed, flow past an obstacle, propeller flow and separation of air from an air-water JICF. These benchmarks cover many aspects of the flow of a dredging plume near a dredging vessel. The CFD model is also validated for actual flow of a dredging plume near a dredging vessel on laboratory scale and on field scale. Dredging plume mixing is simulated accurately and also the measured cases with a large surface plume are reproduced adequately.

Specific conclusions on the processes and conditions favouring the development of a surface plume are given in Section 11.3, but first the new developments of this study are summed up.

## 11.2 New developments

It is the first time LES CFD simulations are conducted for dredging plume mixing. The intermittent plume mixing behaviour with individual eddies being especially important for the possible generation of a surface plume is captured by the LES turbulence approach. The structure of turbulence inside a dredging plume is found to be strongly anisotropic, especially near the edges. Hence, application of a RANS model which assumes isotropic turbulence could be less accurate in simulating the generation of a surface plume.

The pie shaped grid following the downstream widening of the dredging plume in combination with the immersed boundary method to implement the TSHD hull allows for the use of a very rapid structured numerical solver. Novel, simple stream wise and rotational body forces are used to simulate propeller flow in a satisfactory manner. The synthetic eddy method is implemented to include ambient turbulence in the simulations. Sediment settling and air rising is taken into account by the drift velocity approach. A novel momentum advection scheme has been developed to generate accurate and stable simulation results for the challenging high  $Re$  flow of the dredging plume which acts as an obstacle.

New experiments are conducted to find the influence of dredging speed, overflow density, overflow location and propeller on the plume path and mixing. Existing, but unpublished and new field measurements are presented; they show a wide range in plume concentrations and distributions over the water column.

## 11.3 Overflow dredging plume mixing

Near field mixing of the dredging plume determines the initial vertical distribution of the sediment plume, which together with the settling velocity of the sediment determines how much remains in suspension. The settling velocity of the sediment particles in the dredging plume depends on the material being dredged. Only the finer sediment fractions of the dredged material will stay suspended for significant periods, coarser fractions will deposit very close to the dredger. Because of the large sediment concentrations in an overflow plume, flocculation of the finer fractions is likely. The following investigated conditions and processes have a strong influence on near field mixing and can cause significant differences in vertical distribution of the plume and the amount of sediment still in suspension:

- Crossflow velocity

The crossflow velocity consists of the vector sum of the dredging speed and ambient current. Together with the depth, it is the most important investigated factor determining the vertical distribution and amount of the dredging plume which is still in suspension. A high crossflow velocity leads to a larger plume flux still in suspension after a certain settling time, more sediment in higher parts of the water column and thus a large surface plume. A high crossflow velocity increases the interaction between the plume and the TSHD hull and the plume and the TSHD propellers.

- **Depth**

Together with the crossflow velocity, the depth is the most important investigated factor determining the vertical distribution and amount of the dredging plume which is still in suspension. A small depth leads to more sediment in higher parts of the water column and thus a large surface plume. Dredging in a small depth leads to a uniformly mixed plume over the vertical. Although a small depth leads to more surface plume, the plume flux still in suspension with a low depth is lower due to the small vertical settling distance. A small depth increases the interaction between the plume and the TSHD hull and the plume and the TSHD propellers.
- **Air**

Significant amounts of air, easily up to 10% in volume or more, can be entrained in an overflow with plunging inflow. A so-called green valve can reduce the amount of air entrainment by eliminating the plunging manner of inflow. An estimate of the amount of entrained air in the overflow without green valve can be obtained with Equation 2.14 or from Figure 2.4. Entrained air in the overflow generates a surface plume. The influence of entrained air is conditional, largest influence is found with a low crossflow velocity combined with a large depth. With high crossflow velocity and/or small depth a big surface plume with high turbidity at the free surface can be found, independent of the amount of entrained air.
- **Pulsing**

A pulsing, discontinuous flow in the overflow has been measured on a field trip. The pulsing frequency is dependent on the ambient wave period and the dynamic motions of the TSHD. Pulsing has two effects on the dredging plume: it enhances vertical spreading of the plume and it gives a deeper plume path. The deeper plume path is caused by the extra initial inflow momentum compared to a continuous non-pulsed case with similar volume flux. Pulsing can either enhance the formation of a surface plume by the increased vertical spreading or reduce the formation of a surface plume by the deeper plume path which reduces the influence of the TSHD hull and propellers. For a high crossflow velocity it is found that pulsing results in a smaller surface plume and for a low crossflow velocity pulsing results in a larger surface plume. Variation of the pulsing period between 5.5 and 11 seconds has hardly any influence.
- **Angle between TSHD path and ambient current**

When a TSHD is sailing under an angle with the ambient current, the overflow plume is pushed towards the side of the TSHD hull where it can be taken along by the expanding flow towards the free surface. The more the ambient current comes from the side, the more surface plume can be expected.
- **Propeller**

A propeller lifts the dredging plume up by entrainment into the propeller jet and this entrainment partly blocks the counter rotating vortex pair of the dredging plume. There is no indication that significant amounts of the dredging plume are sucked directly into the propeller.

- **Position overflow**  
When the overflow is near the aft of the TSHD then the propellers have more influence on plume mixing than when the overflow is in the front of the TSHD. The position of the overflow is less important with a large crossflow velocity or a small depth, because then the plume is near the propeller also when the overflow is in the front of the TSHD.
- **Overflow density**  
A larger initial overflow density brings the overflow plume quicker to the bed, this increases the deposition in the near field and reduces the interaction between the plume and the TSHD hull and the plume and the TSHD propellers. However, an increased overflow density also means a larger overflow sediment source flux is brought into suspension.
- **Overflow velocity**  
A larger initial overflow velocity brings the overflow plume quicker to the bed, this increases the deposition in the near field and reduces the interaction between the plume and the TSHD hull and the plume and the TSHD propellers. However, an increased overflow velocity also means a larger overflow sediment source flux is brought into suspension.

Guidelines to determine a far field source flux of suspended sediments from a TSHD while dredging in case measurements are lacking are given in Section 9.4.4. All the mentioned near field conditions and processes, which can be summarised by general buoyant JICF behaviour, interaction between plume and TSHD hull/aft/propellers, air entrainment, pulsing and interaction between plume and sea bed, must be incorporated in a near field simulation of TSHD plume mixing. For situations that such model results are not available and measurements are also lacking, a large set of the dredging plume simulation results are translated into mathematical relations in Equations 9.3-9.5, which predict, without computational effort, the vertical distribution and flux of the overflow plume downstream of a TSHD. They implicitly incorporate all investigated near field processes and are robust and reasonably accurate.

The concept of releasing the overflow mixture closer to the seabed by an IMPROVE (impact reducing overflow extension) looks promising for a reduction in the potential environmental impact of a dredging overflow plume. A reduction of 35% in the flux of fines remaining in suspension at the end of near field is found for an overflow extension up to the seabed.

## 11.4 Recommendations

The 3D CFD LES simulations have given valuable new insights in near field overflow dredging plume mixing. Therefore a first recommendation is to apply such rather heavy LES simulations, if necessary even on a supercomputer, also for other engineering cases where the intermittent turbulent behaviour is important and more schematised models like RANS or jet-integrated models might be less accurate. Examples of such cases in hydraulic engineering are the interaction



between a cooling water outlet or sediment plume and a nearby boundary or object, flow past a bridge pier, flow past a trench, turbulent high concentration suspended sediment flow or lock exchange flow. As a nice example of successful valorisation, this first recommendation is being put into practice at the hydraulic specialist consultancy firm Svašek Hydraulics.

Recommended improvements for the CFD model for dredging plume simulations are: adding the effect of a rudder to the propeller; using the real shape of (the aft of) a TSHD; and the implementation of compressibility of air. Implementation of a free surface instead of a rigid lid and being able to have surface waves would make the model applicable for situations where this is important like flow past a groyne, or the wave pattern and turbulent flow generated by a moving ship. In the CFD model a very fast direct FFT based pressure solver is used which only consumes about 15% of the total CPU time of a simulation, but a drawback is that it needs equidistant grid sizes in two directions and only one direction can be non-equidistant. There are situations where it would be beneficial to be able to apply a variable grid size in more than one direction to have increased resolutions in areas of interest. Implementation of a different pressure solver could be considered for those situations.

Extra field measurements are recommended to have field data on dredging plume mixing under an even wider range of conditions. Exact measurements on-board of a TSHD of the amount of entrained air in an overflow are recommended to verify the assessment of Equation 2.14. Exact on-board overflow volume flux measurements instead of using the assumption of an equal overflow and suction-pipe volume flux can show the temporal variation in overflow discharge. Extra dredging plume experiments with air entrainment and detailed measurements of the surface plume can provide extra insight and validation material for the CFD model on the influence of air on dredging plume mixing.



# References

- Aarninkhof, S., W. Rosenbrand, C. van Rhee, and T. Burt (2007). The Day After We Stop Dredging: A World Without Sediment Plumes? *Terra et Aqua* (110).
- Aarninkhof, S., J. Spearman, A. De Heer, and M. Van Koningsveld (2010). Dredging-induced turbidity in a natural context, status and future and perspective of the TASS Program. *Proceedings of the 19th world dredging conference (WODCON XIX)*.
- Amielh, M., T. Djeridane, F. Anselmet, and L. Fulachier (1996). Velocity near-field of variable density turbulent jets. *International Journal of Heat and Mass Transfer* 39(10), 2149 – 2164. URL: <http://www.sciencedirect.com/science/article/pii/S0017931095002944>. doi:[http://dx.doi.org/10.1016/0017-9310\(95\)00294-4](http://dx.doi.org/10.1016/0017-9310(95)00294-4).
- Andreopoulos, J. (1983). Heat transfer measurements in a heated jetpipe flow issuing into a cold cross stream. *Physics of Fluids (1958-1988)* 26(11), 3201–3210. URL: <http://scitation.aip.org/content/aip/journal/pof1/26/11/10.1063/1.864092>. doi:<http://dx.doi.org/10.1063/1.864092>.
- Andreopoulos, J. and W. Rodi (1984). Experimental investigation of jets in a crossflow. *J. Fluid Mech.* 138, 93–127. doi:<http://dx.doi.org/10.1017/S0022112084000057>.
- Ayoub, G. (1973). Test results on buoyant jets injected horizontally in a cross flowing stream. *Water, Air, and Soil Pollution* 2(4), 409–426. URL: <http://dx.doi.org/10.1007/BF00585086>. doi:10.1007/BF00585086.
- Berlamont, J. and E. Toorman (2000). COSINUS Final Scientific Report, part 2b. Technical report, K.U. Leuven.
- Blaauw, H. and J. v. d. Kaa (1978). Erosion of bottom and sloping banks caused by the screw race of manoeuvring schips. *Proceedings of the 7th International Harbour Congress*.
- Boersma, B. J. (2011). A 6th order staggered compact finite difference method for the incompressible NavierStokes and scalar transport equations. *Journal of Computational Physics* 230(12), 4940 – 4954. URL: <http://www.sciencedirect.com/science/article/pii/S0021999111001574>. doi:10.1016/j.jcp.2011.03.014.
- Boot, M. (2000). Near-field dispersal of overflow loss of hopper dredgers (in Dutch). Master's thesis, TU Delft. Civil Engineering.

- Bray, R. (Ed.) (2008). *Environmental aspects of dredging*. Taylor & Francis / Balkema.
- Bricteux, L., M. Duponcheel, and G. Winckelmans (2009). A multiscale subgrid model for both free vortex flows and wall-bounded flows. *Physics of Fluids* 21(10), 105102. URL: <http://link.aip.org/link/?PHF/21/105102/1>. doi:10.1063/1.3241991.
- Britter, R. E. and P. F. Linden (1980, 8). The motion of the front of a gravity current travelling down an incline. *Journal of Fluid Mechanics* 99, 531–543. URL: [http://journals.cambridge.org/article\\_S0022112080000754](http://journals.cambridge.org/article_S0022112080000754). doi:10.1017/S0022112080000754.
- Capello, M., L. Cutroneo, M. P. Ferranti, G. Budillon, R. M. Bertolotto, A. Ciappa, Y. Cotroneo, M. Castellano, P. Povero, and S. Tucci (2013). Simulations of dredged sediment spreading on a *Posidonia oceanica* meadow off the Ligurian coast, Northwestern Mediterranean. *Marine Pollution Bulletin* (0), -. URL: <http://www.sciencedirect.com/science/article/pii/S0025326X13007479>. doi:<http://dx.doi.org/10.1016/j.marpolbul.2013.12.014>.
- Cavar, D. and K. E. Meyer (2012). LES of turbulent jet in cross flow: Part 2 POD analysis and identification of coherent structures. *International Journal of Heat and Fluid Flow* 36(0), 35 – 46. URL: <http://www.sciencedirect.com/science/article/pii/S0142727X1200046X>. doi:<http://dx.doi.org/10.1016/j.ijheatfluidflow.2012.03.010>.
- Chanson, H. (2007). Air entrainment processes in a full-scale rectangular dropshaft at large flows. *Journal of Hydraulic Research* 45(1), 43–53. URL: <http://www.tandfonline.com/doi/abs/10.1080/00221686.2007.9521742>. doi:10.1080/00221686.2007.9521742.
- Chanson, H., S. Aoki, and A. Hoque (2002). Similitude of air bubble entrainment and dispersion in vertical circular plunging jet flows. An experimental study with freshwater, salty freshwater and seawater. Technical report, Toyohashi University of Technology, Japan.
- Chanson, H., S. Aoki, and A. Hoque (2006). Bubble entrainment and dispersion in plunging jet flows: freshwater vs. seawater. *Journal of coastal research*, 664–677. doi:<http://dx.doi.org/10.2112/03-0112.1>.
- Chen, Y., C. Li, and C. Zhang (2008). Numerical Modeling of a Round Jet Discharged into Random Waves. *Ocean Engineering* 35(1), 77 – 89. URL: <http://www.sciencedirect.com/science/article/pii/S0029801807001849>. doi:<http://dx.doi.org/10.1016/j.oceaneng.2007.07.011>.
- Chu, V. and M. Goldberg (1974). Buoyant forced plumes in crossflow. *Journal of Hydraulic Division* 100(9), 1203–1214. ASCE.
- Clift, R., J. Grace, and M. Weber (1978). *Bubbles, drops, and particles*. Academic Press.

- Contini, D. and A. Robins (2001). Water tank measurements of buoyant plume rise and structure in neutral crossflows. *Atmospheric Environment* 35(35), 6105 – 6115. URL: <http://www.sciencedirect.com/science/article/pii/S1352231001003983>. doi:10.1016/S1352-2310(01)00398-3.
- Crabb, D., D. Durao, and J. Whitelaw (1981). A round jet normal to a crossflow. *Journal of Fluids Engineering* 103, 142–153. doi:10.1115/1.3240764.
- Dankers, P. (2002). The behaviour of fines released due to dredging - a literature review. TU Delft.
- Dankers, P. and J. Winterwerp (2007). Hindered settling of mud flocs: Theory and validation. *Cont. Shelf Res.* 27, 1893–1907. doi:10.1016/j.csr.2007.03.005.
- Dantinne, G., H. Jeanmart, G. Winckelmans, V. Legat, and D. Carati (1997). Hyperviscosity and Vorticity-Based Models for Subgrid Scale Modeling. *Applied Scientific Research* 59, 409–420. URL: <http://dx.doi.org/10.1023/A%3A1001179014517>. doi:10.1023/A:1001179014517.
- Devenish, B., G. Rooney, H. Webster, and D. Thomson (2010). The Entrainment Rate for Buoyant Plumes in a Crossflow. *Boundary-Layer Meteorology* 134(3), 411–439. URL: <http://dx.doi.org/10.1007/s10546-009-9464-5>. doi:10.1007/s10546-009-9464-5.
- Djeridane, T., M. Amielh, F. Anselmet, and L. Fulachier (1996). Velocity turbulence properties in the nearfield region of axisymmetric variable density jets. *Physics of Fluids (1994-present)* 8(6), 1614–1630. URL: <http://scitation.aip.org/content/aip/journal/pof2/8/6/10.1063/1.868935>. doi:<http://dx.doi.org/10.1063/1.868935>.
- Ducros, F., F. Laporte, T. Soulres, V. Guinot, P. Moinat, and B. Caruelle (2000). High-Order Fluxes for Conservative Skew-Symmetric-like Schemes in Structured Meshes: Application to Compressible Flows. *Journal of Computational Physics* 161(1), 114 – 139. URL: <http://www.sciencedirect.com/science/article/pii/S0021999100964921>. doi:<http://dx.doi.org/10.1006/jcph.2000.6492>.
- Eekelen, E. (2007). Experimental research on dynamic dredge overflow plumes. Master's thesis, TU Delft. Civil Engineering.
- Erftemeijer, P. L. and R. R. R. Lewis-III (2006). Environmental impacts of dredging on seagrasses: A review. *Marine Pollution Bulletin* 52(12), 1553 – 1572. URL: <http://www.sciencedirect.com/science/article/pii/S0025326X06003778>. doi:10.1016/j.marpolbul.2006.09.006.
- Erftemeijer, P. L., B. Riegl, B. W. Hoeksema, and P. A. Todd (2012). Environmental impacts of dredging and other sediment disturbances on corals: A review. *Marine Pollution Bulletin* 64(9), 1737 – 1765. URL: <http://www.sciencedirect.com/science/article/pii/S0025326X12001981>. doi:10.1016/j.marpolbul.2012.05.008.

- Ervine, D. (1998). Air entrainment in hydraulic structures: A review. *Proceedings of The Institution of Civil Engineers-Water Maritime and Energy* 130(3), 142–153. doi:10.1680/iwtme.1998.30973.
- Fadlun, E., R. Verzicco, P. Orlandi, and J. Mohd-Yusof (2000). Combined Immersed-Boundary Finite-Difference Methods for Three-Dimensional Complex Flow Simulations. *Journal of Computational Physics* 161(1), 35 – 60. URL: <http://www.sciencedirect.com/science/article/pii/S0021999100964842>. doi:10.1006/jcph.2000.6484.
- Fan, L. (1967). Turbulent buoyant jets into stratified or flowing ambient fluids. Technical report, W.M. Keck Lab. of Hydr. and Water Resources, California Inst. of Tech. Report No. KH-R-15.
- Fischer, H., E. List, R. Koh, J. Imberger, and N. Brooks (1979). *Mixing in Inland and Coastal Waters*. Academic Press.
- Franke, J. and W. Frank (2002). Large eddy simulation of the flow past a circular cylinder at  $Re_D=3900$ . *Journal of Wind Engineering and Industrial Aerodynamics* 90(10), 1191 – 1206. URL: <http://www.sciencedirect.com/science/article/pii/S0167610502002325>. doi:10.1016/S0167-6105(02)00232-5.
- Fric, T. and A. Roshko (1994). Vortical structure in the wake of a transverse jet. *Journal of Fluid Mechanics* 279, 1–47. doi:<http://dx.doi.org/10.1017/S0022112094003800>.
- Fuehrer, M., H. Pohl, and K. Römisch (1987). Propeller jet erosion and stability criteria for bottom protections of various constructions. *PIANC Bulletin* (58), 45–56.
- Galeazzo, F. C. C., G. Donnert, P. Habisreuther, N. Zarzalis, R. J. Valdes, and W. Krebs (2011). Measurement and Simulation of Turbulent Mixing in a Jet in Crossflow. *Journal of Engineering for Gas Turbines and Power* 133(6), 061504. URL: <http://link.aip.org/link/?GTP/133/061504/1>. doi:10.1115/1.4002319.
- Gilkinson, K., G. Fader, D. G. Jr., R. Charron, D. McKeown, D. Roddick, E. Kenchington, K. MacIsaac, C. Bourbonnais, P. Vass, and Q. Liu (2003). Immediate and longer-term impacts of hydraulic clam dredging on an offshore sandy seabed: effects on physical habitat and processes of recovery. *Continental Shelf Research* 23(1415), 1315 – 1336. URL: <http://www.sciencedirect.com/science/article/pii/S0278434303001237>. doi:10.1016/S0278-4343(03)00123-7.
- Hallworth, M. A., A. J. Hogg, and H. E. Huppert (1998). Effects of external flow on compositional and particle gravity currents. *Journal of Fluid Mechanics* 359(1), 109–142. doi:<http://dx.doi.org/10.1017/S0022112097008409>.
- Hannot, S. (2014, Royal IHC). Rolling period TSHD. private communication.
- Hartmann, H., J. Derksen, C. Montavon, J. Pearson, I. Hamill, and H. van den Akker (2004). Assessment of large eddy and RANS stirred tank simulations by means of LDA. *Chemical Engineering Science* 59(12), 2419



- 2432. URL: <http://www.sciencedirect.com/science/article/pii/S0009250904001575>. doi:<http://dx.doi.org/10.1016/j.ces.2004.01.065>.
- Hayes, D., G. Raymond, and T. Mc Lellan (1984). Sediment resuspension from dredging activities. *Dredging and dredged material disposal 1*, 72–82. Proc. of Conf. Dredging, Florida, USA.
- Hirsch, C. (1990). *Numerical computation of internal and external flows*. A Wiley Interscience Publication.
- Hughes, T. J. R., L. Mazzei, A. A. Oberai, and A. A. Wray (2001). The multiscale formulation of large eddy simulation: Decay of homogeneous isotropic turbulence. *Physics of Fluids* 13(2), 505–512. URL: <http://link.aip.org/link/?PHF/13/505/1>. doi:10.1063/1.1332391.
- Jacobs, W. (2011). *Sand-mud erosion from a soil mechanical perspective*. Ph. D. thesis, Delft University of Technology.
- Jameson, A., W. Schmidt, and E. Turkel (1981). Numerical Solution of the Euler Equations by Finite Volume Methods Using Runge-Kutta Time-Stepping Schemes. *AIAA Paper*, 81–1259.
- Jarrin, N. (2008). *Synthetic inflow boundary conditions for the numerical simulation of turbulence*. Ph. D. thesis, University of Manchester.
- Jarrin, N., S. Benhamadouche, D. Laurence, and R. Prosser (2006). A synthetic-eddy-method for generating inflow conditions for large-eddy simulations. *International Journal of Heat and Fluid Flow* 27(4), 585 – 593. URL: <http://www.sciencedirect.com/science/article/pii/S0142727X06000282>. doi:<http://dx.doi.org/10.1016/j.ijheatfluidflow.2006.02.006>.
- Jirka, G. (2004). Integral Model for Turbulent Buoyant Jets in Unbounded Stratified Flows. Part I: Single Round Jet. *Environmental Fluid Mechanics* 4(1), 1–56. URL: <http://dx.doi.org/10.1023/A%3A1025583110842>. doi:10.1023/A:1025583110842.
- Jirka, G. (2007). Buoyant Surface Discharges into Water Bodies. II: Jet Integral Model. *Journal of Hydraulic Engineering* 133(9), 1021–1036. doi:10.1061/(ASCE)0733-9429(2007)133:9(1021).
- Kaltenbach, H. and H. Choi (1995). Large eddy simulation of flow around an airfoil on a structured mesh. *Center for turbulence research, annual research briefs*, 51–60.
- Karaca, M., N. Lardjane, and I. Fedoun (2012). Implicit Large Eddy Simulation of high-speed non-reacting and reacting air/H<sub>2</sub> jets with a 5th order WENO scheme. *Computers and Fluids* 62(0), 25 – 44. URL: <http://www.sciencedirect.com/science/article/pii/S0045793012001004>. doi:10.1016/j.compfluid.2012.03.013.
- Kawai, S. and S. Lele (2010). Large-Eddy Simulation of Jet Mixing in Supersonic Crossflows. *AIAA Journal* 48(9), 2063–2083. URL: <http://arc.aiaa.org/doi/abs/10.2514/1.J050282>. doi:10.2514/1.J050282.

- Kawai, S., S. K. Shankar, and S. K. Lele (2010). Assessment of localized artificial diffusivity scheme for large-eddy simulation of compressible turbulent flows. *Journal of Computational Physics* 229(5), 1739 – 1762. URL: <http://www.sciencedirect.com/science/article/pii/S0021999109006160>. doi:10.1016/j.jcp.2009.11.005.
- Kim, C. S. and H.-S. Lim (2009). Sediment dispersal and deposition due to sand mining in the coastal waters of Korea. *Continental Shelf Research* 29(1), 194 – 204. URL: <http://www.sciencedirect.com/science/article/pii/S0278434308000320>. doi:<http://dx.doi.org/10.1016/j.csr.2008.01.017>, Physics of Estuaries and Coastal Seas: Papers from the PECS 2006 Conference.
- Kogaki, T., T. Kobayashi, and N. Taniguchi (1997). Large eddy simulation of flow around a rectangular cylinder. *Fluid Dynamics Research* 20(16), 11 – 24. URL: <http://www.sciencedirect.com/science/article/pii/S0169598396000408>. doi:[http://dx.doi.org/10.1016/S0169-5983\(96\)00040-8](http://dx.doi.org/10.1016/S0169-5983(96)00040-8), International Symposium on Mathematical of Turbulent Flows.
- Kotsovinos, N. E. (1991). Turbulence spectra in free convection flow. *Physics of Fluids A: Fluid Dynamics* 3(1), 163–167. URL: <http://link.aip.org/link/?PFA/3/163/1>. doi:10.1063/1.857875.
- Krajnović, S. and L. Davidson (2002). Large-Eddy Simulation of the Flow Around a Bluff Body. *AIAA Journal* 40(5), 927–936.
- Krajnovic, S., S. Sarmast, and B. Basara (2011). Numerical Investigation of the Flow Around a Simplified Wheel in a Wheelhouse. *Journal of Fluids Engineering* 133(11), 111001. URL: <http://link.aip.org/link/?JFG/133/111001/1>. doi:10.1115/1.4004992.
- Kravchenko, A. and P. Moin (1997). On the Effect of Numerical Errors in Large Eddy Simulations of Turbulent Flows. *Journal of Computational Physics* 131(2), 310 – 322. URL: <http://www.sciencedirect.com/science/article/pii/S0021999196955977>. doi:<http://dx.doi.org/10.1006/jcph.1996.5597>.
- Lai, C. and J. Lee (2013). Initial mixing of inclined dense jet in perpendicular crossflow. *Environmental Fluid Mechanics*, 1–25. URL: <http://dx.doi.org/10.1007/s10652-013-9290-7>. doi:10.1007/s10652-013-9290-7.
- Lam, W., G. Hamill, Y.-c. Song, D. Robinson, and S. Raghunathan (2011). Experimental investigation of the decay from a ships propeller. *China Ocean Engineering* 25(2), 265–284. URL: <http://dx.doi.org/10.1007/s13344-011-0022-9>. doi:10.1007/s13344-011-0022-9.
- Lamarque, N., B. Zopp, O. Lebaigue, Y. Dolias, M. Bertrand, and F. Ducros (2010). Large-eddy simulation of the turbulent free-surface flow in an unbaffled stirred tank reactor. *Chemical Engineering Science* 65(15), 4307 – 4322. URL: <http://www.sciencedirect.com/science/article/pii/S0009250910001624>. doi:10.1016/j.ces.2010.03.014.

- Lee, J. and V. Chu (2003). *Turbulent jets and plumes*. Kluwer Academic Publishers.
- Lele, S. K. (1992). Compact finite difference schemes with spectral-like resolution. *Journal of Computational Physics* 103(1), 16 – 42. URL: <http://www.sciencedirect.com/science/article/pii/002199919290324R>. doi:[http://dx.doi.org/10.1016/0021-9991\(92\)90324-R](http://dx.doi.org/10.1016/0021-9991(92)90324-R).
- Liu, K. (2013). Near field buoyant jet analysis - a study of buoyant jet behaviour at dredging operations. Master's thesis, TU Delft. Dredging Engineering.
- Lumley, J. L. (1978). Computational modeling of turbulent flows. *Advances in applied mechanics* 18(123), 213.
- Makiola, B. (1992). *Experimentelle Untersuchungen zur Strömung über die schräge Stufe*. Ph. D. thesis, Institute für Hydromechanik, Universität.
- Manninen, M., V. Taivassalo, and S. Kallio (1996). On the Mixture Model for Multiphase Flow VTT Publications 288. *Technical Research Center of Finland*.
- Margason, R. (1993). Fifty years of jet in crossflow research. *Proceedings of AGARD conference on Computational and Experimental Assessment of Jets in Cross Flow*. AGARD.
- Martinuzzi, R. and H. Hussein (1993). The flow around surface-mounted prismatic obstacles placed in a fully developed channel flow. *ASME J. of Fluids Eng.* 115, 85–92.
- Mastbergen, D. and J. Winterwerp (1987). Het gedrag van zand-watermengselstromingen boven water; experimentele vervolgstudie. Technical report, WL—Delft Hydraulics (in Dutch).
- Menon, S. and M. Rizk (1996). Large-Eddy Simulations of forced three dimensional impinging jets. *Int. J. Computational Fluid Dynamics* 7, 275–289. URL: <http://dx.doi.org/10.1080/10618569608940766>. doi:10.1080/10618569608940766.
- Mestres, M., J. P. Sierra, C. Mösso, A. Sánchez-Arcilla, M. Hernáez, and J. Morales (2013). Numerical assessment of the dispersion of overspilled sediment from a dredge barge and its sensitivity to various parameters. *Marine Pollution Bulletin* (0). URL: <http://www.sciencedirect.com/science/article/pii/S0025326X1300742X>. doi:<http://dx.doi.org/10.1016/j.marpolbul.2013.12.009>.
- Morinishi, Y. (2010). Skew-symmetric form of convective terms and fully conservative finite difference schemes for variable density low-Mach number flows. *Journal of Computational Physics* 229(2), 276 – 300. URL: <http://www.sciencedirect.com/science/article/pii/S0021999109005130>. doi:<http://dx.doi.org/10.1016/j.jcp.2009.09.021>.
- Morinishi, Y., T. Lund, O. Vasilyev, and P. Moin (1998). Fully Conservative Higher Order Finite Difference Schemes for Incompressible Flow. *Journal of Computational Physics* 143(1), 90 – 124. URL: <http://www.sciencedirect.com>.

- [com/science/article/pii/S0021999198959629](http://com/science/article/pii/S0021999198959629). doi:<http://dx.doi.org/10.1006/jcph.1998.5962>.
- Moser, R. D., J. Kim, and N. N. Mansour (1999). Direct numerical simulation of turbulent channel flow up to  $Re_\tau = 590$ . *Physics of Fluids* 11(4), 943–945. URL: <http://link.aip.org/link/?PHF/11/943/1>. doi:10.1063/1.869966.
- Muldoon, F. and S. Acharya (2010). Direct Numerical Simulation of pulsed jets-in-crossflow. *Computers and Fluids* 39(10), 1745 – 1773. URL: <http://www.sciencedirect.com/science/article/pii/S0045793010000848>. doi:10.1016/j.compfluid.2010.04.008.
- MCloskey, R. T., J. M. King, L. Cortelezzi, and A. R. Karagozian (2002). The actively controlled jet in crossflow. *Journal of Fluid Mechanics* 452, 325–335. URL: <http://dx.doi.org/10.1017/S0022112001006589>. doi:10.1017/S0022112001006589.
- Najm, H. N., P. S. Wyckoff, and O. M. Knio (1998). A Semi-implicit Numerical Scheme for Reacting Flow: I. Stiff Chemistry. *Journal of Computational Physics* 143(2), 381 – 402. URL: <http://www.sciencedirect.com/science/article/pii/S0021999197958563>. doi:<http://dx.doi.org/10.1006/jcph.1997.5856>.
- Nakata, K., Y. Okayama, and J. Lavelle (1989). An attempt to evaluate the effects of an anti-turbidity system on sediment dispersion from a hopper dredge. *NOAA Technical Memorandum ERL PMEL-85 0*, 1–30.
- Narayanan, S., P. Barooah, and J. Cohen (2003). Dynamics and control of an isolated jet in crossflow. *AIAA journal* 41(12), 2316–2330. URL: <http://arc.aiaa.org/doi/abs/10.2514/2.6847>. doi:10.2514/2.6847.
- Newell, R., D. Hitchcock, and L. Seiderer (1999). Organic Enrichment Associated with Outwash from Marine Aggregates Dredging: A Probable Explanation for Surface Sheens and Enhanced Benthic Production in the Vicinity of Dredging Operations. *Marine Pollution Bulletin* 38(9), 809 – 818. URL: <http://www.sciencedirect.com/science/article/pii/S0025326X99000454>. doi:[http://dx.doi.org/10.1016/S0025-326X\(99\)00045-4](http://dx.doi.org/10.1016/S0025-326X(99)00045-4).
- Nichols, M., R. Diaz, and L. Schaffner (1990). Effects of hopper dredging and sediment dispersion, Chesapeake Bay. *Environmental Geology and Water Sciences* 15(1), 31–43. URL: <http://dx.doi.org/10.1007/BF01704879>. doi:10.1007/BF01704879.
- Nicoud, F. and F. Ducros (1999). Subgrid-Scale Stress Modelling Based on the Square of the Velocity Gradient Tensor. *Flow, Turbulence and Combustion* 62(3), 183–200. URL: <http://dx.doi.org/10.1023/A%3A1009995426001>. doi:10.1023/A:1009995426001.
- Nienhuis, U. (1992). *Analysis of thruster effectivity*. Ph. D. thesis, Delft University of Technology.

- Pagliai, A. B., A. C. Varriale, R. Crema, M. C. Galletti, and R. V. Zunarelli (1985). Environmental impact of extensive dredging in a coastal marine area. *Marine Pollution Bulletin* 16(12), 483 – 488. URL: <http://www.sciencedirect.com/science/article/pii/0025326X85903819>. doi:10.1016/0025-326X(85)90381-9.
- Papanicolaou, P. and E. List (1988). Investigations of round vertical turbulent buoyant jets. *Journal of Fluid Mechanics* 195(1), 341–391. doi:<http://dx.doi.org/10.1017/S0022112088002447>.
- Park, N., J. Y. Yoo, and H. Choi (2004). Discretization errors in large eddy simulation: on the suitability of centered and upwind-biased compact difference schemes. *Journal of Computational Physics* 198(2), 580 – 616. URL: <http://www.sciencedirect.com/science/article/pii/S0021999104000531>. doi:<http://dx.doi.org/10.1016/j.jcp.2004.01.017>.
- Parys, M. V., G. Dumon, P. A., S. Claeys, J. Lanckneus, V. V. Lancker, M. Vangheluwe, P. V. Sprang, L. V. Speleers, and C. Janssen (2001). Environmental monitoring of the dredging and relocation operations in the coastal harbours in Belgium: MOBAG 2000. WODCON XVI.
- Pirozzoli, S. (2011). Numerical Methods for High-Speed Flows. *Annual Review of Fluid Mechanics* 43(1), 163–194. URL: <http://dx.doi.org/10.1146/annurev-fluid-122109-160718>. doi:10.1146/annurev-fluid-122109-160718.
- Pope, S. (2000). *Turbulent flows*. Cambridge University Press.
- Pourquié, M. (1994). *Large Eddy Simulation of a turbulent jet*. Ph. D. thesis, Delft University of Technology.
- Prooijen, B. v. and J. Winterwerp (2010). A stochastic formulation for erosion of cohesive sediments. *J. of Geophys. Res.* 115(C01005). doi:10.1029/2008JC005189.
- Prosser, M. (1986). *Propeller induced scour*. BHRA Report RR 2570.
- Rhee, C. v. (2002). *On the sedimentation process in a Trailing Suction Hopper Dredger*. Ph. D. thesis, TU Delft.
- Rhee, S. and H. Kim (2008). A suggestion of gap flow control devices for the suppression of rudder cavitation. *Journal of Maritime Scientific Technology* 13, 356–370. doi:10.1007/s00773-008-0013-6.
- Richardson, Y. and W. Zaki (1954). Sedimentation and Fluidization. *Part I*. *Trans. Inst. Chem. Eng.* 32, 35–53.
- Rijn, L. v. (1993). *Principles of sediment transport in rivers, estuaries and coastal seas*. Aqua Publications.
- RIZA (2005). Vertroebeling tijdens en na baggeren met sleepopperzuiger in het Noordzeekanaal (in Dutch). Technical report, RIZA rapport 2005.006. Kraaijeveld, M., Fioole, A.
- Rodi, W. (1998). Large-Eddy Simulations of the flow past Bluff Bodies: State-of-the-Art. *JSME Int. Journal* 41(2), 361–374.



- Rowe, P. (1987). A convenient empirical equation for estimation of the Richardson-Zaki exponent. *Chemical Engineering Science* 42(11), 2795–2796.
- Sagaut, P. (1999). *Large Eddy Simulation for incompressible flows*. Scientific Computation. Springer.
- Schlüter, J. and T. Schönfeld (2000). LES of Jets in Cross Flow and Its Application to a Gas Turbine Burner. *Flow, Turbulence and Combustion* 65(2), 177–203. URL: <http://dx.doi.org/10.1023/A%3A1011412810639>. doi:10.1023/A:1011412810639.
- Simonsen, A. J. and P.-A. Krogstad (2005). Turbulent stress invariant analysis: Clarification of existing terminology. *Physics of Fluids* 17(8), 088103. URL: <http://link.aip.org/link/?PHF/17/088103/1>. doi:10.1063/1.2009008.
- Smith, S. J. and C. T. Friedrichs (2011). Size and settling velocities of cohesive flocs and suspended sediment aggregates in a trailing suction hopper dredge plume. *Continental Shelf Research* 31(10, Supplement), S50 – S63. URL: <http://www.sciencedirect.com/science/article/pii/S0278434310001160>. doi:10.1016/j.csr.2010.04.002, Proceedings of the 9th International Conference on Nearshore and Estuarine Cohesive Sediment Transport Processes.
- Socolofsky, S. and E. Adams (2002). Multi-phase plumes in uniform and stratified crossflow. *Journal of Hydraulic Research* 40(6), 661–672. doi:10.1080/00221680209499913.
- Spearman, J., A. De Heer, S. Aarninkhof, and M. Van Koningsveld (2011). Validation of the TASS system for predicting the environmental effects of trailing suction hopper dredgers. *Terra et Aqua* (125).
- Stern, F., H. Kim, V. Patel, and H. Chen (1988). A viscous-flow approach to the computation of propeller-hull interaction. *Journal of Ship Research* 32(4), 246–262.
- Sykes, R., W. Lewellen, and S. Parker (1986). On the vorticity dynamics of a turbulent jet in a crossflow. *J. Fluid Mech.* 168, 393–413. doi:<http://dx.doi.org/10.1017/S0022112086000435>.
- VBKO (2003). Protocol for the Field Measurement of Sediment Release from Dredgers Issue 1 August 2003. Technical report, VBKO TASS Project. HR Wallingford Ltd and Dredging Research Ltd.
- Verstappen, R. and A. Veldman (2003). Symmetry-preserving discretization of turbulent flow. *Journal of Computational Physics* 187(1), 343 – 368. URL: <http://www.sciencedirect.com/science/article/pii/S0021999103001268>. doi:[http://dx.doi.org/10.1016/S0021-9991\(03\)00126-8](http://dx.doi.org/10.1016/S0021-9991(03)00126-8).
- Violeau, D., S. Bourban, C. Cheviet, M. Markofsky, O. Petersen, W. Roberts, J. Spearman, E. Toorman, H. Vested, and H. Weilbeer (2002). Numerical simulation of cohesive sediment transport: intercomparison of several numerical models. In J. C. Winterwerp and C. Kranenburg (Eds.), *Fine*



- Sediment Dynamics in the Marine Environment*, Volume 5 of *Proceedings in Marine Science*, pp. 75 – 89. Elsevier. URL: <http://www.sciencedirect.com/science/article/pii/S1568269202800092>. doi:[http://dx.doi.org/10.1016/S1568-2692\(02\)80009-2](http://dx.doi.org/10.1016/S1568-2692(02)80009-2).
- Wakeman, T., J. Sustar, and W. Dickson (1975). Impact of three dredge types compared in San Francisco District. *World Dredging and Marine Construction*, 9–14.
- Wang, P., J. Fröhlich, V. Michelassi, and W. Rodi (2008). Large-eddy simulation of variable-density turbulent axisymmetric jets. *International Journal of Heat and Fluid Flow* 29(3), 654 – 664. URL: <http://www.sciencedirect.com/science/article/pii/S0142727X08000271>. doi:<http://dx.doi.org/10.1016/j.ijheatfluidflow.2008.02.002>, The Fifth International Symposium on Turbulence and Shear Flow Phenomena (TSFP5).
- Wang, Z. and J. Ribberink (1986). The validity of a depth-integrated model for suspended sediment transport. *Journal of Hydraulic Research* 24(1), 53–67. doi:[10.1080/00221688609499332](https://doi.org/10.1080/00221688609499332).
- Wegner, B., Y. Huai, and A. Sadiki (2004). Comparative study of turbulent mixing in jet in cross-flow configurations using LES. *International Journal of Heat and Fluid Flow* 25(5), 767 – 775. URL: <http://www.sciencedirect.com/science/article/pii/S0142727X04000931>. doi:<http://dx.doi.org/10.1016/j.ijheatfluidflow.2004.05.015>, Selected papers from the 4th International Symposium on Turbulence Heat and Mass Transfer.
- Wesseling, P. (2000). *Principles of Computational Fluid Dynamics*. Springer.
- Whiteside, P., K. Ooms, and G. Postma (1995). Generation and decay of sediment plumes from sand dredging overflow. *Proceedings of the 14th world dredging congress*, 877–892.
- Wicker, L. and W. Skamarock (2002). Time-splitting Methods for Elastic Models Using Forward Time Schemes. *Monthly Weather Review* 130, 2088–2097. doi:[http://dx.doi.org/10.1175/1520-0493\(2002\)130<2088:TSMFEM>2.0.CO;2](http://dx.doi.org/10.1175/1520-0493(2002)130<2088:TSMFEM>2.0.CO;2).
- Winterwerp, J. (1999). *On the Dynamics of High-Concentrated Mud Suspensions*. Ph. D. thesis, Delft University of Technology.
- Winterwerp, J. (2002). Near-Field Behavior of Dredging Spill in Shallow Water. *Journal of Waterway, Port, Coastal, and Ocean Engineering* 128(2), 96–98. URL: <http://ascelibrary.org/doi/abs/10.1061/%28ASCE%290733-950X%282002%29128%3A2%2896%29>. doi:[10.1061/\(ASCE\)0733-950X\(2002\)128:2\(96\)](https://doi.org/10.1061/(ASCE)0733-950X(2002)128:2(96)).
- Winterwerp, J. (2007). On the deposition flux of cohesive sediment. *Proceedings of the 8th International Conference on Nearshore and Estuarine Cohesive Sediment Transport Processes INTERCOH-2003*, 209–226. ed. J. Maa, L. Sanford and D. Shoelhamer.
- Winterwerp, J., M. de Groot, D. Mastbergen, and H. Verwoert (1990). Hyperconcentrated SandWater Mixture Flows Over a Flat Bed. *Journal of*

- Hydraulic Engineering* 116(1), 36–54. URL: <http://ascelibrary.org/doi/abs/10.1061/%28ASCE%290733-9429%281990%29116%3A1%2836%29>. doi:10.1061/(ASCE)0733-9429(1990)116:1(36).
- Winterwerp, J. and W. v. Kesteren (2004). *Introduction to the physics of cohesive sediment in the marine environment*. Developments in sedimentology. Elsevier.
- Wood, J. D. and D. Boyé (2007). Monitoring suspended sediment plumes using an Acoustic Doppler Current Profiler. *Oceans*, 1–7. doi:10.1109/OCEANS.2007.4449165.
- Worthy, J. (2003). *Large Eddy Simulation of buoyant plumes*. Ph. D. thesis, Cranfield University.
- Xie, Z.-T. and I. Castro (2008). Efficient Generation of Inflow Conditions for Large Eddy Simulation of Street-Scale Flows. *Flow, Turbulence and Combustion* 81(3), 449–470. URL: <http://dx.doi.org/10.1007/s10494-008-9151-5>. doi:10.1007/s10494-008-9151-5.
- Yuan, L., R. Street, and J. Ferziger (1999). Large eddy simulation of a round jet in crossflow. *J. Fluid Mech.* 379, 71–104. doi:<http://dx.doi.org/10.1017/S0022112098003346>.
- Yuan, L. L. and R. L. Street (1998). Trajectory and entrainment of a round jet in crossflow. *Physics of Fluids* 10(9), 2323–2335. URL: <http://scitation.aip.org/content/aip/journal/pof2/10/9/10.1063/1.869751>. doi:<http://dx.doi.org/10.1063/1.869751>.
- Zhang, W. and D. Z. Zhu (2013). Bubble characteristics of air-water bubbly jets in crossflow. *International Journal of Multiphase Flow* 55(0), 156 – 171. URL: <http://www.sciencedirect.com/science/article/pii/S0301932213000761>. doi:<http://dx.doi.org/10.1016/j.ijmultiphaseflow.2013.05.003>.
- Zhou, X., K. H. Luo, and J. J. Williams (2001). Large-eddy simulation of a turbulent forced plume. *European Journal of Mechanics - B/Fluids* 20(2), 233 – 254. URL: <http://www.sciencedirect.com/science/article/pii/S0997754600011171>. doi:10.1016/S0997-7546(00)01117-1.
- Ziefle, J. and L. Kleiser (2009). Large-Eddy Simulation of a Round jet in Crossflow. *AIAA Journal* 47(5), 1158–1172. doi:10.2514/1.38465.

# List of Symbols

## Roman Symbols

$B_{j0}$	initial buoyancy flux buoyant jet	$[\text{m}^5/\text{s}^2]$
$C$	volume concentration	$[-]$
$C'$	turbulent fluctuation in volume concentration	$[-]$
$C_{floc}$	floc volume concentration	$[-]$
$C_j$	local buoyant jet volume concentration	$[-]$
$C_{j0}$	initial buoyant jet volume concentration	$[-]$
$C_l$	volume concentration of fraction $l$	$[-]$
$C_{max}$	maximum jet volume concentration	$[-]$
$C_s$	constant in sub-grid scale model	$[-]$
$C_t$	total volume concentration	$[-]$
$CFL$	Courant Friedrichs Lewy number	$[-]$
$D$	diameter (of pipe)	$[\text{m}]$
$D_{50}$	50th percentile sediment particle diameter	$[\text{m}]$
$D_{90}$	90th percentile sediment particle diameter	$[\text{m}]$
$D_f$	mud floc diameter	$[\text{m}]$
$D_p$	particle diameter	$[\text{m}]$
$D_{pr}$	propeller diameter	$[\text{m}]$
$Dep_l$	deposition flux of fraction $l$	$[\text{kg}/\text{s}/\text{m}^2]$
$Ero_l$	erosion flux of fraction $l$	$[\text{kg}/\text{s}/\text{m}^2]$
$f$	frequency	$[1/\text{s}]$
$\mathbf{f}$	body force acceleration vector	$[\text{m}^2/\text{s}]$
$FF_{mf}$	mid field suspended fine sediment flux (ratio with $FF_{overflow}$ )	$[-]$
$FF_{nf}$	near field suspended fine sediment flux (ratio with $FF_{overflow}$ )	$[-]$
$FF_{overflow}$	suspended fine sediment flux through overflow	$[\text{kg}/\text{s}]$
$g$	gravity constant	$[\text{m}^2/\text{s}]$
$H$	flow depth	$[\text{m}]$
$k_n$	added mass coefficient	$[-]$
$k_s$	Nikuradse wall roughness	$[\text{m}]$
$k^{res}$	resolved turbulent kinetic energy	$[\text{m}^2/\text{s}^2]$
$k^{sgs}$	unresolved turbulent kinetic energy in sub-grid scales	$[\text{m}^2/\text{s}^2]$
$L$	wave length	$[\text{m}]$
$l_m$	momentum length scale buoyant jet	$[\text{m}]$
$M_l$	erosion rate constant of fraction $l$	$[\text{kg}/\text{s}/\text{m}^2]$
$n_{pr}$	number of propellers	$[\text{m}]$

$P$	pressure	[N/m <sup>2</sup> ]
$P_{pr}$	propeller power	[W]
$PERC^{res}$	percentage resolved turbulent kinetic energy	[-]
$ppw$	number of grid points per wavelength	[-]
$Q$	discharge	[m <sup>3</sup> /s]
$q$	discharge per unit width	[m <sup>2</sup> /s]
$Q_{air}$	air discharge	[m <sup>3</sup> /s]
$q_{air}$	air discharge per unit width	[m <sup>2</sup> /s]
$Q_{j0}$	initial discharge buoyant jet or overflow	[m <sup>3</sup> /s]
$Q_{water}$	water discharge	[m <sup>3</sup> /s]
$r$	coordinate along horizontal axis in cylindrical coordinates	[m]
$r_j$	local buoyant jet radius	[m]
$Re$	Reynolds number	[-]
$Re_f$	Reynolds number based on the mud floc settling velocity	[-]
$Re_p$	Reynolds number based on the particle settling velocity	[-]
$Re_\tau$	Reynolds number based on the friction velocity	[-]
$RHS$	right hand side	[-]
$Ri$	Richardson number	[-]
$S_{j0}$	suspended sediment flux through overflow	[kg/s]
$S_{mf}$	mid field suspended sediment flux	[kg/s]
$S_{nf}$	near field suspended sediment flux	[kg/s]
$Sc$	Schmidt number	[-]
$SSC$	suspended sediment concentration	[kg/m <sup>3</sup> ]
$SSC_{gel}$	gelling concentration mud flocs	[kg/m <sup>3</sup> ]
$St$	Strouhal number	[-]
$t$	time	[s]
$T_p$	pulsing period	[s]
$T_{pr}$	propeller thrust	[N]
$U$	velocity	[m/s]
$u$	horizontal streamwise velocity	[m/s]
$\mathbf{u}$	velocity vector	[m/s]
$u_*$	friction velocity	[m/s]
$u'$	turbulent fluctuation of horizontal streamwise velocity	[m/s]
$u'w'$	turbulent shear stress	[m <sup>2</sup> /s <sup>2</sup> ]
$u_a$	ambient streamwise velocity	[m/s]
$u_{ambient}$	ambient velocity	[m/s]
$u_{cf}$	crossflow velocity	[m/s]
$u_j$	local horizontal streamwise velocity buoyant jet	[m/s]
$\mathbf{u}_l$	velocity vector of fraction $l$	[m/s]
$u_{pr}$	propeller streamwise velocity	[m/s]
$u_{TSHD}$	sailing speed TSHD	[m/s]
$v$	horizontal lateral velocity	[m/s]
$v'$	turbulent fluctuation of horizontal lateral velocity	[m/s]
$v_a$	ambient lateral velocity	[m/s]
$w$	vertical velocity	[m/s]
$w'$	turbulent fluctuation of vertical velocity	[m/s]
$w_{drift,l}$	vertical drift velocity of fraction $l$	[m/s]

$w_j$	local vertical velocity buoyant jet	[m/s]
$w_{j0}$	initial vertical velocity of buoyant jet or overflow plume	[m/s]
$w_l$	vertical velocity of fraction $l$	[m/s]
$w_{mix}$	vertical mixture velocity	[m/s]
$w_s$	hindered sediment settling velocity	[m/s]
$w_{s,f}$	hindered floc settling velocity	[m/s]
$w_{s,l}$	settling velocity of fraction $l$	[m/s]
$w_0$	unhindered sediment settling velocity	[m/s]
$w_{0,f}$	floc settling velocity	[m/s]
$w_{0,p}$	particle settling velocity	[m/s]
$x$	coordinate along horizontal streamwise axis	[m]
$x_j$	local buoyant JICF horizontal streamwise coordinate	[m]
$y$	coordinate along horizontal lateral axis	[m]
$z$	coordinate along vertical axis	[m]
$z_j$	local buoyant JICF vertical coordinate	[m]
$z_B$	buoyancy length scale buoyant JICF	[m]
$z_C$	transition to bent over plume length scale buoyant JICF	[m]
$z_M$	momentum length scale JICF	[m]

### Greek symbols

$\beta$	spreading rate buoyant JICF	[-]
$\Gamma$	diffusion coefficient	[m <sup>2</sup> /s]
$\gamma$	velocity ratio	[-]
$\Delta r$	grid size in $r$ direction	[m]
$\Delta\phi$	grid size in $\phi$ direction	[m]
$\Delta x$	grid size in $x$ direction	[m]
$\Delta y$	grid size in $y$ direction	[m]
$\Delta z$	grid size in $z$ direction	[m]
$\Delta z^+$	grid size in $z$ direction in wall units	[-]
$\kappa$	von Karman constant	[-]
$\nu$	viscosity	[m <sup>2</sup> /s]
$\nu_e$	eddy viscosity	[m <sup>2</sup> /s]
$\nu_{mol}$	molecular viscosity	[m <sup>2</sup> /s]
$\nu_t$	turbulent viscosity	[m <sup>2</sup> /s]
$\rho$	density	[kg/m <sup>3</sup> ]
$\rho_c$	density carrier fluid	[kg/m <sup>3</sup> ]
$\rho_{cf}$	(ambient) density crossflow	[kg/m <sup>3</sup> ]
$\rho_{j0}$	initial density of buoyant jet or overflow mixture	[kg/m <sup>3</sup> ]
$\rho_l$	density of fraction $l$	[kg/m <sup>3</sup> ]
$\rho_{mix}$	mixture density	[kg/m <sup>3</sup> ]
$\rho_s$	sediment density	[kg/m <sup>3</sup> ]
$\rho_w$	water density	[kg/m <sup>3</sup> ]
$\tau$	shear stress	[N/m <sup>2</sup> ]
$\boldsymbol{\tau}$	shear stress tensor	[N/m <sup>2</sup> ]
$\tau_e$	critical erosion bed shear stress	[N/m <sup>2</sup> ]
$\phi$	coordinate along lateral axis in cylindrical coordinates	[m]
$\Psi$	effective angle between TSHD and ambient current	[°]
$\omega$	$2\pi/L$ wave number	[1/m]

## Abbreviations

2D	two-dimensional
3D	three-dimensional
ADCP	acoustic doppler current profiler
AV4	artificial viscosity scheme with fourth derivative damping
AV6	artificial viscosity scheme with sixth derivative damping
CDS2	second order central scheme
CFD	computational fluid dynamics
CVP	counter rotating vortex pair
DNS	direct numerical simulation
IMPROVE	impact reducing overflow extension
JICF	jet in crossflow
LES	large eddy simulation
OBS	optical back-scatter
RANS	Reynolds-averaged Navier-Stokes
RMS	root mean square
RK3	third order Runge Kutta time integration scheme
SEM	synthetic eddy method
SSB	Stichting Speurwerk Baggertechniek
TASS	turbidity assessment software
TDMA	tri diagonal matrix algorithm
TSHD	trailing suction hopper dredger
TVD	total variation diminishing
UPW5	fifth order upwind scheme
WALE	wall adapting local eddy viscosity sub-grid scale model



# List of publications

## Journal publications (peer reviewed)

Wit, L. de, van Rhee, C. (2014), Testing an improved artificial viscosity advection scheme to minimise wiggles in large eddy simulation of buoyant jet in crossflow, *Flow, Turbulence and Combustion*, 92(3):699 - 730.

DOI:[10.1007/s10494-013-9517-1](https://doi.org/10.1007/s10494-013-9517-1)

L. de Wit, G. Keetels and C. van Rhee (2014), Turbulent interaction of a buoyant jet with crossflow, *Journal of Hydraulic Engineering*, 140(12).

DOI:[10.1061/\(ASCE\)HY.1943-7900.0000935](https://doi.org/10.1061/(ASCE)HY.1943-7900.0000935)

L. de Wit, A.M. Talmon and C. van Rhee (2014), Influence of important near field processes on the source term of suspended sediments from a dredging plume caused by a Trailing Suction Hopper Dredger: the effect of dredging speed, propeller, overflow location and pulsing, *in press in Environmental Fluid Mechanics*.

DOI:[10.1007/s10652-014-9357-0](https://doi.org/10.1007/s10652-014-9357-0)

L. de Wit, A.M. Talmon and C. van Rhee, (2014), 3D CFD simulations of trailing suction hopper dredger plume mixing: comparison with field measurements, *Marine Pollution Bulletin*, 88:34 - 46.

DOI:[10.1016/j.marpolbul.2014.08.042](https://doi.org/10.1016/j.marpolbul.2014.08.042)

L. de Wit, A.M. Talmon and C. van Rhee (2014), 3D CFD simulations of trailing suction hopper dredger plume mixing: a parameter study of near field conditions influencing the suspended sediment source flux, *Marine Pollution Bulletin*, 88:47 - 61.

DOI:[10.1016/j.marpolbul.2014.08.043](https://doi.org/10.1016/j.marpolbul.2014.08.043)

## Conference publications

Wit, L de (2010). Near field 3d CFD modelling of overflow plumes. *In J Dobson (Ed.), Proceedings of the 19th world dredging congress* (pp. 712-723). Beijing, China: Chida. (CHIDA best paper award from CEDA Region)

Wit, L. de, Bliet, A.B., Frieling, J.H. (2011). Monitoring impact of land recla-

mation on siltation in an inland lake, *CEDA Dredging Days*, Rotterdam, the The Netherlands

Wit, L. de and C. van Rhee (2012). Testing different advection schemes for coarse high Re LES simulations of jet in crossflow and coflow. *Proceedings of ETMM9*, Thessaloniki (Greece)

Wit, L. de and C. Van Rhee (2013), Detailed full scale simulations of near field overflow plume mixing, *Proceedings of the 20th World Dredging Conference (WODCON XX)*, Brussels (Belgium)

Radermacher, M., Van der Goot, F., Rijks, D. and Wit, L. de (2013), The Art of Screening, Effectiveness of Silt Screens, *Proceedings of the 20th World Dredging Conference (WODCON XX)*, Brussels (Belgium)

Wit, L. de and C. Van Rhee (2013), Large Eddy Simulations of pulsed buoyant jet in crossflow, *14th European Turbulence Conference*, Lyon (France)

# Dankwoord

Terugkijkend was het promotietraject mooi en uitdagend en is er veel om in het dankwoord te verwerken. Allereerst wil ik prof. Van Rhee bedanken, Cees bedankt voor het enthousiasme vanaf de start voor een part-time promotie. Waar veel mensen bang zijn voor vertraging of zelfs afbreken van een promotie, zag jij vooral de voordelen van kruisbestuiving tussen beide banen. Ook bedankt voor alle input voor en terugkoppeling op mijn werk. Het feit dat je als professor toch snel en makkelijk benaderbaar bent is ook zeer gewaardeerd. Er was bijvoorbeeld altijd tijd om te discussieren over numerieke details van het meerfasen CFD model. Mijn dagelijks begeleider Arno Talmon wil ik bedanken voor het grondig doornemen van al mijn geschreven werk en voor alle ideeën met name rondom de metingen in het lab. Alle gesprekken met Geert Keetels over zin en onzin van hogere order numerieke schemas en turbulentie waren nuttig en mooi. De lab metingen werden uitgevoerd samen met afstudeerder Ko Liu, dank voor je werk. Mijn collegas op de TU, Arno, Rik, Joep, Ralf, Jort, Rudy, Xiuhan, Ershad, Bas, Dave, Frans, wil ik bedanken voor alle gezellige koffie momenten en lunches. Belangrijke zaken in het leven als wielrennen en voetbal werden grondig doorgenomen en en passent werden grote (geo)politieke vraagstukken als werkgelegenheid, energie en klimaatverandering eventjes opgelost.

Bram Blik van Svašek Hydraulics wil ik hartelijk bedanken voor de mogelijkheid om drie dagen per week vrijgezet te worden van projecten voor de part-time promotie. En ook mijn collegas bij Svašek worden gewaardeerd om alle interesse in mijn promotie studie en zeker ook om alle gesprekken over het leven naast het werk. Verder worden Svašek Hydraulics en NWO (SurfSARA) bedankt voor gebruik van een rekencluster voor een heel aantal van de zware CFD simulaties die gerapporteerd zijn in deze dissertatie. Het onderzoek is uitgevoerd binnen het Building with Nature innovatie programma. De financiële ondersteuning van Building with Nature en alle interactie met mede promovendi en mensen met veel praktijkervaring met baggerpluimen was doorslaggevend voor het succes van mijn promotietraject. De veldmetingen van baggerpluimen in 2011 zijn ook uitgevoerd binnen Building with Nature met meerdere partners van het consortium en dit was een fantastische en onmisbare ervaring binnen mijn promotie.

Mijn families De Wit, Molenaar en in 't Veld waardeer ik zeer om alle mooie ontmoetingen en de interesse in mijn soms wat abstracte werk. Ook vrienden wil ik bedanken voor interesse en inspiratie (en soms een beetje transpiratie), waarbij ik de groepen van kring, G8, bestuur Visser, oud-huisgenoten en fietsers specifiek wil benoemen.

Tot slot wil ik mijn vrouw Anna bedanken. Bedankt voor je liefde, interesse, terugkoppeling en begrip als ik best wel eens wat later thuis kwam. Echt heel mooi om met je getrouwd te zijn en nu ook gezegend te zijn met een fantastisch zoontje Coen. Ik ben wie ik ben door (mijn geloof in) God, daarom wil ik Hem bovenal bedanken.

# Curriculum Vitae

1981, August 12th	Born in Gouda, The Netherlands
1993-1999	Atheneum, Driestar College Gouda
1999-2004	Bachelor of Science in Civil Engineering, Delft University of Technology (cum laude)
2004-2006	Master of Science in Fluid Mechanics at the Faculty Civil Engineering and Geosciences, Delft University of Technology (cum laude) M.Sc. thesis on the development of a Smoothed Particle Hydrodynamics flow model awarded with the Prof. J.A. Battjes price for excellent student research on hydraulic engineering
2006-present	Hydraulic/morphological engineer and numerical developer at Svašek Hydraulics B.V., Rotterdam
2008-2014	Part-time Ph.D. researcher at the Section of Dredging Engineering, Faculty Mechanical, Maritime and Materials Engineering & Faculty Civil Engineering and Geosciences, Delft University of Technology

